A Polynomial Chaos Approach for Stochastic Modeling of Dynamic Wheel-Rail Friction

HyunWook Lee

Dissertation submitted to the faculty of the Virginia Polytechnic Institute and State University in partial fulfillment of the requirements for the degree of
Doctor of Philosophy
In
Mechanical Engineering

Corina Sandu, Chair
Cornel Sultan
Dan Inman
Mehdi Ahmadian
Shane Ross

August 31, 2010
Blacksburg, VA, USA

Keywords: Wheel-Rail Dynamics, Coefficient of Friction, Polynomial Chaos, Contact Patch, Wheel-Rail Vibration, Uncertain Parameters, Stochastic Analysis

A Polynomial Chaos Approach for Stochastic Modeling of Dynamic Wheel-Rail Friction

HyunWook Lee

ABSTRACT

Accurate estimation of the coefficient of friction (CoF) is essential to accurately modeling railroad dynamics, reducing maintenance costs, and increasing safety factors in rail operations. The assumption of a constant CoF is popularly used in simulation studies for ease of implementation, however many evidences demonstrated that CoF depends on various dynamic parameters and instantaneous conditions. In the real world, accurately estimating the CoF is difficult due to effects of various uncertain parameters, such as wheel and rail materials, rail roughness, contact patch, and so on. In this study, the newly developed 3-D nonlinear CoF model for the dry rail condition is introduced and the CoF variation is tested using this model with dynamic parameters estimated from the wheel-rail simulation model. In order to account for uncertain parameters, a stochastic analysis using the polynomial chaos (poly-chaos) theory is performed using the CoF and wheel-rail dynamics models.

The wheel-rail system at a right traction wheel is modeled as a mass-spring-damper system to simulate the basic wheel-rail dynamics and the CoF variation. The wheel-rail model accounts for wheel-rail contact, creepage effect, and creep force, among others. Simulations are performed at train speed of 20 *m/s* for 4 *sec* using rail roughness as a unique excitation source. The dynamic simulation has been performed for the deterministic model and for the stochastic model. The dynamics results of the deterministic model provide the starting point for the uncertainty analysis. Six uncertain parameters have been studied with an assumption of 50% uncertainty, intentionally imposed for testing extreme conditions. These parameters are: the maximum amplitude of rail roughness (MARR), the wheel lateral displacement, the track stiffness and damping coefficient, the sleeper distance, and semi-elliptical contact lengths. A symmetric beta distribution is assumed for these six uncertain parameters. The PDF of the CoF

has been obtained for each uncertain parameter study, for combinations of two different uncertain parameters, and also for combinations of three different uncertain parameters.

The results from the deterministic model show acceptable vibration results for the body, the wheel, and the rail. The introduced CoF model demonstrates the nonlinear variation of the total CoF, the stick component, and the slip component. In addition, it captures the maximum CoF value (initial peak) successfully. The stochastic analysis results show that the total CoF PDF before 1 *sec* is dominantly affected by the stick phenomenon, while the slip dominantly influences the total CoF PDF after 1 *sec*. Although a symmetric distribution has been used for the uncertain parameters considered, the uncertainty in the response obtained displayed a skewed distribution for some of the situations investigated. The CoF PDFs obtained from simulations with combinations of two and three uncertain parameters have wider PDF ranges than those obtained for only one uncertain parameter.

FFT analysis using the rail displacement has been performed for the qualitative validation of the stochastic simulation result due to the absence of the experimental data. The FFT analysis of the deterministic rail displacement and of the stochastic rail displacement with uncertainties demonstrates consistent trends commensurate with loss of tractive efficiency, such as the bandwidth broadening, peak frequency shifts, and side band occurrence. Thus, the FFT analysis validates qualitatively that the stochastic modeling with various uncertainties is well executed and is reflecting observable, real-world results.

In conclusions, the development of an effective model which helps to understand the nonlinear nature of wheel-rail friction is critical to the progress of railroad component technology and rail safety. In the real world, accurate estimation of the CoF at the wheel-rail interface is very difficult since it is influenced by several uncertain parameters as illustrated in this study. Using the deterministic CoF value can cause underestimation or overestimation of CoF values leading to inaccurate decisions in the design of the wheel-rail system. Thus, the possible PDF ranges of the CoF according to key uncertain parameters must be considered in the design of the wheel-rail system.

ACKNOWLEDGMENTS

I am heartily grateful to my advisor, Dr. Corina Sandu, for her encouragement, support, and guidance. She gave me great help in writing conference and journal papers, in preparing power point for presentations, and in presenting my research to people in conferences and NASA. In addition to the academic support and guidance, she tried to take care of financial supports for me and also gave me great environment that I can focus on my research. I learned how to take care of students in academics as an advisor and as a person from her.

I would like to thank my supervisor, Mr. Carvel Holton. He has been provided financial supports and has given me a lot of knowledge and helps for analyzing experimental data. In addition, he taught me how to connect the theory and the physical phenomena in the real world.

I am grateful to Dr. Ahmadian, one of my committee members and the director of CVeSS. As an expert of the wheel-rail system, he gave me a lot of helps to improve our wheel-rail dynamic model. Without his help, I might not be able to develop a correct wheel-rail dynamic model.

I also want to thank my other committee members, Dr. Dan Inman, Dr. Shane Ross, and Dr. Cornel Sultan, for their valuable opinions, advices, and encouragement. Their opinions have improved my research a lot.

This is also a great opportunity to express my heartful thanks to all biomechanics lab members. Mr. Michael Diersing gave me valuable advices for me as a best friend. Dr. Corrie Spoon helped me improving my English speaking and writing. All other members also gave me a good friendship and helped me adapting American culture. Without all my biomechanics members, I could not overcome the hard time at Blacksburg and I could not improve my English. They will be in my heart during whole my life.

I would also like to thank all my labmates at CVeSS and AVDL for their companionship and for their help. Specifically, Anake Umsrithong shared really good friendship and good discussion related to the research. I cannot forget having good time with him in Thailand. Dr. Emmanuel Blanchard helped me applying the polynomial chaos theory to my research. In addition to labmates, I want to thank Mrs. Sue Teel and Ms. Sarah Sullivan. They took care of all non-academic works for me. I am truly grateful for their assistance. I will keep them in my heart and I will pray for their success in their career and for their happiness in their lives.

I also would like to gratefully acknowledge the support from NASA and the partial support from TTCI/AAR. Without their supports, I could not focus on my research.

Finally, I would like to dedicate my deepest gratitude to my parents, Mr. Hyung Woo Lee and Mrs. Sook Ja Kim, and to my younger brother, Mr. Sang Min Lee, for their endless love and for their endless encouragement. Without them, I could not get Ph.D. degree.

Contents

List of Figures

List of Tables

Chapter 1. Introduction

In this Chapter I discuss the motivation behind this study, define the problem statement, outline the research approach, summarize the dissertation's main contribution, and introduce the topics to be presented in the rest of the document.

1.1 Motivation

Several reasons motivated the study described in this dissertation. They are related to cost and safety for railroad operations and miss-match between experimental and simulation data, and are detailed in this section. Moreover, the need to develop nonlinear, stochastic models for the coefficient of friction is also discussed.

Cost and Safety

The coefficient of friction (CoF) is one of the most important parameters for characterizing the contact between the wheel and the rail. Underestimating the CoF at the wheel-rail interface may lead to skid flats, long braking distances, low locomotive traction, and inadequate wear. Conversely, when the CoF is overestimated, high energy, increased wheel-rail wear, increased wheel-rail noise, and rapid initiation of contact fatigue may occur [81]. Therefore, accurate estimation of the CoF plays a very important role in modeling the railroad dynamics, reducing operational and maintaining cost, and increasing safety factor in the long-term.

Miss-match Between Experimental Data and Simulation Data

At the wheel-rail interface, a common point on the wheel and on the rail has, in general, different velocities on the wheel, respectively on the rail. The difference between the wheel and the rail velocities is critical in estimating the friction in the wheel-rail contact patch. Moreover, measuring rail velocity is very important for the correct calculation of the sliding velocity, which can be defined as the difference between the wheel and rail velocity, which is very important in estimating the CoF. To assess this relative motion, one must accurately measure the two

velocities. While the wheel velocity could be measured relatively easily, currently, there is no commercial sensor which can measure the rail velocity.

In this study, the wheel and rail velocities were measured using a Laser Doppler Velocimetery (LDV) sensor newly developed at Virginia Tech's Railway Technologies Lab. The Transportation Technology Center, Inc. (TTCI) also provided the sliding velocity results from a numerical simulation where a constant CoF was employed into the rail simulation software NUCARS® to compare them with the sliding velocity calculated from the measured wheel and rail velocity collected with the LDV system. This comparison showed a significant difference between the simulation and experiment results. Thus, we concluded that using a constant CoF (i.e., the slip CoF which will be introduced in Chapter 2.) is insufficient, and a new, more accurate CoF model is needed.

Necessity of a Nonlinear CoF Model for Railroad System

For ease of implementation, due to the very complex nature of the wheel-rail contact dynamics, the assumption of a constant CoF is still used in most theoretical studies. As mentioned in the paragraph above, it has been noticed that the sliding velocity from the NUCARS® simulation using a constant CoF was different than the sliding velocity measured experimentally with a LDV sensor. In addition, many experimental studies indicates that the CoF depends on the dynamic changes in various wheel-rail conditions, like material difference, sliding velocity, contact patch area, wheel and rail geometry, relative wheel vibration, wheel-rail surface roughness, temperature, humidity and/or lubrication, etc. [2]. The complex behavior influenced by many material and dynamic parameters cannot be predicted by a simple, linear CoF model. Therefore, a more complex and specialized nonlinear model for CoF in railroad is necessary to improve the correlation between the mathematical models and the experimental observations.

Necessity of Stochastic Analysis

In the real world, accurate estimation of the CoF at the wheel-rail interface is not simple because it is influenced by various uncertain parameters. For examples, the rail material can be different from location to location and the track stiffness and damping may also change at

different locations. Rail roughness is different from rail to rail and from time to time because of difference in grinding, finishing, and so on. Contact patch size cannot be accurately calculated from theory due to hard to measure or calculate changes in railroad dynamics and geometry, such as the relative wheel vibration, wheel-rail roughness, relative lateral wheel displacement, and rail conformity. In addition, estimating one value of the CoF at a specific location or small area is not meaningful because the wheel and rail wear in time, and conditions of the wheel, rail, and environment also change with time. Thus, to better understanding the behavior of the CoF and to obtain meaningful estimates for it, it is needed to explore the CoF in a stochastic framework.

1.2 Problem Statement

This document focuses on the development of a railroad dynamics model and nonlinear CoF model in a stochastic framework using the polynomial chaos theory. Current challenges in this research area are discussed below.

Nonlinear 3-D CoF Model for Dry Rail Condition

Accurate estimation of the CoF is very important in the railroad industry to reduce cost, to increase safety, and to accurately model railroad dynamics. Several CoF models have been developed and are presented in the literature, but they have not succeeded in capturing accurate CoF values. A two dimensional (2-D) nonlinear CoF model (longitudinal and vertical directions) for lubricated surface conditions has been developed by Soom and his colleagues [34], and accurately matches experimental data. However, this model has never been applied to railroad dynamics. In addition, a 3-D nonlinear model has not been developed yet to account for relative wheel lateral motion. Relative lateral wheel motion is an important factor which must be accounted for to correctly model railroad dynamics and CoF since it affects the change of the contact patch size, an important factor for CoF changes. Thus, developing a 3-D CoF model is one of the main goals of this study.

Stochastic analysis of railroad dynamics and CoF

Estimating CoF through simulation is not a simple task, since the real life wheel, rail, and environmental conditions vary with time and location. For example, wheel-rail surfaces are not

perfectly clean, rail materials are not perfectly uniform through locations, humidity and temperature differ with time and location, etc. In other words, there are many uncertainties which influence railroad dynamics and estimating CoF, including those due to the fact that the wheel-rail conditions keep changing as the train runs and due to changes in the dynamics of the system. In order to realistically estimate the railroad dynamics and the uncertain dynamic parameters that affect the CoF must be treated in a stochastic manner.

1.3 Research Approach

The first step of this study was to develop a 3-D nonlinear CoF model for a railroad system including longitudinal, vertical, and lateral motion. For this work, a 2-D nonlinear CoF model for a lubricated condition from Soom's and his colleagues' work was expanded to 3-D and modified for dry conditions using unit analysis. This model was selected as the starting point because it has already been shown that it matches well with 2-D experimental data. The next step was to develop an algorithm to simulate the railroad dynamics, including the CoF, and to implement it. In order to test the feasibility of this algorithm, specific railroad running conditions were considered. Upon completion of this task, possible uncertain railroad dynamic parameters have been selected, quantified using a polynomial chaos approach, and tested independently using a collocation method. The next step was to investigate the effect of considering two and three independent uncertain parameters acting in the same time. Concluding remarks drawn from the preliminary results helped identify those uncertain parameters that, alone or in combinations, may significantly influence the railroad dynamics and the changes in the CoF.

1.4. Main Contribution

This research focuses on the development of a nonlinear coefficient of friction (CoF) model and of an associated railroad dynamic model. In addition, uncertain railroad parameters are quantified using a polynomial chaos theory and the resulting stochastic system has been investigated.

The main contributions of this study are:

1) It is the first systematic study that treats the railroad dynamics and the CoF in a stochastic framework using a polynomial chaos approach.
2) It is the first attempt to develop and apply a 3-D nonlinear CoF model to the railroad system.
3) This study deals with multi-scale problems from micro/nano scale (e.g., local conformities, rail roughness, etc.) to macro scale (e.g., system vibration) for the contact patch model at the wheel-rail interface.

1.5 Dissertation Outline

Chapter 2 introduces the necessary background to understand the basic theory of dry friction, coefficient of friction models, and the basic polynomial chaos theory. It also includes a literature review related to these subjects. In Chapter 3, the wheel-rail simulation model (the deterministic model) with a 3-D nonlinear CoF model is illustrated. First, the development of a 3-D nonlinear CoF model derived starting from Soom's 2-D model is explained. Second, a detailed wheel-rail dynamic model applying the developed CoF model is described. Finally, the stochastic model using polynomial chaos will be introduced. In Chapter 4, results from the deterministic model and results from the stochastic model with one uncertain parameter are shown and discussed. Case studies for combinations of two independent uncertain parameters and for combinations of three independent uncertain parameters are also shown. Chapter 5 includes a summary of the important findings, conclusions, and future studies.

Chapter 2. Dry Friction of Stochastic Modeling Background

The purpose of this chapter is to provide the background for the research conducted in this study. The first section introduces the terminology used. The second section presents the basic theory of general dry friction and discusses published literature on four important dynamic parameters which affect the coefficient of friction (CoF). The third section introduces existing CoF models including one or more parameters. It also presents a specific nonlinear model developed by Soom's group [34], which is considered a good candidate as a starting point in our study. The last section of Chapter 2 explains the background on the polynomial chaos theory and the collocation method used in this study.

2.1 Terminology

Specific railroad terminology used in the context of this specific study is defined in this section.

1) *Slip* – The relative local velocity of two bodies at the contact point is different [35]. In railroad dynamics, slip is the relative local velocity at the contact patch between the wheel and the rail surface while the wheel runs with contact on the rail. This concept is generally used in the micro or nano scale, i.e., the local area in the contact patch where slip is considered is micro or nano scale. In this study, the "slip" term is used only for the contact patch and the corresponding CoF (slip CoF).

2) *Pure rolling (stick)* – Pure rolling is the state in which the velocities of two bodies relative to each other at the contact point is the same. Stick is the state that the relative local velocity of the bodies at a contact point is same. Thus, pure rolling and stick is the same concept while pure rolling is macro scale phenomenon and stick is micro or nano scale phenomenon in the contact patch. In this study, stick is also used only for the contact patch and the CoF (stick CoF).

3) *Sliding* – If the velocities of two bodies at the contact point are not equal, the rolling motion is accompanied by sliding [86]. In railroad dynamics, sliding is defined as the relative velocity between a wheel and a rail at contact patch while a wheel runs on the rail. This sliding concept is used only for macro scale phenomena. Thus, in this study, sliding is used for the velocity difference between a wheel and a rail, not at the microscopic level in the contact patch.

4) *Sliding velocity* – Relative velocity between the wheel and the rail. In this study, the sliding velocity is defined as the difference between wheel velocity and rail velocity, as given by Equation (2.1).

$$V = V^w - V^r \tag{2.1}$$

Many studies work under the assumption that the wheel-rail contact patch has an elliptical shape. In Figure 2.1, a and b are the semi-axes of the contact patch in the longitudinal (along the rail) and lateral (transversal to the direction of the rail) direction, respectively; ω is the angular wheel velocity; R_w is the wheel radius of curvature; V_w and V_r are the wheel velocity and the rail velocity, respectively; V_{train} is the train velocity.

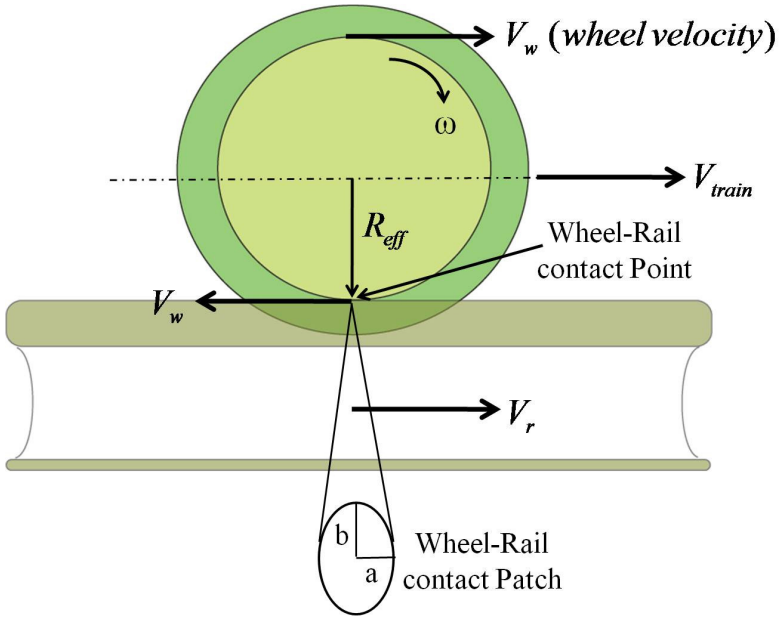

Figure 2.1: Schematic diagram of a wheel-rail contact, and the associated velocities

If no relative lateral motion of the wheel is assumed, the rail velocity is the same as the train's forward velocity. In the case accounting for relative lateral wheel motion, rail velocity is defined as shown in Equation (2.2):

$$V_r = V_{train} \times \frac{R_w}{r_o} \tag{2.2}$$

where r_o is the mean wheel radius of curvature. This equation takes into account the fact that the wheel's radius of curvature changes with changes in the wheel-rail contact position by relative lateral motion.

5) *Dry friction* – Dry friction is the resistant force tangential to the interfaces between two bodies when, under the action of an external force, one body moves or tends to move relative to the other one [76]. In the context of this study, dry friction refers to the friction without any lubricant/top of the rail modifier at the wheel-rail interface. Such friction is traditionally modeled using the Coulomb friction law, as shown in Equation (2.3).

$$F_f = \mu N \tag{2.3}$$

where F_f is the dry friction force, μ is the friction coefficient, and N is the normal force.

6) *Creepage (or Creep)* – The dimensionless term creepage (or creep) is used to define the deviation from a pure rolling motion of two bodies [35]. In the railroad study, the wheel and the rail can be assumed as two rolling bodies if the wheel rolls on the rail with contact. Thus, in this study, creepage is defined as the sliding velocity normalized by the train velocity, as illustrated by Equation (2.4).

$$Creepage = \frac{V^w - V^r}{V_{train}} \tag{2.4}$$

In general, the mean of the wheel and rail velocities is used as a denominator for normalization [35-39]; however, the longitudinal train velocity is used as a denominator in

this study since wheel velocity keeps changing with the lateral motion. Thus, the mean velocity is almost the same as the longitudinal train velocity. Specific definitions for longitudinal, lateral and spin creepages are introduced in Chapter 3.

2. 2 Literature Review and Background

2.2.1 General Dry Friction for Rigid/Deformable Bodies

Brief History of Friction Study

Friction has been studied for very long time. Several researchers, (e.g., Leonardo da Vinci, Guillaume Amontons, Leonard Euler, and Charles-Augustin de Coulomb) contributed to the study of friction. Leonardo da Vinci described the relationship between sliding friction and normal weight without mentioning the term "*friction force*" [77]. In 1699, Amontons, a French architect, proposed two classical friction laws [76]:

1. The force of friction is directly proportional to the applied normal load.
2. The force of friction is independent of the apparent area of contact.

Amontons' first law still holds, and is incorporated in Equation (2.3), commonly known as the Coulomb friction law. However, some studies have shown that the second law is not always valid for elastic, deformable materials like metal-metal interface [4, 11, 12, 29, 76]. An important contribution from Leonhard Euler was to clearly distinguish static friction from kinetic friction. Coulomb developed the model for dry friction, Equation (2.3), and developed Coulomb's law of friction that says kinetic friction is independent of the sliding velocity. Equation (2.3) is still broadly used to find the friction coefficient when we know the normal force and friction force. However, some studies have shown that the friction coefficient changes with sliding velocity [1-5, 30-34] or creepage [21-23]. Recently, a nonlinear dynamic model for the friction coefficient was developed by Polycarpou and Soom [34]. Due to its nonlinear nature and complex behavior, friction continues to be an on-going research topic.

General Dry Friction

Friction occurs when two solid bodies are placed together under non-zero normal force and acted upon by another force that is applied parallel to the contact surface (tangential force) [76]. Relative movement of one solid body to the other may occur or may not, depending on whether the applied force is larger than the friction force opposing it. One possible friction classification is: dry friction, wet (lubricated or fluid) friction, and internal friction. They are defined as follows:

1. Dry friction – the resistant friction of relative tangential motion of two solid surfaces when, under the action of an external force, one body moves or tends to move relative to the other one with which it is in contact [76]. It has two components: static friction (before the surfaces move with respect to each other) and kinetic friction (after the relative motion starts). Sometimes kinetic friction is called sliding friction or dynamic friction. In this study, the term sliding friction will be used instead of kinetic or dynamic friction.

2. Wet friction – the resistant force of relative tangential motion of two solid surfaces separated by a layers of gas or liquid when, under the action of an external force, one body moves or tends to move relative to the other in contact [78, 79]. In the railroad context, wet friction can be obtained when lubricant or top of rail modifier is applied on the rail. Sometimes wet friction is called lubricated friction [78] or fluid friction [79].

3. Internal friction – the force resisting motion between the elements making up a solid material while it undergoes deformation [80].

This study focuses only on friction under dry rail conditions.

A simple force diagram with a block on the ground is introduced in Figure 2.2 to explain dry friction. Using this diagram, the dry friction force (F_f) can be explained by Coulomb's law provided in Equation (2.3). The normal reaction force (N) is equal to the weight (W). The dry friction is proportional to the applied normal load (W), according to Equation (2.3). If the applied force F does not exceed the dry friction force (F_f), no relative motion between the block and the ground will occur. In this case, the dry friction is the equal to the static friction (F_{static}).

However, if F increases to values greater than F_f, the block starts moving to the left relative to the ground. In this case, the dry friction is the sliding friction ($F_{sliding}$).

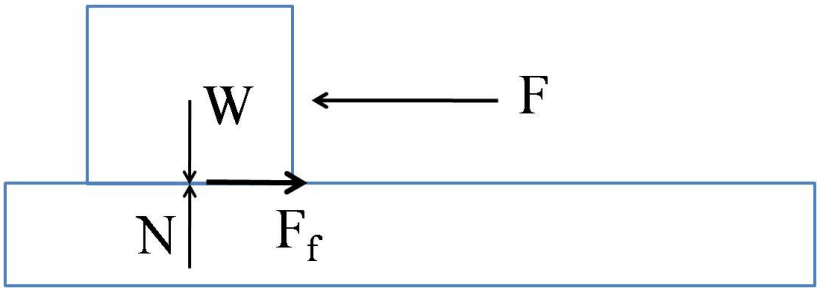

Figure 2.2: Force diagram for block on the ground. W is weight of block; F is an applied external force; N is the normal force; F_f is the friction force; and μ is the coefficient of friction.

The main focus of this study is to model the non-linear CoF, to study its dependencies on various parameters, and to apply the CoF model developed to a railroad dynamic model.

CoF is defined as a dimensionless scalar value which is the ratio of the force resisting tangential motion between two bodies to the normal force pressing those bodies together [76], and it can be derived from Equation (2.3), as shown in Equation (2.5).

$$\mu = \frac{F_f}{N} \tag{2.5}$$

Generally, the CoF ranges from zero to one. In some specific conditions, for example a CoF from clean and well-adhering metals [76], it can be greater than one. A CoF greater than one simply means that the force needed to make an object move is greater than the normal force of the surface between objects or between an object and ground. Zero CoF means that there is no friction at all. Thus, an object keeps moving along in the direction along which a force is applied with an initial force. A space shuttle in space is a good example of zero CoF.

The CoF can also be classified into the static CoF and the kinetic CoF, as shown in Figure. 2.3. The static CoF (μ_{static}) is defined from the static friction (F_{static}), as shown in Equation (2.6 a). If the normal load is constant, the static CoF can take any value between zero and μ_{max} when there is no occurrence of sliding. In the same way, the sliding CoF ($\mu_{sliding}$) is

defined from the sliding friction ($F_{sliding}$), and as shown in Equation (2.6 b). Usually, the static CoF is greater than the sliding CoF as Figure 2.3 shows. Note that Equations (2.5), (2.6 a), and (2.6 b) are not models or laws of CoF but definitions [76].

$$\mu_{static} = \frac{F_{static}}{N} \tag{2.6 a}$$

$$\mu_{sliding} = \frac{F_{sliding}}{N} \tag{2.6 b}$$

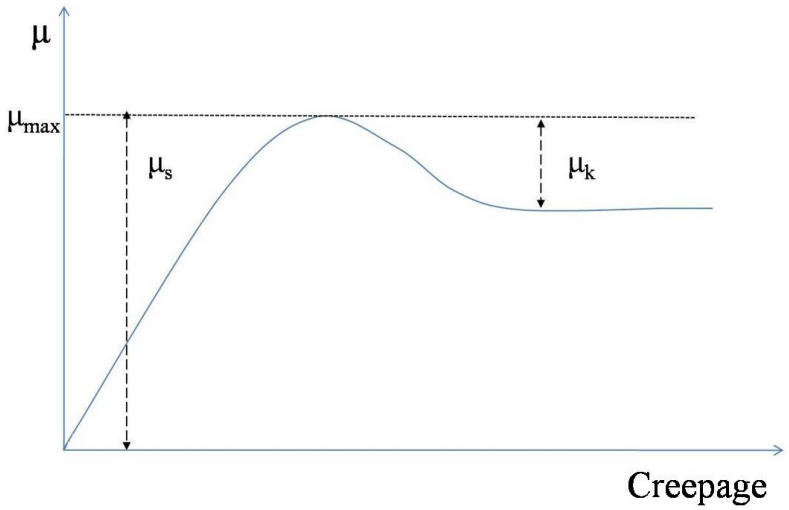

Figure 2.3: General trend of the CoF with time. μ_s is the static CoF; μ_{max} is the maximum static CoF; and $\mu_{sliding}$ is the kinetic/sliding CoF. An object starts sliding relative to another object (or the ground) as soon as CoF changes from the static CoF to the kinetic CoF.

Static Friction and Sliding Friction

The maximum possible friction force (F_{max}) between two surfaces before sliding starts is obtained by multiplying the maximum static CoF (μ_{max}) by the normal force. The static friction force is always smaller than or equal to the maximum static friction force.

$$F_{static} = \mu_{static} N \leq \mu_{\max} N \tag{2.7}$$

The static friction force can be any value between zero and F_{max} while an object has no relative motion. When an applied external force greater than F_{max} overcomes the static friction force, it

leads to the relative motion (sliding or slip) between objects. As soon as sliding or slip occurs, static friction is not applicable anymore and sliding friction starts.

Nonlinearity of the Coefficient of Friction

The typical behavior of the CoF has been discussed above and illustrated in Figure 2.3. However, in reality the CoF does not always follow Figure 2.3 for deformable bodies, because the CoF is in fact dependent on the contact patch size [11, 12, 27-29], In the context of the wheel-rail contact, this means that the sliding CoF ($\mu_{sliding}$) is not always constant [1, 2, 22, 23]. The CoF is dependent on materials. For example, the CoF for ice on steel is much smaller than the CoF for steel on steel. In addition to materials, the CoF is influenced by system dynamic variables like temperature, atmospheric conditions, and other factors [81]. Figure 2.4 shows an example of the nonlinear changes of the CoF with some of these variables (temperature and humidity). The top line in Figure 2.4 (a) and the two top lines in Figure 2.4 (b) are different from general CoF curves shown in Figure 2.3.

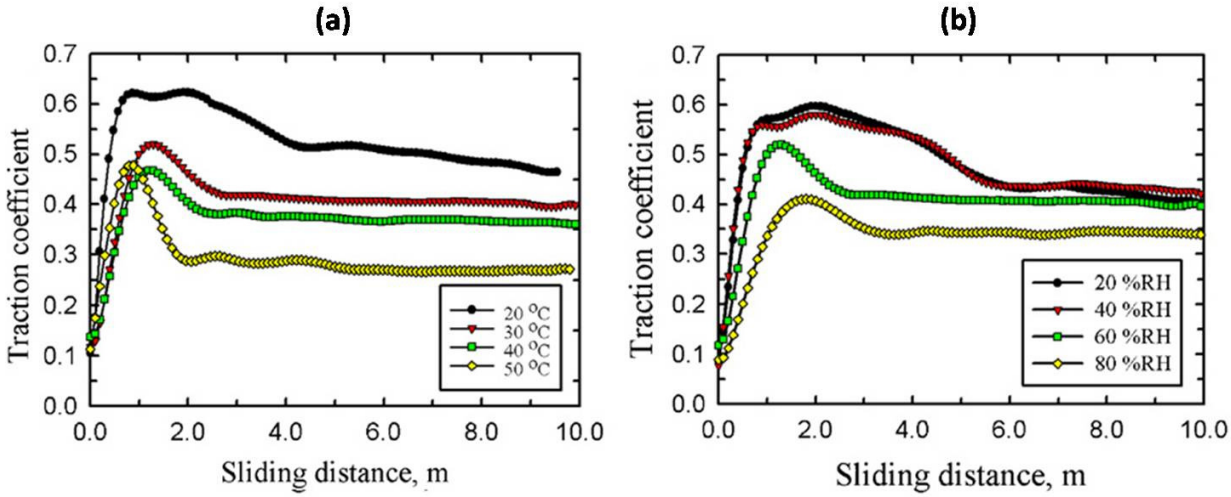

Figure 2.4: An example of the non-linear change of the CoF at different temperatures (a), and at different humidity (b) in dry condition from reference [81].

Key parameters such as material properties, sliding velocity, normal vibration, lateral displacement, and surface roughness (rail roughness in this study) are introduced in section 2.2.2, and discussed in the context of the literature review performed.

2.2.2 Dynamic and Material Parameters Influencing Dynamic CoF Change

For ease of implementation, due to the very complex nature of the wheel-rail contact dynamics, the assumption of a constant CoF is still used in most theoretical studies even though research has shown that the CoF changes dynamically with the dynamic changes in various wheel-rail conditions. Miss-calculation of the CoF impends on efforts towards reducing the cost and improving safety in railroad operations. Thus, it is critical to improve the accuracy of the estimation of the CoF under the specific conditions considered in the study.

To understand and calculate the dynamic CoF correctly, studying the dynamic parameters that have an impact on the CoF variance is very important. Many studies have been conducted to measure or quantify these parameters, and many studies are on-going to deepen our understanding. These dynamic parameters include material parameters [1-2], sliding velocity [1-5], rail roughness [6-10], normal vibration and contact patch size [4, 8, 9, 11-16, 29], wheel lateral motion [17-19], etc. In this section, some of the important parameters which have been reported in literatures are reviewed and discussed.

Material Parameters

Material parameters, for example Poisson ratio, Young's modulus, density, etc., play an important role in changing the CoF [1, 2]. Poisson ratio and Young's modulus are parameters used for calculating contact patch size, one of the dynamic parameters that impacts CoF, based on the Hertzian contact theory (Hertzian contact theory will be explained in Chapter 3). These two material parameters are also used to calculate non-linear Hertzian contact stiffness which shows the non-linear interaction at the contact patch between the wheel and the rail.

The relationship between material parameters and the CoF have been studied by Popov's group using numerical simulation [1, 2]. Popov et al. [1] investigated the dependence of the CoF in the wheel-rail system on the material parameters for the lubricated condition. They developed the linear CoF model expressed by two dimensionless arguments which included material parameters (Young's modulus, Poisson ratio, density, and ultimate strength), normal pressure and sliding velocity to simulate the impact of material parameters under the condition of inelastic processes (plastic deformation and fracture) in the sub-micrometer range. They found that the

CoF depends on these two dimensionless combinations. Bucher et al. [2] applied the same CoF model to the dry condition. They also concluded that material parameters have an important impact on the CoF for the dry condition.

Sliding Velocity

Some studies showed that sliding velocity is one of the parameters that causes dynamic change of the CoF through an experiment and simulation [3], a numerical simulation [1, 2], and an experiment [4, 5]. Hess and Soom [3] ran experiments to investigate CoF-sliding velocity characteristics of line contacts operating under unsteady sliding velocity in the three different lubricated conditions. They developed a simple experimental apparatus consisting of a disk and a circular flat rider button allowing line contact between them. They measured average CoF at velocities ranging between 0.01 and 1.0 m/s. They modeled the CoF based on experimental data and simulation using this model agreed with experimental results. This study showed that the CoF changes dynamically during unsteady sliding velocity.

Popov et al. [1] and Bucher et al. [2] also showed the dependence of sliding velocity on the dynamic change of CoF in the same studies which were introduced in the section "Material Parameters" on the lubricated condition and dry condition in numerical simulation, respectively. They used the same linear CoF model based on the method of movable cellular automata to simulate the CoF variance between surface layers and they calculated the CoF with a moving layer at velocities ranging between 1 and 10 m/s. These studies showed that the sliding velocity is one of the important dynamic parameters affecting the dynamic CoF change for both the lubricated and dry conditions.

Sakamoto [4] studied the dynamic CoF-sliding velocity relationship in the slip stage of stick-slip vibration using a pin-on-flat experimental set-up under dry surface conditions. This study reported that the CoF gradually decreased with sliding velocity. Puchalski et al. [5] reported 30% to 100% dynamic increase of the CoF with sliding velocity, moving the range from 0.42 mm/s to 16.67 mm/s through experiments using apple cultivars and moving surfaces.

Normal Contact Vibration Induced by Surface Roughness

When two bodies roll or slide over one another, the roughness of the contacting surfaces leads the bodies to vibrate [6]. The rolling contact vibrations have been studied by Nayak [6] and Gray and Johnson [7]. Nayak [6] discussed the rolling contact vibrations from an analytical point of view with linearization for relatively small values of the dynamic Hertzian deflection. Gray and Johnson [7] measured normal contact vibrations induced by surface-roughness using the experimental set up of two rollers pressed for rolling contact. In addition, they studied contact vibrations theoretically with an equivalent dynamic system consisting of the Hertzian contact (non-linear) spring and masses which represented the Hertzian contact deformation of two rollers, respectively. They found good agreement between measured and calculated vibration derived from measured and calculated acceleration.

Soom and Kim [8] measured random normal contact vibrations during smoothly sliding hemispherical steel contacts at a constant speed under dry and boundary lubricated conditions. Soom and Chen [9] showed that random surface roughness induced normal vibrations at Hertzian contacts during steady sliding using a physical model consisting of a mass, a spring, and a damper. They found that the simulation results using the nonlinear Hertzian stiffness had good agreement with experimental measurements of contact vibrations by Soom and Kim [8]. Wu et al. [10] developed a finite element model of a vehicle/track system consisting of masses, springs, and dampers to investigate the vehicle/track interaction and stick-slip vibration between wheel-rail surfaces due to rail surface contaminants and roughness. They reported that vertical vibration during the stick-slip motions at the wheel-rail interface occurred when the wheelset met vertical irregularities or contaminants on the track. From these studies we conclude that the surface roughness, such as the wheel-rail surface roughness, is an important factor which affects normal contact vibration.

A reduction in friction due to normal vibration with constant sliding velocity was observed by Tolstoi [15], Tolstoi et al. [16] and Sakamoto [4]. A reduction in friction means a reduction in CoF based on Coulomb's law since normal force oscillates due to normal vibration. Tolstoi [15] and Tolstoi et al. [16] modeled the contact region between two steel surfaces as a

non-linear spring, using an empirical stiffness relation. The relation between the friction force and the normal vibration was calculated by the contact region model and was measured experimentally by an apparatus with and without a damper. The friction reduction due to normal vibration was observed for various steel surfaces. Sakamoto [4] reported that the CoF decreases with normal displacement during the slip motion with a pin-on-flat apparatus under dry condition and varying sliding velocity. Normal vibration was detected by measurement of electrical contact resistance across the contact point. This study concluded that the change of the contact patch area due to normal vibration of the sliding body led to the CoF changes. This conclusion is supported by the finding that the contact patch area changes due to the normal load change by Jin et al. [20] and Hess and Soom [11, 28]. They showed how the contact patch area and shape changes with normal load changes through measurement using the full-scale test rig.

The change of the CoF due to the contact patch area change caused by normal vibration has been observed by Hess and Soom [11] through numerical simulation. They modeled the physical system using a mass, a non-linear spring, and a linear viscous damper and modeled the contact region as a nonlinear spring in parallel with a viscous damper. The externally applied harmonic normal loads induced the vibration.

In this study, the friction force is assumed to be proportional to the contact area. This study showed that dynamic vibrations led to changes in the contact patch area, and this change of the contact patch area led to changes in the friction coefficient. Hess et al. [12] and Hess and Soom [29] simulated the relation between vibration, the contact patch area, and the CoF statistically during constant sliding velocity under either an external or an internal random excitation at a Hertzian contact using the Fokker-Planck equation and a perturbation solution, respectively. The results were compared with experimental data measured by Soom and Kim [13], Soom and Chen [9], Kim [14], and Soom and Kim [8]. They used the same dynamic model and contact region model under external random normal load distributed as a white Gaussian or a rough surface input. The same assumption for the relation between the friction force and the contact area was applied. The statistic results of the stationary response compared with experimental data showed that changes of normal vibration caused the change of the contact patch size and then the contact patch variance results in changes of the CoF.

The relation between the CoF and the normal vibration was studied experimentally with a pin-on-disk type apparatus by Soom and Kim [13]. Measurements were performed during unlubricated smooth sliding between steel surfaces with constant sliding velocities ranging between 4 and 45 cm/s. Normal vibration was induced by surface irregularities being swept through the contact region during sliding. The result showed large normal and CoF oscillations during dry sliding.

Lateral Displacement

The vertical vibration at the wheel-rail interface can change the contact patch size. Then, it will affect the change of the CoF. In the same manner, the relative lateral wheel-rail motion combined with irregularities in the lateral direction on the contact surfaces of the wheel-rail may be able to affect the change of the contact patch size by changing the semi-elliptical contact patch length in the lateral direction. This lateral motion effect was studied by exploring the coupling between the motion in the vertical and in the lateral directions at the wheel-rail interface [17-19]. Thompson [17, 18] studied the wheel-rail interaction with such coupling using linear frequency-domain numerical simulation model. This model assumes a linear dependence between the vertical contact force and the deflection and no loss of contact. Thompson [17] found that height variations in the lateral direction of the surfaces can lead to changes in the lateral position of the contact patch relative to wheel and rail, without the wheel or rail lateral direction movement. Another study from Thompson [18] showed that the lateral movement of the contact patch is a potentially significant source of an additional excitation source for wheel-rail interaction.

Wu and Thompson [19] developed a theoretical time domain model to simulate the high frequency wheel-rail interaction with coupling between the vertical and lateral directions. This model included a wheel mass, a non-linear Hertzian contact stiffness which generates the vertical wheel-rail interaction, track model represented by an infinite Timoshenko beam with continuous spring-mass-spring system, and a rail modeled as an infinite Timoshenko beam. The lateral interaction is modeled as a contact spring and a creep force damper in series. The vibration was caused by the roughness on the wheel and rail contact surfaces. The offset of the wheel-rail

contact point from the rail center line introduced coupling between lateral and vertical directions. This study showed that the lateral force increases and the vertical force decreases with the offset. In addition, the contact patch size change with this coupling was inferred.

2.2.3 Current State of the Art in CoF Models

Many studies have been conducted to find a perfect CoF model. Most of the CoF models have been developed through experimental data. Thus, equations include only one [21] or some parameters [1, 2, 3, 22-25, 31, 33, 34] considered in their specific studies.

Some CoF models were developed in studies of squeal noise at the wheel-rail interaction in tight curved track [21, 24-25]. Rudd [21] presumed that the lateral creepage causes squeal noise and analytically developed the CoF model given by Equation (2.8) dependent on the lateral creepage based on the CoF and creepage curve, as shown in Figure 2.5. This model shows that the CoF is zero when the creepage goes to infinity; however the friction coefficient is not zero in reality, even though the creepage is infinite for the contact between the wheel and rail.

$$\mu = \mu_o \left(\frac{\xi}{\xi_o} \right) e^{\left(1 - \xi / \xi_o\right)} \tag{2.8}$$

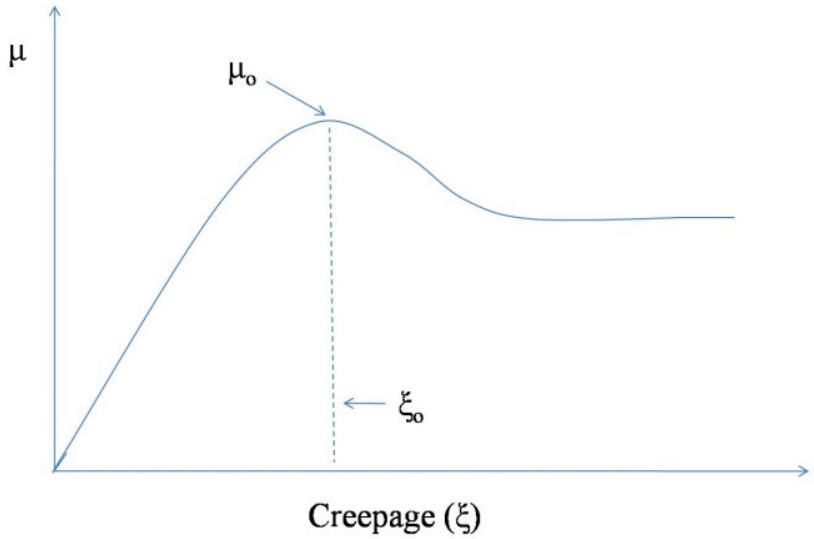

Figure 2.5: The CoF variance based on general dry friction theory

Squeal noise studies showed that the lateral creepage of the contact between the wheel and rail is one of the main sources which generate squeal noise in curved tracks [22-23]. Based on these reports, de Beer et al. [24] modeled the creepage-dependent friction coefficient, $\mu(s)$ as shown in Equation 2.9. This model included lateral creepage, the rolling velocity, the shear strength of the wheel and rail material, and the semi-axis length of the Hertzian contact ellipse in the longitudinal and lateral directions.

$$\mu(s) = \begin{cases} \mu_o \left(s' - \frac{1}{3}s'^2 + \frac{1}{27}s'^3 \right)\left(1 - 0.5e^{-0.138/|sV_o|} - 0.5e^{-6.9/|sV_o|} \right) & for\ s' \le 3 \\ \mu_o \left(1 - 0.5e^{-0.138/|sV_o|} - 0.5e^{-6.9/|sV_o|} \right) & for\ s' > 3 \end{cases} \qquad (2.9)$$

$$\mu_o = \frac{\tau_R \tau_W}{(\tau_R + \tau_W)} \frac{\pi ab}{F_o}, \quad s' = \frac{sGabC_{22}}{\mu_o F_o}$$

where μ_o is the stationary CoF of the non-rolling contact; τ_R and τ_W are the shear strength of the wheel and rail material; a and b are the semi-axis length of the Hertzian contact ellipse in longitudinal and lateral directions; G is the shear modulus of steel; C_{22} is the Kalker constant [83]; and F_o is the constant vertical contact force. Monk-Steel et al. [25] replaced a coefficient of the second exponential term (-0.138) of the Equation (2.9), by -0.05 and then found a better fit to experimental data from a test rig. However, most parameters were constant except the lateral creepage. In addition, this equation did not include relative normal vibration at the wheel-rail even though many studies showed the importance of such phenomenon in calculating the CoF.

Popov et al. [1] and Bucher et al. [2] introduced the CoF model with dimensionless parameters, k_1 and k_2 including material and loading parameters and sliding velocity, as described by Equation (2.10).

$$\mu = 0.15 + 0.0442\frac{k_1}{1 + 0.195k_1} + 0.3243\frac{1}{1 + 0.00212k_2} \qquad (2.10)$$
$$k_1 = \frac{\rho v^2 E}{\sigma_o^2} \ \ and \ \ k_2 = \frac{PE}{\sigma_o^2}$$

where ρ is the density; v is the sliding velocity; E is the Young's modulus; σ_o is the tensile strength; and P is the normal pressure. They showed the sliding velocity dependence and material and loading parameter dependence successively, however the shape of the CoF changes predicted based on Equation (2.10) was still different from the observed CoF changes.

Soom and collaborators [8, 9, 13, 26-34] conducted several studies for modeling the non-linear CoF. The contact vibration due to contact surface roughness was found by Soom and Kim for dry and for boundary lubricated sliding [8]. The oscillatory CoF due to the normal contact vibration was shown by Soom and Kim at dry sliding [9, 13] and at dry and boundary lubricated sliding [8]. Gassenfeit and Soom [26] found that the maximum CoF during the start-up for a planar contact was different for dry and lubricated conditions. Hess and Soom [3] modeled the sliding velocity dependent CoF equation given in Equation (2.11). They found that a definite relationship exists between the CoF and sliding velocity during steady and unsteady sliding under lubricated conditions. They concluded that the normal vibration effect must be included in the model to correctly predict the dynamic CoF.

$$\mu = \frac{\mu_b}{1 + C_1 \left(\frac{\eta V}{\sqrt{WE}} \right)^2} + C_2 \frac{\eta V L}{W}, \qquad V > 0 \tag{2.11}$$

where μ_b is the coefficient of friction in the boundary lubricated regime; W is the normal load; V is the sliding velocity; η is the lubricant viscosity; and L is the contact length. These one dimensional CoF models cannot properly predict unsteady lubricated dynamic changes of CoF.

The change of the contact patch size due to the nonlinear vibration at the Hertzian contact [11, 12, 28, 29] as well as the relationship between the contact patch size and the CoF [11, 12, 27, 29] was reported. Polycarpou and Soom [30] showed the influence of the normal vibration to the CoF and developed the two-dimensional CoF model combined with the normal vibration for lubricated conditions, which is illustrated in Equation (2.12) [31].

$$\mu(t) = \frac{c_1 e^{-c_2 V^*(t)}}{1 + c_3 \left(\frac{a(t)}{b}\right)^2 \left(\frac{\eta_i}{\eta_o}\right) R^*(t)}$$
$$V^* = \frac{\eta_i \alpha V}{a(t)}, \quad R^* = \frac{R}{R_L} = 1 - e^{\frac{-dh_o(t)}{\sigma \frac{a(t)}{b}\sqrt{\frac{\eta_i}{\eta_o}}}} \tag{2.12}$$

where V^* is the dimensionless velocity parameter. V^* includes the sliding velocity (V); the dynamic viscosity of the lubricant at the inlet conditions (η_i); a reference dynamic viscosity (η_o); the pressure viscosity coefficient (α); the semi-elliptical contact longitudinal length ($a(t)$) calculated by Hertzian theory; and the measured semi-elliptical contact lateral length (b). The terms c_1, c_2, and c_3 are empirical dimensionless constant fitted to the experimental data. R^* is a dimensionless contact resistance, and R_L is the limiting contact resistance. This R^* is related to the theoretical film (lubricant) thickness for smooth surfaces (h_o), i.e., relative normal vibration. The term σ is the combined surface roughness calculated by the root-mean-square (RMS) and d = 0.0245 is an empirical constant fitted to the data. a is calculated by Equation (2.13).

$$a(t) = \sqrt{\frac{4W(t)R'}{\pi b E'}} \tag{2.13}$$

where $W(t)$ is the dynamic normal contact load; R' is the effective radius of the contact; and E' is the effective elastic modulus. Thus, the instantaneous CoF, $\mu(t)$, is estimated as Equation (2.14).

$$\mu(t) = \frac{c_1 e^{-c_2 V^*(t)}}{1 + c_3 \left(\frac{a(t)}{b}\right)^2 \left(\frac{\eta_i}{\eta_o}\right)\left(1 - e^{-T}\right)}$$
$$T = \frac{dh_o(t)}{\sigma \frac{a(t)}{b}\sqrt{\frac{\eta_i}{\eta_o}}} \tag{2.14}$$

Polycarpou and Soom [32] studied the transition between stick and slip at a lubricated line contact during unsteady sliding and found that both the stick and the slip component of the total CoF depend on the normal vibration at a given velocity. Based on these findings, they

improved the two-dimensional (longitudinal and lateral directions) CoF model, as shown in Equation (2.15) [33].

$$\mu(t) = c_1 + c_2 V^*(t) + c_3 \left(\frac{\eta_i}{\eta_o}\right)^{0.28} \frac{e^{-c_4\sqrt{V^*(t)}}}{1 + c_5 \left(\frac{a}{b}\right)^2 \left(\frac{\eta_i}{\eta_o}\right) R^*(t)}$$
$$V^* = \frac{\eta_i \alpha V}{a(t)}, \quad R^* = \frac{R}{R_L} = 1 - e^{\frac{-dh_o(t)}{\sigma \frac{a(t)}{b}\sqrt{\frac{\eta_i}{\eta_o}}}} \tag{2.15}$$

where all parameters are the same as in Equation (2.12) and the empirical constant coefficients (c coefficients) fitted to the experimental data are: $c_1 = 7.5\times10^{-2}$; $c_2 = -1.2\times10^{4}$; $c_3 = 1.96$; $c_4 = 9.8\times10^{2}$; $c_5 = 9.38\times10^{3}$. Physically, c_1 is a boundary CoF near zero sliding velocity. When the contact is operating under unsteady sliding conditions, the CoF near zero sliding velocity cannot be interpreted as a constant number. This is due to the fact that the normal vibration continuously changes near zero sliding velocity, influencing both the stick and the slip components of the CoF independent of the sliding velocity [32, 33]. These models, presented in Equations (2.12) and (2.15), include many possible dynamic parameters for the lubricated condition, however stick and slip CoFs are not distinguishable in this model. Finally, a two-component mixed friction model, provided by Polycarpou and Soom [34].

$$\mu(t) = \underbrace{c_1 \left(\frac{\eta_i}{\eta_o}\right)\left(\frac{V^*(t)}{R^*(t)}\right)^{0.28} \frac{e^{-c_2\sqrt{V^*(t)}}}{1 + c_3 \left(\frac{a}{b}\right)^2 \left(\frac{\eta_i}{\eta_o}\right) R^*(t)}}_{Slip\ Component} + \underbrace{\frac{c_4}{1 + c_5 \left(\frac{a}{b}\right)^2 R^*(t)}}_{Stick\ Component}$$
$$V^* = \frac{\eta_i \alpha V}{a(t)}, \quad R^* = \frac{R}{R_L} = 1 - e^{\frac{-dh_o(t)}{\sigma \frac{a(t)}{b}\sqrt{\frac{\eta_i}{\eta_o}}}}, \quad a = \sqrt{\frac{4WR'}{\pi b E'}} \tag{2.16}$$

where the parameters are the same as in Equations (2.12) and (2.13). The *c* coefficients are: $c_1 = 2.31$; $c_2 = 1.1\times10^{3}$; $c_3 = 3.22\times10^{2}$; $c_4 = 7\times10^{-2}$; $c_5 = 3.38\times10^{4}$. This model estimated the stick and the slip CoFs under quasi-steady state sliding and unsteady continuous sliding quite well.

This model is only for the lubricated condition. In addition, this kind of nonlinear CoF model has not been applied to the study of railroad. To apply this approach to the dry wheel-rail condition, several modifications of the CoF model presented in Equation (2.16) are needed.

2.2.4 Background in Stochastic Modeling Using a Polynomial Chaos Approach

Extensive explanations of the polynomial chaos theory and its applications have been described by Sandu et al. [41, 42], Li [39], and Blanchard [40]. Thus, only a brief literature review and a brief overview of polynomial chaos theory will be presented in this section. For more details about the polynomial chaos theory and/or other stochastic analysis methods, the above documents are recommended.

The Polynomial chaos (poly-chaos) theory becomes popular recently since it is an efficient and accurate method to simulate highly nonlinear dynamic systems with a relatively small number of uncertain parameters. Ghanem and Spanos [43-46] attracted researchers in engineering fields by showing the successful application to the study of uncertainties in structural mechanics and vibration using Wiener-Hermite polynomial. They extended the applications to various research areas: soil mechanics [47], porous media [48, 49], heat transfer [50], fluid mechanics [51, 52], combustion [53], bioelectromagnetism [54], environmental and biological systems [55-57], and computational fluid mechanics [58]. Xiu and Karniadakis [59] extended the poly-chaos approach to general formulations based on Wiener-Askey polynomials family and they applied it to fluid mechanics [60-62]. Sandu et al. applied the poly-chaos method to multibody dynamic systems [41, 42, 63, 64], terramechanics [65, 66], and parameter estimation [67, 68].

The polynomial chaos method is more efficient than Monte Carlo simulations in dealing with uncertainties in mechanical systems [41, 42]. Thus, the poly-chaos method is employed to deal with uncertainties in the train dynamics and in the dry CoF in this study. Two approaches of applying the poly-chaos approach were discussed by Sandu et al. [41, 42] and Li [39]: a Galerkin method and a Collocation method. The Galerkin method was found to have longer computational time than the Collocation method [40]. The collocation method does not include the integration of complicated functions, and it is much easier to implement than the Galerkin

method for a highly nonlinear multi-body system such as the railroad system. Thus, a collocation method will be employed for the poly-chaos approach in this study. This section introduces the brief theoretical background of the poly-chaos (orthogonal polynomials) and the formulation of the collocation method.

The basic idea of poly-chaos approach is that random processes of interest can be approximated by sums of orthogonal polynomial chaoses of random independent variables. In the poly-chaos, a random process $X(\theta)$, viewed as a function of the random event θ, is modeled as an expansion in terms of orthogonal polynomial functions [46, 59] as:

$$X(\theta) = \sum_{k=1}^{\infty} c^k \Psi^k \left(\varsigma(\theta)\right) \tag{2.17}$$

where Ψ^k ($\varsigma_1 \cdots \varsigma_n$) are generalized Askey-Wiener poly-chaos of order n in terms of the multidimensional random variables $\varsigma = (\varsigma_1 \cdots \varsigma_n)$ and $\{\Psi^k(\varsigma(\theta))\}$ is the orthogonal polynomial set. In other words, the polynomial chaos is expressed by a linear combination of a set of known random functions and deterministic coefficients found by minimizing certain norm of errors.

The Askey-Wiener polynomial chaoses form is based on the joint probability density, ρ ($\varsigma_1 \cdots \varsigma_n$). This type of random variable functions decides the basis functions. For example, the basis functions of Hermite polynomials are for Gaussian random variables, the basis functions of Legendre polynomials are for uniform distributed random variables, the basis functions of Jacobi polynomials are for beta distributed random variables, and the basis functions of Laguerre polynomials are for the Gamma distributed random variables [59, 61]. Beta distributed, Beta (a+1, b+1) random variables with the Jacobi (a, b) polynomials as the basis functions will be used in this study. The probability density function (PDF) for Beta distribution is defined as Equation (2.18):

$$\rho(\varsigma) = \frac{\Upsilon(a+b+2)}{2^{a+b+1}\Gamma(a+1)\Gamma(b+1)}(1-\varsigma)^a (1-\varsigma)^b, \quad where \quad \Upsilon(x) = \int_0^{\infty} t^{x-1} e^{-t} dt \tag{2.18}$$

The formula of the Jacobi basis functions, $J_n(x)$, for Beta (a+1, b+1) distribution is expressed in Equation (2.19).

$$J_n(x) = \frac{1}{(-1)^n 2^n n!(1-x)^a (1-x)^b} \cdot \frac{d^n}{dx^n}\left((1-x)^a (1-x)^b (1-x^2)^n\right) \tag{2.19}$$

Some examples for PDF of random variables distribution are in Figure 2.6 [40].

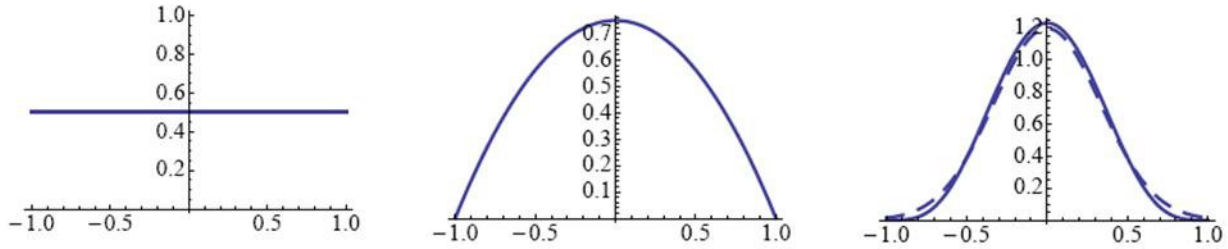

(a) (b) (c)

Figure 2.6: Probability densities for uniform, Gaussian and Beta distributions: (a) Uniform distribution (a=0, b=0); (b) Beta (2, 2) distribution (a=1, b=1); (c) Gaussian distribution (dashed) and Beta (5, 5) distribution (solid) (a=4, b=4) [40]

As Equation (2.17) shows, the general poly-chaos expansion has infinite terms. Thus, practically a truncated expansion is commonly used,

$$X(\theta) = \sum_{k=1}^{S} c^k \Psi^k\left(\varsigma(\theta)\right) \tag{2.20}$$

with the multi-dimensional basis functions expressed by tensor products of 1-dimensional polynomial basis for independent random variables, $(\varsigma_1 \cdots \varsigma_n)$:

$$\Psi^j\left(\varsigma_1, \cdots, \varsigma_n\right) = \prod_{k=1}^{n} (P1d)_k^{l_k}(\varsigma_k), \quad j = 1, 2, \cdots, S; \; l_k = 1, 2, \cdots, p \tag{2.21}$$

where $S = \frac{(n+p)!}{n!\,p!}$, $(P1d)$ is a 1-dimensional polynomial, n is the number of random variables, and p is the maximum order of the polynomial basis.

To present an implementation of the polynomial chaos approach with the collocation method, the dynamics of a deterministic unconstrained mechanical system is considered. The deterministic system can be described by a set of simultaneous first order differential equations (ODE) [41]:

$$\dot{y} = f(y), \quad y(t^0) = y^0, \quad t^0 \le t \le T \tag{2.22}$$

With each state a vector of length *m*. The state vector y can be expanded along the polynomial chaos basis, $\Psi^1(\varsigma_1, \cdots, \varsigma_n), \cdots, \Psi^S(\varsigma_1, \cdots, \varsigma_n)$, in order to express the resulting uncertainty in the state vector *y*:

$$y = \sum_{j=1}^{S} y^j \Psi^j(\varsigma) \tag{2.23}$$

By substituting Equation (2.23) into Equation (2.22), we obtain:

$$\sum_{j=1}^{S} \left(y^j\right)' \Psi^j(\varsigma) = f\left(\sum_{j=1}^{S} y^j \Psi^j(\varsigma)\right) \tag{2.24}$$

Using the poly-chaos expansion, an ODE for the poly-chaos coefficients is substitute for the original ODE and these coefficients include the uncertainty information.

The collocation method is used to obtain the evolution equation for the stochastic coefficients. The collocation approach imposes that Equation (2.24) is satisfied at a given set of collocation points, k^i ($1 \le i \le Q$), which can be the roots of the Q^{th} order polynomial:

$$\sum_{j=1}^{S} \left(y^j\right)' \Psi^j(k) = f\left(\sum_{j=1}^{S} y^j \Psi^j(k)\right), \; 1 \le i \le Q \tag{2.25}$$

The collocation points in the system state space with matrix *A* defined using the basis function values at the collocation points are:

$$A = \left(A_{i,j}\right), \quad A_{i,j} = \Psi^j\left(\kappa^i\right), \ 1 \le j \le S, \ 1 \le i \le Q$$
$$Y^i(t) = \sum_{j=1}^{S} y^j \Psi^j(\kappa^j) = \sum_{j=1}^{S} A_{i,j} y^j(t), \qquad 1 \le i \le Q \tag{2.26}$$

According to Equation (2.17), Equation (2.16) becomes:

$$\left(Y^i(t)\right)' = f\left(Y^i(t)\right), \quad t^0 \le t \le T, \ 1 \le i \le Q \tag{2.27}$$

with the initial conditions:

$$Y^i(t^0) = \sum_{j=1}^{S} A_{i,j} y^j(t^0), \quad 1 \le i \le Q \tag{2.28}$$

After integration, the stochastic solution coefficients are recovered by solving the linear system of equations for y^j:

$$y^j(t) = \sum_{i=1}^{Q} \left(A^{-1}\right)_{j,i} Y^i(t), \ 1 \le j \le S \tag{2.29}$$

where A^{-1} is the pseudo-inverse of A matrix.

The collocation points must be selected where matrix A is not singular or not near singular. Cheng and Sandu [69] have studied some options such as the random data set, the Hammersley/Halton data sets [70, 71], and sparse grid Smolyak data sets [72-74]. To deal with small number of random variables (small n), results from the Hammersley/Halton data sets are more accurate than those from a randomly generated data set. However, both the Hammersley/Halton data sets cause the system matrix A to become singular or near singular when a large number of random variables (big n) are dealt with. In this case, a randomly generated data set must be used since it leads to a non singular system matrix. Applying the inverse Cumulative Distribution Function of the new distribution can transform from the collocation points for a uniform distribution to the points for the new distribution. For example, applying the inverse Cumulative Distribution Function of the Beta (2, 2) distribution transforms from the collocation points for a uniform distribution to the points for a Beta (2, 2) distribution.

Generally, the implementation of the poly-chaos collocation method is done according to the following steps, as explained by Blanchard [40]:

1. Model the source of uncertainty by random variables with appropriate PDFs.
2. Build the S orthogonal polynomials (expansion basis).
3. Generate the polynomial chaos expansion of the uncertain parameters (or uncertain initial conditions).
4. Select $Q \geq S$ collocation points and generate the system matrix A.
5. Run Q deterministic system simulations with the expansion obtained from Equation (2.24).
6. Recover the polynomial chaos coefficients of the results by formulating and solving the linear equation systems.
7. Extract the mean and the standard deviation of the final solution, and generate the PDFs.

After recovering the coefficients, a linear combination of stochastic coefficients multiplied by the corresponding basis functions represents the system solution, as shown in Equation (2.31):

$$y(t) = y^0(t) + y^1(t)\Psi^1(\varsigma) + y^2(t)\Psi^2(\varsigma) + \cdots + y^n(t)\Psi^n(\varsigma) + H.O.T \tag{2.30}$$

The superscripts for the system coefficients represent the stochastic modes. The terms $\Psi^1(\varsigma), \cdots, \Psi^n(\varsigma)$ represent linear polynomials in variables, $\varsigma_1, \cdots, \varsigma_n$, respectively. The $H.O.T$ is the high order terms.

Chapter 3. Wheel-Rail Simulation Model

This chapter discusses the new 3-D nonlinear CoF model and the wheel-rail dynamics model developed in this study. It describes the derivation of the 3-D nonlinear CoF model. Various models for the wheel-rail dynamics are introduced. Dynamic models include the mass-spring-damper model, the elliptical wheel-rail contact patch model, the creepage model, and the creep force model. Then, the algorithm for calculation of these dynamic parameters and CoFs is introduced. Finally, a specific case study of the polynomial chaos application is discussed.

This chapter is organized as follows: section 3.1 introduces the derivation of the new 3-D nonlinear CoF model; section 3.2 presents the wheel-rail dynamics model and introduces the mass-spring-damper model and the wheel-rail contact model; section 3.3 illustrates an example of the polynomial chaos application.

3.1 Nonlinear 3-D Coefficient of Friction Model

Soom and collaborators devoted a lot of effort to model the nonlinear coefficient of friction in order to obtain the closest fit with experimental data. Finally, they developed Equation (2.16) for the lubricated condition [34]. This equation is repeated below:

$$\mu(t) = \underbrace{c_1\left(\frac{\eta_i}{\eta_o}\right)\left(\frac{V^*(t)}{R^*(t)}\right)^{0.28}\frac{e^{-c_2\sqrt{V^*(t)}}}{1+c_3\left(\frac{a}{b}\right)^2\left(\frac{\eta_i}{\eta_o}\right)R^*(t)}}_{Slip\ Component} + \underbrace{\frac{c_4}{1+c_5\left(\frac{a}{b}\right)^2 R^*(t)}}_{Stick\ Component} \tag{3.0}$$

$$V^* = \frac{\eta_i \alpha V}{a(t)}, \quad R^* = \frac{R}{R_L} = 1 - e^{\frac{-dh_o(t)}{\sigma\frac{a(t)}{b}\sqrt{\frac{\eta_i}{\eta_o}}}}, \quad a = \sqrt{\frac{4WR'}{\pi b E'}}$$

where V^* is the dimensionless velocity parameter. V^* includes the sliding velocity (V), the dynamic viscosity of the lubricant at the inlet conditions (η_i), a reference dynamic viscosity (η_o), the pressure viscosity coefficient (α), the semi-elliptical contact longitudinal length ($a(t)$) calculated by Hertzian theory, and the measured semi-elliptical contact lateral length (b). Terms

c_1, c_2, c_3, c_4, and c_5 are empirical dimensionless constant fitted to the experimental data. They are $c_1 = 2.31$; $c_2 = 1.1\times10^3$; $c_3 = 3.22\times10^2$; $c_4 = 7\times10^{-2}$; $c_5 = 3.38\times10^4$. R^* is a dimensionless contact resistance, where R_L is the limiting contact resistance. This R^* is related to the theoretical film (lubricant) thickness for smooth surfaces (h_o), i.e. relative normal vibration. σ is the combined surface roughness and $d = 0.0245$ is an empirical constant fitted to the data. However, this model is for 2 dimensions and it cannot be applied to dry rail conditions. Thus, we developed a 3-D nonlinear CoF model for dry conditions by unit analysis from Equation (3.0).

No lubricant is on the rail for dry rail conditions. In the Equation (3.0), the stick component does not have any lubricant parameter, so, it holds for the dry rail condition. However, the slip component needs to be modified since it contains lubricant parameters (viscosity of lubricant, η_i and η_o, and the pressure viscosity coefficient, α). The dynamic viscosity of the lubricant at the inlet condition (η_i) and a reference dynamic viscosity (η_o) are the same because there is no lubricant. For dry conditions, the viscosity (η) is replaced by a damping coefficient (c) divided by the semi-elliptical contact lateral length (b) using unit analysis, as shown in Equation (3.1).

$$[\eta] = [Pa \cdot s] = \left[\frac{N}{m^2} \cdot s\right] = \left[\frac{N\,s/m}{m}\right] = \frac{c_{\tan}}{b} \tag{3.1}$$

where [] means a unit of a specific variable; Pa is Pascal; s is second; m is meter; and c_{tan} is the damping coefficient in the tangential direction. The semi-elliptical contact lateral length (b) has been arbitrarily selected instead of the semi-elliptical contact longitudinal length (a) for developing the 3-D model. The pressure viscosity coefficient represents the viscosity change with pressure change. As mentioned above, there is no lubricant on the rail for the dry rail condition. Therefore, there is no viscosity change with pressure. The pressure viscosity coefficient becomes new α as shown in Equation (3.2):

$$\alpha = \frac{1}{\eta_i}\frac{\Delta\eta_i}{\Delta P} \quad \Rightarrow \quad \alpha = \frac{1}{\eta_i}\frac{\eta_i}{P} = \frac{1}{P} \tag{3.2}$$

Therefore, the dimensionless velocity parameter (V^*) is modified as Equation (3.3) with new α. The sliding velocity V_{tan} is newly defined for 3-D model.

$$V^* = \frac{\eta_i \alpha V}{a} = \frac{\eta V}{aP} = \frac{c_{\tan} V}{abP} = \frac{\pi V_{\tan}}{F_n} c_{\tan} \qquad \left(V_{\tan} = \sqrt{V_{long}^2 + V_{lat}^2} \right) \tag{3.3}$$

where F_n is the normal contact force at the wheel-rail interface and V_{long}, V_{lat}, and V_{tan} are sliding velocities in the longitudinal, lateral, and tangential directions, respectively. In this study, semi-elliptical contact lengths a and b are calculated by a formula from Hertzian theory instead of using Equation (2.14) with measured b. Calculation of a and b will be introduced later in this chapter. Finally, the new 3-D nonlinear CoF model is obtained as follows:

$$\mu(t) = \underbrace{c_1 \left(\frac{V^*(t)}{R^*(t)} \right)^{0.28} \frac{e^{-c_2 \sqrt{V^*(t)}}}{1 + c_3 \left(\frac{a}{b} \right)^2 R^*(t)}}_{Slip\ Component} + \underbrace{\frac{c_4}{1 + c_5 \left(\frac{a}{b} \right)^2 R^*(t)}}_{Stick\ Component}$$

$$V^* = \frac{\pi V_{\tan}}{F_n} c_{\tan},\ T = \frac{-dh_o b}{\sigma_{\tan} a},\ R^* = \frac{R}{R_L} = 1 - e^T,\ c_{\tan} = \sqrt{c_{long\_contact}^2 + c_{lat\_contact}^2},\ \sigma_{\tan} = \sqrt{\sigma_{long}^2 + \sigma_{lat}^2} \tag{3.4}$$

where subscript *long* and *lat* are longitudinal and lateral directions, respectively. Terms c_2, c_3, and c_4 are changed to 7, 0.322, and 7, respectively, by trial and error for dry rail conditions. All the other parameters have the same values as in Equation (2.17); c_1 = 2.31, c_5 = 33800, and d = 0.0245. Terms $c_{long\_contact}$ and $c_{lat\_contact}$ can be calculated by formulas reported by Wu and Thompson [19, 87] as follows:

$$c_{long\_contact} = \frac{EabC_{11}}{2(1+\nu)V_{Train}} \quad and \quad c_{lat\_contact} = \frac{EabC_{22}}{2(1+\nu)V_{train}} \tag{3.5}$$

where ν is Poisson ratio of the wheel and rail, V_{train} is the train velocity, E is Young's modulus, and C_{11} and C_{22} are creep force coefficients along the longitudinal and lateral directions from Kalker's linearized creep force theory, respectively. C_{11} and C_{22} will be explained later when creep force is introduced. In this study, wheel and rail materials are assumed to be the same, i.e., steel. This CoF model will be applied to this study. Note that the coefficients are not obtained

by curve fitting to experimental data since no measurements were available for a real train in dry rail conditions. Thus, this model is intended to provide a quantitative model for the CoF in this study, without claiming to be able to provide absolute values for the CoF.

3.2 The Wheel-Rail Dynamic Model

3.2.1 General Modeling

Broad Explanation about a Mass-Spring-Damper Model

In this study, no specific train model is considered. Modeling has been done based on a train locomotive having 4 axles (8 wheels). One simplified wheel running on the tangential track is modeled based on the following assumptions:

1. The wheel is perfectly conical 1:20 (2.86°) [38].
2. On the tangential track, there is only one contact point during running, i.e., no flange contact occurs. Thus, lateral displacement will be allowed from 0 to 10 *mm* since the wheel clearance from the rail head is 10 *mm* [38].
3. The track is very rigid. Thus, there is no motion (vertical vibration) of the track.
4. At the tangential track if creepage is small enough, the Kalker's linear creep force theory can be applied [83].
5. The wheel and the rail are made out of the same material, steel.

The dynamic train model considers a main body, a wheelset, rails, and the track. All dynamic movements are obtained at the right passive wheel only. This wheel-rail system is modeled as a mass-spring-damper system as shown in Figure 3.1. This mass-spring-damper system includes a train body mass (1/8 of a typical, total locomotive body mass), a half wheelset mass, an effective rail mass, vertical, and lateral suspensions, and track stiffness and damping. The dynamic train model has three relevant degrees of freedom, i.e. vertical displacement, lateral displacement, and yaw rotation. The vertical dynamic model includes a train body mass, a half wheelset mass, an effective rail mass, vertical suspension stiffness and damping, and track stiffness and damping. The lateral dynamic model includes a half wheelset mass and lateral suspension stiffness and damping. The yawing dynamic model includes the mass moment of inertia of a half wheelset, and yaw suspension stiffness and damping. The vertical force (F_v) and the lateral force (F_l) are

illustrated in the Figure 3.1 to display the contact force between the wheel and the rail including the normal contact force and the creep force, which have an angle equal to the wheel conicity. Nonlinear Hertzian contact stiffness is employed to model the normal contact force between the wheel and the rail as a nonlinear spring [36]. The normal contact force and the creep forces will be explained later in this chapter. Vehicle, rail, track and material parameters are provided in Table 1. These parameters have been obtained from various publications [19, 82-85].

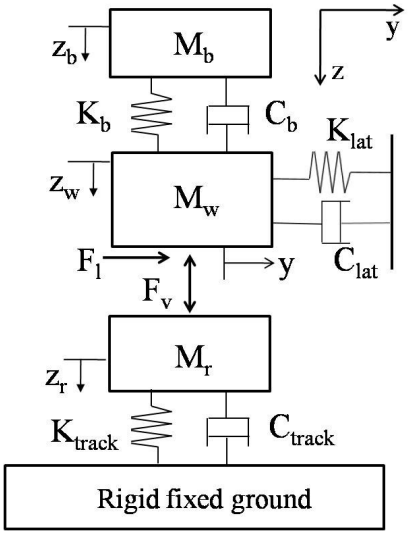

Figure 3.1 A mass-spring-damper model for the wheel-rail interaction with body mass

Rail Mass Model

To model the wheel and rail vibration correctly, the rail mass must be calculated. Not the entire rail vibrates when force is applied to one point of the rail. Thus, an effective vibrating length of the rail at the contact with the wheel is considered here. In this study, the effective rail length for rail vibration is assumed to be the same as the sleeper distance, (0.6 *m*). Rail mass is calculated from a cross-sectional area of the rail, a rail material density, and an effective rail length, as provided in Table 1.

Track Model

The track consists of rail pads, ballast, subgrade, and sleepers with some distance between them, as shown in Figure 3.2. Subgrade is assumed to be a rigid body and no stiffness and damping are considered for it. In this study, the track is modeled as rigidly attached to the ground based on the third assumption presented earlier in this chapter, but stiffness and damping

from the rail pad, sleeper, and ballast are added to the model. At the sleeper, the track stiffness and the damping coefficient are calculated from the rail pad, sleeper, and ballast parameters. However, for the track between sleepers, only the ballast is assumed to exist as shown in Figure 3.2 (b) and the effects of the sleeper and the rail pad decrease with the distance from the sleeper until the middle of the distance between sleepers. Thus, the track stiffness and the damping coefficient have the highest values at the sleeper, they decrease with increasing distance from the sleeper, and they have the lowest value in the middle of the distance between sleepers. Therefore, the stiffness and the damping coefficient are modeled as cosine waves, as follows:

$$\begin{aligned} Stiffness &= 0.5A + 0.5A\cos\left(f_t \cdot t\right) \\ Damping\ coefficient &= 0.5B + 0.5B\cos\left(f_t \cdot t\right) \end{aligned} \tag{3.6}$$

where A is a maximum stiffness, B is a maximum damping coefficient, and f_t is a track excitation frequency. Stiffness and damping from the rail pad, sleeper, and ballast are considered to connect in parallel, respectively, as follows:

$$\begin{aligned} K_{track} &= K_{pad} + K_{sleepr} + K_{ballast} \\ C_{track} &= C_{pad} + C_{sleepr} + C_{ballast} \end{aligned} \tag{3.7}$$

where K_{track} and C_{track} are the track stiffness and the track damping coefficient, respectively. The sleeper distance is defined as the distance between the centers of the sleepers as shown in Figure 3.2 (b). The distance between sleepers is 0.6 m for a concrete sleeper and 0.5 m for a wood sleeper [83]. In this study, a concrete sleeper is used.

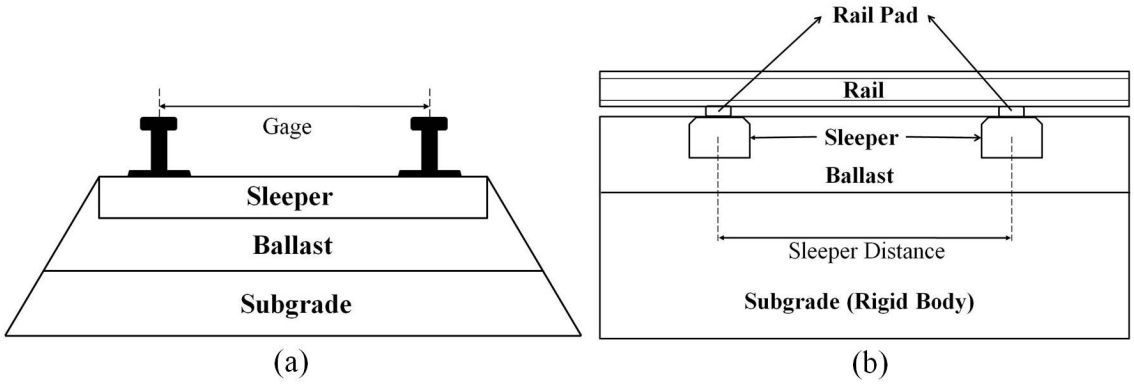

Figure 3.2 Schematic track anatomy. (a) Track front view, (b) Track side view

The Rail Roughness Excitation Model for Wheel-Rail Interaction

In chapter 2, some studies that focused on the wheel-rail vibration induced by surface roughness have been reviewed. The method using surface roughness as an excitation source is called a moving irregularity method. This method has been broadly used to study the wheel-rail interaction and rolling noise [88-91], and it is easy to implement. Thus, a moving irregularity method is employed to give an excitation in this study. This method assumes that the wheel stays at a fixed point on the rail and the combined roughness on wheel and rail surfaces moves at a steady speed between the wheel and rail [88]. An excitation frequency can be calculated [38] as follows:

$$f = \frac{2\pi V_{train}}{\gamma} \tag{3.8}$$

where V_{train} is the train speed and γ is a sinusoidal rail irregularity of wavelength. In this study, wavelength is set as 0.5 m. To calculate the track excitation frequency (f_t), *dist* replaces γ. For simplicity, the wheel surface is assumed very smooth in this study. Thus, only the rail roughness will be considered as an excitation source in this study. In the following, the terminology rail roughness will replace surface roughness.

Table 3. 1 Vehicle, Rail, Track and Material Parameters

Mass

Body mass [82]	M_b	4500 [kg]
Wheel mass [82]	M_w	800 [kg]
Rail mass ($Area \times \rho \times dist$)	M_r	39.56 [kg]
Wheel mass moment of inertia [82]	J_w	480 [$kg{\cdot}m^2$]

Suspension

Vertical stiffness [82]	K_b	550×10^3 [N/m]
Vertical damping [82]	C_b	35×10^3 [$N{\cdot}s/m$]
Lateral stiffness [82]	K_{lat}	2300×10^3 [N/m]
Lateral damping [82]	C_{lat}	10×10^3 [$N{\cdot}s/m$]
Yaw stiffness [82]	K_θ	2500×10^3 [N/m]
Yaw damping [82]	C_θ	5×10^3 [$N{\cdot}s/m$]

Cross-sectional area of rail [84]	$Area$	0.0084 [m^2]
Sleeper distance for concrete [83]	$dist$	0.6 [m]

Track (maximum value)

Rail pad stiffness [85]	K_{pad}	110×10^6 [N/m]
Rail pad damping [85]	C_{pad}	98×10^3 [$N{\cdot}s/m$]
Sleeper stiffness [85]	$K_{sleeper}$	100×10^6 [N/m]
Sleeper damping [85]	$C_{sleeper}$	98×10^3 [$N{\cdot}s/m$]
Ballast stiffness [85]	$K_{ballast}$	200×10^6 [N/m]
Ballast damping [85]	$C_{ballast}$	245×10^3 [$N{\cdot}s/m$]

Material Parameters for steel

Density [19]	ρ	7850 [kg/m^3]
Poisson ratio	v	0.3
Young's modulus [19]	E	2.1×10^{11} [N/m^2]
Shear modulus of rigidity [19]	G	0.77×10^{11} [N/m^2]

3.2.2 The Contact Model

To study the wheel-rail dynamics, the formulation of the contact forces that describe the dynamic interaction at the wheel-rail interface is very important and must be addressed. Various contact models exist and are used in different computer simulations to study wheel-rail interaction. In this study, the Hertz contact theory and Kalker's linear creep force theory will be used to investigate the wheel-rail interaction. The Hertz contact theory and the calculation of the contact patch shape, i.e., semi-elliptical contact longitudinal and lateral lengths, based on Hertz theory will be introduced first. Next, creep phenomena and Kalker's linear creep force theory for the rigid body contact will be discussed.

Hertz Contact Theory

The Hertz theory developed in 1880 has been broadly used for many contact problems in engineering. This theory is also generally used for the railroad contact problems to determine the shape of contact area (the semi-elliptical contact lengths). In general, two rigid bodies have contact at a point if the surfaces of bodies do not fit exactly. If an external force is applied to each body, the two bodies deform at the contact point and then point contact becomes an area contact. Hertz assumed that this contact area is, in general, elliptical based on his observation using two glass lenses. This theory is valid based on the following assumptions made by Hertz:

1. The surfaces of the bodies are continuous and have a point or line contact.
2. The strains at the contact region are small.
3. The stress resulting from the contact force vanishes at a distance far from the contact area.
4. The surfaces are frictionless.
5. The bodies are elastic, and no plastic deformation occurs in the contact area.

These assumptions are verified to be valid for the wheel-rail contact by most researchers [86].

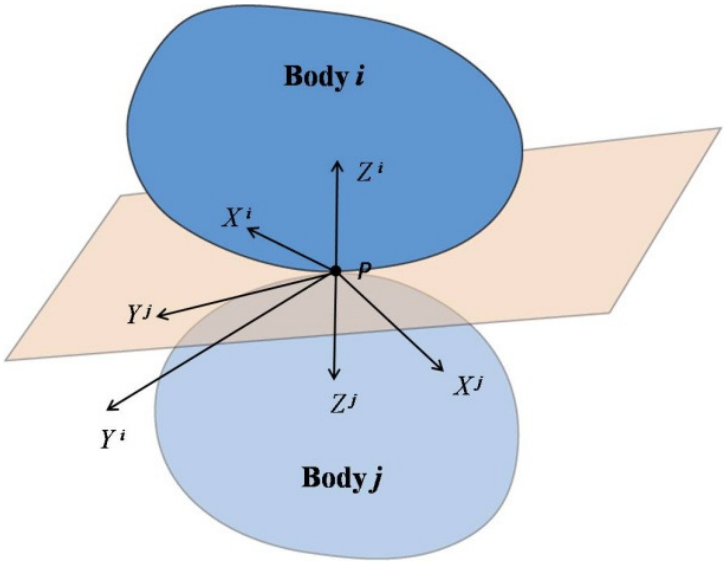

Figure 3.3 Two bodies in contact

This section is based on [86]. Hertz considered two bodies *i* and *j* in contact at a point *P* as shown in Figure 3.3. He assumed that the shape of the surface of each body at *P* can be defined as in Equation (3.9), using the principal radii of curvature of the surfaces of body *i* and j at *P* based on the assumptions above.

$$\begin{aligned} z^i &= \frac{1}{2R_1^i}\left(x^i\right)^2 + \frac{1}{2R_2^i}\left(y^i\right)^2 + C^i\left(x^i y^i\right) + \cdots \\ z^j &= \frac{1}{2R_1^j}\left(x^y\right)^2 + \frac{1}{2R_2^j}\left(y^j\right)^2 + C^j\left(x^j y^j\right) + \cdots \end{aligned} \tag{3.9}$$

where C^k ($k = i, j$) are constants that are a function of R_1^k and R_2^k; and x and y ($k = i, j$) are the axes of two bodies at the contact plane. P is the origin. In general, axes x^i and x^j, as well as y^i and y^j, are not parallel. The distance between two surfaces at the point P can be defined as follows:

$$h = z^i - z^j \tag{3.10}$$

By substituting Equation (3.9) into Equation (3.10), we can obtain:

$$h = Ax^2 + By^2 + Cxy \tag{3.11}$$

where A, B, and C are constants. To simplify these equations, the axes x^k and y^k ($k = i, j$) and x and y can be chosen such that $x^k y^k$ ($k = i, j$) and xy are zero. Moreover, if higher-order terms are neglected, the Equations (3.9) and (3.11) can be written as below:

$$z^i = \frac{1}{2R_1^i}\left(x^i\right)^2 + \frac{1}{2R_2^i}\left(y^i\right)^2$$
$$z^j = \frac{1}{2R_1^j}\left(x^y\right)^2 + \frac{1}{2R_2^j}\left(y^j\right)^2 \tag{3.12}$$

$$h = Ax^2 + By^2 = \frac{1}{2R_1}x^2 + \frac{1}{2R_2}y^2 \tag{3.13}$$

where R_1^k and R_2^k ($k = i, j$) are the principal radii of curvatures of the surfaces of body i and j at P, and R_1 and R_2 are the principal relative radii of curvature. Radii of curvature can be calculated from $\partial^2 z^k \Big/ \left(\partial x^k\right)^2 = 1/R_1^k$ and $\partial^2 z^k \Big/ \left(\partial y^k\right)^2 = 1/R_2^k$.

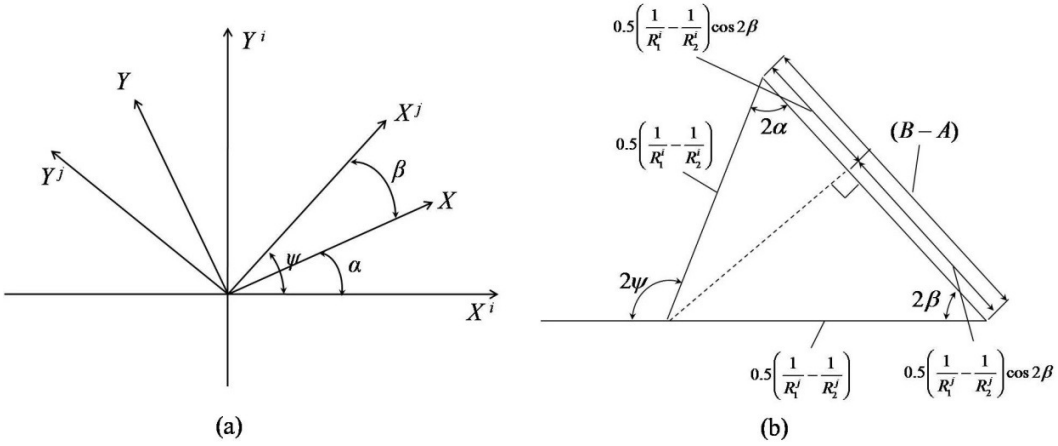

Figure 3.4 Contact plane.

The axes x^i and x^j and y^i and y^j are different from the common axes x and y by an angle α and β, respectively, as seen in Figure 3.4 (a). The difference between x^i and x^j is an angle devoted by ψ. Using Equation (3.10), a constant C from Equation (3.11) can be defined by transforming the axes x^i and x^j to the common x-axis.

$$C = \frac{1}{2}\left(\frac{1}{R_1^i} - \frac{1}{R_2^j}\right)\sin 2\beta - \frac{1}{2}\left(\frac{1}{R_1^i} - \frac{1}{R_2^j}\right)\sin 2\alpha \tag{3.14}$$

If Equation (3.14) is equated to zero, Equation (3.13) holds, which leads to:

$$\frac{\left(\frac{1}{R_1^i} - \frac{1}{R_2^j}\right)}{2\sin 2\alpha} = \frac{\left(\frac{1}{R_1^i} - \frac{1}{R_2^j}\right)}{2\sin 2\beta} \tag{3.15}$$

According to the sine law, Figure 3.4 (b) can be drawn. From the triangle in Figure 3.4 (b), $B - A$ and $B + A$ can be defined as follows:

$$\begin{aligned} B - A &= \frac{1}{2}\left(\frac{1}{R_1^i} - \frac{1}{R_2^i}\right)\cos 2\alpha + \frac{1}{2}\left(\frac{1}{R_1^j} - \frac{1}{R_2^j}\right)\cos 2\alpha \\ &= \frac{1}{2}\sqrt{\left(\frac{1}{R_1^i} - \frac{1}{R_2^i}\right)^2 + \left(\frac{1}{R_1^j} - \frac{1}{R_2^j}\right)^2 + 2\left(\frac{1}{R_1^i} - \frac{1}{R_2^i}\right)\left(\frac{1}{R_1^j} - \frac{1}{R_2^j}\right)\cos 2\psi} \end{aligned} \tag{3.16}$$

and

$$A + B = \frac{1}{2}\left(\frac{1}{R_1^i} + \frac{1}{R_2^i} + \frac{1}{R_1^j} + \frac{1}{R_2^j}\right) \tag{3.17}$$

Equations (3.16) and (3.17) will be applied to calculate semi-elliptical contact lengths for the wheel-rail dynamics. Details will be introduced in section 3.2.2.

Equation (3.13) shows that the contours of the contact between the body i and j is an ellipse with depth h. Let us assume that a normal load F_n is applied to compress the bodies against each other. Based on the elastic bodies assumption, the surfaces of the two bodies in contact will be deformed. If we assume that the surfaces of the two bodies can penetrate each other instead of deforming, the penetrated displacement lengths of the two bodies are the same as the deformed lengths of the bodies. This penetration model is illustrated in Figure 3.5. The terms u_i and u_j represent the displacements of the surfaces of body i and j, respectively. If P_i and P_j are in the same line, the total displacement (δ) is given by Equation (3.18)

$$u^i + u^j + h = \delta^i + \delta^j = \delta \tag{3.18}$$

where h is already given by Equation (3. 10).

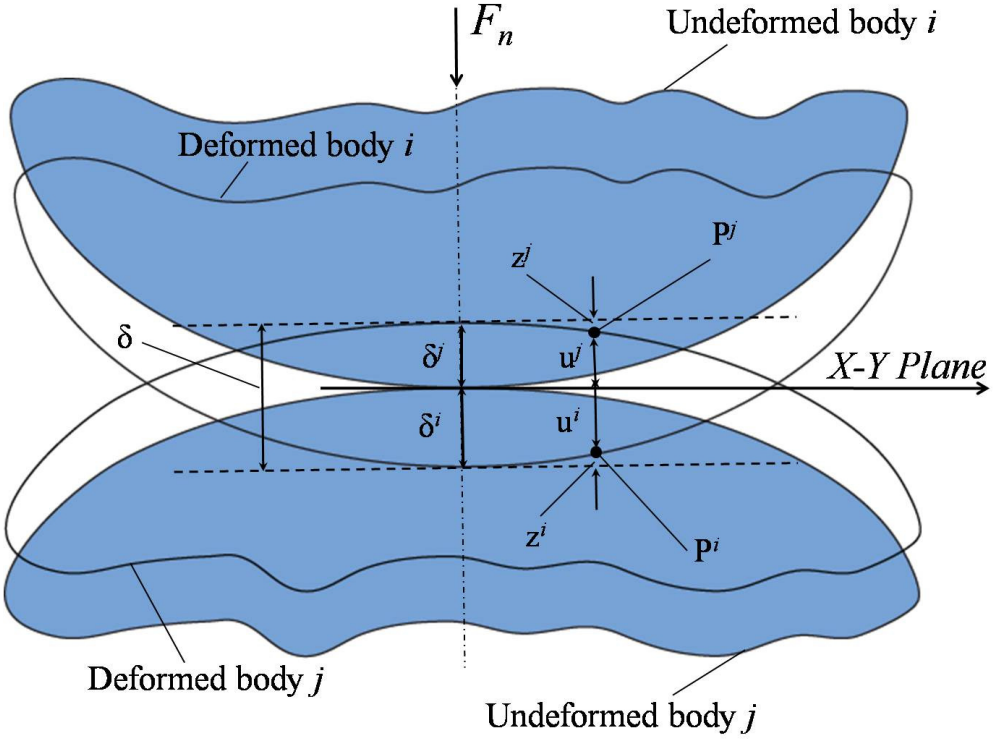

Figure 3.5 Contact bodies under externally applied normal load.

Elliptical Wheel-ail Contact Patch

The shape of the contact patch between the wheel and the rail can be characterized by the semi-elliptical contact longitudinal length, a, and lateral length, b. If a and b are equal, the contact patch shape is a circle; if they are not equal, it is an ellipse. In this study, the semi-elliptical contact lengths a and b will be formulated based on the Hertz theory. The size and the shape of the contact patch for the wheel-rail can be calculated from the normal force, material properties, yaw angle, and the geometry of the wheel and rail at the contact. As the wheel and the rail are both bodies of revolution the geometry can be described by the radii of curvature in the direction of rolling and for the cross sectional geometry [92]. The radius of curvature can be calculated using Equation (3.19).

$$
\begin{aligned}
&y = f(x) \\
&\textit{Radius of curvature at } x = a \\
&R(a) = \left. \frac{\left[1 + \left(\frac{dy}{dx}\right)^2\right]^{\frac{3}{2}}}{\frac{d^2 y}{dx^2}} \right|_{x=a}
\end{aligned}
\tag{3.19}
$$

According to Hertz theory discussed in section 3.2.2, the semi-elliptical contact lengths L_1 and L_2 are defined as shown in Equation (3.20).

$$
\begin{aligned}
L_1 &= m\left(\frac{3\pi F_n \left(K_1 + K_2\right)}{4K_3}\right)^{1/3} \\
L_2 &= n\left(\frac{3\pi F_n \left(K_1 + K_2\right)}{4K_3}\right)^{1/3}
\end{aligned}
\tag{3.20}
$$

where F_n is the normal force; m and n are Hertz coefficients; K_1 and K_2 are constants that depend on the material properties of the two bodies and they are defined in Equation (3.21).

$$
K_1 = \frac{1 - \left(v^w\right)^2}{\pi E^w}, \qquad K_2 = \frac{1 - \left(v^r\right)^2}{\pi E^r} \tag{3.21}
$$

where v^w and v^r are the Poisson ratio for the wheel and rail, respectively; E^w and E^r are the Young's modulus for the wheel and rail, respectively. K_3 is a constant that depends on the geometric properties of the two bodies (Radii of curvature of two bodies at the contact point) and is defined through Equation (3.17).

$$
K_3 = A + B = \frac{1}{2}\left(\frac{1}{R_1^w} + \frac{1}{R_2^w} + \frac{1}{R_1^r} + \frac{1}{R_2^r}\right) \tag{3.22}
$$

where R_1^w and R_1^r are the principal rolling radii of curvature of the wheel and rail, respectively, and R_2^w and R_2^r are the principal transverse radii of curvature of the wheel and rail, respectively, as seen in Figure 3.6.

In this study, a conical wheel profile and a tangential rail segment are considered. R_2^w is equal to ∞ if the wheel is conical, and R_1^r is equal to ∞ if the rail is tangent, i.e., straight rail. Thus, Equation (3.22) becomes:

$$K_3 = A + B = \frac{1}{2}\left(\frac{1}{R_1^w} + \frac{1}{R_2^r}\right) \tag{3.23}$$

Equation (3.23) will be used in this study for calculating K_3.

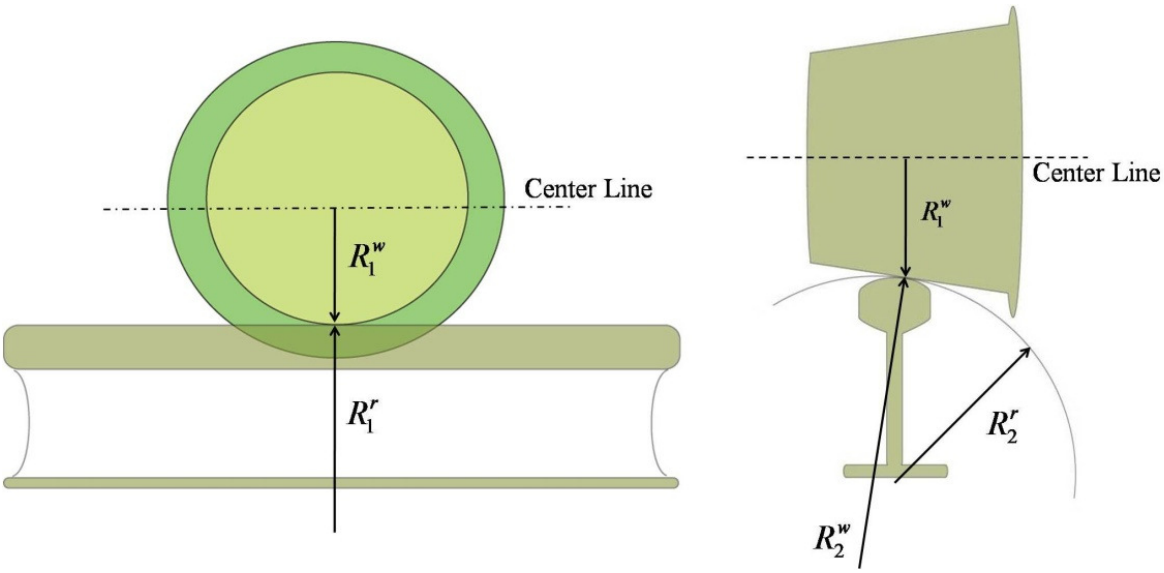

Figure 3.6 Wheel and rail radii of curvature

The coefficients *m* and *n* can be calculated from Equation (3.24) [93]:

$$\begin{aligned} m &= A_m \tan\left(\theta - \pi/2\right) + \frac{B_m}{\theta^{C_m}} + D_m \\ n &= \frac{1}{A_n \tan\left(\theta - \pi/2\right) + 1} + B_n \theta^{C_n} + D_n \sin\theta \end{aligned} \tag{3.24}$$

where the coefficients A_k, B_k, C_k, and D_k ($k = m, n$) are listed in Table 3.2 and θ [*rad*] is defined as shown in Equation (3.25).

$$\theta = \cos^{-1}\left(K_4 \big/ K_3\right)$$

$$K_4 = B - A = \frac{1}{2}\sqrt{\left(\frac{1}{R_1^w} - \frac{1}{R_2^w}\right)^2 + \left(\frac{1}{R_1^r} - \frac{1}{R_2^r}\right)^2 + 2\left(\frac{1}{R_1^w} - \frac{1}{R_2^w}\right)\left(\frac{1}{R_1^r} - \frac{1}{R_2^r}\right)\cos 2\psi} \qquad (3.25)$$

$$= \frac{1}{2}\sqrt{\left(\frac{1}{R_1^w}\right)^2 + \left(-\frac{1}{R_2^r}\right)^2 - 2\frac{1}{R_1^w}\frac{1}{R_2^r}\cos 2\psi}$$

Table 3.2 Coefficients used for the Closed-Form Functions *m* and *n* [93]

Coeff.	**Value**	**Coeff.**	**Value**
A_m	-1.086419051477	A_m	-0.773444080706
B_m	-0.106496432832	B_m	0.256695354565
C_m	1.350000000000	C_m	0.200000000000
D_m	1.057885958251	D_m	-0.280958376499

The normal force at the contact between the wheel and rail can be calculated by Hertz force law based on the concept of the Hertz contact spring. This concept is relies on elastic local deformations of bodies at the contact area. The deformation increases with applied normal load, and the relationship between the normal load and deformation is nonlinear. This nonlinear relationship can be expressed by Hertz force law (For details, the reader is directed to reference [36]).

$$F_n = K_H h_o^{3/2} \qquad (3.26)$$

where K_H is the nonlinear Hertzian stiffness and h_o is relative displacement between wheel and rail. h_o is defined as Equation (3.27) and it is the same as δ in Equation (3.18) (the only difference is the positive or negative direction of application).

$$h_o = u_w - u_r + r \qquad (3.27)$$

where u_w is the wheel displacement, u_r is the rail displacement (both positive downwards), and r is the roughness forming a relative displacement input between the wheel and rail (positive for an asperity) [36]. K_H changes nonlinearly, and it is defined as illustrated in Equation (3.28).

$$K_H = \frac{2E'\sqrt{R_o}}{3}\left(\frac{2}{\Gamma}\right) \tag{3.28}$$

where

$$E' = \frac{E^w + E^r}{2}, \quad v = \frac{v^w + v^r}{2}$$
$$\frac{1}{R_o} = \frac{1}{2}\left(\frac{1}{R_1^w} + \frac{1}{R_2^w} + \frac{1}{R_1^r} + \frac{1}{R_2^r}\right) = \frac{1}{2}\left(\frac{1}{R_1^w} + \frac{1}{R_2^r}\right) \tag{3.29}$$

R_o represents the effective radius of curvature of the surfaces different from the mean wheel radius of curvature (r_o). Equation (3.29) is based on Timoshenko and Goodier [94] and Harris [95]. $\Gamma/2$ is listed in Table 3.3. To calculate $\Gamma/2$, $cos\theta$ must be calculated and is defined as shown in Equation (3.30).

$$\cos\theta = -\frac{R_o}{2}\left(\frac{1}{R_1^w} - \frac{1}{R_2^w} + \frac{1}{R_1^r} - \frac{1}{R_2^r}\right) = -\frac{R_o}{2}\left(\frac{1}{R_1^w} - \frac{1}{R_2^r}\right) \tag{3.30}$$

$\Gamma/2$ is a function of $cos\theta$, and $\Gamma/2$ can be linearly interpolated for a calculated value of $cos\theta$ using the entries of Table 3.3 for the computer implementation. More details regarding the computation of these angles are provided in Thompson [36].

The semi-elliptical contact lengths are calculated from Equation (3.20) when the normal contact force (F_n), the rolling radius of curvature of the wheel (R_1^w), the principal transverse radius of curvature of the rail (R_2^r), and the coefficients m and n are known. However, the directions of the semi-elliptical contact lengths are not specified/computed at this point. Thus, it is important to distinguish between the longitudinal and the lateral semi-elliptical contact lengths since they can decide the shape of the contact patch, as illustrated in Figure 3.7; the creep forces are functions of the dimensions of the contact ellipse, as it will be shown in Equation (3.38).

The general rule for distinguishing semi-elliptical contact lengths is as follows:

1. The semi-elliptical contact lateral length is greater than or equal to the longitudinal length if

$$\frac{1}{R_1^w}+\frac{1}{R_1^j}\geq\frac{1}{R_2^w}+\frac{1}{R_2^j}$$

2. Conversely, the semi-elliptical contact longitudinal length is greater than or equal to the lateral length if

$$\frac{1}{R_1^w}+\frac{1}{R_1^j}\leq\frac{1}{R_2^w}+\frac{1}{R_2^j}$$

In this document, the semi-elliptical contact longitudinal length will be always defined as *a*, and the semi-elliptical contact lateral length will be always defined as *b*. Thus, $a \geq b$ when $R_1^w \geq R_2^r$ and $b \geq a$ when $R_2^r \geq R_1^w$. In general, the contact patch shape is similar to the one shown in Figure 3.7 (a) for the European railroad system, and it is similar to Figure 3.7 (b) for the American railroad system. In this study, the radius of curvature of the wheel and of the rail will be denoted as R_w and R_r, respectively (instead of using R_1^w and R_2^r).

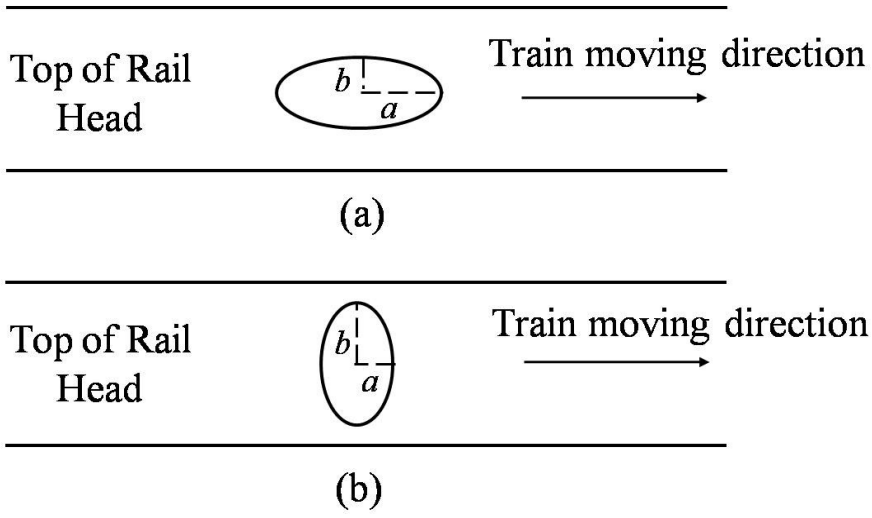

Figure 3.7 Contact patch shapes depending on the wheel-rail geometry. (a) $R_1^w \geq R_2^r$ (b) $R_2^r \geq R_1^w$.

Table 3.3 Parameters for calculating nonlinear Hertzian stiffness. The left table is valid when $a \geq b$, and the right table is valid when $b \geq a$.

a/b	$\cos\theta$	$\Gamma/2$
1.0	0	1
1.259	0.1711	0.9934
1.585	0.3329	0.9741
2.00	0.4781	0.9436
2.51	0.6022	0.9036
3.16	0.7036	0.8566
3.98	0.7836	0.8048
5.01	0.8446	0.7503
6.31	0.8900	0.6949
7.94	0.9231	0.6398
10.0	0.9467	0.5861
12.59	0.9634	0.5346
15.85	0.9750	0.4859
20.0	0.9831	0.4401
25.1	0.9886	0.3974
31.6	0.9923	0.3580
39.8	0.9949	0.3217
50.1	0.9966	0.2885
63.1	0.9977	0.2582
79.4	0.9985	0.2307
100.0	0.9990	0.2058

$\cos\theta$	$\Gamma/2$	b/a
0	1	1.0
-0.1711	0.9934	1.259
-0.3329	0.9741	1.585
-0.4781	0.9436	2.00
-0.6022	0.9036	2.51
-0.7036	0.8566	3.16
-0.7836	0.8048	3.98
-0.8446	0.7503	5.01
-0.8900	0.6949	6.31
-0.9231	0.6398	7.94
-0.9467	0.5861	10.0
-0.9634	0.5346	12.59
-0.9750	0.4859	15.85
-0.9831	0.4401	20.0
-0.9886	0.3974	25.1
-0.9923	0.3580	31.6
-0.9949	0.3217	39.8
-0.9966	0.2885	50.1
-0.9977	0.2582	63.1
-0.9985	0.2307	79.4
-0.9990	0.2058	100.0

Creepage

Creepage, sliding, and pure rolling have already been defined in the Terminology section in Chapter 2. These are very important concepts to understand rolling contact dynamics like the wheel-rail dynamics. In this section, the concept of creepage is further investigated, and several formulations of creepages (longitudinal, lateral, and spin creepages) are discussed.

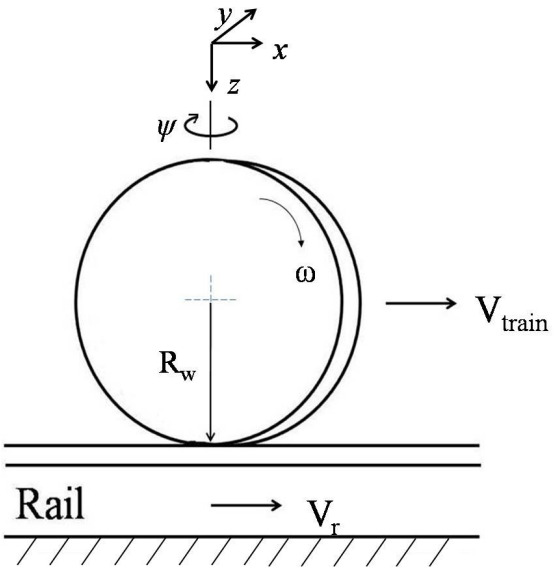

Figure 3.8 Schematic picture of the wheel and rail velocities and effective radius of curvature: *x* is the longitudinal direction; *y* is the lateral direction; and *z* is the vertical direction.

A simplified schematic of a wheel and rail contact is illustrated in Figure 3.8. Wheel velocities for longitudinal and lateral directions and angular wheel velocity can be calculated as presented in Equation (3.31).

$$\begin{aligned} V_{long}^{w} &= \left\{ V_{train} + \dot{\psi}\left(l_o + y\right)\cos\psi \right\}\cos\psi \\ V_{lat}^{w} &= \left(\dot{y}\cos\psi - V_{train}\sin\psi \right)\cos\lambda \\ \Omega^{w} &= \frac{V_{train}}{r_o}\sin\lambda + \dot{\psi}\cos\lambda \end{aligned} \tag{3.31}$$

where V_{train} is the longitudinal train velocity; V_{long}^{w} is the longitudinal wheel velocity; V_{lat}^{w} is the lateral wheel velocity; Ω^{w} is the angular wheel velocity; ψ is the yaw angle of the wheel; λ is the wheel conicity; $\dot{\psi}$ is the yaw angular velocity of the wheel; and l_o is the half gage (0.72365 *m*). Rail velocities for longitudinal and lateral directions and angular rail velocity can be calculated using Equation (3.32).

$$V_{long}^{r} = V_{train}\frac{R_w}{r_o}\cos\psi, \quad V_{lat}^{r} = 0, \quad \Omega^{r} = 0 \tag{3.32}$$

where V_{long}^{r} is the longitudinal rail velocity; r_o is the mean wheel rolling radius of curvature; R^w is the effective wheel radius of curvature, shown in Figure 3.9; V_{lat}^{r} is the lateral rail velocity; and Ω^r is the rail angular velocity of the rail. The reference wheel radius of curvature is defined as the radius of curvature at the moment when the train starts. Effective radius of curvature can be changed with wheel lateral motion. No lateral movement and no angular movement of the rail are assumed. Thus, the lateral rail velocity and the rail angular velocity are zero.

In reality, yaw angle is limited by the flange contact. The conicity in this study is set at 2.86°. In addition, the half-gage length (0.72365 *m*) is much larger than the lateral displacement which is allowed to move less than 10 *mm*. Thus, a small angle approximation for the yaw angle and for the conicity can be applied to Equations (3.31) and (3.32) and the lateral displacement can be ignored in the first part of Equation (3.31). Finally, Equations (3.31) and (3.32) lead to the formulations presented in Equations (3.33) and (3.34).

$$V_{long}^{w} = V_{train} + l_o\dot{\psi}, \quad V_{lat}^{w} = \dot{y} - V_{train}\psi, \quad \Omega^{w} = \frac{V_{train}}{r_o}\lambda + \dot{\psi} \tag{3.33}$$

$$V_{long}^{r} = V_{train}\frac{R_w}{r_o}, \quad V_{lat}^{r} = 0, \quad \Omega^{r} = 0 \tag{3.34}$$

Based on the definition in section 2.1, longitudinal and lateral sliding occurs when $V_{long}^{w} \neq V_{long}^{r}$ and $V_{lat}^{w} \neq V_{lat}^{r}$, respectively. Pure rolling occurs when $V_{long}^{w} = V_{long}^{r}$. Creepage is already defined as the normalized sliding velocity by the longitudinal train velocity in the same section. Creepage is subdivided into three types, i.e., longitudinal creepage, lateral creepage, and spin creepage.

$$\xi_{long} = \frac{V_{long}^{w} - V_{long}^{r}}{V_{train}}, \quad \xi_{lat} = \frac{V_{lat}^{w} - V_{lat}^{r}}{V_{train}}, \quad \xi_{spin} = \frac{\Omega^{w} - \Omega^{r}}{V_{train}} \tag{3.35}$$

In this study, Equations (3.33), (3.34), and (3.35) are used to calculate the velocities of wheel, rail, and creepages.

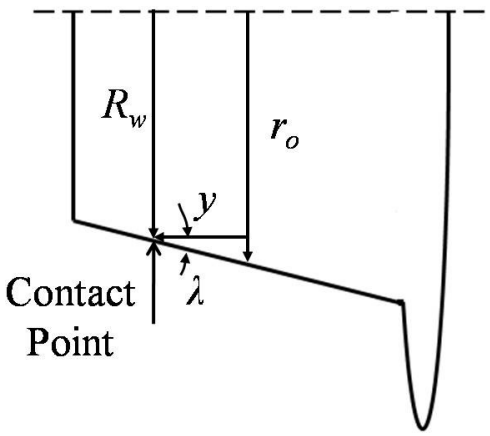

Figure 3.9 Wheel radius of curvature

Radius of curvature of the wheel is calculated from Figure 3.9 by incorporating the lateral displacement (y) as given by Equation (3.36).

$$R^w = r_o - y\tan\lambda \tag{3.36}$$

132RE type rail head data, shown in Figure 3.10 and provided by Norfolk Southern, is used for this simulation study. The equation for the rail head profile is found by using a 5th order polynomial regression model and is used to calculate the radius of curvature of the rail from Equation (3.19). The rail profile is obtained as a function of the lateral displacement. Thus, it can be expressed as follows:

$$\begin{aligned} &f(y) = P_1 y^5 + P_2 y^4 + P_3 y^3 + P_4 y^2 + P_5 y + P_6 \\ &P_1 = -2.4749\times10^{11},\ P_2 = -899,\ P_3 = 8.7881\times10^{-14} \\ &P_4 = -6.8877\times10^{-2},\ P_5 = -4.5924\times10^{-17},\ P_6 = -1.5865\times10^{-4} \end{aligned} \tag{3.37}$$

As mentioned earlier, the radius of curvature of the rail is larger than the radius of curvature of the wheel.

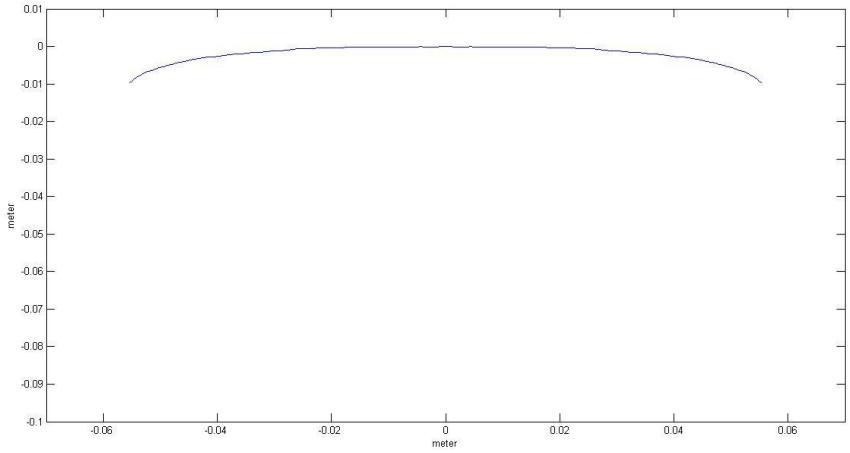

Figure 3.10 Rail head profile

Creep-Force from Kalker's Linear Theory

Forces tangential to the direction of the normal force are transmitted to the rail at the contact patch when sliding occurs between the wheel and rail. These transmitted forces are called creep forces. Creep forces are due to the creepage in the contact patch [92]. Several creep force theories have been developed to study the wheel-rail contact. Kalker's linear theory [83] is one of them, and it has been the extensively used in the wheel-rail dynamics for very small creepage conditions. In this study, the creepage is small enough (much less than 0.01) to be able to apply this theory, when the train is in a steady-state. Thus, Kalker's linear theory is employed. Details about Kalker's linear theory are in [83].

As mentioned earlier, creep forces include longitudinal and lateral creep forces and a spin creep moment. Based on Kalker's linear theory, these creep forces can be calculated as shown in Equation (3.38).

$$\begin{aligned} F_{long} &= -GabC_{11}\xi_{long} \\ F_{lat} &= -Gab\left(C_{22}\xi_{lat} + \sqrt{ab}C_{23}\xi_{spin}\right) \\ M_{spin} &= -Gab\left(-\sqrt{ab}C_{23}\xi_{lat} + abC_{33}\xi_{spin}\right) \end{aligned} \tag{3.38}$$

where G is the shear modulus of rigidity; C_{ij} (i = 1, 2, 3 and j = 1, 2, 3) are creepage and spin coefficients as shown in Table 3.4. G is defined by Kalker as follows:

$$G = \frac{1}{2}\left(\frac{1}{G^w} + \frac{1}{G^r}\right) \tag{3.39}$$

where G_w and G_r are shear modulus of rigidity for the wheel and the rail, respectively. F_{long} points exactly in the longitudinal direction. However, the directions of F_{lat} and M_{spin} have an angle equal to the conicity (λ), as shown in Figure 3. 11.

In reality, contact patch size is millimeter scale to micrometer scale. The contact patch size can be negligible when we consider macro scale such as the wheel-rail system. Thus, we can assume that the contact between the wheel and the rail occurs at the point. Therefore, contact forces are assumed to be point forces applied to the contact point instead of distributed forces applied through the contact patch in this study.

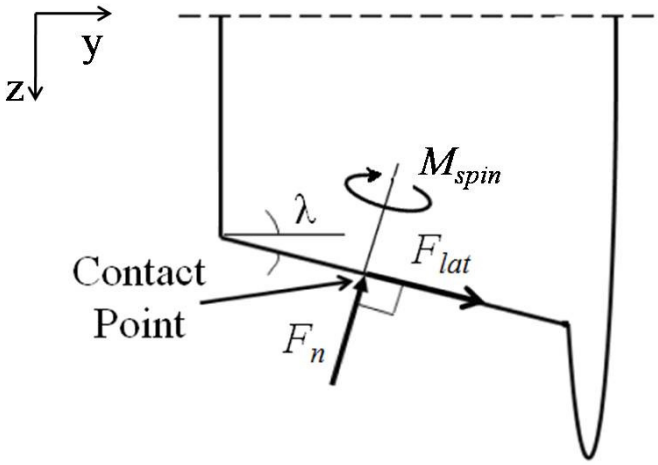

Figure 3.11 Creep force. F_n is the normal contact force.

Table 3.4 Kalker's Creepage and Spin Coefficients [83]

		C_{11}			C_{22}			$C_{23} = -C_{32}$			C_{33}		
	g	$\nu = 0$	0.25	0.5	$\nu = 0$	0.25	0.5	$\nu = 0$	0.25	0.5	$\nu = 0$	0.25	0.5
$\frac{a}{b}$	$\downarrow 0.0$	$\pi^2 / 4(1-\nu)$			$\pi^2/4$			$\frac{\pi\sqrt{g}}{3(1-\nu)}\{1+\nu(0.5\Lambda+\ln 4-5)\}$			$\pi^2/16(1-\nu)g$		
	0.1	2.51	3.31	4.85	2.51	2.52	2.53	0.334	0.473	0.731	6.42	8.28	11.7
	0.2	2.59	3.37	4.81	2.59	2.63	2.66	0.483	0.603	0.809	3.46	4.27	5.66
	0.3	2.68	3.44	4.80	2.68	2.75	2.81	0.607	0.715	0.889	2.49	2.96	3.72
	0.4	2.78	3.53	4.82	2.78	2.88	2.98	0.720	0.823	0.977	2.02	2.32	2.77
	0.5	2.88	3.62	4.83	2.88	3.01	3.14	0.827	0.929	1.07	1.74	1.93	2.22
	0.6	2.98	3.72	4.91	2.98	3.14	3.31	0.930	1.03	1.18	1.56	1.68	1.86
	0.7	3.09	3.81	4.97	3.09	3.28	3.48	1.03	1.14	1.29	1.43	1.50	1.60
	0.8	3.19	3.91	5.05	3.19	3.41	3.65	1.13	1.25	1.40	1.34	1.37	1.42
	0.9	3.29	4.01	5.12	3.29	3.54	3.82	1.23	1.36	1.51	1.27	1.27	1.27
$\frac{b}{a}$	1.0	3.40	4.12	5.20	3.40	3.67	3.98	1.33	1.47	1.63	1.21	1.19	1.16
	0.9	3.51	4.22	5.30	3.51	3.81	4.16	1.44	1.59	1.77	1.16	1.11	1.06
	0.8	3.65	4.36	5.42	3.65	3.99	4.39	1.58	1.75	1.94	1.10	1.04	0.954
	0.7	3.82	4.54	5.58	3.82	4.21	4.67	1.76	1.95	2.18	1.05	0.965	0.852
	0.6	4.06	4.78	5.80	4.06	4.50	5.04	2.01	2.23	2.50	1.01	0.892	0.751
	0.5	4.37	5.10	6.11	4.37	4.90	5.56	2.35	2.62	2.96	0.958	0.819	0.650
	0.4	4.84	5.57	6.57	4.84	5.48	6.31	2.88	3.24	3.70	0.912	0.747	0.549
	0.3	5.57	6.34	7.34	5.57	6.40	7.51	3.79	4.32	5.01	0.868	0.674	0.446
	0.2	6.96	7.78	8.82	6.96	8.14	9.79	5.72	6.63	7.89	0.828	0.601	0.341
	0.1	10.7	11.7	12.9	10.7	12.8	16.0	12.2	14.6	18.0	0.795	0.526	0.228
	$\downarrow 0.0$	$\frac{2\pi}{(\Lambda-2\nu)g}\left\{1+\frac{3-\ln 4}{\Lambda-2\nu}\right\}$			$\frac{2\pi\left\{1+\frac{(1-\nu)(3-\ln 4)}{g(1-\nu)\Lambda+2\nu}\right\}}{g(1-\nu)\Lambda+2\nu}$			$\frac{2\pi}{3g\sqrt{g}\{(1-\nu)\Lambda-2+4\nu\}}$			$\frac{\pi}{4}\left\{1-\frac{\nu(\Lambda-2)}{(1-\nu)\Lambda-2+4\nu}\right\}$		

$$\Lambda = \ln\left(16/g^2\right); \quad g = \min\left(\frac{a}{b}; \frac{b}{a}\right); \quad \ln 4 = 1.386$$

3.2.3 Dynamic Train Model

A dynamic train model at a right passive wheel using a mass-spring-damper system has already been introduced in Section 3.2.1, and is illustrated here in Figure 3.12. In this section, the equations of motions (EOMs) for this model are developed, and the associated free body diagram is presented.

The train model developed in this study has vertical, lateral, and yaw motions. The supporting free body diagrams (FBDs) are illustrated in Figure 3.13. The vertical contact force and the vertical moment between the wheel and the rail can be calculated from the normal contact force, the lateral creep force and the spin moment, respectively. The lateral force applied to the wheel needs to be calculated from the normal contact force and the lateral creep force based on Figure 3.11, as shown in Equation (3.40).

$$F_v = F_n \cos\lambda - F_{lat} \sin\lambda,\ \ F_l = F_n \sin\lambda + F_{lat} \cos\lambda,\ \ M_z = M_{spin} \cos\lambda \qquad (3.40)$$

Equation (3.40) includes the coupling between vertical and lateral directions since the normal contact force and the lateral creep force include the vertical and lateral force components which are a function of vertical and lateral motions. This coupling between vertical and lateral directions is well established by Wu and Thompson [19].

EOMs can be derived from Figure 3.13 and Equation (3.40), and are presented in Equation (3.41).

$$\begin{aligned}
&\textit{Vertical Motion}\\
&a)\ \textit{Body}: \quad M_b \ddot{z}_b = -F_{Cb} - F_{Kb} \qquad \textit{where } F_{Cb} = C_b\left(\dot{z}_b - \dot{z}_w\right),\ F_{Kb} = K_b\left(z_b - z_w\right)\\
&b)\ \textit{Wheel}: \quad M_w \ddot{z}_w = F_{Cb} + F_{Kb} - F_v + M_w g\\
&c)\ \textit{Rail}: \quad M_r \ddot{z}_r = F_v - F_{Ct} - F_{Kt} \qquad \textit{where } F_{Ct} = C_{track}\left(\dot{z}_w - \dot{z}_r\right),\ F_{Kt} = K_{track}\left(z_w - z_r\right)\\
&\textit{Lateral Motion}\\
&\textit{Wheel}: \quad M_w \ddot{y} = F_l - F_{Clat} - F_{Klat} \qquad \textit{where } F_{Clat} = C_{lat}\dot{y},\ F_{Klat} = K_{lat} y\\
&\textit{Yaw Motion}\\
&\textit{Wheel}: \quad J_w \ddot{\psi} = M_z - C_\theta \dot{\psi} - K_\theta \psi
\end{aligned} \qquad (3.41)$$

For Matlab implementation, the state-space representation of the EOMs is derived and presented in Equation (3.42).

$$x_1(0)=z_b(0),\ x_2(0)=\dot{z}_b(0),\ x_3(0)=z_w(0),\ x_4(0)=\dot{z}_w(0),\ x_5(0)=z_r(0)$$
$$x_6(0)=\dot{z}_r(0),\ x_7(0)=y(0),\ x_8(0)=\dot{y}(0),\ x_9(0)=\psi(0),\ x_{10}(0)=\dot{\psi}(0)$$

$$\begin{cases} \dot{x}_1=x_2, \quad \dot{x}_2=-\dfrac{C_b\left(x_2-x_4\right)+K_b\left(x_1-x_3\right)}{M_b} \\ \dot{x}_3=x_4, \quad \dot{x}_4=\dfrac{C_b\left(x_2-x_4\right)+K_b\left(x_1-x_3\right)-F_v+M_w g}{M_w} \\ \dot{x}_5=x_6, \quad \dot{x}_6=\dfrac{F_v-C_{track}\left(x_4-x_6\right)-K_{track}\left(x_3-x_5\right)}{M_r} \\ \dot{x}_7=x_8, \quad \dot{x}_8=\dfrac{F_l-C_{lat}x_8-K_{lat}x_7}{M_w} \\ \dot{x}_9=x_{10}, \quad \dot{x}_{10}=\dfrac{M_z-C_\theta x_{10}-K_\theta x_9}{J_w} \end{cases} \tag{3.42}$$

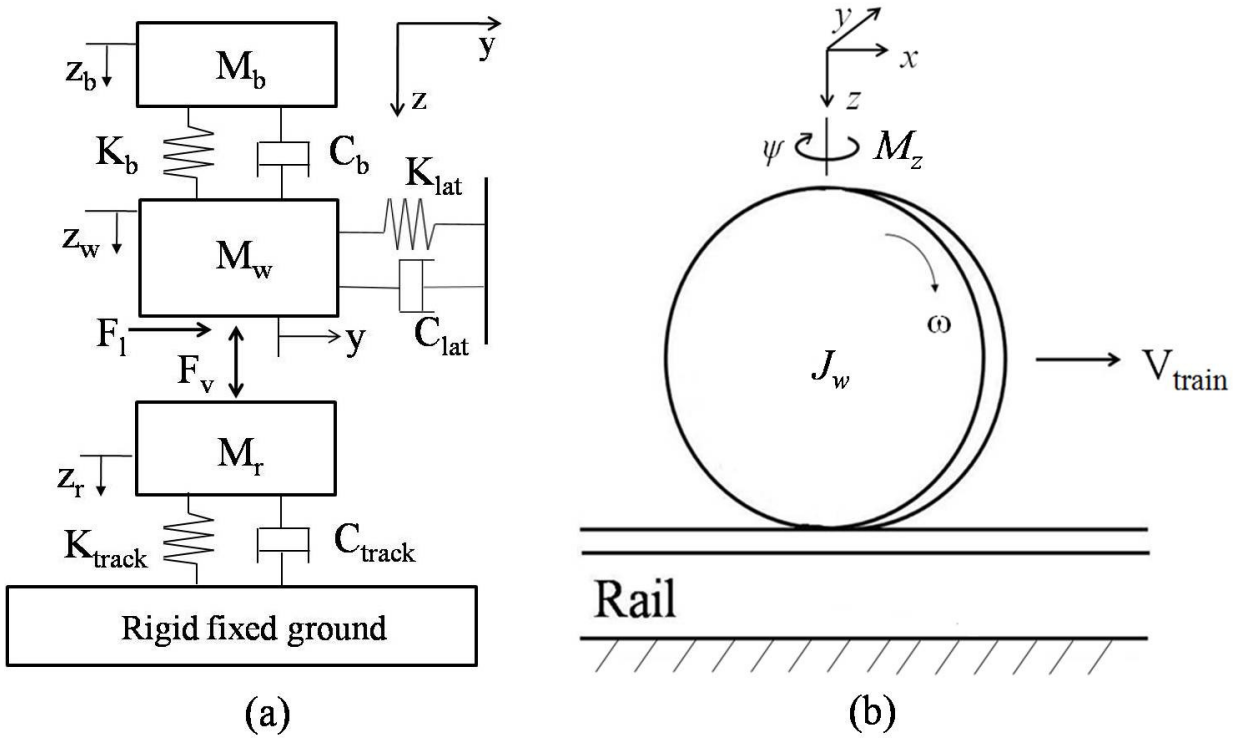

Figure 3.12 Vertical, lateral vibrations, and yaw motion model of the train at the right wheel

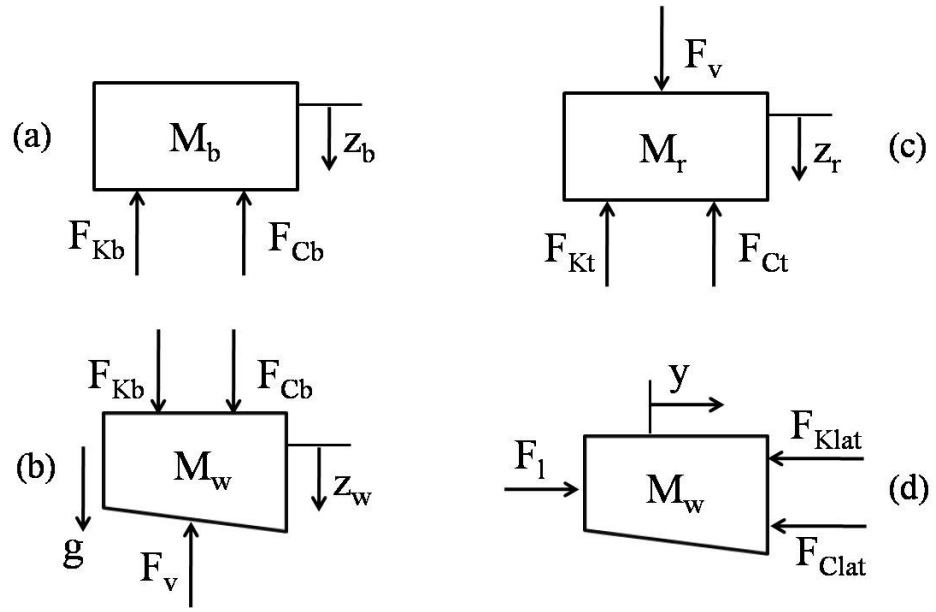

Figure 3.13 FBDs for wheel and rail vertical and lateral motion: (a) train body vertical motion, (b) wheel vertical motion, (c) rail vertical motion, and (d) wheel lateral motion. The yaw motion is shown in Figure 3.12 (b).

3.2.4 Algorithm

An algorithm was developed to calculate all variables modeled in the wheel-rail dynamics and CoF equations. In the real world, variables of the wheel-rail dynamics influence each other and change in a closed-loop, feedback manner. For example, the semi-elliptical contact lengths *a* and *b* influence the Hertzian stiffness calculation which in turn influences the normal contact force calculation. Closing the feedback loop, the normal contact force influences the calculation of *a* and *b*. Thus, it is necessary to calculate some input variables prior to starting the algorithm. These inputs will be recalculated in an iterative fashion as the algorithm progresses.

To better understand the algorithm, a flow chart is introduced in Figure 3.14. The calculation starts from stop at $t = 0$. The initial conditions include the following:

1. Vertical train body displacement and velocity.
2. Vertical wheel displacement and velocity.
3. Vertical rail displacement and velocity.
4. Lateral wheel displacement and velocity.

5. Yaw wheel displacement and angular velocity.

In addition, the normal contact force, semi-elliptical contact lengths, and Kalker's coefficients at $t = 0$ are calculated and used as input data when needed.

As presented earlier, the rail roughness is a source of internal excitation. This study assumes that there are no external sources of excitation. The lateral displacement of the wheel and the rail profile are used to find contact locations between the wheel and the rail. A contact point at $t = 0$ is assumed to occur between the center point of the rail profile and the mean wheel radius of curvature point. If the wheel moves 5 *mm* to the left of the center point of the rail profile, the contact point of the wheel will be 5 *mm* to the right of the mean radius of curvature, as it can be seen from Figure 3.9, and the contact point of the rail is 5 *mm* to the left of the center of the rail profile; the center of the profile is set as a zero and to the left from the center point is considered the negative direction, while to the right from the center point is considered the positive direction, while referring to Figure 3.10. Based on these conventions, the calculations employed by the algorithm developed follows the steps presented below:

Step 1. Radii of curvatures of the wheel (R_w) and rail (R_r)

The radii of curvature are calculated from Equations (3.19) and (3.36) using lateral displacement.

Step 2. Hertzian stiffness (K_H) and the normal contact force (F_n)

Hertzian stiffness is calculated using Equations (3.28)-(3.30) and Table 3.3. The input values are the semi-elliptical contact lengths (a and b), Young's modulus for steel (E), R_w and R_r from step 1, Poisson ratio for steel (v), train velocity (V_{train}), and Kalker's coefficients (C_{ij}). When the relative wheel-rail vibration (δ) from Equation (3.27) is equal to or is less than zero, the wheel and rail do not deform since there is no contact. Thus, K_H is defined as zero when $\delta \leq 0$ or $t = 0$.

Using calculated values of K_H, the normal contact force is determined using Equations (3.26) and (3.27). The inputs are K_H, vertical wheel and rail displacements, and rail roughness.

The normal contact force (F_n) at $t = 0$ is the static normal contact load which is defined as the gravitational force on the rail when the train is stopped.

Step 3.

i) Semi-elliptical contact longitudinal length (a) and lateral length (b)

Using F_n calculated from step 2, semi-elliptical contact lengths are calculated with Equations (3.20)-(3.25) and Table 3.2. Semi-elliptical contact lengths at $t = 0$ are calculated using the static normal contact load. A decision for a and b based on lengths of R_w and R_r as shown in Figure 3.7 is made after calculating the semi-elliptical contact lengths. In addition to F_n, the other input variables are R_w and R_r from step 1, yaw angle (ψ), and lateral displacement (y).

ii) Creepage

Velocities of the wheel and rail are calculated using Equations (3.33) and (3.34), and then values of creepage are calculated using Equation (3.35). The input values are V_{train}, mean wheel radius of curvature (r_o), yaw angle (ψ), yaw angular velocity ($\dot{\psi}$), conicity (λ), half-gage length (l_o), R_w from step 1, and lateral velocity ($\dot{y}$).

Step 4. Kalker's C coefficients

Kalker's C coefficients are dependent on the Poisson ratio (v) of the wheel and rail materials and the semi-elliptical contact lengths. From these input values, C coefficients can be determined from Table 3.4. Table 3.4 does not provide every possible value of Poisson ratio and a/b or b/a ratio. Thus, interpolation is necessary to find the C coefficient for the specific v and a/b or b/a ratio. In this study, a linear interpolation is used. The C coefficients are defined as zero when a and b are zero, i.e., no contact.

Step 5. Creep forces

Creep forces are calculated using Equations (3.38) and (3.39). The input values are the creepage and the semi-elliptical contact lengths from step 3, Kalker's C coefficients from step 4, and shear moduli of rigidity for the wheel and the rail.

Step 6. Vertical (F_v) and lateral (F_l) contact forces and contact moment (M_z)

Values of F_v, F_l, and M_z are calculated from Equation (3.40) using the normal contact force from step 2, lateral creep force from step 5, and the spin creep moment.

Step 7. Displacements and velocities from EOMs (State-space)

Displacements and velocities from Equations (3.40) and (3.42) are calculated using Matlab's ode45 differential equation solver. Calculated displacements and velocities become the new initial conditions and serve as inputs for iterative calculations of steps 1 through 7.

Step 8. Coefficient of Friction (CoF)

The CoF is calculated from Equation (3.4) using variables from steps 1 through 6. Displacements from initial conditions instead of displacements newly calculated from step 7 are used to calculate the CoF. Damping coefficients for the longitudinal and lateral directions at the contact patch are calculated using Equation (3.5).

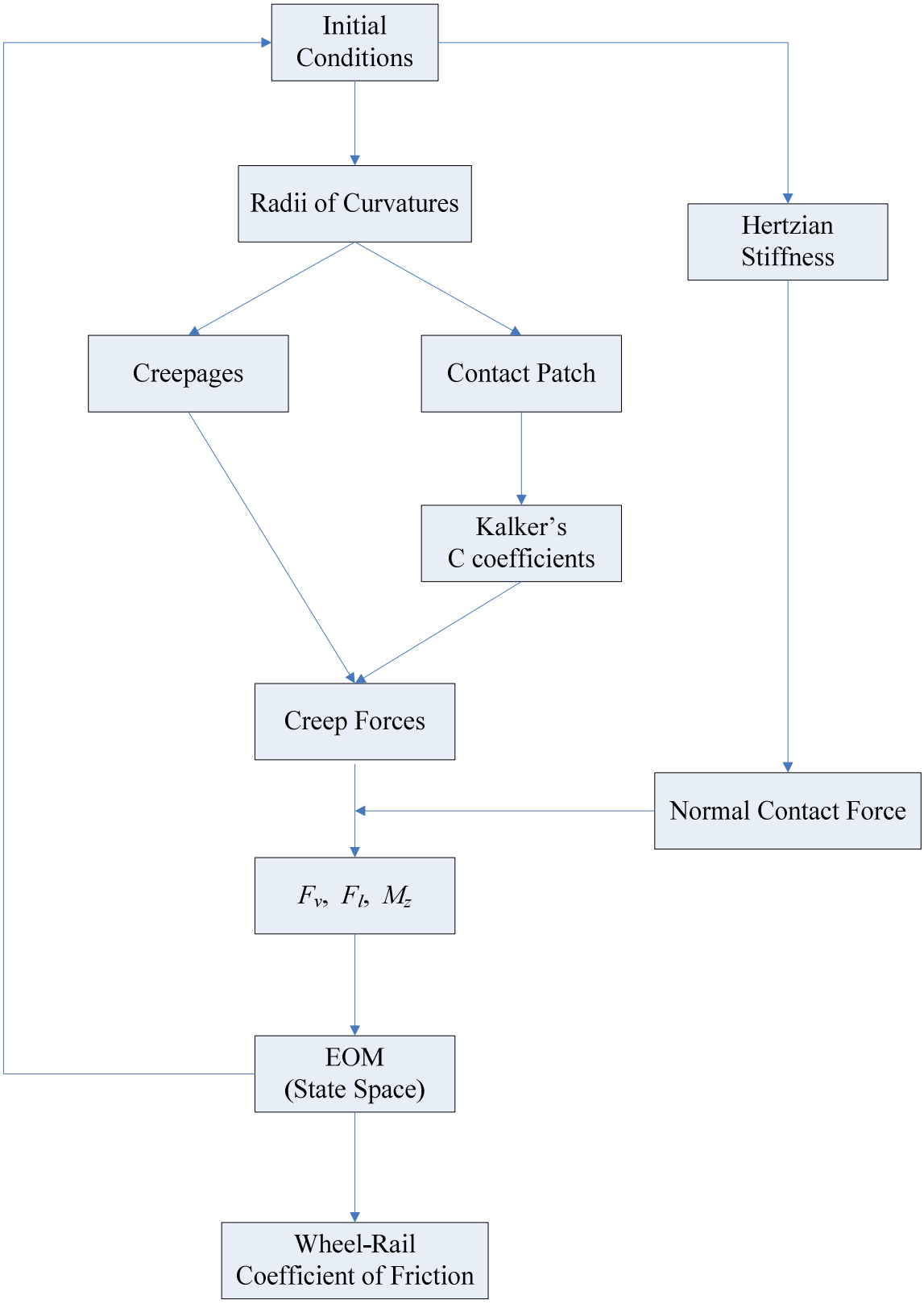

Figure 3.14 Algorithm flow chart

3.3 Stochastic Analysis of the Wheel-Rail Friction

The state-space equations for a deterministic model are introduced in section 3.2.3 through Equation (3.42). To deal with uncertain random variables, the polynomial chaos theory is employed in this study. Five poly-chaos expansion terms and 15 collocation points are used for studying the effects of one uncertain random variable. Fifteen poly-chaos expansion terms and 30 collocation points are used for studying the simultaneous effects of two independent uncertain random variables on the CoF. Finally, thirty five poly-chaos expansion terms and 70 collocation points are used for studying the simultaneous effects of three independent uncertain random variables on the CoF. Random (uncertain) variables on this study include the maximum amplitude of rail roughness (MARR), semi-elliptical contact lengths (a and b), track stiffness and damping, lateral displacement, and sleeper distance. Random variables are assumed to have a symmetric beta distribution. (Other types of distributions can be easily employed, if needed.)

In this section, generalized examples for applying the poly-chaos theory to a system of ordinary differential equations (ODEs) are introduced. Then, a stochastic CoF model with one uncertainty, two independent uncertainties, and three independent uncertainties are introduced as specific case studies.

3.3.1 A Stochastic CoF Model with One Uncertainty

Uncertain Maximum Amplitude of Rail Roughness

The maximum amplitude of rail roughness (MARR) is considered as an uncertain variable. Uncertain MARR can be expressed using a truncated Karhunen-Loeve expansion as follows:

$$r = \sum_{i=1}^{S} r^i \Psi^i \tag{3.43}$$

Equation (3.43) propagates from the calculation of the normal force to the calculation of the CoF model following the steps presented below.

Step 1. The stochastic normal contact force

The r value from Equation (3.43) and the wheel displacement (x_3) and the rail displacement (x_5) from Equation (3.53) are substituted into Equation (3.27), yielding Equation (3.44).

$$\sum_{i=1}^{S} h_o{}^i\Psi^i = \sum_{i=1}^{S} x_3{}^i\Psi^i - \sum_{i=1}^{S} x_5{}^i\Psi^i + \sum_{i=1}^{S} r^i\Psi^i \tag{3.44}$$

Then Equation (3.44) is substituted into Equation (3.26) to obtain the stochastic normal contact force as follows:

$$\sum_{i=1}^{S} F_n{}^i\Psi^i = K_H \left(\sum_{i=1}^{S} h_o{}^i\Psi^i \right)^{3/2} \tag{3.45}$$

Step 2. The stochastic semi-elliptical contact lengths

Equation (3.45) is substituted into Equation (3.20) to calculate the stochastic semi-elliptical contact lengths while assuming that L_1 is always a and L_2 is always b (in this study).

$$\begin{aligned} \sum_{i=1}^{S} L_1{}^i\Psi^i &= m\left(\frac{3\pi\left(K_1+K_2\right)}{4K_3} \sum_{i=1}^{S} F_n{}^i\Psi^i \right)^{1/3} = \sum_{i=1}^{S} a^i\Psi^i = m\left(\frac{3\pi\left(K_1+K_2\right)}{4K_3} \sum_{i=1}^{S} F_n{}^i\Psi^i \right)^{1/3} \\ \sum_{i=1}^{S} L_2{}^i\Psi^i &= n\left(\frac{3\pi\left(K_1+K_2\right)}{4K_3} \sum_{i=1}^{S} F_n{}^i\Psi^i \right)^{1/3} = \sum_{i=1}^{S} b^i\Psi^i = n\left(\frac{3\pi\left(K_1+K_2\right)}{4K_3} \sum_{i=1}^{S} F_n{}^i\Psi^i \right)^{1/3} \end{aligned} \tag{3.46}$$

Step 3. The stochastic Kalker's C coefficient

There is no specific formula to calculate the C coefficients since they are calculated by interpolation using semi-elliptical contact lengths. Thus, they are expressed as the truncated Karhunen-Loeve expansions presented in Equation (3.47).

$$\sum_{i=1}^{S} C_{11}{}^i\Psi^i,\ \sum_{i=1}^{S} C_{22}{}^i\Psi^i,\ \sum_{i=1}^{S} C_{33}{}^i\Psi^i,\ \sum_{i=1}^{S} C_{23}{}^i\Psi^i \tag{3.47}$$

Step 4. The stochastic creep forces

By substituting Equation (3.53) into Equation (3.33), the stochastic wheel velocities are found as presented in Equation (3.48).

$$\sum_{i=1}^{S}\left(V_{long}^{w}\right)^{i}\Psi^{i}=V_{train}+l_{o}\sum_{i=1}^{S}\left(x_{10}\right)^{i}\Psi^{i},\ \sum_{i=1}^{S}\left(V_{lat}^{w}\right)^{i}\Psi^{i}=\sum_{i=1}^{S}x_{8}{}^{i}\Psi^{i}+V_{train}\sum_{i=1}^{S}\left(x_{9}\right)^{i}\Psi^{i},\ \sum_{i=1}^{S}\left(\Omega^{w}\right)^{i}\Psi^{i}=\omega\lambda+\sum_{i=1}^{S}\left(x_{10}\right)^{i}\Psi^{i} \tag{3.48}$$

The stochastic creepage can be found by substituting Equation (3.48) into Equation (3.49).

$$\sum_{i=1}^{S}\left(\xi_{long}\right)^{i}\Psi^{i}=\frac{\sum_{i=1}^{S}\left(V_{long}^{w}\right)^{i}\Psi^{i}-V_{long}^{r}}{V_{train}},\ \sum_{i=1}^{S}\left(\xi_{lat}\right)^{i}\Psi^{i}=\frac{\sum_{i=1}^{S}\left(V_{lat}^{w}\right)^{i}\Psi^{i}-V_{long}^{r}}{V_{train}},\ \sum_{i=1}^{S}\left(\xi_{spin}\right)^{i}\Psi^{i}=\frac{\sum_{i=1}^{S}\left(\Omega^{w}\right)^{i}\Psi^{i}-\Omega^{r}}{V_{train}} \tag{3.49}$$

Equations (3.46), (3.47), and (3.49) are substituted into Equation (3.38) to obtain the stochastic creep forces of Equation (3.50).

$$\begin{aligned}
&\sum_{i=1}^{S}F_{long}{}^{i}\Psi^{i}=-G\left(\sum_{i=1}^{S}a^{i}\Psi^{i}\right)\left(\sum_{i=1}^{S}b^{i}\Psi^{i}\right)\left(\sum_{i=1}^{S}C_{11}{}^{i}\Psi^{i}\right)\left(\sum_{i=1}^{S}\xi_{long}{}^{i}\Psi^{i}\right)\\
&\sum_{i=1}^{S}F_{lat}{}^{i}\Psi^{i}=-G\left(\sum_{i=1}^{S}a^{i}\Psi^{i}\right)\left(\sum_{i=1}^{S}b^{i}\Psi^{i}\right)\left\{\left(\sum_{i=1}^{S}C_{22}{}^{i}\Psi^{i}\right)\left(\sum_{i=1}^{S}\xi_{lat}{}^{i}\Psi^{i}\right)+\sqrt{\left(\sum_{i=1}^{S}a^{i}\Psi^{i}\right)\left(\sum_{i=1}^{S}b^{i}\Psi^{i}\right)}\left(\sum_{i=1}^{S}C_{23}{}^{i}\Psi^{i}\right)\left(\sum_{i=1}^{S}\xi_{spin}{}^{i}\Psi^{i}\right)\right\}\\
&\sum_{i=1}^{S}M_{spin}{}^{i}\Psi^{i}=-G\left(\sum_{i=1}^{S}a^{i}\Psi^{i}\right)\left(\sum_{i=1}^{S}b^{i}\Psi^{i}\right)\left\{-\sqrt{\left(\sum_{i=1}^{S}a^{i}\Psi^{i}\right)\left(\sum_{i=1}^{S}b^{i}\Psi^{i}\right)}\left(\sum_{i=1}^{S}C_{23}{}^{i}\Psi^{i}\right)\left(\sum_{i=1}^{S}\xi_{lat}{}^{i}\Psi^{i}\right)+\left(\sum_{i=1}^{S}a^{i}\Psi^{i}\right)\left(\sum_{i=1}^{S}b^{i}\Psi^{i}\right)\left(\sum_{i=1}^{S}C_{33}{}^{i}\Psi^{i}\right)\left(\sum_{i=1}^{S}\xi_{spin}{}^{i}\Psi^{i}\right)\right\}
\end{aligned} \tag{3.50}$$

Step 5. The stochastic ODEs

Equations (3.45) and (3.50) are substituted into Equation (3.40) to find the stochastic vertical and lateral contact forces and the stochastic moment with respect to the vertical axis (z).

$$\begin{aligned}
\sum_{i=1}^{S}F_{v}{}^{i}\Psi^{i}&=\left(\sum_{i=1}^{S}F_{n}{}^{i}\Psi^{i}\right)\cos\lambda-\left(\sum_{i=1}^{S}F_{lat}{}^{i}\Psi^{i}\right)\sin\lambda\\
\sum_{i=1}^{S}F_{l}{}^{i}\Psi^{i}&=\left(\sum_{i=1}^{S}F_{n}{}^{i}\Psi^{i}\right)\sin\lambda+\left(\sum_{i=1}^{S}F_{lat}{}^{i}\Psi^{i}\right)\cos\lambda\\
\sum_{i=1}^{S}M_{z}{}^{i}\Psi^{i}&=\left(\sum_{i=1}^{S}M_{spin}{}^{i}\Psi^{i}\right)\cos\lambda
\end{aligned} \tag{3.51}$$

Equation (3.51) and (3.53) are substituted into Equation (3.42) to obtain the stochastic ODEs.

$$
\begin{cases}
\sum_{i=1}^{S} \dot{x}_1{}^i\Psi^i = \left(\sum_{i=1}^{S} x_2{}^i\Psi^i\right) \\
\sum_{i=1}^{S} \dot{x}_2{}^i\Psi^i = -\dfrac{C_b\left(\left(\sum_{i=1}^{S} x_2{}^i\Psi^i\right)-\left(\sum_{i=1}^{S} x_4{}^i\Psi^i\right)\right)+K_b\left(\left(\sum_{i=1}^{S} x_1{}^i\Psi^i\right)-\left(\sum_{i=1}^{S} x_3{}^i\Psi^i\right)\right)}{M_b} \\
\sum_{i=1}^{S} \dot{x}_3{}^i\Psi^i = \left(\sum_{i=1}^{S} x_4{}^i\Psi^i\right) \\
\sum_{i=1}^{S} \dot{x}_4{}^i\Psi^i = \dfrac{C_b\left(\left(\sum_{i=1}^{S} x_2{}^i\Psi^i\right)-\left(\sum_{i=1}^{S} x_4{}^i\Psi^i\right)\right)+K_b\left(\left(\sum_{i=1}^{S} x_1{}^i\Psi^i\right)-\left(\sum_{i=1}^{S} x_3{}^i\Psi^i\right)\right)-\left(\sum_{i=1}^{S} F_v{}^i\Psi^i\right)}{M_w} \\
\sum_{i=1}^{S} \dot{x}_5{}^i\Psi^i = \left(\sum_{i=1}^{S} x_6{}^i\Psi^i\right) \\
\sum_{i=1}^{S} \dot{x}_6{}^i\Psi^i = \dfrac{\left(\sum_{i=1}^{S} F_v{}^i\Psi^i\right)-C_{track}\left(\left(\sum_{i=1}^{S} x_4{}^i\Psi^i\right)-\left(\sum_{i=1}^{S} x_6{}^i\Psi^i\right)\right)-K_{track}\left(\left(\sum_{i=1}^{S} x_3{}^i\Psi^i\right)-\left(\sum_{i=1}^{S} x_5{}^i\Psi^i\right)\right)}{M_r} \\
\sum_{i=1}^{S} \dot{x}_7{}^i\Psi^i = \left(\sum_{i=1}^{S} x_8{}^i\Psi^i\right) \\
\sum_{i=1}^{S} \dot{x}_8{}^i\Psi^i = \dfrac{\left(\sum_{i=1}^{S} F_l{}^i\Psi^i\right)-C_{lat}\left(\sum_{i=1}^{S} x_8{}^i\Psi^i\right)-K_{lat}\left(\sum_{i=1}^{S} x_7{}^i\Psi^i\right)}{M_w} \\
\sum_{i=1}^{S} \dot{x}_9{}^i\Psi^i = \left(\sum_{i=1}^{S} x_{10}{}^i\Psi^i\right) \\
\sum_{i=1}^{S} \dot{x}_{10}{}^i\Psi^i = \dfrac{\left(\sum_{i=1}^{S} M_z{}^i\Psi^i\right)-C_\theta\left(\sum_{i=1}^{S} x_{10}{}^i\Psi^i\right)-K_\theta\left(\sum_{i=1}^{S} x_9{}^i\Psi^i\right)}{J_w}
\end{cases}
\tag{3.52}
$$

By integrating Equation (3.52), the stochastic displacements and velocities can be found as follows:

$$
\begin{aligned}
&\sum_{i=1}^{S} x_1{}^i\Psi^i, \quad \sum_{i=1}^{S} x_3{}^i\Psi^i, \quad \sum_{i=1}^{S} x_5{}^i\Psi^i, \quad \sum_{i=1}^{S} x_7{}^i\Psi^i, \quad \sum_{i=1}^{S} x_9{}^i\Psi^i \\
&\sum_{i=1}^{S} x_2{}^i\Psi^i, \quad \sum_{i=1}^{S} x_4{}^i\Psi^i, \quad \sum_{i=1}^{S} x_6{}^i\Psi^i, \quad \sum_{i=1}^{S} x_8{}^i\Psi^i, \quad \sum_{i=1}^{S} x_{10}{}^i\Psi^i
\end{aligned}
\tag{3.53}
$$

Step 6. The stochastic CoF

Equations (3.46) and (3.47) are substituted into Equation (3.5) to find the stochastic longitudinal and lateral damping coefficients at the contact patch.

$$\sum_{i=1}^{S} c_{long\_contact}{}^{i}\Psi^{i} = \frac{E\left(\sum_{i=1}^{S} a^{i}\Psi^{i}\right)\left(\sum_{i=1}^{S} b^{i}\Psi^{i}\right)\left(\sum_{i=1}^{S} C_{11}{}^{i}\Psi^{i}\right)}{2(1+v)V_{train}}$$
$$\sum_{i=1}^{S} c_{lat\_contact}{}^{i}\Psi^{i} = \frac{E\left(\sum_{i=1}^{S} a^{i}\Psi^{i}\right)\left(\sum_{i=1}^{S} b^{i}\Psi^{i}\right)\left(\sum_{i=1}^{S} C_{22}{}^{i}\Psi^{i}\right)}{2(1+v)V_{train}} \tag{3.54}$$

All stochastic and deterministic dynamic parameters are substituted into Equation (3.4) and then the stochastic CoFs are obtained.

$$\sum_{i=i}^{S}\mu(t)^{i}\Psi^{i} = \underbrace{c_1\left(\frac{\left(\sum_{i=1}^{S} V^{*}(t)^{i}\Psi^{i}\right)}{\left(\sum_{i=i}^{S} R^{*}(t)^{i}\Psi^{i}\right)}\right)^{0.28}\frac{e^{-c_2\sqrt{\left(\sum_{i=1}^{S} V^{*}(t)^{i}\Psi^{i}\right)}}}{1+c_3\left(\frac{\left(\sum_{i=1}^{S} a^{i}\Psi^{i}\right)}{\left(\sum_{i=1}^{S} b^{i}\Psi^{i}\right)}\right)^{2}\left(\sum_{i=i}^{S} R^{*}(t)^{i}\Psi^{i}\right)}}_{Slip\ Component} + \underbrace{\frac{c_4}{1+c_5\left(\frac{\left(\sum_{i=1}^{S} a^{i}\Psi^{i}\right)}{\left(\sum_{i=1}^{S} b^{i}\Psi^{i}\right)}\right)^{2}\left(\sum_{i=i}^{S} R^{*}(t)^{i}\Psi^{i}\right)}}_{Stick\ Component}$$

$$\sum_{i=1}^{S} c_{\tan}{}^{i}\Psi^{i} = \sqrt{\left(\sum_{i=1}^{S} c_{long\_contact}{}^{i}\Psi^{i}\right)^{2} + \left(\sum_{i=1}^{S} c_{lat\_contact}{}^{i}\Psi^{i}\right)^{2}}, \quad \sum_{i=1}^{S} V^{*}(t)^{i}\Psi^{i} = \frac{V_{\tan}}{\left(\sum_{i=1}^{S} F_{n}{}^{i}\Psi^{i}\right)}\left(\sum_{i=1}^{S} c_{\tan}{}^{i}\Psi^{i}\right)$$

$$\sum_{i=1}^{S} T^{i}\Psi^{i} = \frac{-d\left(\sum_{i=1}^{S} h_{o}{}^{i}\Psi^{i}\right)\left(\sum_{i=1}^{S} b^{i}\Psi^{i}\right)}{\sigma_{\tan}\left(\sum_{i=1}^{S} a^{i}\Psi^{i}\right)}, \quad \sum_{i=i}^{S} R^{*}(t)^{i}\Psi^{i} = 1 - e^{\left(\sum_{i=1}^{S} T^{i}\Psi^{i}\right)} \tag{3.55}$$

Uncertain *a/b*

The ratio of semi-elliptical contact lengths is considered as an uncertain variable. Uncertain *a/b* can be expressed using a truncated Karhunen-Loeve expansion as follows:

$$\frac{a}{b} = \sum_{i=1}^{S}\left(\frac{a}{b}\right)^{i}\Psi^{i} \tag{3.56}$$

Equation (3.56) is substituted into Equation (3.4) and then the stochastic CoF is obtained.

$$\sum_{i=i}^{S}\mu(t)^{i}\Psi^{i}=\underbrace{c_1\left(\frac{V^{*}(t)}{\sum_{i=i}^{S}R^{*}(t)^{i}\Psi^{i}}\right)^{0.28}\frac{e^{-c_2\sqrt{V^{*}(t)}}}{1+c_3\left(\sum_{i=i}^{S}\left(\frac{a}{b}\right)^{i}\Psi^{i}\right)^{2}\left(\sum_{i=i}^{S}R^{*}(t)^{i}\Psi^{i}\right)}}_{Slip\ Component}+\underbrace{\frac{c_4}{1+c_5\left(\sum_{i=i}^{S}\left(\frac{a}{b}\right)^{i}\Psi^{i}\right)^{2}\left(\sum_{i=i}^{S}R^{*}(t)^{i}\Psi^{i}\right)}}_{Stick\ Component} \tag{3.57}$$

$$\sum_{i=1}^{S}T^{i}\Psi^{i}=\frac{-dh_o}{\sigma_{\tan}\left(\sum_{i=i}^{S}\left(\frac{a}{b}\right)^{i}\Psi^{i}\right)},\qquad \sum_{i=i}^{S}R^{*}(t)^{i}\Psi^{i}=1-e^{\left(\sum_{i=1}^{S}T^{i}\Psi^{i}\right)}$$

Uncertain Track Stiffness

The track stiffness is considered as an uncertain variable. Uncertain track stiffness can be expressed using a truncated Karhunen-Loeve expansion as follows:

$$K_{track}=\sum_{i=1}^{S}K_{track}{}^{i}\Psi^{i} \tag{3.58}$$

Equation (3.58) propagates from the calculation of the normal force to the calculation of the CoF model following the steps presented below.

Step 1. The stochastic normal contact force

The stochastic wheel displacement (x_3) and rail displacement (x_5) from Equation (3.68) are substituted into Equation (3.27) given Equation (3.59).

$$\sum_{i=1}^{S}h_o{}^{i}\Psi^{i}=\sum_{i=1}^{S}x_3{}^{i}\Psi^{i}-\sum_{i=1}^{S}x_5{}^{i}\Psi^{i}+r \tag{3.59}$$

Then Equation (3.59) is substituted into Equation (3.26) to obtain the stochastic normal contact force as follows:

$$\sum_{i=1}^{S}F_n{}^{i}\Psi^{i}=K_H\left(\sum_{i=1}^{S}h_o{}^{i}\Psi^{i}\right)^{3/2} \tag{3.60}$$

Step 2. The stochastic semi-elliptical contact lengths

Equation (3.60) is substituted into Equation (3.20) to calculate the stochastic semi-elliptical contact lengths.

$$\begin{aligned}\sum_{i=1}^{S} L_1{}^i\Psi^i &= m\left(\frac{3\pi\left(K_1+K_2\right)}{4K_3}\sum_{i=1}^{S} F_n{}^i\Psi^i\right)^{1/3} = \sum_{i=1}^{S} a^i\Psi^i = m\left(\frac{3\pi\left(K_1+K_2\right)}{4K_3}\sum_{i=1}^{S} F_n{}^i\Psi^i\right)^{1/3} \\ \sum_{i=1}^{S} L_2{}^i\Psi^i &= n\left(\frac{3\pi\left(K_1+K_2\right)}{4K_3}\sum_{i=1}^{S} F_n{}^i\Psi^i\right)^{1/3} = \sum_{i=1}^{S} b^i\Psi^i = n\left(\frac{3\pi\left(K_1+K_2\right)}{4K_3}\sum_{i=1}^{S} F_n{}^i\Psi^i\right)^{1/3}\end{aligned} \tag{3.61}$$

Step 3. The stochastic Kalker's C coefficient

The *C* coefficients are expressed as the truncated Karhunen-Loeve expansions presented in Equation (3.62).

$$\sum_{i=1}^{S} C_{11}{}^i\Psi^i,\ \sum_{i=1}^{S} C_{22}{}^i\Psi^i,\ \sum_{i=1}^{S} C_{33}{}^i\Psi^i,\ \sum_{i=1}^{S} C_{23}{}^i\Psi^i \tag{3.62}$$

Step 4. The stochastic creep forces

By substituting Equation (3.68) into Equation (3.33), the stochastic wheel velocities are found as presented in Equation (3.63).

$$\sum_{i=1}^{S}\left(V_{long}^{w}\right)^i\Psi^i = V_{train} + l_o\sum_{i=1}^{S}\left(x_{10}\right)^i\Psi^i,\ \sum_{i=1}^{S}\left(V_{lat}^{w}\right)^i\Psi^i = \sum_{i=1}^{S} x_8{}^i\Psi^i + V_{train}\sum_{i=1}^{S}\left(x_9\right)^i\Psi^i,\ \sum_{i=1}^{S}\left(\Omega^w\right)^i\Psi^i = \omega\lambda + \sum_{i=1}^{S}\left(x_{10}\right)^i\Psi^i \tag{3.63}$$

The stochastic creepage can be found by substituting Equation (3.63) into Equation (3.49).

$$\sum_{i=1}^{S}\left(\xi_{long}\right)^i\Psi^i = \frac{\sum_{i=1}^{S}\left(V_{long}^{w}\right)^i\Psi^i - V_{long}^{r}}{V_{train}},\ \sum_{i=1}^{S}\left(\xi_{lat}\right)^i\Psi^i = \frac{\sum_{i=1}^{S}\left(V_{lat}^{w}\right)^i\Psi^i - V_{long}^{r}}{V_{train}},\ \sum_{i=1}^{S}\left(\xi_{spin}\right)^i\Psi^i = \frac{\sum_{i=1}^{S}\left(\Omega^w\right)^i\Psi^i - \Omega^r}{V_{train}} \tag{3.64}$$

Equations (3.61), (3.62), and (3.64) are substituted into Equation (3.38) to obtain the stochastic creep forces of Equation (3.65).

$$\begin{aligned}\sum_{i=1}^{S} F_{long}{}^i\Psi^i &= -G\left(\sum_{i=1}^{S} a^i\Psi^i\right)\left(\sum_{i=1}^{S} b^i\Psi^i\right)\left(\sum_{i=1}^{S} C_{11}{}^i\Psi^i\right)\left(\sum_{i=1}^{S}\xi_{long}{}^i\Psi^i\right) \\ \sum_{i=1}^{S} F_{lat}{}^i\Psi^i &= -G\left(\sum_{i=1}^{S} a^i\Psi^i\right)\left(\sum_{i=1}^{S} b^i\Psi^i\right)\left\{\left(\sum_{i=1}^{S} C_{22}{}^i\Psi^i\right)\left(\sum_{i=1}^{S}\xi_{lat}{}^i\Psi^i\right) + \sqrt{\left(\sum_{i=1}^{S} a^i\Psi^i\right)\left(\sum_{i=1}^{S} b^i\Psi^i\right)}\left(\sum_{i=1}^{S} C_{23}{}^i\Psi^i\right)\left(\sum_{i=1}^{S}\xi_{spin}{}^i\Psi^i\right)\right\} \\ \sum_{i=1}^{S} M_{spin}{}^i\Psi^i &= -G\left(\sum_{i=1}^{S} a^i\Psi^i\right)\left(\sum_{i=1}^{S} b^i\Psi^i\right)\left\{-\sqrt{\left(\sum_{i=1}^{S} a^i\Psi^i\right)\left(\sum_{i=1}^{S} b^i\Psi^i\right)}\left(\sum_{i=1}^{S} C_{23}{}^i\Psi^i\right)\left(\sum_{i=1}^{S}\xi_{lat}{}^i\Psi^i\right) + \left(\sum_{i=1}^{S} a^i\Psi^i\right)\left(\sum_{i=1}^{S} b^i\Psi^i\right)\left(\sum_{i=1}^{S} C_{33}{}^i\Psi^i\right)\left(\sum_{i=1}^{S}\xi_{spin}{}^i\Psi^i\right)\right\}\end{aligned} \tag{3.65}$$

Step 5. The stochastic ODEs

Equations (3.60) and (3.65) are substituted into Equation (3.40) to find the stochastic vertical and lateral contact forces and the stochastic moment with respect to the vertical axis (z).

$$\begin{aligned}
\sum_{i=1}^{S} F_v{}^i\Psi^i &= \left(\sum_{i=1}^{S} F_n{}^i\Psi^i\right)\cos\lambda - \left(\sum_{i=1}^{S} F_{lat}{}^i\Psi^i\right)\sin\lambda \\
\sum_{i=1}^{S} F_l{}^i\Psi^i &= \left(\sum_{i=1}^{S} F_n{}^i\Psi^i\right)\sin\lambda + \left(\sum_{i=1}^{S} F_{lat}{}^i\Psi^i\right)\cos\lambda \\
\sum_{i=1}^{S} M_z{}^i\Psi^i &= \left(\sum_{i=1}^{S} M_{spin}{}^i\Psi^i\right)\cos\lambda
\end{aligned} \tag{3.66}$$

Equation (3.58), (3.66) and (3.68) are substituted into Equation (3.42) to find the stochastic ODEs.

$$\begin{cases}
\sum_{i=1}^{S} \dot{x}_1{}^i\Psi^i = \left(\sum_{i=1}^{S} x_2{}^i\Psi^i\right) \\
\sum_{i=1}^{S} \dot{x}_2{}^i\Psi^i = -\dfrac{C_b\left(\left(\sum_{i=1}^{S} x_2{}^i\Psi^i\right)-\left(\sum_{i=1}^{S} x_4{}^i\Psi^i\right)\right)+K_b\left(\left(\sum_{i=1}^{S} x_1{}^i\Psi^i\right)-\left(\sum_{i=1}^{S} x_3{}^i\Psi^i\right)\right)}{M_b} \\
\sum_{i=1}^{S} \dot{x}_3{}^i\Psi^i = \left(\sum_{i=1}^{S} x_4{}^i\Psi^i\right) \\
\sum_{i=1}^{S} \dot{x}_4{}^i\Psi^i = \dfrac{C_b\left(\left(\sum_{i=1}^{S} x_2{}^i\Psi^i\right)-\left(\sum_{i=1}^{S} x_4{}^i\Psi^i\right)\right)+K_b\left(\left(\sum_{i=1}^{S} x_1{}^i\Psi^i\right)-\left(\sum_{i=1}^{S} x_3{}^i\Psi^i\right)\right)-\left(\sum_{i=1}^{S} F_v{}^i\Psi^i\right)}{M_w} \\
\sum_{i=1}^{S} \dot{x}_5{}^i\Psi^i = \left(\sum_{i=1}^{S} x_6{}^i\Psi^i\right) \\
\sum_{i=1}^{S} \dot{x}_6{}^i\Psi^i = \dfrac{\left(\sum_{i=1}^{S} F_v{}^i\Psi^i\right)-C_{track}\left(\left(\sum_{i=1}^{S} x_4{}^i\Psi^i\right)-\left(\sum_{i=1}^{S} x_6{}^i\Psi^i\right)\right)-\left(\sum_{i=1}^{S} K_{track}{}^i\Psi^i\right)\left(\left(\sum_{i=1}^{S} x_3{}^i\Psi^i\right)-\left(\sum_{i=1}^{S} x_5{}^i\Psi^i\right)\right)}{M_r} \\
\sum_{i=1}^{S} \dot{x}_7{}^i\Psi^i = \left(\sum_{i=1}^{S} x_8{}^i\Psi^i\right) \\
\sum_{i=1}^{S} \dot{x}_8{}^i\Psi^i = \dfrac{\left(\sum_{i=1}^{S} F_l{}^i\Psi^i\right)-C_{lat}\left(\sum_{i=1}^{S} x_8{}^i\Psi^i\right)-K_{lat}\left(\sum_{i=1}^{S} x_7{}^i\Psi^i\right)}{M_w} \\
\sum_{i=1}^{S} \dot{x}_9{}^i\Psi^i = \left(\sum_{i=1}^{S} x_{10}{}^i\Psi^i\right) \\
\sum_{i=1}^{S} \dot{x}_{10}{}^i\Psi^i = \dfrac{\left(\sum_{i=1}^{S} M_z{}^i\Psi^i\right)-C_\theta\left(\sum_{i=1}^{S} x_{10}{}^i\Psi^i\right)-K_\theta\left(\sum_{i=1}^{S} x_9{}^i\Psi^i\right)}{J_w}
\end{cases} \tag{3.67}$$

By integrating Equation (3.63), the stochastic displacements and velocities can be found as follows:

$$\begin{aligned}&\sum_{i=1}^{S} x_1{}^i\Psi^i, \quad \sum_{i=1}^{S} x_3{}^i\Psi^i, \quad \sum_{i=1}^{S} x_5{}^i\Psi^i, \quad \sum_{i=1}^{S} x_7{}^i\Psi^i, \quad \sum_{i=1}^{S} x_9{}^i\Psi^i \\ &\sum_{i=1}^{S} x_2{}^i\Psi^i, \quad \sum_{i=1}^{S} x_4{}^i\Psi^i, \quad \sum_{i=1}^{S} x_6{}^i\Psi^i, \quad \sum_{i=1}^{S} x_8{}^i\Psi^i, \quad \sum_{i=1}^{S} x_{10}{}^i\Psi^i\end{aligned} \tag{3.68}$$

Step 6. The stochastic CoF

Equations (3.61) and (3.62) are substituted into Equation (3.5) to find the stochastic longitudinal and lateral damping coefficients at the contact patch.

$$\begin{aligned}\sum_{i=1}^{S} c_{long\_contact}{}^i\Psi^i &= \frac{E\left(\sum_{i=1}^{S} a^i\Psi^i\right)\left(\sum_{i=1}^{S} b^i\Psi^i\right)\left(\sum_{i=1}^{S} C_{11}{}^i\Psi^i\right)}{2(1+v)V_{train}} \\ \sum_{i=1}^{S} c_{lat\_contact}{}^i\Psi^i &= \frac{E\left(\sum_{i=1}^{S} a^i\Psi^i\right)\left(\sum_{i=1}^{S} b^i\Psi^i\right)\left(\sum_{i=1}^{S} C_{22}{}^i\Psi^i\right)}{2(1+v)V_{train}}\end{aligned} \tag{3.69}$$

All stochastic and deterministic dynamic parameters are substituted into Equation (3.4) and then the stochastic CoFs are obtained.

$$\sum_{i=i}^{S} \mu(t)^i\Psi^i = \underbrace{c_1\left(\frac{\left(\sum_{i=1}^{S} V^*(t)^i\Psi^i\right)}{\left(\sum_{i=i}^{S} R^*(t)^i\Psi^i\right)}\right)^{0.28} \frac{e^{-c_2\sqrt{\left(\sum_{i=1}^{S} V^*(t)^i\Psi^i\right)}}}{1+c_3\left(\frac{\left(\sum_{i=1}^{S} a^i\Psi^i\right)}{\left(\sum_{i=1}^{S} b^i\Psi^i\right)}\right)^2\left(\sum_{i=i}^{S} R^*(t)^i\Psi^i\right)}}_{Slip\ Component} + \underbrace{\frac{c_4}{1+c_5\left(\frac{\left(\sum_{i=1}^{S} a^i\Psi^i\right)}{\left(\sum_{i=1}^{S} b^i\Psi^i\right)}\right)^2\left(\sum_{i=i}^{S} R^*(t)^i\Psi^i\right)}}_{Stick\ Component} \tag{3.70}$$

$$\sum_{i=1}^{S} c_{\tan}{}^i\Psi^i = \sqrt{\left(\sum_{i=1}^{S} c_{long\_contact}{}^i\Psi^i\right)^2 + \left(\sum_{i=1}^{S} c_{lat\_contact}{}^i\Psi^i\right)^2}, \quad \sum_{i=1}^{S} V^*(t)^i\Psi^i = \frac{V_{\tan}}{\left(\sum_{i=1}^{S} F_n{}^i\Psi^i\right)}\left(\sum_{i=1}^{S} c_{\tan}{}^i\Psi^i\right)$$

$$\sum_{i=1}^{S} T^i\Psi^i = \frac{-d\left(\sum_{i=1}^{S} h_o{}^i\Psi^i\right)\left(\sum_{i=1}^{S} b^i\Psi^i\right)}{\sigma_{\tan}\left(\sum_{i=1}^{S} a^i\Psi^i\right)}, \quad \sum_{i=i}^{S} R^*(t)^i\Psi^i = 1-e^{\left(\sum_{i=1}^{S} T^i\Psi^i\right)}$$

Uncertain Track Damping Coefficient

The track damping coefficient is considered as an uncertain variable. Uncertain track damping coefficient can be expressed using a truncated Karhunen-Loeve expansion as follows:

$$C_{track} = \sum_{i=1}^{S} C_{track}{}^{i}\Psi^{i} \tag{3.71}$$

Equation (3.71) propagates from the calculation of the normal force to the calculation of the CoF model following the steps presented below.

Step 1. The stochastic normal contact force

The stochastic wheel and rail displacements, x_3 and x_5, from Equation (3.81) are substituted into Equation (3.27) given Equation (3.72).

$$\sum_{i=1}^{S} h_o{}^{i}\Psi^{i} = \sum_{i=1}^{S} x_3{}^{i}\Psi^{i} - \sum_{i=1}^{S} x_5{}^{i}\Psi^{i} + r \tag{3.72}$$

Then Equation (3.72) is substituted into Equation (3.26) to obtain the stochastic normal contact force as follows:

$$\sum_{i=1}^{S} F_n{}^{i}\Psi^{i} = K_H \left(\sum_{i=1}^{S} h_o{}^{i}\Psi^{i} \right)^{3/2} \tag{3.73}$$

Step 2. The stochastic semi-elliptical contact lengths

Equation (3.73) is substituted into Equation (3.20) to calculate the stochastic semi-elliptical contact lengths.

$$\begin{aligned} \sum_{i=1}^{S} L_1{}^{i}\Psi^{i} &= m\left(\frac{3\pi\left(K_1+K_2\right)}{4K_3} \sum_{i=1}^{S} F_n{}^{i}\Psi^{i} \right)^{1/3} = \sum_{i=1}^{S} a^{i}\Psi^{i} = m\left(\frac{3\pi\left(K_1+K_2\right)}{4K_3} \sum_{i=1}^{S} F_n{}^{i}\Psi^{i} \right)^{1/3} \\ \sum_{i=1}^{S} L_2{}^{i}\Psi^{i} &= n\left(\frac{3\pi\left(K_1+K_2\right)}{4K_3} \sum_{i=1}^{S} F_n{}^{i}\Psi^{i} \right)^{1/3} = \sum_{i=1}^{S} b^{i}\Psi^{i} = n\left(\frac{3\pi\left(K_1+K_2\right)}{4K_3} \sum_{i=1}^{S} F_n{}^{i}\Psi^{i} \right)^{1/3} \end{aligned} \tag{3.74}$$

Step 3. The stochastic Kalker's C coefficient

The C coefficients are expressed as the truncated Karhunen-Loeve expansions presented in Equation (3.75).

$$\sum_{i=1}^{S} C_{11}{}^{i}\Psi^{i},\ \sum_{i=1}^{S} C_{22}{}^{i}\Psi^{i},\ \sum_{i=1}^{S} C_{33}{}^{i}\Psi^{i},\ \sum_{i=1}^{S} C_{23}{}^{i}\Psi^{i} \tag{3.75}$$

Step 4. The stochastic creep forces

By substituting Equation (3.81) into Equation (3.33), the stochastic wheel velocities are found as presented in Equation (3.76).

$$\sum_{i=1}^{S}\left(V_{long}^{w}\right)^{i}\Psi^{i} = V_{train} + l_o\sum_{i=1}^{S}\left(x_{10}\right)^{i}\Psi^{i},\ \sum_{i=1}^{S}\left(V_{lat}^{w}\right)^{i}\Psi^{i} = \sum_{i=1}^{S} x_8{}^{i}\Psi^{i} + V_{train}\sum_{i=1}^{S}\left(x_9\right)^{i}\Psi^{i},\ \sum_{i=1}^{S}\left(\Omega^{w}\right)^{i}\Psi^{i} = \omega\lambda + \sum_{i=1}^{S}\left(x_{10}\right)^{i}\Psi^{i} \tag{3.76}$$

The stochastic creepage can be found by substituting Equation (3.76) into Equation (3.49).

$$\sum_{i=1}^{S}\left(\xi_{long}\right)^{i}\Psi^{i} = \frac{\sum_{i=1}^{S}\left(V_{long}^{w}\right)^{i}\Psi^{i} - V_{long}^{r}}{V_{train}},\ \sum_{i=1}^{S}\left(\xi_{lat}\right)^{i}\Psi^{i} = \frac{\sum_{i=1}^{S}\left(V_{lat}^{w}\right)^{i}\Psi^{i} - V_{long}^{r}}{V_{train}},\ \sum_{i=1}^{S}\left(\xi_{spin}\right)^{i}\Psi^{i} = \frac{\sum_{i=1}^{S}\left(\Omega^{w}\right)^{i}\Psi^{i} - \Omega^{r}}{V_{train}} \tag{3.77}$$

Equations (3.74), (3.75), and (3.77) are substituted into Equation (3.38) to obtain the stochastic creep forces of Equation (3.78).

$$\begin{aligned}
&\sum_{i=1}^{S} F_{long}{}^{i}\Psi^{i} = -G\left(\sum_{i=1}^{S} a^{i}\Psi^{i}\right)\left(\sum_{i=1}^{S} b^{i}\Psi^{i}\right)\left(\sum_{i=1}^{S} C_{11}{}^{i}\Psi^{i}\right)\left(\sum_{i=1}^{S} \xi_{long}{}^{i}\Psi^{i}\right)\\
&\sum_{i=1}^{S} F_{lat}{}^{i}\Psi^{i} = -G\left(\sum_{i=1}^{S} a^{i}\Psi^{i}\right)\left(\sum_{i=1}^{S} b^{i}\Psi^{i}\right)\left\{\left(\sum_{i=1}^{S} C_{22}{}^{i}\Psi^{i}\right)\left(\sum_{i=1}^{S} \xi_{lat}{}^{i}\Psi^{i}\right) + \sqrt{\left(\sum_{i=1}^{S} a^{i}\Psi^{i}\right)\left(\sum_{i=1}^{S} b^{i}\Psi^{i}\right)}\left(\sum_{i=1}^{S} C_{23}{}^{i}\Psi^{i}\right)\left(\sum_{i=1}^{S} \xi_{spin}{}^{i}\Psi^{i}\right)\right\}\\
&\sum_{i=1}^{S} M_{spin}{}^{i}\Psi^{i} = -G\left(\sum_{i=1}^{S} a^{i}\Psi^{i}\right)\left(\sum_{i=1}^{S} b^{i}\Psi^{i}\right)\left\{-\sqrt{\left(\sum_{i=1}^{S} a^{i}\Psi^{i}\right)\left(\sum_{i=1}^{S} b^{i}\Psi^{i}\right)}\left(\sum_{i=1}^{S} C_{23}{}^{i}\Psi^{i}\right)\left(\sum_{i=1}^{S} \xi_{lat}{}^{i}\Psi^{i}\right) + \left(\sum_{i=1}^{S} a^{i}\Psi^{i}\right)\left(\sum_{i=1}^{S} b^{i}\Psi^{i}\right)\left(\sum_{i=1}^{S} C_{33}{}^{i}\Psi^{i}\right)\left(\sum_{i=1}^{S} \xi_{spin}{}^{i}\Psi^{i}\right)\right\}
\end{aligned} \tag{3.78}$$

Step 5. The stochastic ODEs

Equations (3.73) and (3.78) are substituted into Equation (3.40) to find the stochastic vertical and lateral contact forces and the stochastic moment with respect to the vertical axis (z).

$$\begin{aligned}
\sum_{i=1}^{S} F_{v}{}^{i}\Psi^{i} &= \left(\sum_{i=1}^{S} F_{n}{}^{i}\Psi^{i}\right)\cos\lambda - \left(\sum_{i=1}^{S} F_{lat}{}^{i}\Psi^{i}\right)\sin\lambda\\
\sum_{i=1}^{S} F_{l}{}^{i}\Psi^{i} &= \left(\sum_{i=1}^{S} F_{n}{}^{i}\Psi^{i}\right)\sin\lambda + \left(\sum_{i=1}^{S} F_{lat}{}^{i}\Psi^{i}\right)\cos\lambda\\
\sum_{i=1}^{S} M_{z}{}^{i}\Psi^{i} &= \left(\sum_{i=1}^{S} M_{spin}{}^{i}\Psi^{i}\right)\cos\lambda
\end{aligned} \tag{3.79}$$

The stochastic ODEs are obtained as presented in Equation (3.80).

$$
\begin{cases}
\sum_{i=1}^{S} \dot{x}_1{}^i\Psi^i = \left(\sum_{i=1}^{S} x_2{}^i\Psi^i\right) \\
\sum_{i=1}^{S} \dot{x}_2{}^i\Psi^i = -\dfrac{C_b\left(\left(\sum_{i=1}^{S} x_2{}^i\Psi^i\right)-\left(\sum_{i=1}^{S} x_4{}^i\Psi^i\right)\right)+K_b\left(\left(\sum_{i=1}^{S} x_1{}^i\Psi^i\right)-\left(\sum_{i=1}^{S} x_3{}^i\Psi^i\right)\right)}{M_b} \\
\sum_{i=1}^{S} \dot{x}_3{}^i\Psi^i = \left(\sum_{i=1}^{S} x_4{}^i\Psi^i\right) \\
\sum_{i=1}^{S} \dot{x}_4{}^i\Psi^i = \dfrac{C_b\left(\left(\sum_{i=1}^{S} x_2{}^i\Psi^i\right)-\left(\sum_{i=1}^{S} x_4{}^i\Psi^i\right)\right)+K_b\left(\left(\sum_{i=1}^{S} x_1{}^i\Psi^i\right)-\left(\sum_{i=1}^{S} x_3{}^i\Psi^i\right)\right)-\left(\sum_{i=1}^{S} F_v{}^i\Psi^i\right)}{M_w} \\
\sum_{i=1}^{S} \dot{x}_5{}^i\Psi^i = \left(\sum_{i=1}^{S} x_6{}^i\Psi^i\right) \\
\sum_{i=1}^{S} \dot{x}_6{}^i\Psi^i = \dfrac{\left(\sum_{i=1}^{S} F_v{}^i\Psi^i\right)-\left(\sum_{i=1}^{S} C_{track}{}^i\Psi^i\right)\left(\left(\sum_{i=1}^{S} x_4{}^i\Psi^i\right)-\left(\sum_{i=1}^{S} x_6{}^i\Psi^i\right)\right)-K_{track}\left(\left(\sum_{i=1}^{S} x_3{}^i\Psi^i\right)-\left(\sum_{i=1}^{S} x_5{}^i\Psi^i\right)\right)}{M_r} \\
\sum_{i=1}^{S} \dot{x}_7{}^i\Psi^i = \left(\sum_{i=1}^{S} x_8{}^i\Psi^i\right) \\
\sum_{i=1}^{S} \dot{x}_8{}^i\Psi^i = \dfrac{\left(\sum_{i=1}^{S} F_l{}^i\Psi^i\right)-C_{lat}\left(\sum_{i=1}^{S} x_8{}^i\Psi^i\right)-K_{lat}\left(\sum_{i=1}^{S} x_7{}^i\Psi^i\right)}{M_w} \\
\sum_{i=1}^{S} \dot{x}_9{}^i\Psi^i = \left(\sum_{i=1}^{S} x_{10}{}^i\Psi^i\right) \\
\sum_{i=1}^{S} \dot{x}_{10}{}^i\Psi^i = \dfrac{\left(\sum_{i=1}^{S} M_z{}^i\Psi^i\right)-C_\theta\left(\sum_{i=1}^{S} x_{10}{}^i\Psi^i\right)-K_\theta\left(\sum_{i=1}^{S} x_9{}^i\Psi^i\right)}{J_w}
\end{cases}
\tag{3.80}
$$

By integrating Equation (3.80), the stochastic displacements and velocities can be expressed as Equation (3.81):

$$
\begin{aligned}
&\sum_{i=1}^{S} x_1{}^i\Psi^i, \quad \sum_{i=1}^{S} x_3{}^i\Psi^i, \quad \sum_{i=1}^{S} x_5{}^i\Psi^i, \quad \sum_{i=1}^{S} x_7{}^i\Psi^i, \quad \sum_{i=1}^{S} x_9{}^i\Psi^i \\
&\sum_{i=1}^{S} x_2{}^i\Psi^i, \quad \sum_{i=1}^{S} x_4{}^i\Psi^i, \quad \sum_{i=1}^{S} x_6{}^i\Psi^i, \quad \sum_{i=1}^{S} x_8{}^i\Psi^i, \quad \sum_{i=1}^{S} x_{10}{}^i\Psi^i
\end{aligned}
\tag{3.81}
$$

Step 6. The stochastic CoF

Equations (3.74) and (3.75) are substituted into Equation (3.5) to find the stochastic longitudinal and lateral damping coefficients at the contact patch.

$$\sum_{i=1}^{S} c_{long\_contact}{}^{i}\Psi^{i} = \frac{E\left(\sum_{i=1}^{S} a^{i}\Psi^{i}\right)\left(\sum_{i=1}^{S} b^{i}\Psi^{i}\right)\left(\sum_{i=1}^{S} C_{11}{}^{i}\Psi^{i}\right)}{2(1+v)V_{train}}$$
$$\sum_{i=1}^{S} c_{lat\_contact}{}^{i}\Psi^{i} = \frac{E\left(\sum_{i=1}^{S} a^{i}\Psi^{i}\right)\left(\sum_{i=1}^{S} b^{i}\Psi^{i}\right)\left(\sum_{i=1}^{S} C_{22}{}^{i}\Psi^{i}\right)}{2(1+v)V_{train}} \quad (3.82)$$

All stochastic and deterministic dynamic parameters are substituted into Equation (3.4) and then the stochastic CoFs are obtained.

$$\sum_{i=i}^{S} \mu(t)^{i}\Psi^{i} = c_1\left(\frac{\left(\sum_{i=1}^{S} V^{*}(t)^{i}\Psi^{i}\right)}{\left(\sum_{i=i}^{S} R^{*}(t)^{i}\Psi^{i}\right)}\right)^{0.28} \underbrace{\frac{e^{-c_2\sqrt{\left(\sum_{i=1}^{S} V^{*}(t)^{i}\Psi^{i}\right)}}}{1+c_3\left(\frac{\left(\sum_{i=1}^{S} a^{i}\Psi^{i}\right)}{\left(\sum_{i=1}^{S} b^{i}\Psi^{i}\right)}\right)^{2}\left(\sum_{i=i}^{S} R^{*}(t)^{i}\Psi^{i}\right)}}_{Slip\ Component} + \underbrace{\frac{c_4}{1+c_5\left(\frac{\left(\sum_{i=1}^{S} a^{i}\Psi^{i}\right)}{\left(\sum_{i=1}^{S} b^{i}\Psi^{i}\right)}\right)^{2}\left(\sum_{i=i}^{S} R^{*}(t)^{i}\Psi^{i}\right)}}_{Stick\ Component} \quad (3.83)$$

$$\sum_{i=1}^{S} c_{\tan}{}^{i}\Psi^{i} = \sqrt{\left(\sum_{i=1}^{S} c_{long\_contact}{}^{i}\Psi^{i}\right)^{2} + \left(\sum_{i=1}^{S} c_{lat\_contact}{}^{i}\Psi^{i}\right)^{2}}, \quad \sum_{i=1}^{S} V^{*}(t)^{i}\Psi^{i} = \frac{V_{\tan}}{\left(\sum_{i=1}^{S} F_n{}^{i}\Psi^{i}\right)}\left(\sum_{i=1}^{S} c_{\tan}{}^{i}\Psi^{i}\right)$$

$$\sum_{i=1}^{S} T^{i}\Psi^{i} = \frac{-d\left(\sum_{i=1}^{S} h_o{}^{i}\Psi^{i}\right)\left(\sum_{i=1}^{S} b^{i}\Psi^{i}\right)}{\sigma_{\tan}\left(\sum_{i=1}^{S} a^{i}\Psi^{i}\right)}, \quad \sum_{i=i}^{S} R^{*}(t)^{i}\Psi^{i} = 1 - e^{\left(\sum_{i=1}^{S} T^{i}\Psi^{i}\right)}$$

Uncertain Sleeper Distance

The sleeper distance, *dist*, is considered as an uncertain variable. Uncertain sleeper distance can be expressed using a truncated Karhunen-Loeve expansion as follows:

$$dist = \sum_{i=1}^{S} dist^{i}\Psi^{i} \quad (3.84)$$

Equation (3.84) propagates from the calculation of the normal force to the calculation of the CoF model following the steps presented below.

Step 1. The stochastic normal contact force

The stochastic wheel and rail displacements, x_3 and x_5, from Equation (3.97) are substituted into Equation (3.27) given Equation (3.85).

$$\sum_{i=1}^{S} h_o{}^i\Psi^i = \sum_{i=1}^{S} x_3{}^i\Psi^i - \sum_{i=1}^{S} x_5{}^i\Psi^i + r \tag{3.85}$$

Then Equation (3.85) is substituted into Equation (3.26) to obtain the stochastic normal contact force as follows:

$$\sum_{i=1}^{S} F_n{}^i\Psi^i = K_H \left(\sum_{i=1}^{S} h_o{}^i\Psi^i \right)^{3/2} \tag{3.86}$$

Step 2. The stochastic semi-elliptical contact lengths

Equation (3.86) is substituted into Equation (3.20) to calculate the stochastic semi-elliptical contact lengths.

$$\begin{aligned}
\sum_{i=1}^{S} L_1{}^i\Psi^i &= m\left(\frac{3\pi\left(K_1+K_2\right)}{4K_3} \sum_{i=1}^{S} F_n{}^i\Psi^i \right)^{1/3} = \sum_{i=1}^{S} a^i\Psi^i = m\left(\frac{3\pi\left(K_1+K_2\right)}{4K_3} \sum_{i=1}^{S} F_n{}^i\Psi^i \right)^{1/3} \\
\sum_{i=1}^{S} L_2{}^i\Psi^i &= n\left(\frac{3\pi\left(K_1+K_2\right)}{4K_3} \sum_{i=1}^{S} F_n{}^i\Psi^i \right)^{1/3} = \sum_{i=1}^{S} b^i\Psi^i = n\left(\frac{3\pi\left(K_1+K_2\right)}{4K_3} \sum_{i=1}^{S} F_n{}^i\Psi^i \right)^{1/3}
\end{aligned} \tag{3.87}$$

Step 3. The stochastic Kalker's C coefficient

The C coefficients are expressed as the truncated Karhunen-Loeve expansions presented in Equation (3.88).

$$\sum_{i=1}^{S} C_{11}{}^i\Psi^i,\ \sum_{i=1}^{S} C_{22}{}^i\Psi^i,\ \sum_{i=1}^{S} C_{33}{}^i\Psi^i,\ \sum_{i=1}^{S} C_{23}{}^i\Psi^i \tag{3.88}$$

Step 4. The stochastic creep forces

By substituting Equation (3.97) into Equation (3.33), the stochastic wheel velocities are found as presented in Equation (3.89).

$$\sum_{i=1}^{S} \left(V_{long}^{w}\right)^i \Psi^i = V_{train} + l_o \sum_{i=1}^{S} \left(x_{10}\right)^i\Psi^i,\ \sum_{i=1}^{S} \left(V_{lat}^{w}\right)^i \Psi^i = \sum_{i=1}^{S} x_8{}^i\Psi^i + V_{train} \sum_{i=1}^{S} \left(x_9\right)^i\Psi^i,\ \sum_{i=1}^{S} \left(\Omega^w\right)^i \Psi^i = \omega\lambda + \sum_{i=1}^{S} \left(x_{10}\right)^i\Psi^i \tag{3.89}$$

The stochastic creepage can be found by substituting Equation (3.89) into Equation (3.49).

$$\sum_{i=1}^{S}\left(\xi_{long}\right)^{i}\Psi^{i}=\frac{\sum_{i=1}^{S}\left(V_{long}^{w}\right)^{i}\Psi^{i}-V_{long}^{r}}{V_{train}},\quad \sum_{i=1}^{S}\left(\xi_{lat}\right)^{i}\Psi^{i}=\frac{\sum_{i=1}^{S}\left(V_{lat}^{w}\right)^{i}\Psi^{i}-V_{long}^{r}}{V_{train}},\quad \sum_{i=1}^{S}\left(\xi_{spin}\right)^{i}\Psi^{i}=\frac{\sum_{i=1}^{S}\left(\Omega^{w}\right)^{i}\Psi^{i}-\Omega^{r}}{V_{train}} \tag{3.90}$$

Equations (3.87), (3.88), and (3.90) are substituted into Equation (3.38) to obtain the stochastic creep forces of Equation (3.91).

$$\begin{aligned}
&\sum_{i=1}^{S}F_{long}{}^{i}\Psi^{i}=-G\left(\sum_{i=1}^{S}a^{i}\Psi^{i}\right)\left(\sum_{i=1}^{S}b^{i}\Psi^{i}\right)\left(\sum_{i=1}^{S}C_{11}{}^{i}\Psi^{i}\right)\left(\sum_{i=1}^{S}\xi_{long}{}^{i}\Psi^{i}\right)\\
&\sum_{i=1}^{S}F_{lat}{}^{i}\Psi^{i}=-G\left(\sum_{i=1}^{S}a^{i}\Psi^{i}\right)\left(\sum_{i=1}^{S}b^{i}\Psi^{i}\right)\left\{\left(\sum_{i=1}^{S}C_{22}{}^{i}\Psi^{i}\right)\left(\sum_{i=1}^{S}\xi_{lat}{}^{i}\Psi^{i}\right)+\sqrt{\left(\sum_{i=1}^{S}a^{i}\Psi^{i}\right)\left(\sum_{i=1}^{S}b^{i}\Psi^{i}\right)}\left(\sum_{i=1}^{S}C_{23}{}^{i}\Psi^{i}\right)\left(\sum_{i=1}^{S}\xi_{spin}{}^{i}\Psi^{i}\right)\right\}\\
&\sum_{i=1}^{S}M_{spin}{}^{i}\Psi^{i}=-G\left(\sum_{i=1}^{S}a^{i}\Psi^{i}\right)\left(\sum_{i=1}^{S}b^{i}\Psi^{i}\right)\left\{-\sqrt{\left(\sum_{i=1}^{S}a^{i}\Psi^{i}\right)\left(\sum_{i=1}^{S}b^{i}\Psi^{i}\right)}\left(\sum_{i=1}^{S}C_{23}{}^{i}\Psi^{i}\right)\left(\sum_{i=1}^{S}\xi_{lat}{}^{i}\Psi^{i}\right)+\left(\sum_{i=1}^{S}a^{i}\Psi^{i}\right)\left(\sum_{i=1}^{S}b^{i}\Psi^{i}\right)\left(\sum_{i=1}^{S}C_{33}{}^{i}\Psi^{i}\right)\left(\sum_{i=1}^{S}\xi_{spin}{}^{i}\Psi^{i}\right)\right\}
\end{aligned} \tag{3.91}$$

Step 5. The stochastic ODEs

Equations (3.86) and (3.91) are substituted into Equation (3.40) to find the stochastic vertical and lateral contact forces and the stochastic moment with respect to the vertical axis (z).

$$\begin{aligned}
\sum_{i=1}^{S}F_{v}{}^{i}\Psi^{i}&=\left(\sum_{i=1}^{S}F_{n}{}^{i}\Psi^{i}\right)\cos\lambda-\left(\sum_{i=1}^{S}F_{lat}{}^{i}\Psi^{i}\right)\sin\lambda\\
\sum_{i=1}^{S}F_{l}{}^{i}\Psi^{i}&=\left(\sum_{i=1}^{S}F_{n}{}^{i}\Psi^{i}\right)\sin\lambda+\left(\sum_{i=1}^{S}F_{lat}{}^{i}\Psi^{i}\right)\cos\lambda\\
\sum_{i=1}^{S}M_{z}{}^{i}\Psi^{i}&=\left(\sum_{i=1}^{S}M_{spin}{}^{i}\Psi^{i}\right)\cos\lambda
\end{aligned} \tag{3.92}$$

Equation (3.84) is used to calculate the stochastic rail mass of Equation (3.93) and it is substituted into Equation (3.8) to obtain the stochastic track excitation frequency of Equation (3.94).

$$\sum_{i=1}^{S}M_{r}{}^{i}\Psi^{i}=A\times density\times\sum_{i=1}^{S}dist^{i}\Psi^{i} \tag{3.93}$$

$$\sum_{i=1}^{S}f^{i}\Psi^{i}=\frac{2\pi V_{train}}{\sum_{i=1}^{S}dist^{i}\Psi^{i}} \tag{3.94}$$

The stochastic track stiffness and damping coefficient is calculated as shown in Equation (3.95).

$$\sum_{i=1}^{S} K_{track}{}^{i}\Psi^{i} = \sum_{i=1}^{S} K_{pad}{}^{i}\Psi^{i} + \sum_{i=1}^{S} K_{sleeper}{}^{i}\Psi^{i} + K_{ballast}$$

$$\sum_{i=1}^{S} C_{track}{}^{i}\Psi^{i} = \sum_{i=1}^{S} C_{pad}{}^{i}\Psi^{i} + \sum_{i=1}^{S} C_{sleeper}{}^{i}\Psi^{i} + C_{ballast}$$

whrer

$$\sum_{i=1}^{S} K_{pad}{}^{i}\Psi^{i} = 0.5K_{pad}\cos\left(\left(\sum_{i=1}^{S} f^{i}\Psi^{i}\right)\cdot t\right) + 0.5K_{pad},\ \sum_{i=1}^{S} K_{sleeper}{}^{i}\Psi^{i} = 0.5K_{sleeper}\cos\left(\left(\sum_{i=1}^{S} f^{i}\Psi^{i}\right)\cdot t\right) + 0.5K_{sleeper}$$

$$\sum_{i=1}^{S} C_{pad}{}^{i}\Psi^{i} = 0.5C_{pad}\cos\left(\left(\sum_{i=1}^{S} f^{i}\Psi^{i}\right)\cdot t\right) + 0.5C_{pad},\ \sum_{i=1}^{S} C_{sleeper}{}^{i}\Psi^{i} = 0.5C_{sleeper}\cos\left(\left(\sum_{i=1}^{S} f^{i}\Psi^{i}\right)\cdot t\right) + 0.5C_{sleeper}$$

(3.95)

The stochastic ODEs are obtained as presented in Equation (3.96).

$$\begin{cases}
\sum_{i=1}^{S} \dot{x}_1{}^{i}\Psi^{i} = \left(\sum_{i=1}^{S} x_2{}^{i}\Psi^{i}\right) \\
\sum_{i=1}^{S} \dot{x}_2{}^{i}\Psi^{i} = -\dfrac{C_b\left(\left(\sum_{i=1}^{S} x_2{}^{i}\Psi^{i}\right) - \left(\sum_{i=1}^{S} x_4{}^{i}\Psi^{i}\right)\right) + K_b\left(\left(\sum_{i=1}^{S} x_1{}^{i}\Psi^{i}\right) - \left(\sum_{i=1}^{S} x_3{}^{i}\Psi^{i}\right)\right)}{M_b} \\
\sum_{i=1}^{S} \dot{x}_3{}^{i}\Psi^{i} = \left(\sum_{i=1}^{S} x_4{}^{i}\Psi^{i}\right) \\
\sum_{i=1}^{S} \dot{x}_4{}^{i}\Psi^{i} = \dfrac{C_b\left(\left(\sum_{i=1}^{S} x_2{}^{i}\Psi^{i}\right) - \left(\sum_{i=1}^{S} x_4{}^{i}\Psi^{i}\right)\right) + K_b\left(\left(\sum_{i=1}^{S} x_1{}^{i}\Psi^{i}\right) - \left(\sum_{i=1}^{S} x_3{}^{i}\Psi^{i}\right)\right) - \left(\sum_{i=1}^{S} F_v{}^{i}\Psi^{i}\right)}{M_w} \\
\sum_{i=1}^{S} \dot{x}_5{}^{i}\Psi^{i} = \left(\sum_{i=1}^{S} x_6{}^{i}\Psi^{i}\right) \\
\sum_{i=1}^{S} \dot{x}_6{}^{i}\Psi^{i} = \dfrac{\left(\sum_{i=1}^{S} F_v{}^{i}\Psi^{i}\right) - \left(\sum_{i=1}^{S} C_{track}{}^{i}\Psi^{i}\right)\left(\left(\sum_{i=1}^{S} x_4{}^{i}\Psi^{i}\right) - \left(\sum_{i=1}^{S} x_6{}^{i}\Psi^{i}\right)\right) - \left(\sum_{i=1}^{S} K_{track}{}^{i}\Psi^{i}\right)\left(\left(\sum_{i=1}^{S} x_3{}^{i}\Psi^{i}\right) - \left(\sum_{i=1}^{S} x_5{}^{i}\Psi^{i}\right)\right)}{\sum_{i=1}^{S} M_r{}^{i}\Psi^{i}} \\
\sum_{i=1}^{S} \dot{x}_7{}^{i}\Psi^{i} = \left(\sum_{i=1}^{S} x_8{}^{i}\Psi^{i}\right) \\
\sum_{i=1}^{S} \dot{x}_8{}^{i}\Psi^{i} = \dfrac{\left(\sum_{i=1}^{S} F_l{}^{i}\Psi^{i}\right) - C_{lat}\left(\sum_{i=1}^{S} x_8{}^{i}\Psi^{i}\right) - K_{lat}\left(\sum_{i=1}^{S} x_7{}^{i}\Psi^{i}\right)}{M_w} \\
\sum_{i=1}^{S} \dot{x}_9{}^{i}\Psi^{i} = \left(\sum_{i=1}^{S} x_{10}{}^{i}\Psi^{i}\right) \\
\sum_{i=1}^{S} \dot{x}_{10}{}^{i}\Psi^{i} = \dfrac{\left(\sum_{i=1}^{S} M_z{}^{i}\Psi^{i}\right) - C_\theta\left(\sum_{i=1}^{S} x_{10}{}^{i}\Psi^{i}\right) - K_\theta\left(\sum_{i=1}^{S} x_9{}^{i}\Psi^{i}\right)}{J_w}
\end{cases}$$

(3.96)

By integrating Equation (3.96), the stochastic displacements and velocities can be found as follows:

$$\begin{aligned}&\sum_{i=1}^{S} x_1{}^i\Psi^i, \quad \sum_{i=1}^{S} x_3{}^i\Psi^i, \quad \sum_{i=1}^{S} x_5{}^i\Psi^i, \quad \sum_{i=1}^{S} x_7{}^i\Psi^i, \quad \sum_{i=1}^{S} x_9{}^i\Psi^i \\ &\sum_{i=1}^{S} x_2{}^i\Psi^i, \quad \sum_{i=1}^{S} x_4{}^i\Psi^i, \quad \sum_{i=1}^{S} x_6{}^i\Psi^i, \quad \sum_{i=1}^{S} x_8{}^i\Psi^i, \quad \sum_{i=1}^{S} x_{10}{}^i\Psi^i\end{aligned} \tag{3.97}$$

Step 6. The stochastic CoF

Equations (3.87) and (3.88) are substituted into Equation (3.5) to find the stochastic longitudinal and lateral damping coefficients at the contact patch.

$$\begin{aligned}\sum_{i=1}^{S} c_{long\_contact}{}^i\Psi^i &= \frac{E\left(\sum_{i=1}^{S} a^i\Psi^i\right)\left(\sum_{i=1}^{S} b^i\Psi^i\right)\left(\sum_{i=1}^{S} C_{11}{}^i\Psi^i\right)}{2(1+v)V_{train}} \\ \sum_{i=1}^{S} c_{lat\_contact}{}^i\Psi^i &= \frac{E\left(\sum_{i=1}^{S} a^i\Psi^i\right)\left(\sum_{i=1}^{S} b^i\Psi^i\right)\left(\sum_{i=1}^{S} C_{22}{}^i\Psi^i\right)}{2(1+v)V_{train}}\end{aligned} \tag{3.98}$$

All stochastic and deterministic dynamic parameters are substituted into Equation (3.4) and then the stochastic CoFs are obtained.

$$\sum_{i=i}^{S}\mu(t)^i\Psi^i = \underbrace{c_1\left(\frac{\left(\sum_{i=1}^{S} V^*(t)^i\Psi^i\right)}{\left(\sum_{i=i}^{S} R^*(t)^i\Psi^i\right)}\right)^{0.28} \frac{e^{-c_2\sqrt{\left(\sum_{i=1}^{S} V^*(t)^i\Psi^i\right)}}}{1+c_3\left(\frac{\left(\sum_{i=1}^{S} a^i\Psi^i\right)}{\left(\sum_{i=1}^{S} b^i\Psi^i\right)}\right)^2\left(\sum_{i=i}^{S} R^*(t)^i\Psi^i\right)}}_{Slip\ Component} + \underbrace{\frac{c_4}{1+c_5\left(\frac{\left(\sum_{i=1}^{S} a^i\Psi^i\right)}{\left(\sum_{i=1}^{S} b^i\Psi^i\right)}\right)^2\left(\sum_{i=i}^{S} R^*(t)^i\Psi^i\right)}}_{Stick\ Component}$$

$$\sum_{i=1}^{S} c_{\tan}{}^i\Psi^i = \sqrt{\left(\sum_{i=1}^{S} c_{long\_contact}{}^i\Psi^i\right)^2 + \left(\sum_{i=1}^{S} c_{lat\_contact}{}^i\Psi^i\right)^2}, \quad \sum_{i=1}^{S} V^*(t)^i\Psi^i = \frac{V_{\tan}}{\left(\sum_{i=1}^{S} F_n{}^i\Psi^i\right)}\left(\sum_{i=1}^{S} c_{\tan}{}^i\Psi^i\right)$$

$$\sum_{i=1}^{S} T^i\Psi^i = \frac{-d\left(\sum_{i=1}^{S} h_o{}^i\Psi^i\right)\left(\sum_{i=1}^{S} b^i\Psi^i\right)}{\sigma_{\tan}\left(\sum_{i=1}^{S} a^i\Psi^i\right)}, \quad \sum_{i=i}^{S} R^*(t)^i\Psi^i = 1-e^{\left(\sum_{i=1}^{S} T^i\Psi^i\right)} \tag{3.99}$$

Uncertain Lateral Displacement

The lateral displacement, x_7, is considered as an uncertain variable. Uncertain lateral displacement can be expressed using a truncated Karhunen-Loeve expansion as follows:

$$x_7 = \sum_{i=1}^{S} x_7{}^i \Psi^i \tag{3.100}$$

Equation (3.100) propagates from the calculation of the normal force to the calculation of the CoF model following the steps presented below.

Step 1. The stochastic normal contact force

The stochastic wheel and rail displacements, x_3 and x_5, from Equation (3.113) are substituted into Equation (3.27) given Equation (3.101).

$$\sum_{i=1}^{S} h_o{}^i \Psi^i = \sum_{i=1}^{S} u_w{}^i \Psi^i - \sum_{i=1}^{S} u_r{}^i \Psi^i + r \tag{3.101}$$

Then Equation (3.101) is substituted into Equation (3.26) to obtain the stochastic normal contact force as follows:

$$\sum_{i=1}^{S} F_n{}^i \Psi^i = K_H \left(\sum_{i=1}^{S} h_o{}^i \Psi^i \right)^{3/2} \tag{3.102}$$

Step 2. The stochastic semi-elliptical contact lengths

The uncertain lateral displacement leads to uncertain radii of curvatures since they are the function of the lateral displacement as shown in Equation (3.19), (3.36), and (3.37). Thus, the stochastic radii of curvatures are expressed as Equation (3.103) and (3.104).

$$\sum_{i=1}^{S} \left(R^r(a) \right)^i \Psi^i = \left. \frac{\left[1 + \left(\frac{d\left(\sum_{i=1}^{S} y^i \Psi^i \right)}{dx} \right)^2 \right]}{\frac{d^2\left(\sum_{i=1}^{S} y^i \Psi^i \right)}{dx^2}} \right|_{x=a} \tag{3.103}$$

$$where \sum_{i=1}^{S} y^i \Psi^i = f(x_7) = P_1 \left(\sum_{i=1}^{S} x_7{}^i \Psi^i \right)^5 + P_2 \left(\sum_{i=1}^{S} x_7{}^i \Psi^i \right)^4 + P_3 \left(\sum_{i=1}^{S} x_7{}^i \Psi^i \right)^3 + P_4 \left(\sum_{i=1}^{S} x_7{}^i \Psi^i \right)^2 + P_5 \left(\sum_{i=1}^{S} x_7{}^i \Psi^i \right) + P_6$$

$$\sum_{i=1}^{S}\left(R^{w}\right)^{i}\Psi^{i}=r_{o}-\tan\lambda\left(\sum_{i=1}^{S}x_{7}{}^{i}\Psi^{i}\right) \tag{3.104}$$

K_3 is a function of radii of curvatures. Thus, Equation (3.103) and (3.104) are substituted into Equation (3.23) to find the stochastic K_3.

$$\sum_{i=1}^{S}K_{3}{}^{i}\Psi^{i}=\frac{1}{2}\left(\frac{1}{R^{w}}+\frac{1}{R^{r}}\right)=\frac{1}{2}\left(\frac{1}{\sum_{i=1}^{S}\left(R^{w}\right)^{i}\Psi^{i}}+\frac{1}{\sum_{i=1}^{S}\left(R^{r}\right)^{i}\Psi^{i}}\right) \tag{3.105}$$

Equation (3.102) and (3.105) are substituted into Equation (3.20) to calculate the stochastic semi-elliptical contact lengths.

$$\begin{aligned}\sum_{i=1}^{S}L_{1}{}^{i}\Psi^{i}&=m\left(\frac{3\pi\left(K_{1}+K_{2}\right)}{4K_{3}}\sum_{i=1}^{S}F_{n}{}^{i}\Psi^{i}\right)^{1/3}=\sum_{i=1}^{S}a^{i}\Psi^{i}=m\left(\frac{3\pi\left(K_{1}+K_{2}\right)}{4\sum_{i=1}^{S}K_{3}{}^{i}\Psi^{i}}\sum_{i=1}^{S}F_{n}{}^{i}\Psi^{i}\right)^{1/3}\\ \sum_{i=1}^{S}L_{2}{}^{i}\Psi^{i}&=n\left(\frac{3\pi\left(K_{1}+K_{2}\right)}{4K_{3}}\sum_{i=1}^{S}F_{n}{}^{i}\Psi^{i}\right)^{1/3}=\sum_{i=1}^{S}b^{i}\Psi^{i}=n\left(\frac{3\pi\left(K_{1}+K_{2}\right)}{4\sum_{i=1}^{S}K_{3}{}^{i}\Psi^{i}}\sum_{i=1}^{S}F_{n}{}^{i}\Psi^{i}\right)^{1/3}\end{aligned} \tag{3.106}$$

Step 3. The stochastic Kalker's C coefficient

The *C* coefficients are expressed as the truncated Karhunen-Loeve expansions presented in Equation (3.107).

$$\sum_{i=1}^{S}C_{11}{}^{i}\Psi^{i},\ \sum_{i=1}^{S}C_{22}{}^{i}\Psi^{i},\ \sum_{i=1}^{S}C_{33}{}^{i}\Psi^{i},\ \sum_{i=1}^{S}C_{23}{}^{i}\Psi^{i} \tag{3.107}$$

Step 4. The stochastic creep forces

By substituting Equation (3.113) into Equation (3.33), the stochastic wheel velocities are found as presented in Equation (3.108).

$$\sum_{i=1}^{S}\left(V_{long}^{w}\right)^{i}\Psi^{i}=V_{train}+l_{o}\sum_{i=1}^{S}\left(x_{10}\right)^{i}\Psi^{i},\ \sum_{i=1}^{S}\left(V_{lat}^{w}\right)^{i}\Psi^{i}=\sum_{i=1}^{S}x_{8}{}^{i}\Psi^{i}+V_{train}\sum_{i=1}^{S}\left(x_{9}\right)^{i}\Psi^{i},\ \sum_{i=1}^{S}\left(\Omega^{w}\right)^{i}\Psi^{i}=\omega\lambda+\sum_{i=1}^{S}\left(x_{10}\right)^{i}\Psi^{i} \tag{3.108}$$

The stochastic creepage can be found by substituting Equation (3.108) into Equation (3.49).

$$\sum_{i=1}^{S}\left(\xi_{long}\right)^{i}\Psi^{i}=\frac{\sum_{i=1}^{S}\left(V_{long}^{w}\right)^{i}\Psi^{i}-V_{long}^{r}}{V_{train}},\quad \sum_{i=1}^{S}\left(\xi_{lat}\right)^{i}\Psi^{i}=\frac{\sum_{i=1}^{S}\left(V_{lat}^{w}\right)^{i}\Psi^{i}-V_{long}^{r}}{V_{train}},\quad \sum_{i=1}^{S}\left(\xi_{spin}\right)^{i}\Psi^{i}=\frac{\sum_{i=1}^{S}\left(\Omega^{w}\right)^{i}\Psi^{i}-\Omega^{r}}{V_{train}} \tag{3.109}$$

Equations (3.106), (3.107), and (3.109) are substituted into Equation (3.38) to obtain the stochastic creep forces of Equation (3.110).

$$\begin{aligned}
&\sum_{i=1}^{S}F_{long}{}^{i}\Psi^{i}=-G\left(\sum_{i=1}^{S}a^{i}\Psi^{i}\right)\left(\sum_{i=1}^{S}b^{i}\Psi^{i}\right)\left(\sum_{i=1}^{S}C_{11}{}^{i}\Psi^{i}\right)\left(\sum_{i=1}^{S}\xi_{long}{}^{i}\Psi^{i}\right)\\
&\sum_{i=1}^{S}F_{lat}{}^{i}\Psi^{i}=-G\left(\sum_{i=1}^{S}a^{i}\Psi^{i}\right)\left(\sum_{i=1}^{S}b^{i}\Psi^{i}\right)\left\{\left(\sum_{i=1}^{S}C_{22}{}^{i}\Psi^{i}\right)\left(\sum_{i=1}^{S}\xi_{lat}{}^{i}\Psi^{i}\right)+\sqrt{\left(\sum_{i=1}^{S}a^{i}\Psi^{i}\right)\left(\sum_{i=1}^{S}b^{i}\Psi^{i}\right)}\left(\sum_{i=1}^{S}C_{23}{}^{i}\Psi^{i}\right)\left(\sum_{i=1}^{S}\xi_{spin}{}^{i}\Psi^{i}\right)\right\}\\
&\sum_{i=1}^{S}M_{spin}{}^{i}\Psi^{i}=-G\left(\sum_{i=1}^{S}a^{i}\Psi^{i}\right)\left(\sum_{i=1}^{S}b^{i}\Psi^{i}\right)\left\{-\sqrt{\left(\sum_{i=1}^{S}a^{i}\Psi^{i}\right)\left(\sum_{i=1}^{S}b^{i}\Psi^{i}\right)}\left(\sum_{i=1}^{S}C_{23}{}^{i}\Psi^{i}\right)\left(\sum_{i=1}^{S}\xi_{lat}{}^{i}\Psi^{i}\right)+\left(\sum_{i=1}^{S}a^{i}\Psi^{i}\right)\left(\sum_{i=1}^{S}b^{i}\Psi^{i}\right)\left(\sum_{i=1}^{S}C_{33}{}^{i}\Psi^{i}\right)\left(\sum_{i=1}^{S}\xi_{spin}{}^{i}\Psi^{i}\right)\right\}
\end{aligned} \tag{3.110}$$

Step 5. The stochastic ODEs

Equations (3.102) and (3.110) are substituted into Equation (3.40) to find the stochastic vertical and lateral contact forces and the stochastic moment with respect to the vertical axis (z).

$$\begin{aligned}
\sum_{i=1}^{S}F_{v}{}^{i}\Psi^{i}&=\left(\sum_{i=1}^{S}F_{n}{}^{i}\Psi^{i}\right)\cos\lambda-\left(\sum_{i=1}^{S}F_{lat}{}^{i}\Psi^{i}\right)\sin\lambda\\
\sum_{i=1}^{S}F_{l}{}^{i}\Psi^{i}&=\left(\sum_{i=1}^{S}F_{n}{}^{i}\Psi^{i}\right)\sin\lambda+\left(\sum_{i=1}^{S}F_{lat}{}^{i}\Psi^{i}\right)\cos\lambda\\
\sum_{i=1}^{S}M_{z}{}^{i}\Psi^{i}&=\left(\sum_{i=1}^{S}M_{spin}{}^{i}\Psi^{i}\right)\cos\lambda
\end{aligned} \tag{3.111}$$

The stochastic ODEs are obtained as presented in Equation (3.112).

$$
\begin{cases}
\sum_{i=1}^{S} \dot{x}_1{}^i\Psi^i = \left(\sum_{i=1}^{S} x_2{}^i\Psi^i\right) \\
\sum_{i=1}^{S} \dot{x}_2{}^i\Psi^i = -\dfrac{C_b\left(\left(\sum_{i=1}^{S} x_2{}^i\Psi^i\right)-\left(\sum_{i=1}^{S} x_4{}^i\Psi^i\right)\right)+K_b\left(\left(\sum_{i=1}^{S} x_1{}^i\Psi^i\right)-\left(\sum_{i=1}^{S} x_3{}^i\Psi^i\right)\right)}{M_b} \\
\sum_{i=1}^{S} \dot{x}_3{}^i\Psi^i = \left(\sum_{i=1}^{S} x_4{}^i\Psi^i\right) \\
\sum_{i=1}^{S} \dot{x}_4{}^i\Psi^i = \dfrac{C_b\left(\left(\sum_{i=1}^{S} x_2{}^i\Psi^i\right)-\left(\sum_{i=1}^{S} x_4{}^i\Psi^i\right)\right)+K_b\left(\left(\sum_{i=1}^{S} x_1{}^i\Psi^i\right)-\left(\sum_{i=1}^{S} x_3{}^i\Psi^i\right)\right)-\left(\sum_{i=1}^{S} F_v{}^i\Psi^i\right)}{M_w} \\
\sum_{i=1}^{S} \dot{x}_5{}^i\Psi^i = \left(\sum_{i=1}^{S} x_6{}^i\Psi^i\right) \\
\sum_{i=1}^{S} \dot{x}_6{}^i\Psi^i = \dfrac{\left(\sum_{i=1}^{S} F_v{}^i\Psi^i\right)-C_{track}\left(\left(\sum_{i=1}^{S} x_4{}^i\Psi^i\right)-\left(\sum_{i=1}^{S} x_6{}^i\Psi^i\right)\right)-K_{track}\left(\left(\sum_{i=1}^{S} x_3{}^i\Psi^i\right)-\left(\sum_{i=1}^{S} x_5{}^i\Psi^i\right)\right)}{M_r} \\
\sum_{i=1}^{S} \dot{x}_7{}^i\Psi^i = \left(\sum_{i=1}^{S} x_8{}^i\Psi^i\right) \\
\sum_{i=1}^{S} \dot{x}_8{}^i\Psi^i = \dfrac{\left(\sum_{i=1}^{S} F_l{}^i\Psi^i\right)-C_{lat}\left(\sum_{i=1}^{S} x_8{}^i\Psi^i\right)-K_{lat}\left(\sum_{i=1}^{S} x_7{}^i\Psi^i\right)}{M_w} \\
\sum_{i=1}^{S} \dot{x}_9{}^i\Psi^i = \left(\sum_{i=1}^{S} x_{10}{}^i\Psi^i\right) \\
\sum_{i=1}^{S} \dot{x}_{10}{}^i\Psi^i = \dfrac{\left(\sum_{i=1}^{S} M_z{}^i\Psi^i\right)-C_\theta\left(\sum_{i=1}^{S} x_{10}{}^i\Psi^i\right)-K_\theta\left(\sum_{i=1}^{S} x_9{}^i\Psi^i\right)}{J_w}
\end{cases}
\tag{3.112}
$$

By integrating Equation (3.112), the stochastic displacements and velocities can be found as follows:

$$
\begin{matrix}
\sum_{i=1}^{S} x_1{}^i\Psi^i, & \sum_{i=1}^{S} x_3{}^i\Psi^i, & \sum_{i=1}^{S} x_5{}^i\Psi^i, & \sum_{i=1}^{S} x_7{}^i\Psi^i, & \sum_{i=1}^{S} x_9{}^i\Psi^i \\
\sum_{i=1}^{S} x_2{}^i\Psi^i, & \sum_{i=1}^{S} x_4{}^i\Psi^i, & \sum_{i=1}^{S} x_6{}^i\Psi^i, & \sum_{i=1}^{S} x_8{}^i\Psi^i, & \sum_{i=1}^{S} x_{10}{}^i\Psi^i
\end{matrix}
\tag{3.113}
$$

Step 6. The stochastic CoF

Equations (3.106) and (3.107) are substituted into Equation (3.5) to find the stochastic longitudinal and lateral damping coefficients at the contact patch.

$$\sum_{i=1}^{S} c_{long\_contact}{}^{i}\Psi^{i} = \frac{E\left(\sum_{i=1}^{S} a^{i}\Psi^{i}\right)\left(\sum_{i=1}^{S} b^{i}\Psi^{i}\right)\left(\sum_{i=1}^{S} C_{11}{}^{i}\Psi^{i}\right)}{2(1+v)V_{train}}$$
$$\sum_{i=1}^{S} c_{lat\_contact}{}^{i}\Psi^{i} = \frac{E\left(\sum_{i=1}^{S} a^{i}\Psi^{i}\right)\left(\sum_{i=1}^{S} b^{i}\Psi^{i}\right)\left(\sum_{i=1}^{S} C_{22}{}^{i}\Psi^{i}\right)}{2(1+v)V_{train}} \tag{3.114}$$

All stochastic and deterministic dynamic parameters are substituted into Equation (3.4) and then the stochastic CoFs are obtained.

$$\sum_{i=i}^{S} \mu(t)^{i}\Psi^{i} = \underbrace{c_1\left(\frac{\left(\sum_{i=1}^{S} V^{*}(t)^{i}\Psi^{i}\right)}{\left(\sum_{i=i}^{S} R^{*}(t)^{i}\Psi^{i}\right)}\right)^{0.28} \frac{e^{-c_2\sqrt{\left(\sum_{i=1}^{S} V^{*}(t)^{i}\Psi^{i}\right)}}}{1+c_3\left(\frac{\left(\sum_{i=1}^{S} a^{i}\Psi^{i}\right)}{\left(\sum_{i=1}^{S} b^{i}\Psi^{i}\right)}\right)^{2}\left(\sum_{i=i}^{S} R^{*}(t)^{i}\Psi^{i}\right)}}_{Slip\ Component} + \underbrace{\frac{c_4}{1+c_5\left(\frac{\left(\sum_{i=1}^{S} a^{i}\Psi^{i}\right)}{\left(\sum_{i=1}^{S} b^{i}\Psi^{i}\right)}\right)^{2}\left(\sum_{i=i}^{S} R^{*}(t)^{i}\Psi^{i}\right)}}_{Stick\ Component}$$

$$\sum_{i=1}^{S} c_{\tan}{}^{i}\Psi^{i} = \sqrt{\left(\sum_{i=1}^{S} c_{long\_contact}{}^{i}\Psi^{i}\right)^{2} + \left(\sum_{i=1}^{S} c_{lat\_contact}{}^{i}\Psi^{i}\right)^{2}}, \quad \sum_{i=1}^{S} V^{*}(t)^{i}\Psi^{i} = \frac{V_{\tan}}{\left(\sum_{i=1}^{S} F_{n}{}^{i}\Psi^{i}\right)}\left(\sum_{i=1}^{S} c_{\tan}{}^{i}\Psi^{i}\right)$$

$$\sum_{i=1}^{S} T^{i}\Psi^{i} = \frac{-d\left(\sum_{i=1}^{S} h_{o}{}^{i}\Psi^{i}\right)\left(\sum_{i=1}^{S} b^{i}\Psi^{i}\right)}{\sigma_{\tan}\left(\sum_{i=1}^{S} a^{i}\Psi^{i}\right)}, \quad \sum_{i=i}^{S} R^{*}(t)^{i}\Psi^{i} = 1 - e^{\left(\sum_{i=1}^{S} T^{i}\Psi^{i}\right)} \tag{3.115}$$

3.3.2 A Stochastic CoF Model with Two Uncertainties

Uncertain Independent *a* and *b*

Independent semi-elliptical contact length a and b are considered as uncertain variables. Uncertain a and b can be expressed using a truncated Karhunen-Loeve expansion as follows

$$a = \sum_{i=1}^{S} a^i \Psi^i, \qquad b = \sum_{i=1}^{S} b^i \Psi^i \tag{3.116}$$

Equation (3.116) propagates from the calculation of the normal force to the calculation of the CoF model following the steps presented below.

Step 1. The stochastic normal contact force

The stochastic wheel and rail displacements, x_3 and x_5, from Equation (3.125) are substituted into Equation (3.27) given Equation (3.117).

$$\sum_{i=1}^{S} h_o{}^i \Psi^i = \sum_{i=1}^{S} x_3{}^i \Psi^i - \sum_{i=1}^{S} x_5{}^i \Psi^i + r \tag{3.117}$$

Then Equation (3.117) is substituted into Equation (3.26) to obtain the stochastic normal contact force as follows:

$$\sum_{i=1}^{S} F_n{}^i \Psi^i = K_H \left(\sum_{i=1}^{S} h_o{}^i \Psi^i \right)^{3/2} \tag{3.118}$$

Step 2. The stochastic Kalker's C coefficient

The C coefficients are expressed as the truncated Karhunen-Loeve expansions presented in Equation (3.119).

$$\sum_{i=1}^{S} C_{11}{}^i \Psi^i, \ \sum_{i=1}^{S} C_{22}{}^i \Psi^i, \ \sum_{i=1}^{S} C_{33}{}^i \Psi^i, \ \sum_{i=1}^{S} C_{23}{}^i \Psi^i \tag{3.119}$$

Step 4. The stochastic creep forces

By substituting Equation (3.125) into Equation (3.33), the stochastic wheel velocities are found as presented in Equation (3.120).

$$\sum_{i=1}^{S}\left(V_{long}^{w}\right)^{i}\Psi^{i}=V_{train}+l_{o}\sum_{i=1}^{S}\left(x_{10}\right)^{i}\Psi^{i},\ \sum_{i=1}^{S}\left(V_{lat}^{w}\right)^{i}\Psi^{i}=\sum_{i=1}^{S}x_{8}{}^{i}\Psi^{i}+V_{train}\sum_{i=1}^{S}\left(x_{9}\right)^{i}\Psi^{i},\ \sum_{i=1}^{S}\left(\Omega^{w}\right)^{i}\Psi^{i}=\omega\lambda+\sum_{i=1}^{S}\left(x_{10}\right)^{i}\Psi^{i} \tag{3.120}$$

The stochastic creepage can be found by substituting Equation (3.120) into Equation (3.49).

$$\sum_{i=1}^{S}\left(\xi_{long}\right)^{i}\Psi^{i}=\frac{\sum_{i=1}^{S}\left(V_{long}^{w}\right)^{i}\Psi^{i}-V_{long}^{r}}{V_{train}},\quad \sum_{i=1}^{S}\left(\xi_{lat}\right)^{i}\Psi^{i}=\frac{\sum_{i=1}^{S}\left(V_{lat}^{w}\right)^{i}\Psi^{i}-V_{long}^{r}}{V_{train}},\quad \sum_{i=1}^{S}\left(\xi_{spin}\right)^{i}\Psi^{i}=\frac{\sum_{i=1}^{S}\left(\Omega^{w}\right)^{i}\Psi^{i}-\Omega^{r}}{V_{train}} \tag{3.121}$$

Equations (3.118), (3.119), and (3.121) are substituted into Equation (3.38) to obtain the stochastic creep forces of Equation (3.122).

$$\begin{aligned}
&\sum_{i=1}^{S}F_{long}{}^{i}\Psi^{i}=-G\left(\sum_{i=1}^{S}a^{i}\Psi^{i}\right)\left(\sum_{i=1}^{S}b^{i}\Psi^{i}\right)\left(\sum_{i=1}^{S}C_{11}{}^{i}\Psi^{i}\right)\left(\sum_{i=1}^{S}\xi_{long}{}^{i}\Psi^{i}\right)\\
&\sum_{i=1}^{S}F_{lat}{}^{i}\Psi^{i}=-G\left(\sum_{i=1}^{S}a^{i}\Psi^{i}\right)\left(\sum_{i=1}^{S}b^{i}\Psi^{i}\right)\left\{\left(\sum_{i=1}^{S}C_{22}{}^{i}\Psi^{i}\right)\left(\sum_{i=1}^{S}\xi_{lat}{}^{i}\Psi^{i}\right)+\sqrt{\left(\sum_{i=1}^{S}a^{i}\Psi^{i}\right)\left(\sum_{i=1}^{S}b^{i}\Psi^{i}\right)}\left(\sum_{i=1}^{S}C_{23}{}^{i}\Psi^{i}\right)\left(\sum_{i=1}^{S}\xi_{spin}{}^{i}\Psi^{i}\right)\right\}\\
&\sum_{i=1}^{S}M_{spin}{}^{i}\Psi^{i}=-G\left(\sum_{i=1}^{S}a^{i}\Psi^{i}\right)\left(\sum_{i=1}^{S}b^{i}\Psi^{i}\right)\left\{-\sqrt{\left(\sum_{i=1}^{S}a^{i}\Psi^{i}\right)\left(\sum_{i=1}^{S}b^{i}\Psi^{i}\right)}\left(\sum_{i=1}^{S}C_{23}{}^{i}\Psi^{i}\right)\left(\sum_{i=1}^{S}\xi_{lat}{}^{i}\Psi^{i}\right)+\left(\sum_{i=1}^{S}a^{i}\Psi^{i}\right)\left(\sum_{i=1}^{S}b^{i}\Psi^{i}\right)\left(\sum_{i=1}^{S}C_{33}{}^{i}\Psi^{i}\right)\left(\sum_{i=1}^{S}\xi_{spin}{}^{i}\Psi^{i}\right)\right\}
\end{aligned} \tag{3.122}$$

Step 5. The stochastic ODEs

Equations (3.118) and (3.122) are substituted into Equation (3.40) to find the stochastic vertical and lateral contact forces and the stochastic moment with respect to the vertical axis (z).

$$\begin{aligned}
\sum_{i=1}^{S}F_{v}{}^{i}\Psi^{i}&=\left(\sum_{i=1}^{S}F_{n}{}^{i}\Psi^{i}\right)\cos\lambda-\left(\sum_{i=1}^{S}F_{lat}{}^{i}\Psi^{i}\right)\sin\lambda\\
\sum_{i=1}^{S}F_{l}{}^{i}\Psi^{i}&=\left(\sum_{i=1}^{S}F_{n}{}^{i}\Psi^{i}\right)\sin\lambda+\left(\sum_{i=1}^{S}F_{lat}{}^{i}\Psi^{i}\right)\cos\lambda\\
\sum_{i=1}^{S}M_{z}{}^{i}\Psi^{i}&=\left(\sum_{i=1}^{S}M_{spin}{}^{i}\Psi^{i}\right)\cos\lambda
\end{aligned} \tag{3.123}$$

Equation (3.123) is substituted into Equation (3.42) to find the stochastic ODEs.

$$
\begin{cases}
\sum_{i=1}^{S} \dot{x}_1{}^i\Psi^i = \left(\sum_{i=1}^{S} x_2{}^i\Psi^i\right) \\
\sum_{i=1}^{S} \dot{x}_2{}^i\Psi^i = -\dfrac{C_b\left(\left(\sum_{i=1}^{S} x_2{}^i\Psi^i\right)-\left(\sum_{i=1}^{S} x_4{}^i\Psi^i\right)\right)+K_b\left(\left(\sum_{i=1}^{S} x_1{}^i\Psi^i\right)-\left(\sum_{i=1}^{S} x_3{}^i\Psi^i\right)\right)}{M_b} \\
\sum_{i=1}^{S} \dot{x}_3{}^i\Psi^i = \left(\sum_{i=1}^{S} x_4{}^i\Psi^i\right) \\
\sum_{i=1}^{S} \dot{x}_4{}^i\Psi^i = \dfrac{C_b\left(\left(\sum_{i=1}^{S} x_2{}^i\Psi^i\right)-\left(\sum_{i=1}^{S} x_4{}^i\Psi^i\right)\right)+K_b\left(\left(\sum_{i=1}^{S} x_1{}^i\Psi^i\right)-\left(\sum_{i=1}^{S} x_3{}^i\Psi^i\right)\right)-\left(\sum_{i=1}^{S} F_v{}^i\Psi^i\right)}{M_w} \\
\sum_{i=1}^{S} \dot{x}_5{}^i\Psi^i = \left(\sum_{i=1}^{S} x_6{}^i\Psi^i\right) \\
\sum_{i=1}^{S} \dot{x}_6{}^i\Psi^i = \dfrac{\left(\sum_{i=1}^{S} F_v{}^i\Psi^i\right)-C_{track}\left(\left(\sum_{i=1}^{S} x_4{}^i\Psi^i\right)-\left(\sum_{i=1}^{S} x_6{}^i\Psi^i\right)\right)-K_{track}\left(\left(\sum_{i=1}^{S} x_3{}^i\Psi^i\right)-\left(\sum_{i=1}^{S} x_5{}^i\Psi^i\right)\right)}{M_r} \\
\sum_{i=1}^{S} \dot{x}_7{}^i\Psi^i = \left(\sum_{i=1}^{S} x_8{}^i\Psi^i\right) \\
\sum_{i=1}^{S} \dot{x}_8{}^i\Psi^i = \dfrac{\left(\sum_{i=1}^{S} F_l{}^i\Psi^i\right)-C_{lat}\left(\sum_{i=1}^{S} x_8{}^i\Psi^i\right)-K_{lat}\left(\sum_{i=1}^{S} x_7{}^i\Psi^i\right)}{M_w} \\
\sum_{i=1}^{S} \dot{x}_9{}^i\Psi^i = \left(\sum_{i=1}^{S} x_{10}{}^i\Psi^i\right) \\
\sum_{i=1}^{S} \dot{x}_{10}{}^i\Psi^i = \dfrac{\left(\sum_{i=1}^{S} M_z{}^i\Psi^i\right)-C_\theta\left(\sum_{i=1}^{S} x_{10}{}^i\Psi^i\right)-K_\theta\left(\sum_{i=1}^{S} x_9{}^i\Psi^i\right)}{J_w}
\end{cases}
\tag{3.124}
$$

By integrating Equation (3.124), the stochastic displacements and velocities can be found as follows:

$$
\begin{matrix}
\sum_{i=1}^{S} x_1{}^i\Psi^i, & \sum_{i=1}^{S} x_3{}^i\Psi^i, & \sum_{i=1}^{S} x_5{}^i\Psi^i, & \sum_{i=1}^{S} x_7{}^i\Psi^i, & \sum_{i=1}^{S} x_9{}^i\Psi^i \\
\sum_{i=1}^{S} x_2{}^i\Psi^i, & \sum_{i=1}^{S} x_4{}^i\Psi^i, & \sum_{i=1}^{S} x_6{}^i\Psi^i, & \sum_{i=1}^{S} x_8{}^i\Psi^i, & \sum_{i=1}^{S} x_{10}{}^i\Psi^i
\end{matrix}
\tag{3.125}
$$

Step 6. The stochastic CoF

Equations (3.118) and (3.119) are substituted into Equation (3.5) to find the stochastic longitudinal and lateral damping coefficients at the contact patch.

$$\sum_{i=1}^{S} c_{long\_contact}{}^{i}\Psi^{i} = \frac{E\left(\sum_{i=1}^{S} a^{i}\Psi^{i}\right)\left(\sum_{i=1}^{S} b^{i}\Psi^{i}\right)\left(\sum_{i=1}^{S} C_{11}{}^{i}\Psi^{i}\right)}{2(1+v)V_{train}}$$
$$\sum_{i=1}^{S} c_{lat\_contact}{}^{i}\Psi^{i} = \frac{E\left(\sum_{i=1}^{S} a^{i}\Psi^{i}\right)\left(\sum_{i=1}^{S} b^{i}\Psi^{i}\right)\left(\sum_{i=1}^{S} C_{22}{}^{i}\Psi^{i}\right)}{2(1+v)V_{train}} \quad (3.126)$$

All stochastic and deterministic dynamic parameters are substituted into Equation (3.4) and then the stochastic CoFs are obtained.

$$\sum_{i=i}^{S} \mu(t)^{i}\Psi^{i} = c_1\left(\frac{\left(\sum_{i=1}^{S} V^{*}(t)^{i}\Psi^{i}\right)}{\left(\sum_{i=i}^{S} R^{*}(t)^{i}\Psi^{i}\right)}\right)^{0.28} \underbrace{\frac{e^{-c_2\sqrt{\left(\sum_{i=1}^{S} V^{*}(t)^{i}\Psi^{i}\right)}}}{1+c_3\left(\frac{\left(\sum_{i=1}^{S} a^{i}\Psi^{i}\right)}{\left(\sum_{i=1}^{S} b^{i}\Psi^{i}\right)}\right)^{2}\left(\sum_{i=i}^{S} R^{*}(t)^{i}\Psi^{i}\right)}}_{Slip\ Component} + \underbrace{\frac{c_4}{1+c_5\left(\frac{\left(\sum_{i=1}^{S} a^{i}\Psi^{i}\right)}{\left(\sum_{i=1}^{S} b^{i}\Psi^{i}\right)}\right)^{2}\left(\sum_{i=i}^{S} R^{*}(t)^{i}\Psi^{i}\right)}}_{Stick\ Component}$$

$$\sum_{i=1}^{S} c_{\tan}{}^{i}\Psi^{i} = \sqrt{\left(\sum_{i=1}^{S} c_{long\_contact}{}^{i}\Psi^{i}\right)^{2} + \left(\sum_{i=1}^{S} c_{lat\_contact}{}^{i}\Psi^{i}\right)^{2}}, \quad \sum_{i=1}^{S} V^{*}(t)^{i}\Psi^{i} = \frac{V_{\tan}}{\left(\sum_{i=1}^{S} F_{n}{}^{i}\Psi^{i}\right)}\left(\sum_{i=1}^{S} c_{\tan}{}^{i}\Psi^{i}\right)$$

$$\sum_{i=1}^{S} T^{i}\Psi^{i} = \frac{-d\left(\sum_{i=1}^{S} h_{o}{}^{i}\Psi^{i}\right)\left(\sum_{i=1}^{S} b^{i}\Psi^{i}\right)}{\sigma_{\tan}\left(\sum_{i=1}^{S} a^{i}\Psi^{i}\right)}, \quad \sum_{i=i}^{S} R^{*}(t)^{i}\Psi^{i} = 1 - e^{\left(\sum_{i=1}^{S} T^{i}\Psi^{i}\right)} \quad (3.127)$$

Uncertain MARR and Lateral Displacement

Independent MARR and lateral displacement are considered as uncertain variables. Uncertain MARR and lateral displacement can be expressed using a truncated Karhunen-Loeve expansion as follows:

$$r = \sum_{i=1}^{S} r^i \Psi^i, \qquad x_7 = \sum_{i=1}^{S} x_7{}^i \Psi^i \tag{3.128}$$

Equation (3.128) propagates from the calculation of the normal force to the calculation of the CoF model following the steps presented below.

Step 1. The stochastic normal contact force

The stochastic wheel and rail displacements, x_3 and x_5, from Equation (3.141) are substituted into Equation (3.27) given Equation (3.129).

$$\sum_{i=1}^{S} h_o{}^i \Psi^i = \sum_{i=1}^{S} x_3{}^i \Psi^i - \sum_{i=1}^{S} x_5{}^i \Psi^i + \sum_{i=1}^{S} r^i \Psi^i \tag{3.129}$$

Then Equation (3.129) is substituted into Equation (3.26) to obtain the stochastic normal contact force as follows:

$$\sum_{i=1}^{S} F_n{}^i \Psi^i = K_H \left(\sum_{i=1}^{S} h_o{}^i \Psi^i \right)^{3/2} \tag{3.130}$$

Step 2. The stochastic semi-elliptical contact lengths

The uncertain lateral displacement leads to uncertain radii of curvatures since they are the function of the lateral displacement as shown in Equation (3.19), (3.36), and (3.37). Thus, the stochastic radii of curvatures are expressed as in Equation (3.131) and (3.132).

$$\sum_{i=1}^{S} \left(R^w \right)^i \Psi^i = r_o - \tan\lambda \left(\sum_{i=1}^{S} x_7{}^i \Psi^i \right) \tag{3.131}$$

$$\sum_{i=1}^{S} \left(R^r(a) \right)^i \Psi^i = \left. \frac{\left[1 + \left(\frac{d\left(\sum_{i=1}^{S} y^i \Psi^i \right)}{dx} \right)^2 \right]}{\frac{d^2 \left(\sum_{i=1}^{S} y^i \Psi^i \right)}{dx^2}} \right|_{x=a} \tag{3.132}$$

$$where \sum_{i=1}^{S} y^i \Psi^i = f\left(x_7\right) = P_1 \left(\sum_{i=1}^{S} x_7^i \Psi^i \right)^5 + P_2 \left(\sum_{i=1}^{S} x_7^i \Psi^i \right)^4 + P_3 \left(\sum_{i=1}^{S} x_7^i \Psi^i \right)^3 + P_4 \left(\sum_{i=1}^{S} x_7^i \Psi^i \right)^2 + P_5 \left(\sum_{i=1}^{S} x_7^i \Psi^i \right) + P_6$$

K_3 is a function of radii of curvatures. Thus, Equation (3.131) and (3.132) are substituted into Equation (3.23) to find the stochastic K_3.

$$\sum_{i=1}^{S} {K_3}^i \Psi^i = \frac{1}{2}\left(\frac{1}{R^w} + \frac{1}{R^r}\right) = \frac{1}{2}\left(\frac{1}{\sum_{i=1}^{S}\left(R^w\right)^i \Psi^i} + \frac{1}{\sum_{i=1}^{S}\left(R^r\right)^i \Psi^i}\right) \tag{3.133}$$

Equation (3.130) and (3.133) are substituted into Equation (3.20) to calculate the stochastic semi-elliptical contact lengths.

$$\begin{aligned}
\sum_{i=1}^{S} {L_1}^i \Psi^i &= m\left(\frac{3\pi\left(K_1+K_2\right)}{4K_3}\sum_{i=1}^{S} {F_n}^i \Psi^i\right)^{1/3} = \sum_{i=1}^{S} a^i \Psi^i = m\left(\frac{3\pi\left(K_1+K_2\right)}{4\sum_{i=1}^{S} {K_3}^i \Psi^i}\sum_{i=1}^{S} {F_n}^i \Psi^i\right)^{1/3} \\
\sum_{i=1}^{S} {L_2}^i \Psi^i &= n\left(\frac{3\pi\left(K_1+K_2\right)}{4K_3}\sum_{i=1}^{S} {F_n}^i \Psi^i\right)^{1/3} = \sum_{i=1}^{S} b^i \Psi^i = n\left(\frac{3\pi\left(K_1+K_2\right)}{4\sum_{i=1}^{S} {K_3}^i \Psi^i}\sum_{i=1}^{S} {F_n}^i \Psi^i\right)^{1/3}
\end{aligned} \tag{3.134}$$

Step 3. The stochastic Kalker's C coefficient

The *C* coefficients are expressed as the truncated Karhunen-Loeve expansions presented in Equation (3.135).

$$\sum_{i=1}^{S} {C_{11}}^i \Psi^i,\ \sum_{i=1}^{S} {C_{22}}^i \Psi^i,\ \sum_{i=1}^{S} {C_{33}}^i \Psi^i,\ \sum_{i=1}^{S} {C_{23}}^i \Psi^i \tag{3.135}$$

Step 4. The stochastic creep forces

By substituting Equation (3.141) into Equation (3.33), the stochastic wheel velocities are found as presented in Equation (3.136).

$$\sum_{i=1}^{S}\left(V_{long}^w\right)^i \Psi^i = V_{train} + l_o\sum_{i=1}^{S}\left(x_{10}\right)^i \Psi^i,\ \sum_{i=1}^{S}\left(V_{lat}^w\right)^i \Psi^i = \sum_{i=1}^{S} {x_8}^i \Psi^i + V_{train}\sum_{i=1}^{S}\left(x_9\right)^i \Psi^i,\ \sum_{i=1}^{S}\left(\Omega^w\right)^i \Psi^i = \omega\lambda + \sum_{i=1}^{S}\left(x_{10}\right)^i \Psi^i \tag{3.136}$$

The stochastic creepage can be found by substituting Equation (3.136) into Equation (3.49).

$$\sum_{i=1}^{S}\left(\xi_{long}\right)^{i}\Psi^{i}=\frac{\sum_{i=1}^{S}\left(V_{long}^{w}\right)^{i}\Psi^{i}-V_{long}^{r}}{V_{train}},\quad \sum_{i=1}^{S}\left(\xi_{lat}\right)^{i}\Psi^{i}=\frac{\sum_{i=1}^{S}\left(V_{lat}^{w}\right)^{i}\Psi^{i}-V_{long}^{r}}{V_{train}},\quad \sum_{i=1}^{S}\left(\xi_{spin}\right)^{i}\Psi^{i}=\frac{\sum_{i=1}^{S}\left(\Omega^{w}\right)^{i}\Psi^{i}-\Omega^{r}}{V_{train}} \tag{3.137}$$

Equations (3.134), (3.135), and (3.137) are substituted into Equation (3.38) to obtain the stochastic creep forces of Equation (3.138).

$$\begin{aligned}
&\sum_{i=1}^{S}F_{long}{}^{i}\Psi^{i}=-G\left(\sum_{i=1}^{S}a^{i}\Psi^{i}\right)\left(\sum_{i=1}^{S}b^{i}\Psi^{i}\right)\left(\sum_{i=1}^{S}C_{11}{}^{i}\Psi^{i}\right)\left(\sum_{i=1}^{S}\xi_{long}{}^{i}\Psi^{i}\right)\\
&\sum_{i=1}^{S}F_{lat}{}^{i}\Psi^{i}=-G\left(\sum_{i=1}^{S}a^{i}\Psi^{i}\right)\left(\sum_{i=1}^{S}b^{i}\Psi^{i}\right)\left\{\left(\sum_{i=1}^{S}C_{22}{}^{i}\Psi^{i}\right)\left(\sum_{i=1}^{S}\xi_{lat}{}^{i}\Psi^{i}\right)+\sqrt{\left(\sum_{i=1}^{S}a^{i}\Psi^{i}\right)\left(\sum_{i=1}^{S}b^{i}\Psi^{i}\right)}\left(\sum_{i=1}^{S}C_{23}{}^{i}\Psi^{i}\right)\left(\sum_{i=1}^{S}\xi_{spin}{}^{i}\Psi^{i}\right)\right\}\\
&\sum_{i=1}^{S}M_{spin}{}^{i}\Psi^{i}=-G\left(\sum_{i=1}^{S}a^{i}\Psi^{i}\right)\left(\sum_{i=1}^{S}b^{i}\Psi^{i}\right)\left\{-\sqrt{\left(\sum_{i=1}^{S}a^{i}\Psi^{i}\right)\left(\sum_{i=1}^{S}b^{i}\Psi^{i}\right)}\left(\sum_{i=1}^{S}C_{23}{}^{i}\Psi^{i}\right)\left(\sum_{i=1}^{S}\xi_{lat}{}^{i}\Psi^{i}\right)+\left(\sum_{i=1}^{S}a^{i}\Psi^{i}\right)\left(\sum_{i=1}^{S}b^{i}\Psi^{i}\right)\left(\sum_{i=1}^{S}C_{33}{}^{i}\Psi^{i}\right)\left(\sum_{i=1}^{S}\xi_{spin}{}^{i}\Psi^{i}\right)\right\}
\end{aligned} \tag{3.138}$$

Step 5. The stochastic ODEs

Equations (3.130) and (3.138) are substituted into Equation (3.40) to find the stochastic vertical and lateral contact forces and the stochastic moment with respect to the vertical axis (z).

$$\begin{aligned}
\sum_{i=1}^{S}F_{v}{}^{i}\Psi^{i}&=\left(\sum_{i=1}^{S}F_{n}{}^{i}\Psi^{i}\right)\cos\lambda-\left(\sum_{i=1}^{S}F_{lat}{}^{i}\Psi^{i}\right)\sin\lambda\\
\sum_{i=1}^{S}F_{l}{}^{i}\Psi^{i}&=\left(\sum_{i=1}^{S}F_{n}{}^{i}\Psi^{i}\right)\sin\lambda+\left(\sum_{i=1}^{S}F_{lat}{}^{i}\Psi^{i}\right)\cos\lambda\\
\sum_{i=1}^{S}M_{z}{}^{i}\Psi^{i}&=\left(\sum_{i=1}^{S}M_{spin}{}^{i}\Psi^{i}\right)\cos\lambda
\end{aligned} \tag{3.139}$$

Equation (3.139) and (3.141) are substituted into Equation (3.42) to find the stochastic ODEs.

$$\begin{cases}
\sum_{i=1}^{S} \dot{x}_1{}^i\Psi^i = \left(\sum_{i=1}^{S} x_2{}^i\Psi^i\right) \\
\sum_{i=1}^{S} \dot{x}_2{}^i\Psi^i = -\dfrac{C_b\left(\left(\sum_{i=1}^{S} x_2{}^i\Psi^i\right)-\left(\sum_{i=1}^{S} x_4{}^i\Psi^i\right)\right)+K_b\left(\left(\sum_{i=1}^{S} x_1{}^i\Psi^i\right)-\left(\sum_{i=1}^{S} x_3{}^i\Psi^i\right)\right)}{M_b} \\
\sum_{i=1}^{S} \dot{x}_3{}^i\Psi^i = \left(\sum_{i=1}^{S} x_4{}^i\Psi^i\right) \\
\sum_{i=1}^{S} \dot{x}_4{}^i\Psi^i = \dfrac{C_b\left(\left(\sum_{i=1}^{S} x_2{}^i\Psi^i\right)-\left(\sum_{i=1}^{S} x_4{}^i\Psi^i\right)\right)+K_b\left(\left(\sum_{i=1}^{S} x_1{}^i\Psi^i\right)-\left(\sum_{i=1}^{S} x_3{}^i\Psi^i\right)\right)-\left(\sum_{i=1}^{S} F_v{}^i\Psi^i\right)}{M_w} \\
\sum_{i=1}^{S} \dot{x}_5{}^i\Psi^i = \left(\sum_{i=1}^{S} x_6{}^i\Psi^i\right) \\
\sum_{i=1}^{S} \dot{x}_6{}^i\Psi^i = \dfrac{\left(\sum_{i=1}^{S} F_v{}^i\Psi^i\right)-C_{track}\left(\left(\sum_{i=1}^{S} x_4{}^i\Psi^i\right)-\left(\sum_{i=1}^{S} x_6{}^i\Psi^i\right)\right)-K_{track}\left(\left(\sum_{i=1}^{S} x_3{}^i\Psi^i\right)-\left(\sum_{i=1}^{S} x_5{}^i\Psi^i\right)\right)}{M_r} \\
\sum_{i=1}^{S} \dot{x}_7{}^i\Psi^i = \left(\sum_{i=1}^{S} x_8{}^i\Psi^i\right) \\
\sum_{i=1}^{S} \dot{x}_8{}^i\Psi^i = \dfrac{\left(\sum_{i=1}^{S} F_l{}^i\Psi^i\right)-C_{lat}\left(\sum_{i=1}^{S} x_8{}^i\Psi^i\right)-K_{lat}\left(\sum_{i=1}^{S} x_7{}^i\Psi^i\right)}{M_w} \\
\sum_{i=1}^{S} \dot{x}_9{}^i\Psi^i = \left(\sum_{i=1}^{S} x_{10}{}^i\Psi^i\right) \\
\sum_{i=1}^{S} \dot{x}_{10}{}^i\Psi^i = \dfrac{\left(\sum_{i=1}^{S} M_z{}^i\Psi^i\right)-C_\theta\left(\sum_{i=1}^{S} x_{10}{}^i\Psi^i\right)-K_\theta\left(\sum_{i=1}^{S} x_9{}^i\Psi^i\right)}{J_w}
\end{cases} \tag{3.140}$$

By integrating Equation (3.140), the stochastic displacements and velocities can be found as follows:

$$\begin{aligned}
&\sum_{i=1}^{S} x_1{}^i\Psi^i, \quad \sum_{i=1}^{S} x_3{}^i\Psi^i, \quad \sum_{i=1}^{S} x_5{}^i\Psi^i, \quad \sum_{i=1}^{S} x_7{}^i\Psi^i, \quad \sum_{i=1}^{S} x_9{}^i\Psi^i \\
&\sum_{i=1}^{S} x_2{}^i\Psi^i, \quad \sum_{i=1}^{S} x_4{}^i\Psi^i, \quad \sum_{i=1}^{S} x_6{}^i\Psi^i, \quad \sum_{i=1}^{S} x_8{}^i\Psi^i, \quad \sum_{i=1}^{S} x_{10}{}^i\Psi^i
\end{aligned} \tag{3.141}$$

Step 6. The stochastic CoF

Equations (3.134) and (3.135) are substituted into Equation (3.5) to find the stochastic longitudinal and lateral damping coefficients at the contact patch.

$$\sum_{i=1}^{S} c_{long\_contact}{}^{i}\Psi^{i} = \frac{E\left(\sum_{i=1}^{S} a^{i}\Psi^{i}\right)\left(\sum_{i=1}^{S} b^{i}\Psi^{i}\right)\left(\sum_{i=1}^{S} C_{11}{}^{i}\Psi^{i}\right)}{2(1+v)V_{train}}$$
$$\sum_{i=1}^{S} c_{lat\_contact}{}^{i}\Psi^{i} = \frac{E\left(\sum_{i=1}^{S} a^{i}\Psi^{i}\right)\left(\sum_{i=1}^{S} b^{i}\Psi^{i}\right)\left(\sum_{i=1}^{S} C_{22}{}^{i}\Psi^{i}\right)}{2(1+v)V_{train}} \quad (3.142)$$

All stochastic and deterministic dynamic parameters are substituted into Equation (3.4) and then the stochastic CoFs are obtained.

$$\sum_{i=i}^{S} \mu(t)^{i}\Psi^{i} = c_1 \left(\frac{\left(\sum_{i=1}^{S} V^{*}(t)^{i}\Psi^{i}\right)}{\left(\sum_{i=i}^{S} R^{*}(t)^{i}\Psi^{i}\right)}\right)^{0.28} \underbrace{\frac{e^{-c_2\sqrt{\left(\sum_{i=1}^{S} V^{*}(t)^{i}\Psi^{i}\right)}}}{1+c_3\left(\frac{\left(\sum_{i=1}^{S} a^{i}\Psi^{i}\right)}{\left(\sum_{i=1}^{S} b^{i}\Psi^{i}\right)}\right)^{2}\left(\sum_{i=i}^{S} R^{*}(t)^{i}\Psi^{i}\right)}}_{Slip\ Component} + \underbrace{\frac{c_4}{1+c_5\left(\frac{\left(\sum_{i=1}^{S} a^{i}\Psi^{i}\right)}{\left(\sum_{i=1}^{S} b^{i}\Psi^{i}\right)}\right)^{2}\left(\sum_{i=i}^{S} R^{*}(t)^{i}\Psi^{i}\right)}}_{Stick\ Component}$$

$$where \quad \sum_{i=1}^{S} c_{\tan}{}^{i}\Psi^{i} = \sqrt{\left(\sum_{i=1}^{S} c_{long\_contact}{}^{i}\Psi^{i}\right)^{2} + \left(\sum_{i=1}^{S} c_{lat\_contact}{}^{i}\Psi^{i}\right)^{2}}, \quad \sum_{i=1}^{S} V^{*}(t)^{i}\Psi^{i} = \frac{V_{\tan}}{\left(\sum_{i=1}^{S} F_n{}^{i}\Psi^{i}\right)}\left(\sum_{i=1}^{S} c_{\tan}{}^{i}\Psi^{i}\right)$$

$$\sum_{i=1}^{S} T^{i}\Psi^{i} = \frac{-d\left(\sum_{i=1}^{S} h_o{}^{i}\Psi^{i}\right)\left(\sum_{i=1}^{S} b^{i}\Psi^{i}\right)}{\sigma_{\tan}\left(\sum_{i=1}^{S} a^{i}\Psi^{i}\right)}, \qquad \sum_{i=i}^{S} R^{*}(t)^{i}\Psi^{i} = 1 - e^{\left(\sum_{i=1}^{S} T^{i}\Psi^{i}\right)} \quad (3.143)$$

Uncertain MARR and Sleeper Distance

Independent MARR and sleeper distance are considered as uncertain variables. Uncertain MARR and sleeper distance can be expressed using a truncated Karhunen-Loeve expansion as follows:

$$r = \sum_{i=1}^{S} r^i \Psi^i, \qquad dist = \sum_{i=1}^{S} dist^i \Psi^i \tag{3.144}$$

Equation (3.144) propagates from the calculation of the normal force to the calculation of the CoF model following the steps presented below.

Step 1. The stochastic normal contact force

The uncertain MARR and the stochastic wheel and rail displacements, x_3 and x_5, from Equation (3.157) are substituted into Equation (3.27) given Equation (3.145).

$$\sum_{i=1}^{S} h_o{}^i \Psi^i = \sum_{i=1}^{S} x_3{}^i \Psi^i - \sum_{i=1}^{S} x_5{}^i \Psi^i + \sum_{i=1}^{S} r^i \Psi^i \tag{3.145}$$

Then Equation (3.145) is substituted into Equation (3.26) to obtain the stochastic normal contact force as follows:

$$\sum_{i=1}^{S} F_n{}^i \Psi^i = K_H \left(\sum_{i=1}^{S} h_o{}^i \Psi^i \right)^{3/2} \tag{3.146}$$

Step 2. The stochastic semi-elliptical contact lengths

Equation (3.146) is substituted into Equation (3.20) to calculate the stochastic semi-elliptical contact lengths.

$$\begin{aligned} \sum_{i=1}^{S} L_1{}^i \Psi^i &= m \left(\frac{3\pi (K_1 + K_2)}{4K_3} \sum_{i=1}^{S} F_n{}^i \Psi^i \right)^{1/3} = \sum_{i=1}^{S} a^i \Psi^i = m \left(\frac{3\pi (K_1 + K_2)}{4K_3} \sum_{i=1}^{S} F_n{}^i \Psi^i \right)^{1/3} \\ \sum_{i=1}^{S} L_2{}^i \Psi^i &= n \left(\frac{3\pi (K_1 + K_2)}{4K_3} \sum_{i=1}^{S} F_n{}^i \Psi^i \right)^{1/3} = \sum_{i=1}^{S} b^i \Psi^i = n \left(\frac{3\pi (K_1 + K_2)}{4K_3} \sum_{i=1}^{S} F_n{}^i \Psi^i \right)^{1/3} \end{aligned} \tag{3.147}$$

Step 3. The stochastic Kalker's C coefficient

The *C* coefficients are expressed as the truncated Karhunen-Loeve expansions presented in Equation (3.148).

$$\sum_{i=1}^{S} C_{11}{}^{i}\Psi^{i},\ \sum_{i=1}^{S} C_{22}{}^{i}\Psi^{i},\ \sum_{i=1}^{S} C_{33}{}^{i}\Psi^{i},\ \sum_{i=1}^{S} C_{23}{}^{i}\Psi^{i} \tag{3.148}$$

Step 4. The stochastic creep forces

By substituting Equation (3.157) into Equation (3.33), the stochastic wheel velocities are found as presented in Equation (3.149).

$$\sum_{i=1}^{S}\left(V_{long}^{w}\right)^{i}\Psi^{i} = V_{train} + l_{o}\sum_{i=1}^{S}\left(x_{10}\right)^{i}\Psi^{i},\ \sum_{i=1}^{S}\left(V_{lat}^{w}\right)^{i}\Psi^{i} = \sum_{i=1}^{S} x_{8}{}^{i}\Psi^{i} + V_{train}\sum_{i=1}^{S}\left(x_{9}\right)^{i}\Psi^{i},\ \sum_{i=1}^{S}\left(\Omega^{w}\right)^{i}\Psi^{i} = \omega\lambda + \sum_{i=1}^{S}\left(x_{10}\right)^{i}\Psi^{i} \tag{3.149}$$

The stochastic creepage can be found by substituting Equation (3.149) into Equation (3.49).

$$\sum_{i=1}^{S}\left(\xi_{long}\right)^{i}\Psi^{i} = \frac{\sum_{i=1}^{S}\left(V_{long}^{w}\right)^{i}\Psi^{i} - V_{long}^{r}}{V_{train}},\quad \sum_{i=1}^{S}\left(\xi_{lat}\right)^{i}\Psi^{i} = \frac{\sum_{i=1}^{S}\left(V_{lat}^{w}\right)^{i}\Psi^{i} - V_{long}^{r}}{V_{train}},\quad \sum_{i=1}^{S}\left(\xi_{spin}\right)^{i}\Psi^{i} = \frac{\sum_{i=1}^{S}\left(\Omega^{w}\right)^{i}\Psi^{i} - \Omega^{r}}{V_{train}} \tag{3.150}$$

Equations (3.147), (3.148), and (3.150) are substituted into Equation (3.38) to obtain the stochastic creep forces of Equation (3.151).

$$\begin{aligned}
&\sum_{i=1}^{S} F_{long}{}^{i}\Psi^{i} = -G\left(\sum_{i=1}^{S} a^{i}\Psi^{i}\right)\left(\sum_{i=1}^{S} b^{i}\Psi^{i}\right)\left(\sum_{i=1}^{S} C_{11}{}^{i}\Psi^{i}\right)\left(\sum_{i=1}^{S}\xi_{long}{}^{i}\Psi^{i}\right)\\
&\sum_{i=1}^{S} F_{lat}{}^{i}\Psi^{i} = -G\left(\sum_{i=1}^{S} a^{i}\Psi^{i}\right)\left(\sum_{i=1}^{S} b^{i}\Psi^{i}\right)\left\{\left(\sum_{i=1}^{S} C_{22}{}^{i}\Psi^{i}\right)\left(\sum_{i=1}^{S}\xi_{lat}{}^{i}\Psi^{i}\right) + \sqrt{\left(\sum_{i=1}^{S} a^{i}\Psi^{i}\right)\left(\sum_{i=1}^{S} b^{i}\Psi^{i}\right)}\left(\sum_{i=1}^{S} C_{23}{}^{i}\Psi^{i}\right)\left(\sum_{i=1}^{S}\xi_{spin}{}^{i}\Psi^{i}\right)\right\}\\
&\sum_{i=1}^{S} M_{spin}{}^{i}\Psi^{i} = -G\left(\sum_{i=1}^{S} a^{i}\Psi^{i}\right)\left(\sum_{i=1}^{S} b^{i}\Psi^{i}\right)\left\{-\sqrt{\left(\sum_{i=1}^{S} a^{i}\Psi^{i}\right)\left(\sum_{i=1}^{S} b^{i}\Psi^{i}\right)}\left(\sum_{i=1}^{S} C_{23}{}^{i}\Psi^{i}\right)\left(\sum_{i=1}^{S}\xi_{lat}{}^{i}\Psi^{i}\right) + \left(\sum_{i=1}^{S} a^{i}\Psi^{i}\right)\left(\sum_{i=1}^{S} b^{i}\Psi^{i}\right)\left(\sum_{i=1}^{S} C_{33}{}^{i}\Psi^{i}\right)\left(\sum_{i=1}^{S}\xi_{spin}{}^{i}\Psi^{i}\right)\right\}
\end{aligned} \tag{3.151}$$

Step 5. The stochastic ODEs

Equations (3.146) and (3.151) are substituted into Equation (3.40) to find the stochastic vertical and lateral contact forces and the stochastic moment with respect to the vertical axis (z).

$$\begin{aligned}
\sum_{i=1}^{S} F_v{}^i\Psi^i &= \left(\sum_{i=1}^{S} F_n{}^i\Psi^i\right)\cos\lambda - \left(\sum_{i=1}^{S} F_{lat}{}^i\Psi^i\right)\sin\lambda \\
\sum_{i=1}^{S} F_l{}^i\Psi^i &= \left(\sum_{i=1}^{S} F_n{}^i\Psi^i\right)\sin\lambda + \left(\sum_{i=1}^{S} F_{lat}{}^i\Psi^i\right)\cos\lambda \\
\sum_{i=1}^{S} M_z{}^i\Psi^i &= \left(\sum_{i=1}^{S} M_{spin}{}^i\Psi^i\right)\cos\lambda
\end{aligned} \tag{3.152}$$

Uncertain sleeper distance is used to calculate the stochastic rail mass of Equation (3.153) and it is substituted into Equation (3.8) to obtain the stochastic track excitation frequency of Equation (3.154).

$$\sum_{i=1}^{S} M_r{}^i\Psi^i = A \times density \times \sum_{i=1}^{S} dist^i\Psi^i \tag{3.153}$$

$$\sum_{i=1}^{S} f^i\Psi^i = \frac{2\pi V_{train}}{\sum_{i=1}^{S} dist^i\Psi^i} \tag{3.154}$$

The stochastic track stiffness and damping coefficient is calculated as below using Equation (3.155).

$$\begin{aligned}
\sum_{i=1}^{S} K_{track}{}^i\Psi^i &= \sum_{i=1}^{S} K_{pad}{}^i\Psi^i + \sum_{i=1}^{S} K_{sleeper}{}^i\Psi^i + K_{ballast} \\
\sum_{i=1}^{S} C_{track}{}^i\Psi^i &= \sum_{i=1}^{S} C_{pad}{}^i\Psi^i + \sum_{i=1}^{S} C_{sleeper}{}^i\Psi^i + C_{ballast}
\end{aligned}$$

whrer

$$\sum_{i=1}^{S} K_{pad}{}^i\Psi^i = 0.5K_{pad}\cos\left(\left(\sum_{i=1}^{S} f^i\Psi^i\right)\cdot t\right) + 0.5K_{pad},\ \sum_{i=1}^{S} K_{sleeper}{}^i\Psi^i = 0.5K_{sleeper}\cos\left(\left(\sum_{i=1}^{S} f^i\Psi^i\right)\cdot t\right) + 0.5K_{sleeper}$$

$$\sum_{i=1}^{S} C_{pad}{}^i\Psi^i = 0.5C_{pad}\cos\left(\left(\sum_{i=1}^{S} f^i\Psi^i\right)\cdot t\right) + 0.5C_{pad},\ \sum_{i=1}^{S} C_{sleeper}{}^i\Psi^i = 0.5C_{sleeper}\cos\left(\left(\sum_{i=1}^{S} f^i\Psi^i\right)\cdot t\right) + 0.5C_{sleeper}$$

(3.155)

Equation (3.152), (3.153), (3.155) and (3.157) are substituted into Equation (3.42) to find the stochastic ODEs.

$$
\begin{cases}
\sum_{i=1}^{S} \dot{x}_1{}^i\Psi^i = \left(\sum_{i=1}^{S} x_2{}^i\Psi^i\right) \\
\sum_{i=1}^{S} \dot{x}_2{}^i\Psi^i = -\dfrac{C_b\left(\left(\sum_{i=1}^{S} x_2{}^i\Psi^i\right)-\left(\sum_{i=1}^{S} x_4{}^i\Psi^i\right)\right)+K_b\left(\left(\sum_{i=1}^{S} x_1{}^i\Psi^i\right)-\left(\sum_{i=1}^{S} x_3{}^i\Psi^i\right)\right)}{M_b} \\
\sum_{i=1}^{S} \dot{x}_3{}^i\Psi^i = \left(\sum_{i=1}^{S} x_4{}^i\Psi^i\right) \\
\sum_{i=1}^{S} \dot{x}_4{}^i\Psi^i = \dfrac{C_b\left(\left(\sum_{i=1}^{S} x_2{}^i\Psi^i\right)-\left(\sum_{i=1}^{S} x_4{}^i\Psi^i\right)\right)+K_b\left(\left(\sum_{i=1}^{S} x_1{}^i\Psi^i\right)-\left(\sum_{i=1}^{S} x_3{}^i\Psi^i\right)\right)-\left(\sum_{i=1}^{S} F_v{}^i\Psi^i\right)}{M_w} \\
\sum_{i=1}^{S} \dot{x}_5{}^i\Psi^i = \left(\sum_{i=1}^{S} x_6{}^i\Psi^i\right) \\
\sum_{i=1}^{S} \dot{x}_6{}^i\Psi^i = \dfrac{\left(\sum_{i=1}^{S} F_v{}^i\Psi^i\right)-\left(\sum_{i=1}^{S} C_{track}{}^i\Psi^i\right)\left(\left(\sum_{i=1}^{S} x_4{}^i\Psi^i\right)-\left(\sum_{i=1}^{S} x_6{}^i\Psi^i\right)\right)-\left(\sum_{i=1}^{S} K_{track}{}^i\Psi^i\right)\left(\left(\sum_{i=1}^{S} x_3{}^i\Psi^i\right)-\left(\sum_{i=1}^{S} x_5{}^i\Psi^i\right)\right)}{\sum_{i=1}^{S} M_r{}^i\Psi^i} \\
\sum_{i=1}^{S} \dot{x}_7{}^i\Psi^i = \left(\sum_{i=1}^{S} x_8{}^i\Psi^i\right) \\
\sum_{i=1}^{S} \dot{x}_8{}^i\Psi^i = \dfrac{\left(\sum_{i=1}^{S} F_l{}^i\Psi^i\right)-C_{lat}\left(\sum_{i=1}^{S} x_8{}^i\Psi^i\right)-K_{lat}\left(\sum_{i=1}^{S} x_7{}^i\Psi^i\right)}{M_w} \\
\sum_{i=1}^{S} \dot{x}_9{}^i\Psi^i = \left(\sum_{i=1}^{S} x_{10}{}^i\Psi^i\right) \\
\sum_{i=1}^{S} \dot{x}_{10}{}^i\Psi^i = \dfrac{\left(\sum_{i=1}^{S} M_z{}^i\Psi^i\right)-C_\theta\left(\sum_{i=1}^{S} x_{10}{}^i\Psi^i\right)-K_\theta\left(\sum_{i=1}^{S} x_9{}^i\Psi^i\right)}{J_w}
\end{cases}
\tag{3.156}
$$

By integrating Equation (3.156), the stochastic displacements and velocities can be found as follows:

$$
\begin{aligned}
&\sum_{i=1}^{S} x_1{}^i\Psi^i, \quad \sum_{i=1}^{S} x_3{}^i\Psi^i, \quad \sum_{i=1}^{S} x_5{}^i\Psi^i, \quad \sum_{i=1}^{S} x_7{}^i\Psi^i, \quad \sum_{i=1}^{S} x_9{}^i\Psi^i \\
&\sum_{i=1}^{S} x_2{}^i\Psi^i, \quad \sum_{i=1}^{S} x_4{}^i\Psi^i, \quad \sum_{i=1}^{S} x_6{}^i\Psi^i, \quad \sum_{i=1}^{S} x_8{}^i\Psi^i, \quad \sum_{i=1}^{S} x_{10}{}^i\Psi^i
\end{aligned}
\tag{3.157}
$$

Step 6. The stochastic CoF

Equations (3.147) and (3.148) are substituted into Equation (3.5) to find the stochastic longitudinal and lateral damping coefficients at the contact patch.

$$\sum_{i=1}^{S} c_{long\_contact}{}^{i}\Psi^{i} = \frac{E\left(\sum_{i=1}^{S} a^{i}\Psi^{i}\right)\left(\sum_{i=1}^{S} b^{i}\Psi^{i}\right)\left(\sum_{i=1}^{S} C_{11}{}^{i}\Psi^{i}\right)}{2(1+v)V_{train}}$$
$$\sum_{i=1}^{S} c_{lat\_contact}{}^{i}\Psi^{i} = \frac{E\left(\sum_{i=1}^{S} a^{i}\Psi^{i}\right)\left(\sum_{i=1}^{S} b^{i}\Psi^{i}\right)\left(\sum_{i=1}^{S} C_{22}{}^{i}\Psi^{i}\right)}{2(1+v)V_{train}} \tag{3.158}$$

All stochastic and deterministic dynamic parameters are substituted into Equation (3.4) and then the stochastic CoFs are obtained.

$$\sum_{i=i}^{S}\mu(t)^{i}\Psi^{i} = c_1\left(\frac{\left(\sum_{i=1}^{S} V^{*}(t)^{i}\Psi^{i}\right)}{\left(\sum_{i=i}^{S} R^{*}(t)^{i}\Psi^{i}\right)}\right)^{0.28}\underbrace{\frac{e^{-c_2\sqrt{\left(\sum_{i=1}^{S} V^{*}(t)^{i}\Psi^{i}\right)}}}{1+c_3\left(\frac{\left(\sum_{i=1}^{S} a^{i}\Psi^{i}\right)}{\left(\sum_{i=1}^{S} b^{i}\Psi^{i}\right)}\right)^{2}\left(\sum_{i=i}^{S} R^{*}(t)^{i}\Psi^{i}\right)}}_{Slip\ Component} + \underbrace{\frac{c_4}{1+c_5\left(\frac{\left(\sum_{i=1}^{S} a^{i}\Psi^{i}\right)}{\left(\sum_{i=1}^{S} b^{i}\Psi^{i}\right)}\right)^{2}\left(\sum_{i=i}^{S} R^{*}(t)^{i}\Psi^{i}\right)}}_{Stick\ Component}$$

$$\sum_{i=1}^{S} c_{\tan}{}^{i}\Psi^{i} = \sqrt{\left(\sum_{i=1}^{S} c_{long\_contact}{}^{i}\Psi^{i}\right)^{2} + \left(\sum_{i=1}^{S} c_{lat\_contact}{}^{i}\Psi^{i}\right)^{2}}, \quad \sum_{i=1}^{S} V^{*}(t)^{i}\Psi^{i} = \frac{V_{\tan}}{\left(\sum_{i=1}^{S} F_{n}{}^{i}\Psi^{i}\right)}\left(\sum_{i=1}^{S} c_{\tan}{}^{i}\Psi^{i}\right)$$

$$\sum_{i=1}^{S} T^{i}\Psi^{i} = \frac{-d\left(\sum_{i=1}^{S} h_{o}{}^{i}\Psi^{i}\right)\left(\sum_{i=1}^{S} b^{i}\Psi^{i}\right)}{\sigma_{\tan}\left(\sum_{i=1}^{S} a^{i}\Psi^{i}\right)}, \quad \sum_{i=i}^{S} R^{*}(t)^{i}\Psi^{i} = 1 - e^{\left(\sum_{i=1}^{S} T^{i}\Psi^{i}\right)} \tag{3.159}$$

Uncertain Track Stiffness and Track Damping Coefficient

Independent track stiffness and track damping coefficient are considered as uncertain variables. Uncertain track stiffness and damping coefficient can be expressed using a truncated Karhunen-Loeve expansion as follows:

$$K_{track} = \sum_{i=1}^{S} K_{track}{}^{i}\Psi^{i}, \qquad C_{track} = \sum_{i=1}^{S} C_{track}{}^{i}\Psi^{i} \tag{3.160}$$

Equation (3.160) propagates from the calculation of the normal force to the calculation of the CoF model following the steps presented below.

Step 1. The stochastic normal contact force

The stochastic wheel and rail displacements, x_3 and x_5, from Equation (3.170) are substituted into Equation (3.27) given Equation (3.161).

$$\sum_{i=1}^{S} h_o{}^{i}\Psi^{i} = \sum_{i=1}^{S} x_3{}^{i}\Psi^{i} - \sum_{i=1}^{S} x_5{}^{i}\Psi^{i} + r \tag{3.161}$$

Then Equation (3.161) is substituted into Equation (3.26) to obtain the stochastic normal contact force as follows:

$$\sum_{i=1}^{S} F_n{}^{i}\Psi^{i} = K_H \left(\sum_{i=1}^{S} h_o{}^{i}\Psi^{i} \right)^{3/2} \tag{3.162}$$

Step 2. The stochastic semi-elliptical contact lengths

Equation (3.162) is substituted into Equation (3.20) to calculate the stochastic semi-elliptical contact lengths.

$$\begin{aligned} \sum_{i=1}^{S} L_1{}^{i}\Psi^{i} &= m\left(\frac{3\pi\left(K_1+K_2\right)}{4K_3} \sum_{i=1}^{S} F_n{}^{i}\Psi^{i} \right)^{1/3} = \sum_{i=1}^{S} a^{i}\Psi^{i} = m\left(\frac{3\pi\left(K_1+K_2\right)}{4K_3} \sum_{i=1}^{S} F_n{}^{i}\Psi^{i} \right)^{1/3} \\ \sum_{i=1}^{S} L_2{}^{i}\Psi^{i} &= n\left(\frac{3\pi\left(K_1+K_2\right)}{4K_3} \sum_{i=1}^{S} F_n{}^{i}\Psi^{i} \right)^{1/3} = \sum_{i=1}^{S} b^{i}\Psi^{i} = n\left(\frac{3\pi\left(K_1+K_2\right)}{4K_3} \sum_{i=1}^{S} F_n{}^{i}\Psi^{i} \right)^{1/3} \end{aligned} \tag{3.163}$$

Step 3. The stochastic Kalker's C coefficient

The C coefficients are expressed as the truncated Karhunen-Loeve expansions presented in Equation (3.164).

$$\sum_{i=1}^{S} C_{11}{}^{i}\Psi^{i}, \ \sum_{i=1}^{S} C_{22}{}^{i}\Psi^{i}, \ \sum_{i=1}^{S} C_{33}{}^{i}\Psi^{i}, \ \sum_{i=1}^{S} C_{23}{}^{i}\Psi^{i} \tag{3.164}$$

Step 4. The stochastic creep forces

By substituting Equation (3.170) into Equation (3.33), the stochastic wheel velocities are found as presented in Equation (3.165).

$$\sum_{i=1}^{S}\left(V_{long}^{w}\right)^{i}\Psi^{i}=V_{train}+l_{o}\sum_{i=1}^{S}\left(x_{10}\right)^{i}\Psi^{i},\ \sum_{i=1}^{S}\left(V_{lat}^{w}\right)^{i}\Psi^{i}=\sum_{i=1}^{S}x_{8}{}^{i}\Psi^{i}+V_{train}\sum_{i=1}^{S}\left(x_{9}\right)^{i}\Psi^{i},\ \sum_{i=1}^{S}\left(\Omega^{w}\right)^{i}\Psi^{i}=\omega\lambda+\sum_{i=1}^{S}\left(x_{10}\right)^{i}\Psi^{i} \tag{3.165}$$

The stochastic creepage can be found by substituting Equation (3.63) into Equation (3.166).

$$\sum_{i=1}^{S}\left(\xi_{long}\right)^{i}\Psi^{i}=\frac{\sum_{i=1}^{S}\left(V_{long}^{w}\right)^{i}\Psi^{i}-V_{long}^{r}}{V_{train}},\quad \sum_{i=1}^{S}\left(\xi_{lat}\right)^{i}\Psi^{i}=\frac{\sum_{i=1}^{S}\left(V_{lat}^{w}\right)^{i}\Psi^{i}-V_{long}^{r}}{V_{train}},\quad \sum_{i=1}^{S}\left(\xi_{spin}\right)^{i}\Psi^{i}=\frac{\sum_{i=1}^{S}\left(\Omega^{w}\right)^{i}\Psi^{i}-\Omega^{r}}{V_{train}} \tag{3.166}$$

Equations (3.163), (3.164), and (3.166) are substituted into Equation (3.38) to obtain the stochastic creep forces of Equation (3.167).

$$\begin{aligned}
&\sum_{i=1}^{S}F_{long}{}^{i}\Psi^{i}=-G\left(\sum_{i=1}^{S}a^{i}\Psi^{i}\right)\left(\sum_{i=1}^{S}b^{i}\Psi^{i}\right)\left(\sum_{i=1}^{S}C_{11}{}^{i}\Psi^{i}\right)\left(\sum_{i=1}^{S}\xi_{long}{}^{i}\Psi^{i}\right)\\
&\sum_{i=1}^{S}F_{lat}{}^{i}\Psi^{i}=-G\left(\sum_{i=1}^{S}a^{i}\Psi^{i}\right)\left(\sum_{i=1}^{S}b^{i}\Psi^{i}\right)\left\{\left(\sum_{i=1}^{S}C_{22}{}^{i}\Psi^{i}\right)\left(\sum_{i=1}^{S}\xi_{lat}{}^{i}\Psi^{i}\right)+\sqrt{\left(\sum_{i=1}^{S}a^{i}\Psi^{i}\right)\left(\sum_{i=1}^{S}b^{i}\Psi^{i}\right)}\left(\sum_{i=1}^{S}C_{23}{}^{i}\Psi^{i}\right)\left(\sum_{i=1}^{S}\xi_{spin}{}^{i}\Psi^{i}\right)\right\}\\
&\sum_{i=1}^{S}M_{spin}{}^{i}\Psi^{i}=-G\left(\sum_{i=1}^{S}a^{i}\Psi^{i}\right)\left(\sum_{i=1}^{S}b^{i}\Psi^{i}\right)\left\{-\sqrt{\left(\sum_{i=1}^{S}a^{i}\Psi^{i}\right)\left(\sum_{i=1}^{S}b^{i}\Psi^{i}\right)}\left(\sum_{i=1}^{S}C_{23}{}^{i}\Psi^{i}\right)\left(\sum_{i=1}^{S}\xi_{lat}{}^{i}\Psi^{i}\right)+\left(\sum_{i=1}^{S}a^{i}\Psi^{i}\right)\left(\sum_{i=1}^{S}b^{i}\Psi^{i}\right)\left(\sum_{i=1}^{S}C_{33}{}^{i}\Psi^{i}\right)\left(\sum_{i=1}^{S}\xi_{spin}{}^{i}\Psi^{i}\right)\right\}
\end{aligned} \tag{3.167}$$

Step 5. The stochastic ODEs

Equations (3.162) and (3.167) are substituted into Equation (3.40) to find the stochastic vertical and lateral contact forces and the stochastic moment with respect to the vertical axis (z).

$$\begin{aligned}
\sum_{i=1}^{S}F_{v}{}^{i}\Psi^{i}&=\left(\sum_{i=1}^{S}F_{n}{}^{i}\Psi^{i}\right)\cos\lambda-\left(\sum_{i=1}^{S}F_{lat}{}^{i}\Psi^{i}\right)\sin\lambda\\
\sum_{i=1}^{S}F_{l}{}^{i}\Psi^{i}&=\left(\sum_{i=1}^{S}F_{n}{}^{i}\Psi^{i}\right)\sin\lambda+\left(\sum_{i=1}^{S}F_{lat}{}^{i}\Psi^{i}\right)\cos\lambda\\
\sum_{i=1}^{S}M_{z}{}^{i}\Psi^{i}&=\left(\sum_{i=1}^{S}M_{spin}{}^{i}\Psi^{i}\right)\cos\lambda
\end{aligned} \tag{3.168}$$

Equation (3.160), (3.168), and (3.170) are substituted into Equation (3.42) to find the stochastic ODEs.

$$
\begin{cases}
\sum_{i=1}^{S} \dot{x}_1{}^i\Psi^i = \left(\sum_{i=1}^{S} x_2{}^i\Psi^i\right) \\
\sum_{i=1}^{S} \dot{x}_2{}^i\Psi^i = -\dfrac{C_b\left(\left(\sum_{i=1}^{S} x_2{}^i\Psi^i\right)-\left(\sum_{i=1}^{S} x_4{}^i\Psi^i\right)\right)+K_b\left(\left(\sum_{i=1}^{S} x_1{}^i\Psi^i\right)-\left(\sum_{i=1}^{S} x_3{}^i\Psi^i\right)\right)}{M_b} \\
\sum_{i=1}^{S} \dot{x}_3{}^i\Psi^i = \left(\sum_{i=1}^{S} x_4{}^i\Psi^i\right) \\
\sum_{i=1}^{S} \dot{x}_4{}^i\Psi^i = \dfrac{C_b\left(\left(\sum_{i=1}^{S} x_2{}^i\Psi^i\right)-\left(\sum_{i=1}^{S} x_4{}^i\Psi^i\right)\right)+K_b\left(\left(\sum_{i=1}^{S} x_1{}^i\Psi^i\right)-\left(\sum_{i=1}^{S} x_3{}^i\Psi^i\right)\right)-\left(\sum_{i=1}^{S} F_v{}^i\Psi^i\right)}{M_w} \\
\sum_{i=1}^{S} \dot{x}_5{}^i\Psi^i = \left(\sum_{i=1}^{S} x_6{}^i\Psi^i\right) \\
\sum_{i=1}^{S} \dot{x}_6{}^i\Psi^i = \dfrac{\left(\sum_{i=1}^{S} F_v{}^i\Psi^i\right)-\left(\sum_{i=1}^{S} C_{track}{}^i\Psi^i\right)\left(\left(\sum_{i=1}^{S} x_4{}^i\Psi^i\right)-\left(\sum_{i=1}^{S} x_6{}^i\Psi^i\right)\right)-\left(\sum_{i=1}^{S} K_{track}{}^i\Psi^i\right)\left(\left(\sum_{i=1}^{S} x_3{}^i\Psi^i\right)-\left(\sum_{i=1}^{S} x_5{}^i\Psi^i\right)\right)}{M_r} \\
\sum_{i=1}^{S} \dot{x}_7{}^i\Psi^i = \left(\sum_{i=1}^{S} x_8{}^i\Psi^i\right) \\
\sum_{i=1}^{S} \dot{x}_8{}^i\Psi^i = \dfrac{\left(\sum_{i=1}^{S} F_l{}^i\Psi^i\right)-C_{lat}\left(\sum_{i=1}^{S} x_8{}^i\Psi^i\right)-K_{lat}\left(\sum_{i=1}^{S} x_7{}^i\Psi^i\right)}{M_w} \\
\sum_{i=1}^{S} \dot{x}_9{}^i\Psi^i = \left(\sum_{i=1}^{S} x_{10}{}^i\Psi^i\right) \\
\sum_{i=1}^{S} \dot{x}_{10}{}^i\Psi^i = \dfrac{\left(\sum_{i=1}^{S} M_z{}^i\Psi^i\right)-C_\theta\left(\sum_{i=1}^{S} x_{10}{}^i\Psi^i\right)-K_\theta\left(\sum_{i=1}^{S} x_9{}^i\Psi^i\right)}{J_w}
\end{cases}
\tag{3.169}
$$

By integrating Equation (3.169), the stochastic displacements and velocities can be found as follows:

$$
\begin{aligned}
&\sum_{i=1}^{S} x_1{}^i\Psi^i, \quad \sum_{i=1}^{S} x_3{}^i\Psi^i, \quad \sum_{i=1}^{S} x_5{}^i\Psi^i, \quad \sum_{i=1}^{S} x_7{}^i\Psi^i, \quad \sum_{i=1}^{S} x_9{}^i\Psi^i \\
&\sum_{i=1}^{S} x_2{}^i\Psi^i, \quad \sum_{i=1}^{S} x_4{}^i\Psi^i, \quad \sum_{i=1}^{S} x_6{}^i\Psi^i, \quad \sum_{i=1}^{S} x_8{}^i\Psi^i, \quad \sum_{i=1}^{S} x_{10}{}^i\Psi^i
\end{aligned}
\tag{3.170}
$$

Step 6. The stochastic CoF

Equations (3.163) and (3.164) are substituted into Equation (3.5) to find the stochastic longitudinal and lateral damping coefficients at the contact patch.

$$\sum_{i=1}^{S} c_{long\_contact}{}^{i}\Psi^{i} = \frac{E\left(\sum_{i=1}^{S} a^{i}\Psi^{i}\right)\left(\sum_{i=1}^{S} b^{i}\Psi^{i}\right)\left(\sum_{i=1}^{S} C_{11}{}^{i}\Psi^{i}\right)}{2(1+v)V_{train}}$$
$$\sum_{i=1}^{S} c_{lat\_contact}{}^{i}\Psi^{i} = \frac{E\left(\sum_{i=1}^{S} a^{i}\Psi^{i}\right)\left(\sum_{i=1}^{S} b^{i}\Psi^{i}\right)\left(\sum_{i=1}^{S} C_{22}{}^{i}\Psi^{i}\right)}{2(1+v)V_{train}} \tag{3.171}$$

All stochastic and deterministic dynamic parameters are substituted into Equation (3.4) and then the stochastic CoFs are obtained.

$$\sum_{i=i}^{S}\mu(t)^{i}\Psi^{i} = c_1\left(\frac{\left(\sum_{i=1}^{S} V^{*}(t)^{i}\Psi^{i}\right)}{\left(\sum_{i=i}^{S} R^{*}(t)^{i}\Psi^{i}\right)}\right)^{0.28}\underbrace{\frac{e^{-c_2\sqrt{\left(\sum_{i=1}^{S} V^{*}(t)^{i}\Psi^{i}\right)}}}{1+c_3\left(\frac{\left(\sum_{i=1}^{S} a^{i}\Psi^{i}\right)}{\left(\sum_{i=1}^{S} b^{i}\Psi^{i}\right)}\right)^{2}\left(\sum_{i=i}^{S} R^{*}(t)^{i}\Psi^{i}\right)}}_{Slip\ Component} + \underbrace{\frac{c_4}{1+c_5\left(\frac{\left(\sum_{i=1}^{S} a^{i}\Psi^{i}\right)}{\left(\sum_{i=1}^{S} b^{i}\Psi^{i}\right)}\right)^{2}\left(\sum_{i=i}^{S} R^{*}(t)^{i}\Psi^{i}\right)}}_{Stick\ Component}$$

$$where\quad \sum_{i=1}^{S} c_{\tan}{}^{i}\Psi^{i} = \sqrt{\left(\sum_{i=1}^{S} c_{long\_contact}{}^{i}\Psi^{i}\right)^{2} + \left(\sum_{i=1}^{S} c_{lat\_contact}{}^{i}\Psi^{i}\right)^{2}},\quad \sum_{i=1}^{S} V^{*}(t)^{i}\Psi^{i} = \frac{V_{\tan}}{\left(\sum_{i=1}^{S} F_{n}{}^{i}\Psi^{i}\right)}\left(\sum_{i=1}^{S} c_{\tan}{}^{i}\Psi^{i}\right)$$

$$\sum_{i=1}^{S} T^{i}\Psi^{i} = \frac{-d\left(\sum_{i=1}^{S} h_{o}{}^{i}\Psi^{i}\right)\left(\sum_{i=1}^{S} b^{i}\Psi^{i}\right)}{\sigma_{\tan}\left(\sum_{i=1}^{S} a^{i}\Psi^{i}\right)},\qquad \sum_{i=i}^{S} R^{*}(t)^{i}\Psi^{i} = 1 - e^{\left(\sum_{i=1}^{S} T^{i}\Psi^{i}\right)} \tag{3.172}$$

3.3.3 A Stochastic CoF Model with Three Uncertainties

Uncertain Independent *a*, *b*, and x_7

Independent semi-elliptical contact lengths, *a* and *b*, and lateral displacement (x_7) are considered as uncertain variables. Uncertain *a*, *b*, and x_7 can be expressed using a truncated Karhunen-Loeve expansion as follows:

$$a = \sum_{i=1}^{S} a^i \Psi^i, \quad b = \sum_{i=1}^{S} b^i \Psi^i, \quad x_7 = \sum_{i=1}^{S} {x_7}^i \Psi^i \tag{3.173}$$

Equation (3.173) propagates from the calculation of the normal force to the calculation of the CoF model following the steps presented below.

Step 1. The stochastic normal contact force

The stochastic wheel and rail displacements, x_3 and x_5, from Equation (3.185) are substituted into Equation (3.27) given Equation (3.174).

$$\sum_{i=1}^{S} {h_o}^i \Psi^i = \sum_{i=1}^{S} {x_3}^i \Psi^i - \sum_{i=1}^{S} {x_5}^i \Psi^i + r \tag{3.174}$$

Then Equation (3.174) is substituted into Equation (3.26) to obtain the stochastic normal contact force as follows:

$$\sum_{i=1}^{S} {F_n}^i \Psi^i = K_H \left(\sum_{i=1}^{S} {h_o}^i \Psi^i \right)^{3/2} \tag{3.175}$$

Step 2. The stochastic semi-elliptical contact lengths

The uncertain lateral displacement leads to uncertain radii of curvatures since they are the function of the lateral displacement as shown in Equation (3.19), (3.36), and (3.37). Thus, the stochastic radii of curvatures are expressed as in Equation (3.176) and (3.177).

$$\sum_{i=1}^{S} \left(R^w \right)^i \Psi^i = r_o - \tan\lambda \left(\sum_{i=1}^{S} {x_7}^i \Psi^i \right) \tag{3.176}$$

$$\sum_{i=1}^{S}\left(R^{r}(a)\right)^{i}\Psi^{i}=\left.\frac{\left[1+\left(\frac{d\left(\sum_{i=1}^{S}y^{i}\Psi^{i}\right)}{dx}\right)^{2}\right]}{\frac{d^{2}\left(\sum_{i=1}^{S}y^{i}\Psi^{i}\right)}{dx^{2}}}\right|_{x=a} \tag{3.177}$$

$$where\ \sum_{i=1}^{S}y^{i}\Psi^{i}=f(x_7)=P_1\left(\sum_{i=1}^{S}x_7^{i}\Psi^{i}\right)^{5}+P_2\left(\sum_{i=1}^{S}x_7^{i}\Psi^{i}\right)^{4}+P_3\left(\sum_{i=1}^{S}x_7^{i}\Psi^{i}\right)^{3}+P_4\left(\sum_{i=1}^{S}x_7^{i}\Psi^{i}\right)^{2}+P_5\left(\sum_{i=1}^{S}x_7^{i}\Psi^{i}\right)+P_6$$

K_3 is a function of radii of curvatures. Thus, Equation (3.176) and (3.177) are substituted into Equation (3.23) to find the stochastic K_3.

$$\sum_{i=1}^{S}K_3{}^{i}\Psi^{i}=\frac{1}{2}\left(\frac{1}{R^{w}}+\frac{1}{R^{r}}\right)=\frac{1}{2}\left(\frac{1}{\sum_{i=1}^{S}\left(R^{w}\right)^{i}\Psi^{i}}+\frac{1}{\sum_{i=1}^{S}\left(R^{r}\right)^{i}\Psi^{i}}\right) \tag{3.178}$$

Step 3. The stochastic Kalker's C coefficient

The *C* coefficients are expressed as the truncated Karhunen-Loeve expansions presented in Equation (3.179).

$$\sum_{i=1}^{S}C_{11}{}^{i}\Psi^{i},\ \sum_{i=1}^{S}C_{22}{}^{i}\Psi^{i},\ \sum_{i=1}^{S}C_{33}{}^{i}\Psi^{i},\ \sum_{i=1}^{S}C_{23}{}^{i}\Psi^{i} \tag{3.179}$$

Step 4. The stochastic creep forces

By substituting Equation (3.185) into Equation (3.33), the stochastic wheel velocities are found as presented in Equation (3.180).

$$\sum_{i=1}^{S}\left(V_{long}^{w}\right)^{i}\Psi^{i}=V_{train}+l_o\sum_{i=1}^{S}(x_{10})^{i}\Psi^{i},\ \sum_{i=1}^{S}\left(V_{lat}^{w}\right)^{i}\Psi^{i}=\sum_{i=1}^{S}x_8{}^{i}\Psi^{i}+V_{train}\sum_{i=1}^{S}(x_9)^{i}\Psi^{i},\ \sum_{i=1}^{S}\left(\Omega^{w}\right)^{i}\Psi^{i}=\omega\lambda+\sum_{i=1}^{S}(x_{10})^{i}\Psi^{i} \tag{3.180}$$

The stochastic creepage can be found by substituting Equation (3.63) into Equation (3.181).

$$\sum_{i=1}^{S}\left(\xi_{long}\right)^{i}\Psi^{i}=\frac{\sum_{i=1}^{S}\left(V_{long}^{w}\right)^{i}\Psi^{i}-V_{long}^{r}}{V_{train}},\quad \sum_{i=1}^{S}\left(\xi_{lat}\right)^{i}\Psi^{i}=\frac{\sum_{i=1}^{S}\left(V_{lat}^{w}\right)^{i}\Psi^{i}-V_{long}^{r}}{V_{train}},\quad \sum_{i=1}^{S}\left(\xi_{spin}\right)^{i}\Psi^{i}=\frac{\sum_{i=1}^{S}\left(\Omega^{w}\right)^{i}\Psi^{i}-\Omega^{r}}{V_{train}} \tag{3.181}$$

Equations (3.173), (3.179), and (3.181) are substituted into Equation (3.38) to obtain the stochastic creep forces of Equation (3.182).

$$\begin{aligned}
&\sum_{i=1}^{S}F_{long}{}^{i}\Psi^{i}=-G\left(\sum_{i=1}^{S}a^{i}\Psi^{i}\right)\left(\sum_{i=1}^{S}b^{i}\Psi^{i}\right)\left(\sum_{i=1}^{S}C_{11}{}^{i}\Psi^{i}\right)\left(\sum_{i=1}^{S}\xi_{long}{}^{i}\Psi^{i}\right)\\
&\sum_{i=1}^{S}F_{lat}{}^{i}\Psi^{i}=-G\left(\sum_{i=1}^{S}a^{i}\Psi^{i}\right)\left(\sum_{i=1}^{S}b^{i}\Psi^{i}\right)\left\{\left(\sum_{i=1}^{S}C_{22}{}^{i}\Psi^{i}\right)\left(\sum_{i=1}^{S}\xi_{lat}{}^{i}\Psi^{i}\right)+\sqrt{\left(\sum_{i=1}^{S}a^{i}\Psi^{i}\right)\left(\sum_{i=1}^{S}b^{i}\Psi^{i}\right)}\left(\sum_{i=1}^{S}C_{23}{}^{i}\Psi^{i}\right)\left(\sum_{i=1}^{S}\xi_{spin}{}^{i}\Psi^{i}\right)\right\}\\
&\sum_{i=1}^{S}M_{spin}{}^{i}\Psi^{i}=-G\left(\sum_{i=1}^{S}a^{i}\Psi^{i}\right)\left(\sum_{i=1}^{S}b^{i}\Psi^{i}\right)\left\{-\sqrt{\left(\sum_{i=1}^{S}a^{i}\Psi^{i}\right)\left(\sum_{i=1}^{S}b^{i}\Psi^{i}\right)}\left(\sum_{i=1}^{S}C_{23}{}^{i}\Psi^{i}\right)\left(\sum_{i=1}^{S}\xi_{lat}{}^{i}\Psi^{i}\right)+\left(\sum_{i=1}^{S}a^{i}\Psi^{i}\right)\left(\sum_{i=1}^{S}b^{i}\Psi^{i}\right)\left(\sum_{i=1}^{S}C_{33}{}^{i}\Psi^{i}\right)\left(\sum_{i=1}^{S}\xi_{spin}{}^{i}\Psi^{i}\right)\right\}
\end{aligned} \tag{3.182}$$

Step 5. The stochastic ODEs

Equations (3.175) and (3.182) are substituted into Equation (3.40) to find the stochastic vertical and lateral contact forces and the stochastic moment with respect to the vertical axis (z).

$$\begin{aligned}
\sum_{i=1}^{S}F_{v}{}^{i}\Psi^{i}&=\left(\sum_{i=1}^{S}F_{n}{}^{i}\Psi^{i}\right)\cos\lambda-\left(\sum_{i=1}^{S}F_{lat}{}^{i}\Psi^{i}\right)\sin\lambda\\
\sum_{i=1}^{S}F_{l}{}^{i}\Psi^{i}&=\left(\sum_{i=1}^{S}F_{n}{}^{i}\Psi^{i}\right)\sin\lambda+\left(\sum_{i=1}^{S}F_{lat}{}^{i}\Psi^{i}\right)\cos\lambda\\
\sum_{i=1}^{S}M_{z}{}^{i}\Psi^{i}&=\left(\sum_{i=1}^{S}M_{spin}{}^{i}\Psi^{i}\right)\cos\lambda
\end{aligned} \tag{3.183}$$

Equation (3.183) and (3.185) are substituted into Equation (3.42) to find the stochastic ODEs.

$$
\begin{cases}
\sum_{i=1}^{S} \dot{x}_1{}^i\Psi^i = \left(\sum_{i=1}^{S} x_2{}^i\Psi^i\right) \\
\sum_{i=1}^{S} \dot{x}_2{}^i\Psi^i = -\dfrac{C_b\left(\left(\sum_{i=1}^{S} x_2{}^i\Psi^i\right)-\left(\sum_{i=1}^{S} x_4{}^i\Psi^i\right)\right)+K_b\left(\left(\sum_{i=1}^{S} x_1{}^i\Psi^i\right)-\left(\sum_{i=1}^{S} x_3{}^i\Psi^i\right)\right)}{M_b} \\
\sum_{i=1}^{S} \dot{x}_3{}^i\Psi^i = \left(\sum_{i=1}^{S} x_4{}^i\Psi^i\right) \\
\sum_{i=1}^{S} \dot{x}_4{}^i\Psi^i = \dfrac{C_b\left(\left(\sum_{i=1}^{S} x_2{}^i\Psi^i\right)-\left(\sum_{i=1}^{S} x_4{}^i\Psi^i\right)\right)+K_b\left(\left(\sum_{i=1}^{S} x_1{}^i\Psi^i\right)-\left(\sum_{i=1}^{S} x_3{}^i\Psi^i\right)\right)-\left(\sum_{i=1}^{S} F_v{}^i\Psi^i\right)}{M_w} \\
\sum_{i=1}^{S} \dot{x}_5{}^i\Psi^i = \left(\sum_{i=1}^{S} x_6{}^i\Psi^i\right) \\
\sum_{i=1}^{S} \dot{x}_6{}^i\Psi^i = \dfrac{\left(\sum_{i=1}^{S} F_v{}^i\Psi^i\right)-C_{track}\left(\left(\sum_{i=1}^{S} x_4{}^i\Psi^i\right)-\left(\sum_{i=1}^{S} x_6{}^i\Psi^i\right)\right)-K_{track}\left(\left(\sum_{i=1}^{S} x_3{}^i\Psi^i\right)-\left(\sum_{i=1}^{S} x_5{}^i\Psi^i\right)\right)}{M_r} \\
\sum_{i=1}^{S} \dot{x}_7{}^i\Psi^i = \left(\sum_{i=1}^{S} x_8{}^i\Psi^i\right) \\
\sum_{i=1}^{S} \dot{x}_8{}^i\Psi^i = \dfrac{\left(\sum_{i=1}^{S} F_l{}^i\Psi^i\right)-C_{lat}\left(\sum_{i=1}^{S} x_8{}^i\Psi^i\right)-K_{lat}\left(\sum_{i=1}^{S} x_7{}^i\Psi^i\right)}{M_w} \\
\sum_{i=1}^{S} \dot{x}_9{}^i\Psi^i = \left(\sum_{i=1}^{S} x_{10}{}^i\Psi^i\right) \\
\sum_{i=1}^{S} \dot{x}_{10}{}^i\Psi^i = \dfrac{\left(\sum_{i=1}^{S} M_z{}^i\Psi^i\right)-C_\theta\left(\sum_{i=1}^{S} x_{10}{}^i\Psi^i\right)-K_\theta\left(\sum_{i=1}^{S} x_9{}^i\Psi^i\right)}{J_w}
\end{cases}
\tag{3.184}
$$

By integrating Equation (3.184), the stochastic displacements and velocities can be found as follows:

$$
\begin{aligned}
&\sum_{i=1}^{S} x_1{}^i\Psi^i, \quad \sum_{i=1}^{S} x_3{}^i\Psi^i, \quad \sum_{i=1}^{S} x_5{}^i\Psi^i, \quad \sum_{i=1}^{S} x_7{}^i\Psi^i, \quad \sum_{i=1}^{S} x_9{}^i\Psi^i \\
&\sum_{i=1}^{S} x_2{}^i\Psi^i, \quad \sum_{i=1}^{S} x_4{}^i\Psi^i, \quad \sum_{i=1}^{S} x_6{}^i\Psi^i, \quad \sum_{i=1}^{S} x_8{}^i\Psi^i, \quad \sum_{i=1}^{S} x_{10}{}^i\Psi^i
\end{aligned}
\tag{3.185}
$$

Step 6. The stochastic CoF

Equations (3.173) and (3.179) are substituted into Equation (3.5) to find the stochastic longitudinal and lateral damping coefficients at the contact patch.

$$\sum_{i=1}^{S} c_{long\_contact}{}^{i}\Psi^{i} = \frac{E\left(\sum_{i=1}^{S} a^{i}\Psi^{i}\right)\left(\sum_{i=1}^{S} b^{i}\Psi^{i}\right)\left(\sum_{i=1}^{S} C_{11}{}^{i}\Psi^{i}\right)}{2(1+v)V_{train}}$$
$$\sum_{i=1}^{S} c_{lat\_contact}{}^{i}\Psi^{i} = \frac{E\left(\sum_{i=1}^{S} a^{i}\Psi^{i}\right)\left(\sum_{i=1}^{S} b^{i}\Psi^{i}\right)\left(\sum_{i=1}^{S} C_{22}{}^{i}\Psi^{i}\right)}{2(1+v)V_{train}} \tag{3.186}$$

All stochastic and deterministic dynamic parameters are substituted into Equation (3.4) and then the stochastic CoFs are obtained.

$$\sum_{i=i}^{S}\mu(t)^{i}\Psi^{i} = c_1\left(\frac{\left(\sum_{i=1}^{S} V^{*}(t)^{i}\Psi^{i}\right)}{\left(\sum_{i=i}^{S} R^{*}(t)^{i}\Psi^{i}\right)}\right)^{0.28} \underbrace{\frac{e^{-c_2\sqrt{\left(\sum_{i=1}^{S} V^{*}(t)^{i}\Psi^{i}\right)}}}{1+c_3\left(\frac{\left(\sum_{i=1}^{S} a^{i}\Psi^{i}\right)}{\left(\sum_{i=1}^{S} b^{i}\Psi^{i}\right)}\right)^{2}\left(\sum_{i=i}^{S} R^{*}(t)^{i}\Psi^{i}\right)}}_{Slip\ Component} + \underbrace{\frac{c_4}{1+c_5\left(\frac{\left(\sum_{i=1}^{S} a^{i}\Psi^{i}\right)}{\left(\sum_{i=1}^{S} b^{i}\Psi^{i}\right)}\right)^{2}\left(\sum_{i=i}^{S} R^{*}(t)^{i}\Psi^{i}\right)}}_{Stick\ Component} \tag{3.187}$$

$$where\ \sum_{i=1}^{S} c_{\tan}{}^{i}\Psi^{i} = \sqrt{\left(\sum_{i=1}^{S} c_{long\_contact}{}^{i}\Psi^{i}\right)^{2} + \left(\sum_{i=1}^{S} c_{lat\_contact}{}^{i}\Psi^{i}\right)^{2}},\quad \sum_{i=1}^{S} V^{*}(t)^{i}\Psi^{i} = \frac{V_{\tan}}{\left(\sum_{i=1}^{S} F_n{}^{i}\Psi^{i}\right)}\left(\sum_{i=1}^{S} c_{\tan}{}^{i}\Psi^{i}\right)$$

$$\sum_{i=1}^{S} T^{i}\Psi^{i} = \frac{-d\left(\sum_{i=1}^{S} h_o{}^{i}\Psi^{i}\right)\left(\sum_{i=1}^{S} b^{i}\Psi^{i}\right)}{\sigma_{\tan}\left(\sum_{i=1}^{S} a^{i}\Psi^{i}\right)},\qquad \sum_{i=i}^{S} R^{*}(t)^{i}\Psi^{i} = 1-e^{\left(\sum_{i=1}^{S} T^{i}\Psi^{i}\right)}$$

Uncertain Independent MARR, Track Stiffness, and Sleeper Distance

Independent MARR (r), track stiffness (K_{track}), and sleeper distance ($dist$) are considered as uncertain variables. Uncertain r, K_{track}, and $dist$ can be expressed using a truncated Karhunen-Loeve expansion as follows:

$$r = \sum_{i=1}^{S} r^{i}\Psi^{i},\quad K_{track} = \sum_{i=1}^{S} K_{track}{}^{i}\Psi^{i},\quad dist = \sum_{i=1}^{S} dist^{i}\Psi^{i} \tag{3.188}$$

Equation (3.188) propagates from the calculation of the normal force to the calculation of the CoF model following the steps presented below.

Step 1. The stochastic normal contact force

The stochastic roughness from Equation (3.188) and the stochastic wheel and rail displacements, x_3 and x_5, from Equation (3.200) are substituted into Equation (3.27) given Equation (3.189).

$$\sum_{i=1}^{S} h_o{}^i\Psi^i = \sum_{i=1}^{S} x_3{}^i\Psi^i - \sum_{i=1}^{S} x_5{}^i\Psi^i + \sum_{i=1}^{S} r^i\Psi^i \tag{3.189}$$

Then Equation (3.189) is substituted into Equation (3.26) to obtain the stochastic normal contact force as follows:

$$\sum_{i=1}^{S} F_n{}^i\Psi^i = K_H \left(\sum_{i=1}^{S} h_o{}^i\Psi^i \right)^{3/2} \tag{3.190}$$

Step 2. The stochastic semi-elliptical contact lengths

Equation (3.190) is substituted into Equation (3.20) to calculate the stochastic semi-elliptical contact lengths.

$$\begin{aligned} \sum_{i=1}^{S} L_1{}^i\Psi^i &= m\left(\frac{3\pi\left(K_1+K_2\right)}{4K_3} \sum_{i=1}^{S} F_n{}^i\Psi^i \right)^{1/3} = \sum_{i=1}^{S} a^i\Psi^i = m\left(\frac{3\pi\left(K_1+K_2\right)}{4K_3} \sum_{i=1}^{S} F_n{}^i\Psi^i \right)^{1/3} \\ \sum_{i=1}^{S} L_2{}^i\Psi^i &= n\left(\frac{3\pi\left(K_1+K_2\right)}{4K_3} \sum_{i=1}^{S} F_n{}^i\Psi^i \right)^{1/3} = \sum_{i=1}^{S} b^i\Psi^i = n\left(\frac{3\pi\left(K_1+K_2\right)}{4K_3} \sum_{i=1}^{S} F_n{}^i\Psi^i \right)^{1/3} \end{aligned} \tag{3.191}$$

Step 3. The stochastic Kalker's C coefficient

The C coefficients are expressed as the truncated Karhunen-Loeve expansions presented in Equation (3.192).

$$\sum_{i=1}^{S} C_{11}{}^i\Psi^i,\ \sum_{i=1}^{S} C_{22}{}^i\Psi^i,\ \sum_{i=1}^{S} C_{33}{}^i\Psi^i,\ \sum_{i=1}^{S} C_{23}{}^i\Psi^i \tag{3.192}$$

Step 4. The stochastic creep forces

By substituting Equation (3.200) into Equation (3.33), the stochastic wheel velocities are found as presented in Equation (3.192).

$$\sum_{i=1}^{S}\left(V_{long}^{w}\right)^{i}\Psi^{i}=V_{train}+l_{o}\sum_{i=1}^{S}\left(x_{10}\right)^{i}\Psi^{i},\ \sum_{i=1}^{S}\left(V_{lat}^{w}\right)^{i}\Psi^{i}=\sum_{i=1}^{S}x_{8}{}^{i}\Psi^{i}+V_{train}\sum_{i=1}^{S}\left(x_{9}\right)^{i}\Psi^{i},\ \sum_{i=1}^{S}\left(\Omega^{w}\right)^{i}\Psi^{i}=\omega\lambda+\sum_{i=1}^{S}\left(x_{10}\right)^{i}\Psi^{i} \tag{3.192}$$

The stochastic creepage can be found by substituting Equation (3.63) into Equation (3.193).

$$\sum_{i=1}^{S}\left(\xi_{long}\right)^{i}\Psi^{i}=\frac{\sum_{i=1}^{S}\left(V_{long}^{w}\right)^{i}\Psi^{i}-V_{long}^{r}}{V_{train}},\quad \sum_{i=1}^{S}\left(\xi_{lat}\right)^{i}\Psi^{i}=\frac{\sum_{i=1}^{S}\left(V_{lat}^{w}\right)^{i}\Psi^{i}-V_{long}^{r}}{V_{train}},\quad \sum_{i=1}^{S}\left(\xi_{spin}\right)^{i}\Psi^{i}=\frac{\sum_{i=1}^{S}\left(\Omega^{w}\right)^{i}\Psi^{i}-\Omega^{r}}{V_{train}} \tag{3.193}$$

Equations (3.191), (3.192), and (3.193) are substituted into Equation (3.38) to obtain the stochastic creep forces of Equation (3.194).

$$\begin{aligned}
&\sum_{i=1}^{S}F_{long}{}^{i}\Psi^{i}=-G\left(\sum_{i=1}^{S}a^{i}\Psi^{i}\right)\left(\sum_{i=1}^{S}b^{i}\Psi^{i}\right)\left(\sum_{i=1}^{S}C_{11}{}^{i}\Psi^{i}\right)\left(\sum_{i=1}^{S}\xi_{long}{}^{i}\Psi^{i}\right)\\
&\sum_{i=1}^{S}F_{lat}{}^{i}\Psi^{i}=-G\left(\sum_{i=1}^{S}a^{i}\Psi^{i}\right)\left(\sum_{i=1}^{S}b^{i}\Psi^{i}\right)\left\{\left(\sum_{i=1}^{S}C_{22}{}^{i}\Psi^{i}\right)\left(\sum_{i=1}^{S}\xi_{lat}{}^{i}\Psi^{i}\right)+\sqrt{\left(\sum_{i=1}^{S}a^{i}\Psi^{i}\right)\left(\sum_{i=1}^{S}b^{i}\Psi^{i}\right)}\left(\sum_{i=1}^{S}C_{23}{}^{i}\Psi^{i}\right)\left(\sum_{i=1}^{S}\xi_{spin}{}^{i}\Psi^{i}\right)\right\}\\
&\sum_{i=1}^{S}M_{spin}{}^{i}\Psi^{i}=-G\left(\sum_{i=1}^{S}a^{i}\Psi^{i}\right)\left(\sum_{i=1}^{S}b^{i}\Psi^{i}\right)\left\{-\sqrt{\left(\sum_{i=1}^{S}a^{i}\Psi^{i}\right)\left(\sum_{i=1}^{S}b^{i}\Psi^{i}\right)}\left(\sum_{i=1}^{S}C_{23}{}^{i}\Psi^{i}\right)\left(\sum_{i=1}^{S}\xi_{lat}{}^{i}\Psi^{i}\right)+\left(\sum_{i=1}^{S}a^{i}\Psi^{i}\right)\left(\sum_{i=1}^{S}b^{i}\Psi^{i}\right)\left(\sum_{i=1}^{S}C_{33}{}^{i}\Psi^{i}\right)\left(\sum_{i=1}^{S}\xi_{spin}{}^{i}\Psi^{i}\right)\right\}
\end{aligned} \tag{3.194}$$

Step 5. The stochastic ODEs

Equations (3.190) and (3.194) are substituted into Equation (3.40) to find the stochastic vertical and lateral contact forces and the stochastic moment with respect to the vertical axis (z).

$$\begin{aligned}
\sum_{i=1}^{S}F_{v}{}^{i}\Psi^{i}&=\left(\sum_{i=1}^{S}F_{n}{}^{i}\Psi^{i}\right)\cos\lambda-\left(\sum_{i=1}^{S}F_{lat}{}^{i}\Psi^{i}\right)\sin\lambda\\
\sum_{i=1}^{S}F_{l}{}^{i}\Psi^{i}&=\left(\sum_{i=1}^{S}F_{n}{}^{i}\Psi^{i}\right)\sin\lambda+\left(\sum_{i=1}^{S}F_{lat}{}^{i}\Psi^{i}\right)\cos\lambda\\
\sum_{i=1}^{S}M_{z}{}^{i}\Psi^{i}&=\left(\sum_{i=1}^{S}M_{spin}{}^{i}\Psi^{i}\right)\cos\lambda
\end{aligned} \tag{3.195}$$

Uncertain sleeper distance is used to calculate the stochastic rail mass of Equation (3.196) and it is substituted into Equation (3.8) to obtain the stochastic track excitation frequency of Equation (3.197).

$$\sum_{i=1}^{S} M_r{}^i\Psi^i = A \times density \times \sum_{i=1}^{S} dist^i\Psi^i \tag{3.196}$$

$$\sum_{i=1}^{S} f^i\Psi^i = \frac{2\pi V_{train}}{\sum_{i=1}^{S} dist^i\Psi^i} \tag{3.197}$$

Thus, the stochastic damping coefficient is calculated as below.

$$\sum_{i=1}^{S} C_{track}{}^i\Psi^i = \sum_{i=1}^{S} C_{pad}{}^i\Psi^i + \sum_{i=1}^{S} C_{sleeper}{}^i\Psi^i + C_{ballast}$$

whrer

$$\sum_{i=1}^{S} C_{pad}{}^i\Psi^i = 0.5C_{pad}\cos\left(\left(\sum_{i=1}^{S} f^i\Psi^i\right)\cdot t\right) + 0.5C_{pad},\ \sum_{i=1}^{S} C_{sleeper}{}^i\Psi^i = 0.5C_{sleeper}\cos\left(\left(\sum_{i=1}^{S} f^i\Psi^i\right)\cdot t\right) + 0.5C_{sleeper} \tag{3.198}$$

Equation (3.188), (3.195), (3.196), (3.198) and (3.200) are substituted into Equation (3.42) to find the stochastic ODEs.

$$\begin{cases}
\sum_{i=1}^{S}\dot{x}_1{}^i\Psi^i = \left(\sum_{i=1}^{S} x_2{}^i\Psi^i\right) \\
\sum_{i=1}^{S}\dot{x}_2{}^i\Psi^i = -\dfrac{C_b\left(\left(\sum_{i=1}^{S} x_2{}^i\Psi^i\right)-\left(\sum_{i=1}^{S} x_4{}^i\Psi^i\right)\right)+K_b\left(\left(\sum_{i=1}^{S} x_1{}^i\Psi^i\right)-\left(\sum_{i=1}^{S} x_3{}^i\Psi^i\right)\right)}{M_b} \\
\sum_{i=1}^{S}\dot{x}_3{}^i\Psi^i = \left(\sum_{i=1}^{S} x_4{}^i\Psi^i\right) \\
\sum_{i=1}^{S}\dot{x}_4{}^i\Psi^i = \dfrac{C_b\left(\left(\sum_{i=1}^{S} x_2{}^i\Psi^i\right)-\left(\sum_{i=1}^{S} x_4{}^i\Psi^i\right)\right)+K_b\left(\left(\sum_{i=1}^{S} x_1{}^i\Psi^i\right)-\left(\sum_{i=1}^{S} x_3{}^i\Psi^i\right)\right)-\left(\sum_{i=1}^{S} F_v{}^i\Psi^i\right)}{M_w} \\
\sum_{i=1}^{S}\dot{x}_5{}^i\Psi^i = \left(\sum_{i=1}^{S} x_6{}^i\Psi^i\right) \\
\sum_{i=1}^{S}\dot{x}_6{}^i\Psi^i = \dfrac{\left(\sum_{i=1}^{S} F_v{}^i\Psi^i\right)-\left(\sum_{i=1}^{S} C_{track}{}^i\Psi^i\right)\left(\left(\sum_{i=1}^{S} x_4{}^i\Psi^i\right)-\left(\sum_{i=1}^{S} x_6{}^i\Psi^i\right)\right)-\left(\sum_{i=1}^{S} K_{track}{}^i\Psi^i\right)\left(\left(\sum_{i=1}^{S} x_3{}^i\Psi^i\right)-\left(\sum_{i=1}^{S} x_5{}^i\Psi^i\right)\right)}{\sum_{i=1}^{S} M_r{}^i\Psi^i} \\
\sum_{i=1}^{S}\dot{x}_7{}^i\Psi^i = \left(\sum_{i=1}^{S} x_8{}^i\Psi^i\right) \\
\sum_{i=1}^{S}\dot{x}_8{}^i\Psi^i = \dfrac{\left(\sum_{i=1}^{S} F_l{}^i\Psi^i\right)-C_{lat}\left(\sum_{i=1}^{S} x_8{}^i\Psi^i\right)-K_{lat}\left(\sum_{i=1}^{S} x_7{}^i\Psi^i\right)}{M_w} \\
\sum_{i=1}^{S}\dot{x}_9{}^i\Psi^i = \left(\sum_{i=1}^{S} x_{10}{}^i\Psi^i\right) \\
\sum_{i=1}^{S}\dot{x}_{10}{}^i\Psi^i = \dfrac{\left(\sum_{i=1}^{S} M_z{}^i\Psi^i\right)-C_\theta\left(\sum_{i=1}^{S} x_{10}{}^i\Psi^i\right)-K_\theta\left(\sum_{i=1}^{S} x_9{}^i\Psi^i\right)}{J_w}
\end{cases} \tag{3.199}$$

By integrating Equation (3.199), the stochastic displacements and velocities can be found as follows:

$$\begin{aligned}&\sum_{i=1}^{S} x_1{}^i\Psi^i, \quad \sum_{i=1}^{S} x_3{}^i\Psi^i, \quad \sum_{i=1}^{S} x_5{}^i\Psi^i, \quad \sum_{i=1}^{S} x_7{}^i\Psi^i, \quad \sum_{i=1}^{S} x_9{}^i\Psi^i \\ &\sum_{i=1}^{S} x_2{}^i\Psi^i, \quad \sum_{i=1}^{S} x_4{}^i\Psi^i, \quad \sum_{i=1}^{S} x_6{}^i\Psi^i, \quad \sum_{i=1}^{S} x_8{}^i\Psi^i, \quad \sum_{i=1}^{S} x_{10}{}^i\Psi^i\end{aligned} \tag{3.200}$$

Step 6. The stochastic CoF

Equations (3.191) and (3.192) are substituted into Equation (3.5) to find the stochastic longitudinal and lateral damping coefficients at the contact patch.

$$\begin{aligned}\sum_{i=1}^{S} c_{long\_contact}{}^i\Psi^i &= \frac{E\left(\sum_{i=1}^{S} a^i\Psi^i\right)\left(\sum_{i=1}^{S} b^i\Psi^i\right)\left(\sum_{i=1}^{S} C_{11}{}^i\Psi^i\right)}{2(1+\nu)V_{train}} \\ \sum_{i=1}^{S} c_{lat\_contact}{}^i\Psi^i &= \frac{E\left(\sum_{i=1}^{S} a^i\Psi^i\right)\left(\sum_{i=1}^{S} b^i\Psi^i\right)\left(\sum_{i=1}^{S} C_{22}{}^i\Psi^i\right)}{2(1+\nu)V_{train}}\end{aligned} \tag{3.201}$$

All stochastic and deterministic dynamic parameters are substituted into Equation (3.4) and then the stochastic CoFs are obtained.

$$\sum_{i=i}^{S} \mu(t)^i\Psi^i = c_1\left(\frac{\left(\sum_{i=1}^{S} V^*(t)^i\Psi^i\right)}{\left(\sum_{i=i}^{S} R^*(t)^i\Psi^i\right)}\right)^{0.28} \underbrace{\frac{e^{-c_2\sqrt{\left(\sum_{i=1}^{S} V^*(t)^i\Psi^i\right)}}}{1+c_3\left(\frac{\left(\sum_{i=1}^{S} a^i\Psi^i\right)}{\left(\sum_{i=1}^{S} b^i\Psi^i\right)}\right)^2\left(\sum_{i=i}^{S} R^*(t)^i\Psi^i\right)}}_{Slip\ Component} + \underbrace{\frac{c_4}{1+c_5\left(\frac{\left(\sum_{i=1}^{S} a^i\Psi^i\right)}{\left(\sum_{i=1}^{S} b^i\Psi^i\right)}\right)^2\left(\sum_{i=i}^{S} R^*(t)^i\Psi^i\right)}}_{Stick\ Component} \tag{3.202}$$

$$where \quad \sum_{i=1}^{S} c_{\tan}{}^i\Psi^i = \sqrt{\left(\sum_{i=1}^{S} c_{long\_contact}{}^i\Psi^i\right)^2 + \left(\sum_{i=1}^{S} c_{lat\_contact}{}^i\Psi^i\right)^2}, \quad \sum_{i=1}^{S} V^*(t)^i\Psi^i = \frac{V_{\tan}}{\left(\sum_{i=1}^{S} F_n{}^i\Psi^i\right)}\left(\sum_{i=1}^{S} c_{\tan}{}^i\Psi^i\right)$$

$$\sum_{i=1}^{S} T^i\Psi^i = \frac{-d\left(\sum_{i=1}^{S} h_o{}^i\Psi^i\right)\left(\sum_{i=1}^{S} b^i\Psi^i\right)}{\sigma_{\tan}\left(\sum_{i=1}^{S} a^i\Psi^i\right)}, \qquad \sum_{i=i}^{S} R^*(t)^i\Psi^i = 1-e^{\left(\sum_{i=1}^{S} T^i\Psi^i\right)}$$

Chapter 4. Results and Discussion

This chapter discusses several simulation tests for the wheel-rail deterministic dynamic model and for the poly-chaos model using different uncertain parameters. A qualitative validation of simulation using FFT analysis is included. In this chapter, section 4.1 illustrates simulation results for the deterministic wheel-rail dynamic model with CoF. Section 4.2 presents simulation results for the poly-chaos model including cases with one, two, and three uncertain parameters. Section 4.3 briefly introduces FFT analysis results for the deterministic rail displacement and for the rail displacement with uncertainties for the qualitative validation of the simulation model.

4.1 Deterministic Wheel-Rail Model

The wheel-rail dynamic model runs at 20 *m/sec* on the rail with rail roughness as an input excitation source. Some specific parameter values used in this study are introduced in Table 3.1 and detailed explanations of the model are in section 3.2. All of the parameters used in this study are listed below and do not change through the course of this study.

1. The excitation frequency of rail roughness from Equation (3.8) is 80π *Hz*, and the maximum amplitude of rail roughness (MARR) (r_{max}) is 20 μm. Rail roughness is expressed as follows:

$$r = r_{\max} \sin\left(f \cdot t\right) = \left(20\times10^{-6}\right)\sin\left(80\pi \cdot t\right)$$

   Only vertical rail roughness is modeled in this study. It is assumed that there is no change in rail roughness amplitude in the lateral direction.
2. It is assumed that the wheel and the rail are made of the same material (steel). The Poisson ratio is 0.3; Young's modulus is 2.1×10^{11} *N/m*; steel density is 7850 kg/m^3; and shear modulus of rigidity is 0.77×10^{11} *N/m*.
3. The mass of the train body, a half wheelset, and the rail are 4500 *kg*, 800 *kg*, and 1549.119 *kg*, respectively. Mass moment of inertia for the half wheelset is 480 $kg\cdot m^2$.

4. The track consists of rail pads, sleeper, and ballast. Track stiffness and damping from Equations (3.6) and (3.7) are shown in Table 4.1.

Table 4.1 Track stiffness and track damping coefficients

$K_{pad} = 55\times10^6 \cos(f_t \cdot t) + 55\times10^6\ N/m$	$C_{pad} = 49\times10^3 \cos(f_t \cdot t) + 49\times10^3\ N\cdot s/m$
$K_{sleeper} = 50\times10^6 \cos(f_t \cdot t) + 50\times10^6\ N/m$	$C_{sleeper} = 49\times10^3 \cos(f_t \cdot t) + 49\times10^3\ N\cdot s/m$
$K_{ballast} = 200\times10^6\ N/m$	$C_{ballast} = 0.245\times10^6\ N\cdot s/m$
$K_{track} = K_{pad} + K_{sleeper} + K_{ballast}$	$C_{track} = C_{pad} + C_{sleeper} + C_{ballast}$

5. The suspension stiffness is 550×10^3 *N/m*, 2300×10^3 *N/m*, and 2500×10^3 *N/m* for the vertical, lateral, and yaw directions, respectively. Suspension damping is 35×10^3 *Ns/m*, 10×10^3 *Ns/m*, and 5×10^3 *Ns/m* for the vertical direction, the lateral direction, and yaw direction, respectively. The track excitation frequency (f_t) is 66.7π *Hz*.
6. Sleeper distance is 0.6 *m* for concrete, and the half-gage length is 0.72365 *m*.
7. Gravitational acceleration is 9.81 *m/s*.
8. Conicity is 2.86°.
9. Mean radius of curvature for the wheel is $r_o = 0.46$ *m*.
10. Initial conditions for the ODEs, as shown in Equation (3.42) and Figure 3.13, are arbitrarily selected and they are shown below.

$$[z_b,\ \dot{z}_b,\ z_w,\ \dot{z}_w,\ z_r,\ \dot{z}_r,\ y,\ \dot{y},\ \psi,\ \dot{\psi}] = [0,\ 0.4,\ 0,\ 0.4,\ 0,\ 0.4,\ 0,\ 0.4,\ 0,\ 0.4]$$

In this section, the results of the deterministic wheel-rail dynamics model will be discussed in the order of their calculation as shown by the flow chart of Figure 3.14. The total CoF result is at steady state after 2 sec without any periodic motion. Thus, the train's running time is set as 4 *sec* to display dynamic changes as well as steady state regions for this study.

The wheel-rail dynamic model runs at 20 *m/s* for 4 *sec* on the rail. Sampling rate is set as 525 *Hz*, i.e., 2100 samples for 4 *sec*. In this study, no uncertain variable is considered, and all parameters are deterministic. Rail roughness for 0.1 *sec*, an excitation source, is displayed in Figure 4.1. It repeats for 4 *sec*. As mentioned earlier, the periodic rail roughness is the only excitation source.

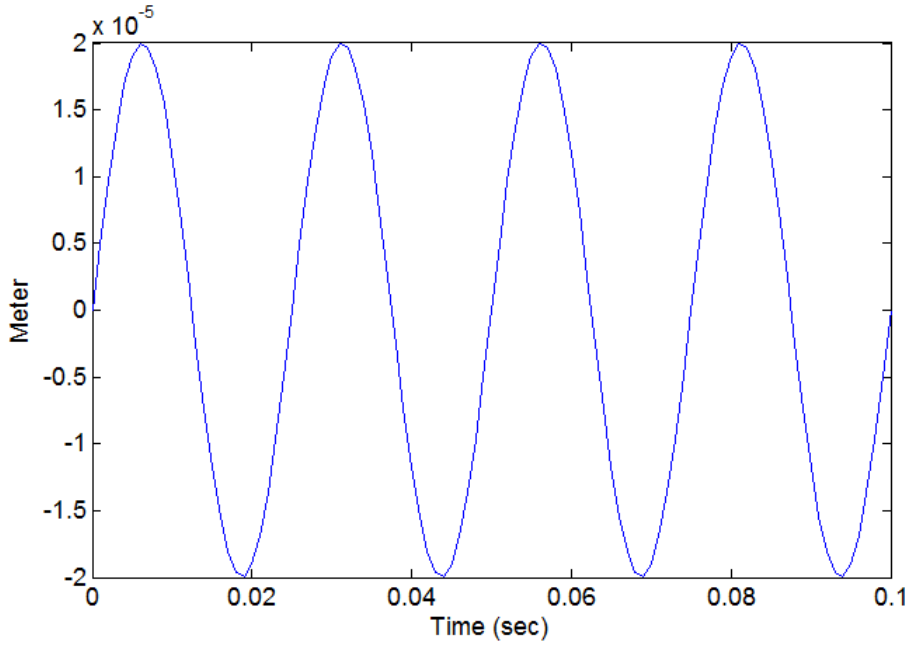

Figure 4.1 Rail roughness for 0.1 *sec*

Vertical displacements for the train body, wheel, and rail are displayed in Figure 4.2. Body displacements settle to zero at around 2 *sec* of simulation because of vertical suspension damping, as displayed in Figure 4.2 (a). The maximum displacement is less than 5 *cm* due to the initial body velocity and suspension stiffness, it decreases with time and becomes steady at around 2 *sec*. The displacement of the body does not show a high frequency movement since the suspension may act as a low-pass filter. The wheel and rail displacements generally follow the rail roughness input, although their amplitudes are not equal. Both displacements show high frequency movements, i.e., 40.25 Hz (from 1.7 *sec* to 4 *sec*) for both displacements. The average wheel displacement (1.3×10^{-5} *m*) is relatively larger than that of the rail (-5.6×10^{-7} *m*) due to the body and rail dynamics. The average rail displacement is very close to zero since the dynamic force from the wheel is only applied to the rail.

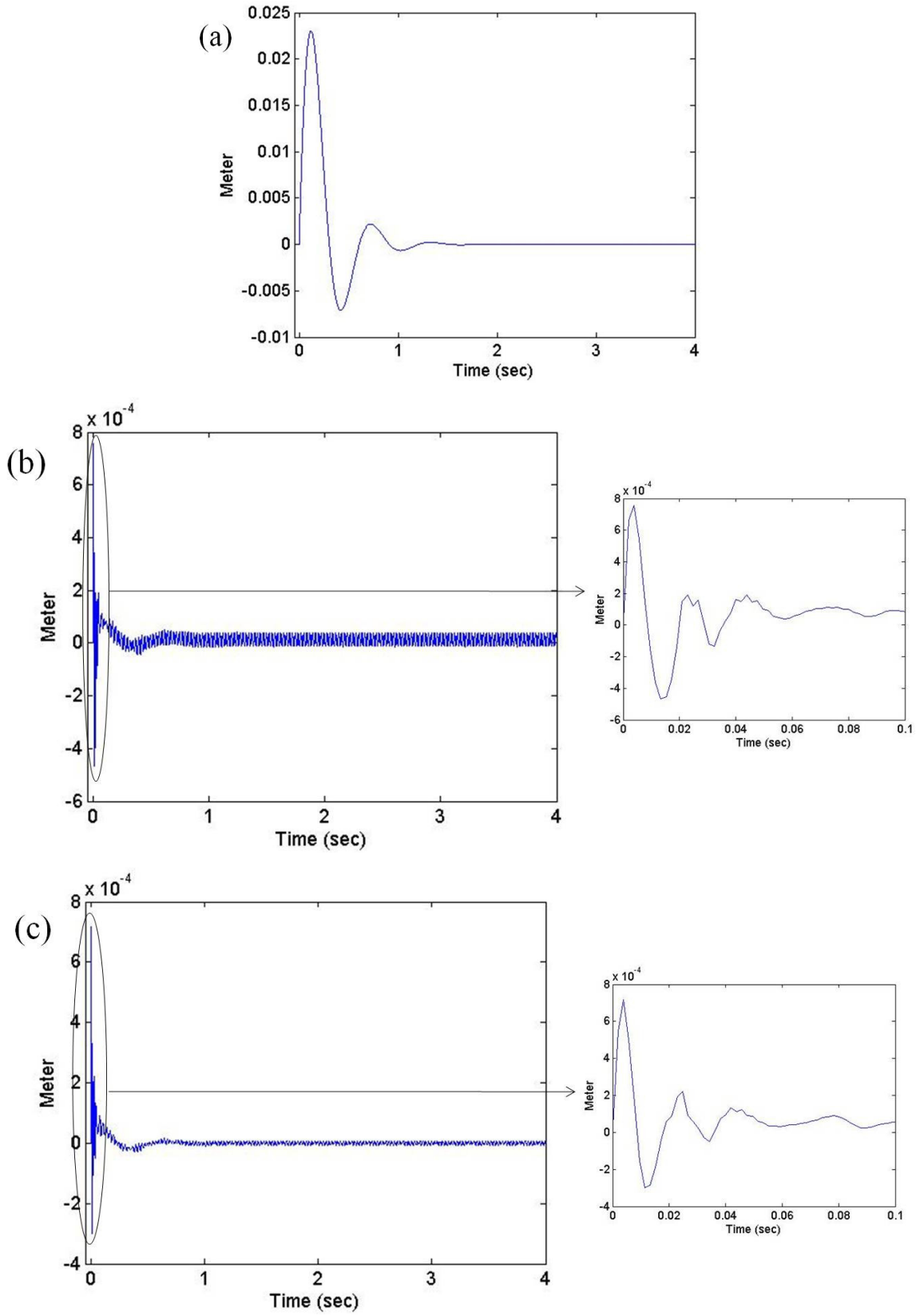

Figure 4.2 Vertical displacements of (a) the body, (b) the wheel, and (c) the rail

Lateral displacements and yaw angle changes of the wheel are illustrated in Figure 4.3. They are not influenced by rail roughness since it was assumed that the rail roughness had no change in the lateral direction. The maximum amplitude of the lateral wheel displacements is 2.2 *mm* due to the lateral suspension stiffness and initial velocity. Lateral displacements of the wheel decrease with time, however they never settle to zero as small scale oscillations ($\pm 6.2\times10^{-7}$ *m*) persist. Yaw angle changes of the wheel demonstrate similar behavior. The maximum yaw angle is 0.283° due to the suspension stiffness and initial velocity. Yaw angle decreases with time and asymptotically approaches zero within the first 2 *sec*, however very small oscillations ($\pm 4\times10^{-8}$ °) persist.

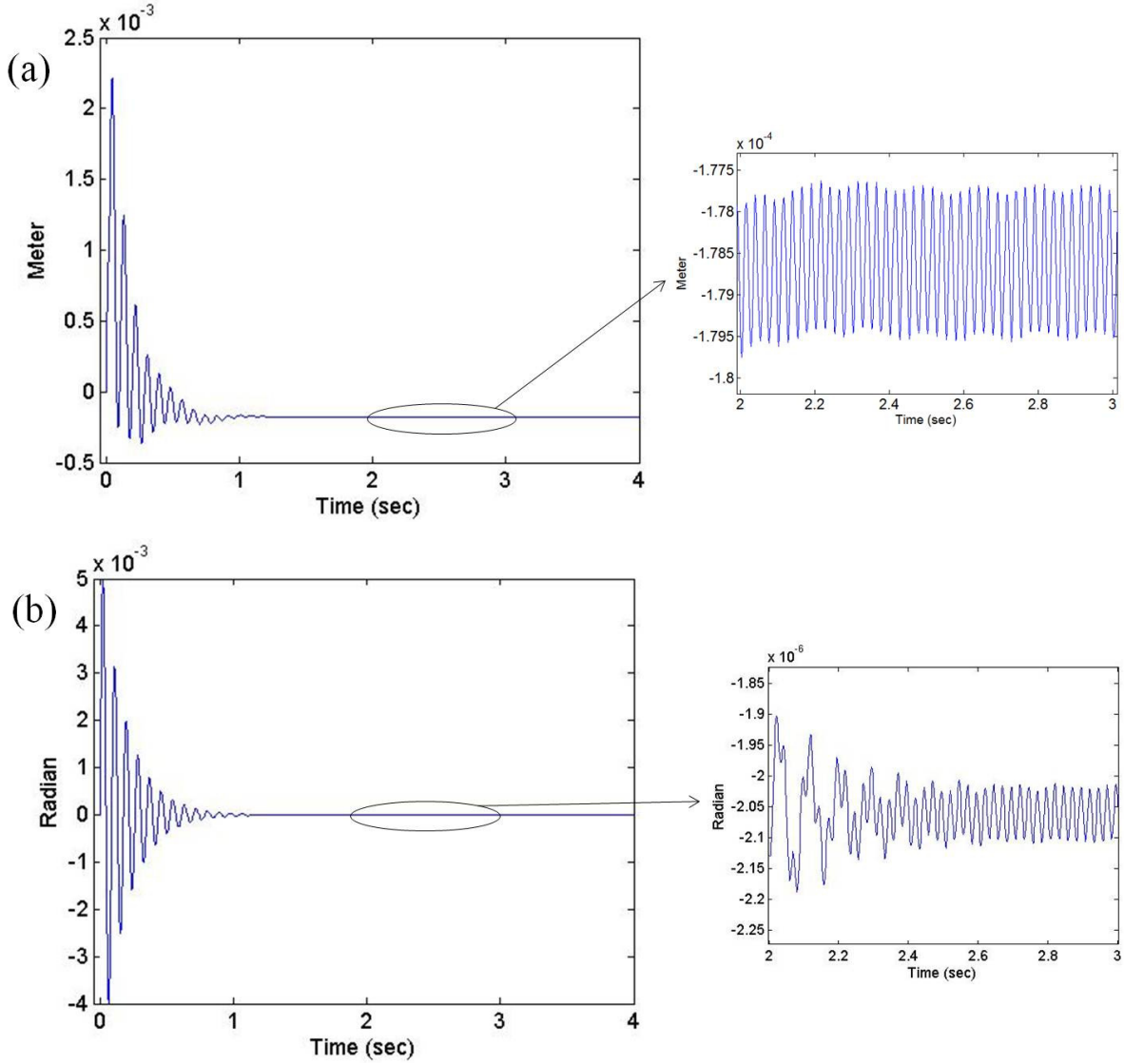

Figure 4.3 (a) Lateral displacements of the wheel and (b) yaw angle changes of the wheel

Radii of curvature are displayed in Figure 4.4. Results show no effect of rail roughness since radii of curvature are not a function of rail roughness but a function of the lateral displacement of the wheel. Initial values of R_w and R_r are 0.46 m and 7.259 m. R_r is much greater than R_w yielding a contact patch shaped like that shown in Figure 3.7 (b). Radius of curvature for the wheel decreases and radius of curvature for the rail increases with time and continue oscillating within a very small range ($\pm 3\times10^{-8}$ m and $\pm 1.3\times10^{-4}$ m, respectively).

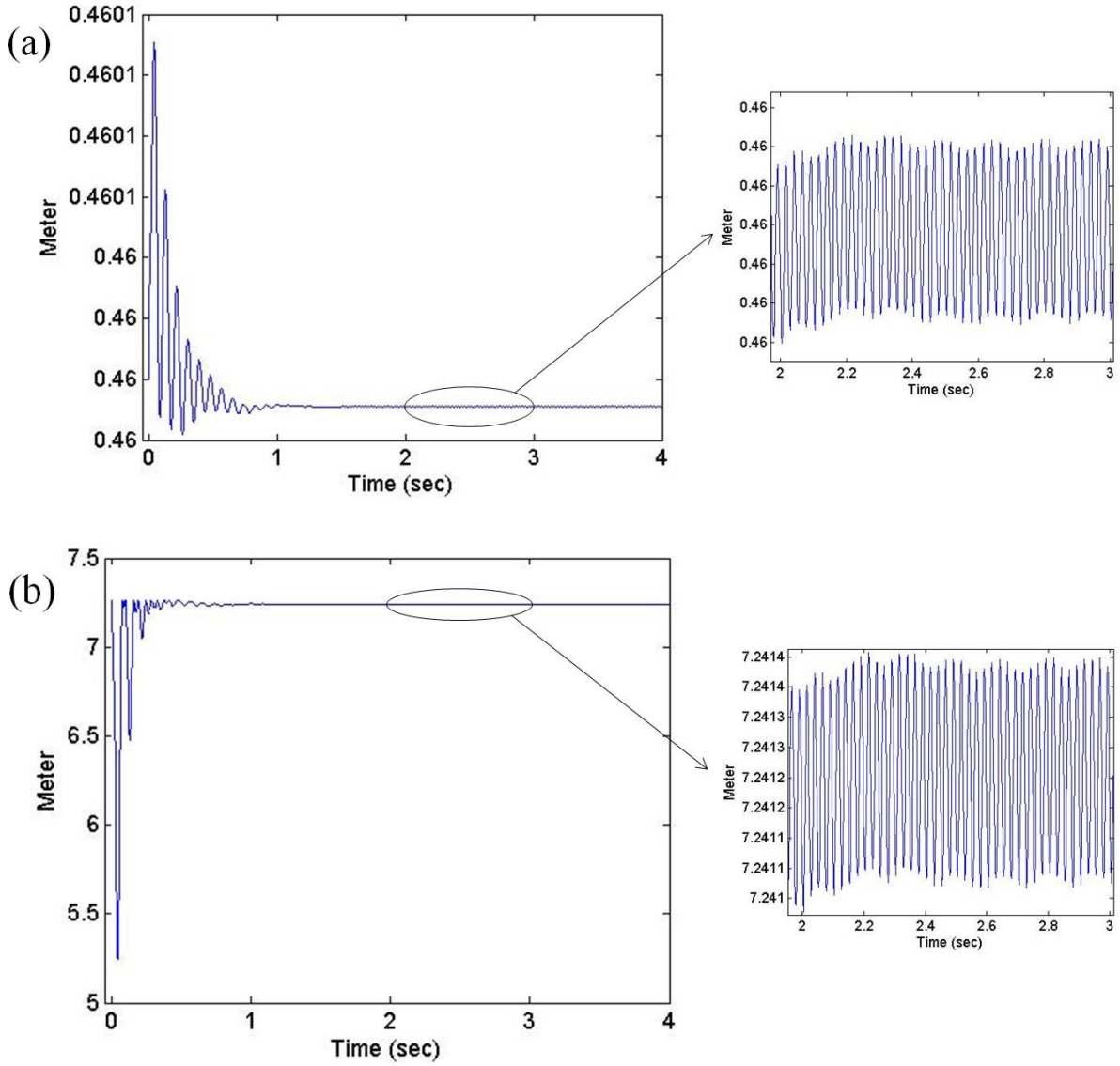

Figure 4.4 Radii of curvature for (a) the wheel and (b) the rail

The normal contact force is a function of the relative wheel-rail vibration and Hertzian stiffness based on Equation (3.26). K_H is oscillating within a very small range (1.54484×10^{11} *N/m*). Thus, the normal contact force is mostly affected by relative wheel-rail vibrations, as presented in Figure 4.5. Frequency of h_o between 1.7 *sec* and 4 *sec* is 40.25 *Hz* the same as the frequency of the wheel and rail displacements.

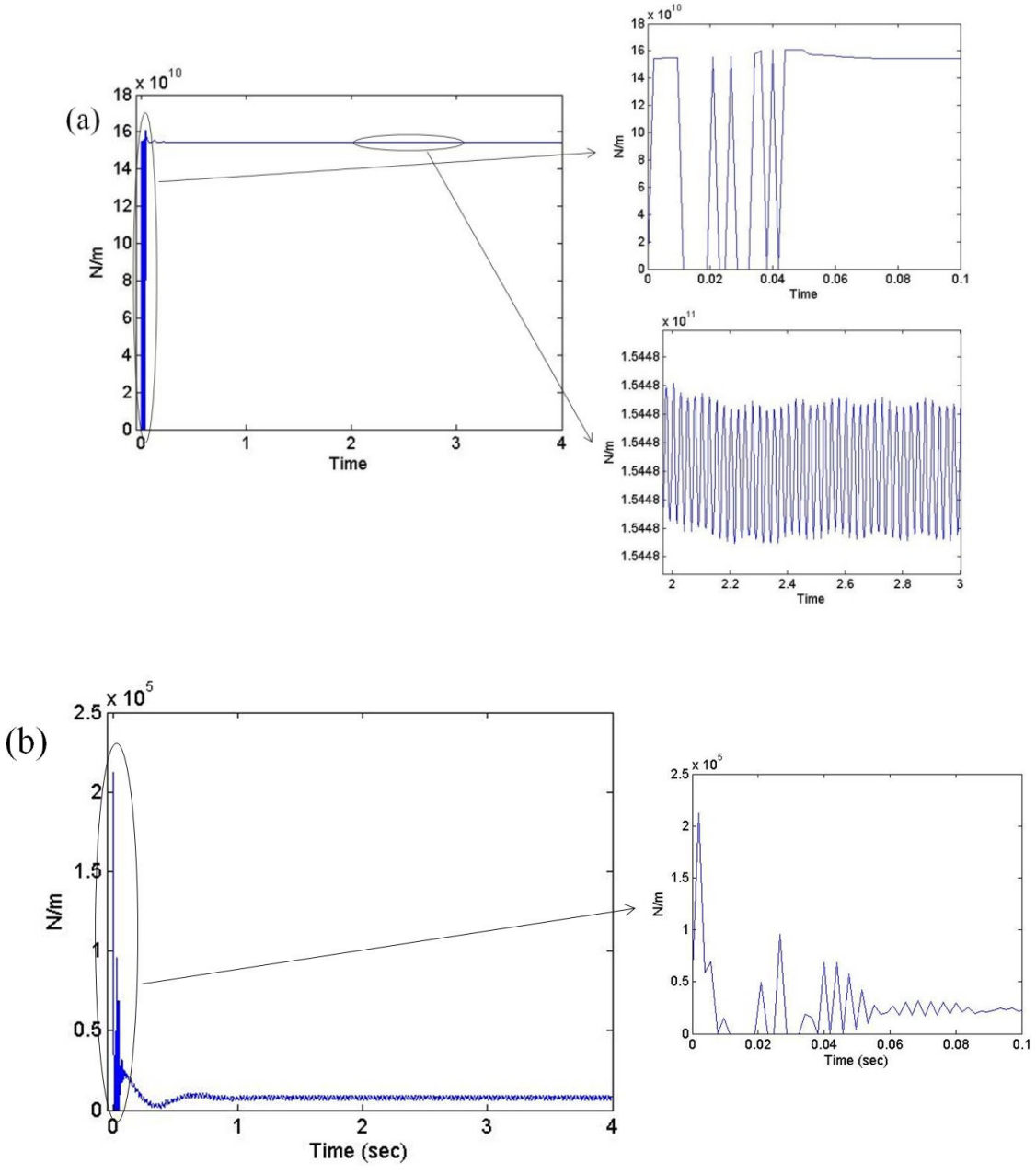

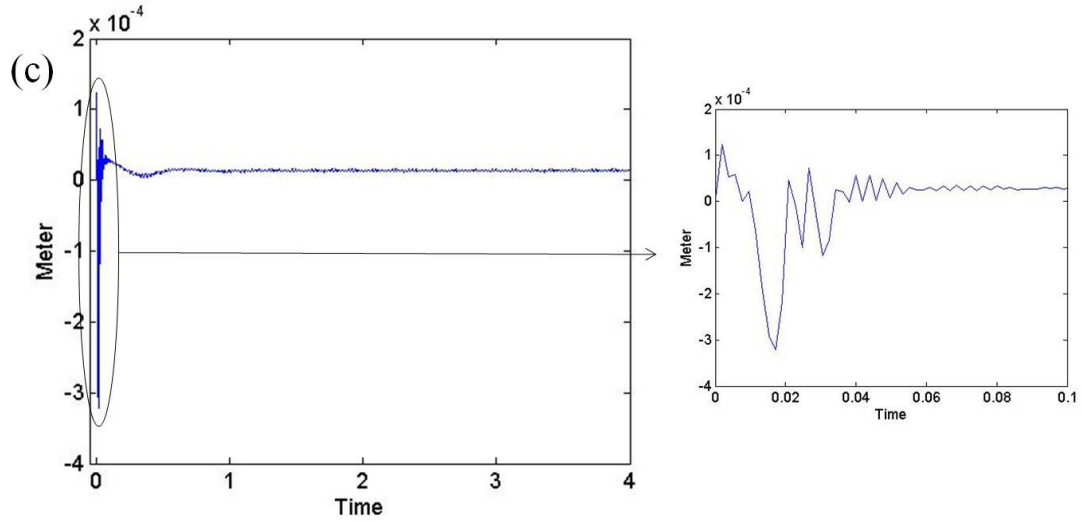

Figure 4.5 (a) Hertzian stiffness, (b) normal contact force, and (c) relative wheel-rail vibration

Based on Equations (3.20)-(3.25), semi-elliptical contact lengths are a function of the normal contact force and the radii of curvature of the wheel and rail. Figure 4.6 shows that the semi-elliptical contact lengths follow changes of the normal contact force since the radii of curvature change very little, as illustrated in Figure 4.4 through Figure 4.6. The trends of a and b are very similar to each other, however b has greater magnitude than a since R_r is larger than R_w, as shown in Figure 4.4.

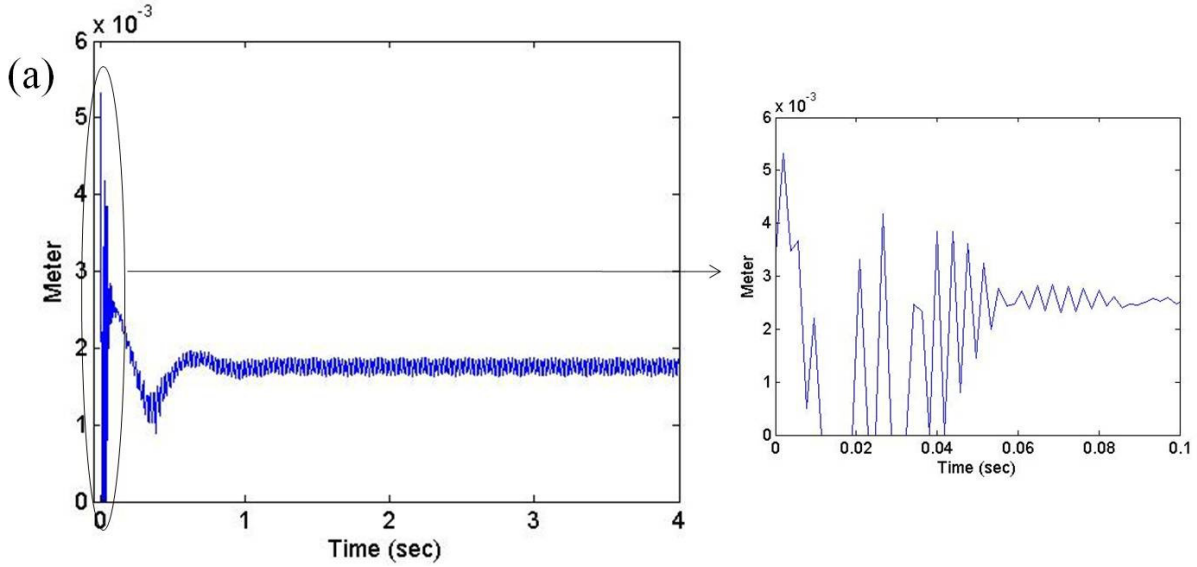

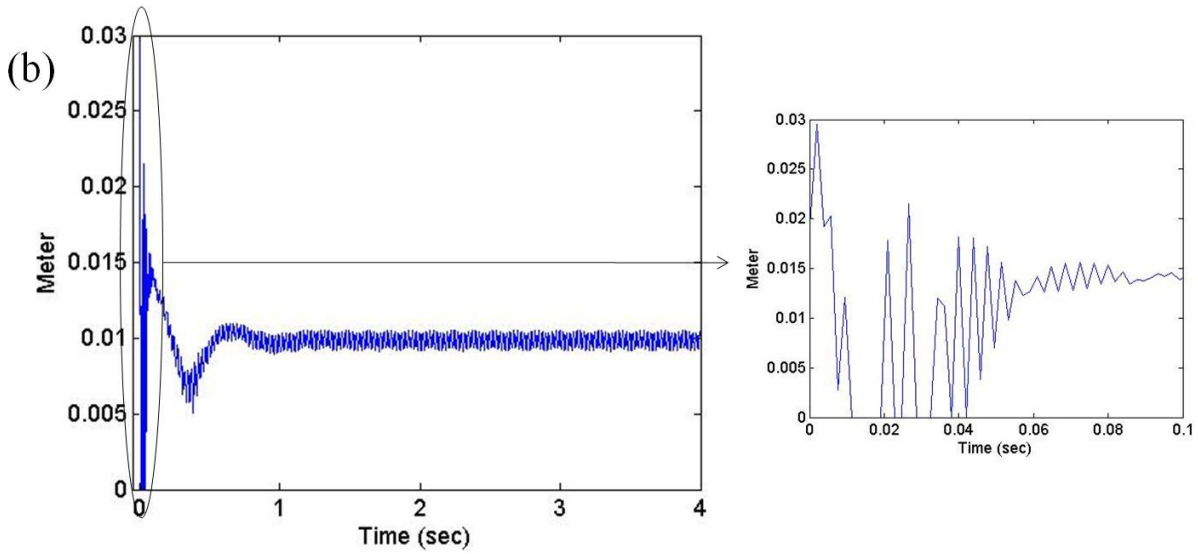

Figure 4.6 Semi-elliptical contact lengths: (a) *a* and (b) *b*

Figure 4.7 illustrates creepage. The three types of creepage each appear to approach a constant value; however they are oscillating within very small ranges (1.9×10^{-5} $\pm2.4\times10^{-7}$ for longitudinal creepage, 2×10^{-6} $\pm7.9\times10^{-6}$ for lateral creepage, and 0.11 $\pm4\times10^{-7}$ for spin creepage). Figure 4.3 (b) shows that the change in yaw angle over time is minimal. The changes of the yaw angular velocity are also minimal over time. Thus, the longitudinal wheel velocity is almost the same as the train velocity, with minor oscillations. Figure 4.4 (b) demonstrates that the wheel radius of curvature does not change much and is almost the same as r_o. This means that the longitudinal rail velocity is almost the same as the train velocity with minor oscillation, as described in Equation (3.34). Thus, the sliding velocity is very close to zero. It follows that the longitudinal creepage is almost zero, however it also demonstrates minor oscillation, as displayed in Figure 4.7 (a).

Figure 4.3 shows that lateral displacements and yaw angles have minor oscillations that are close to zero. Thus, Equation (3.33) describes that the wheel lateral velocity over time is almost zero with minor oscillations, and the rail lateral velocity is zero by definition in Equation (3.34). Thus, the lateral creepage behaves in the same manner as the longitudinal creepage. The wheel conicity is a constant and the wheel angular velocity (ω) does not change much according to the wheel radius of curvature change. The angular velocity is defined as the train velocity

divided by the effective wheel radius of curvature ($\omega = V_{train} / R_w$). The rail angular velocity is zero by definition in Equation (3.34). Thus, the spin creepage has small oscillations with respect to $\omega_o \lambda$ with changes in ω. The term ω_o is the mean angular velocity when $R_w = r_o$, as shown in Figure 4.7 (c).

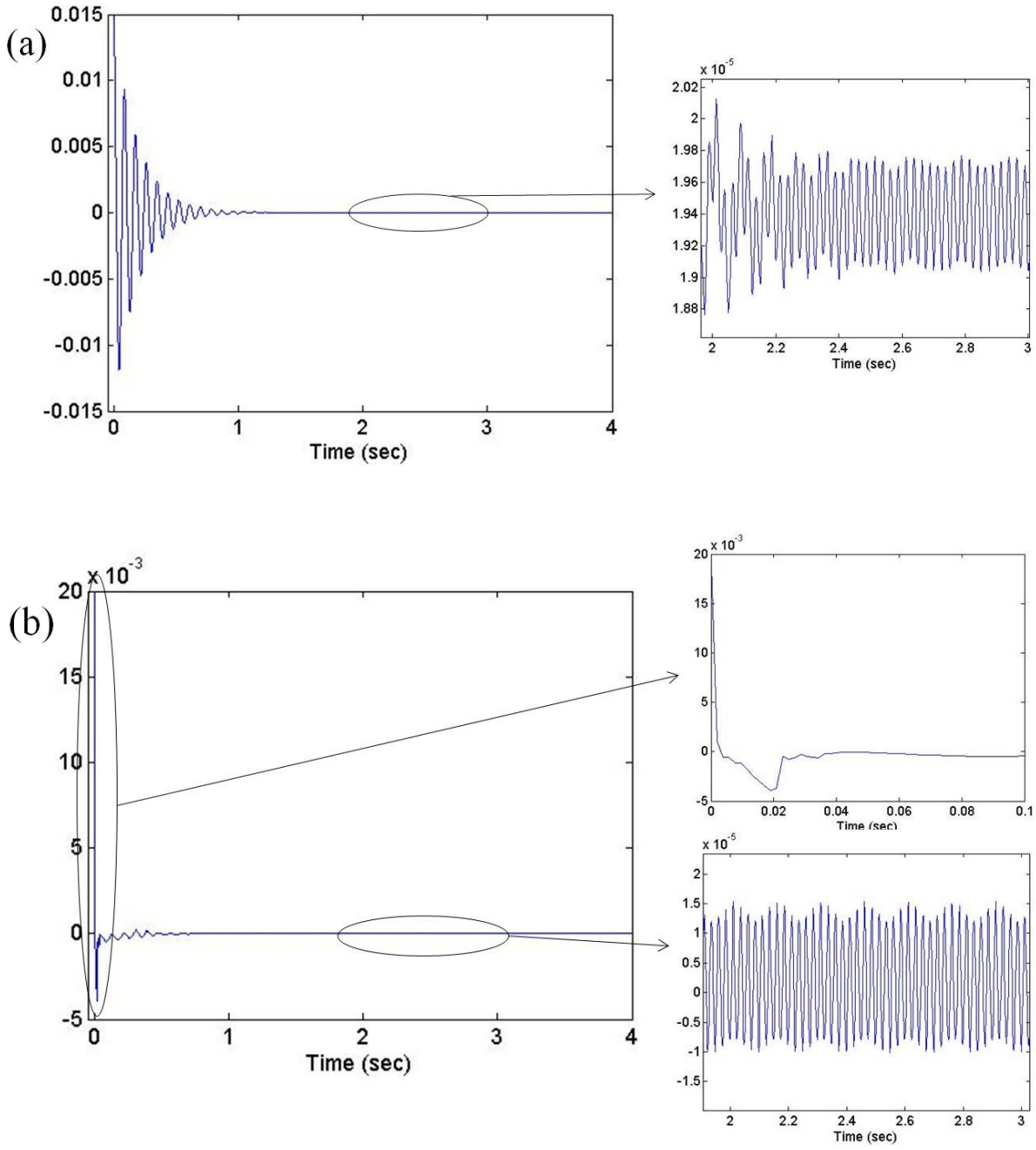

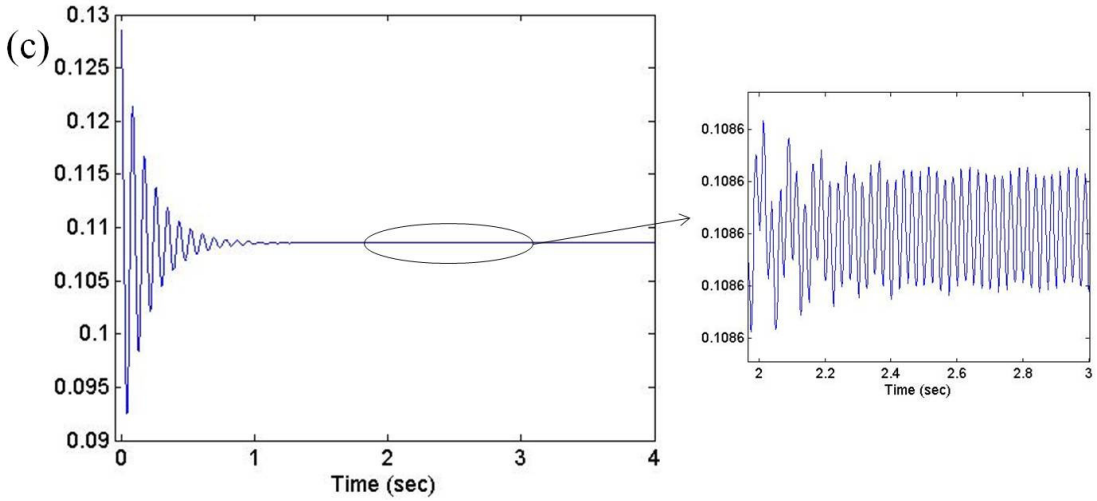

Figure 4.7 Creepages: (a) the longitudinal creepage, (b) the lateral creepage, and (c) the spin creepage

Creep forces are shown in Figure 4.8 and Figure 4.9. The shapes of the creep force plots are very similar to those for creepage since creep forces are a function of creepage, as shown in Equation (3.38). Longitudinal and lateral creep forces settle down at -109 *N* and -807 *N*, respectively, and oscillate in very small ranges ±8.6 *N* and ±69.9 *N*, respectively, like both longitudinal and lateral creepage. The spin creep force settles down at -5.21 *Nm* and oscillates in the range ±70 *N* like the spin creepage.

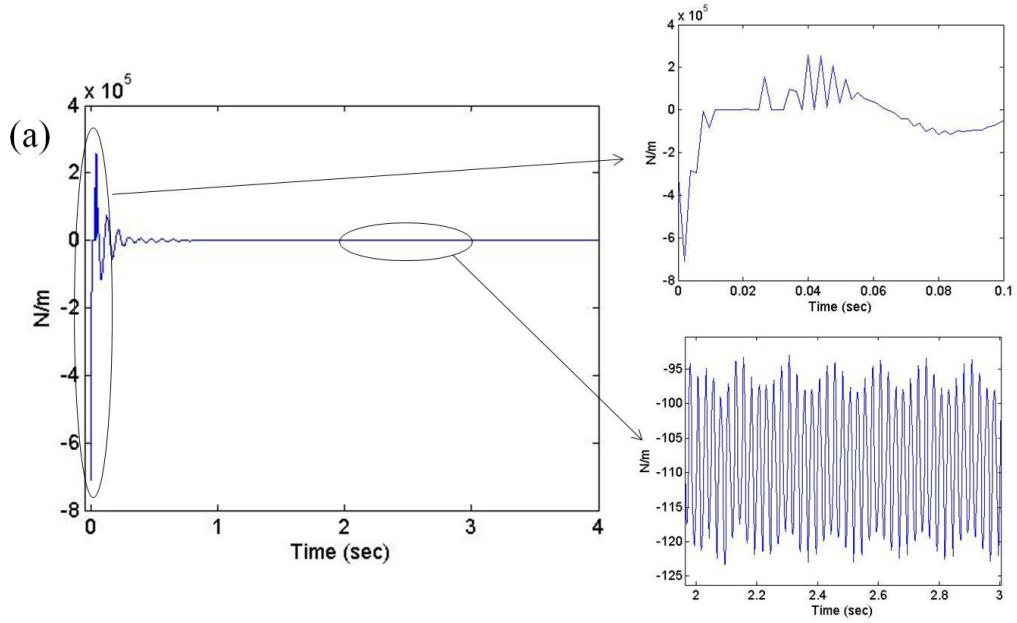

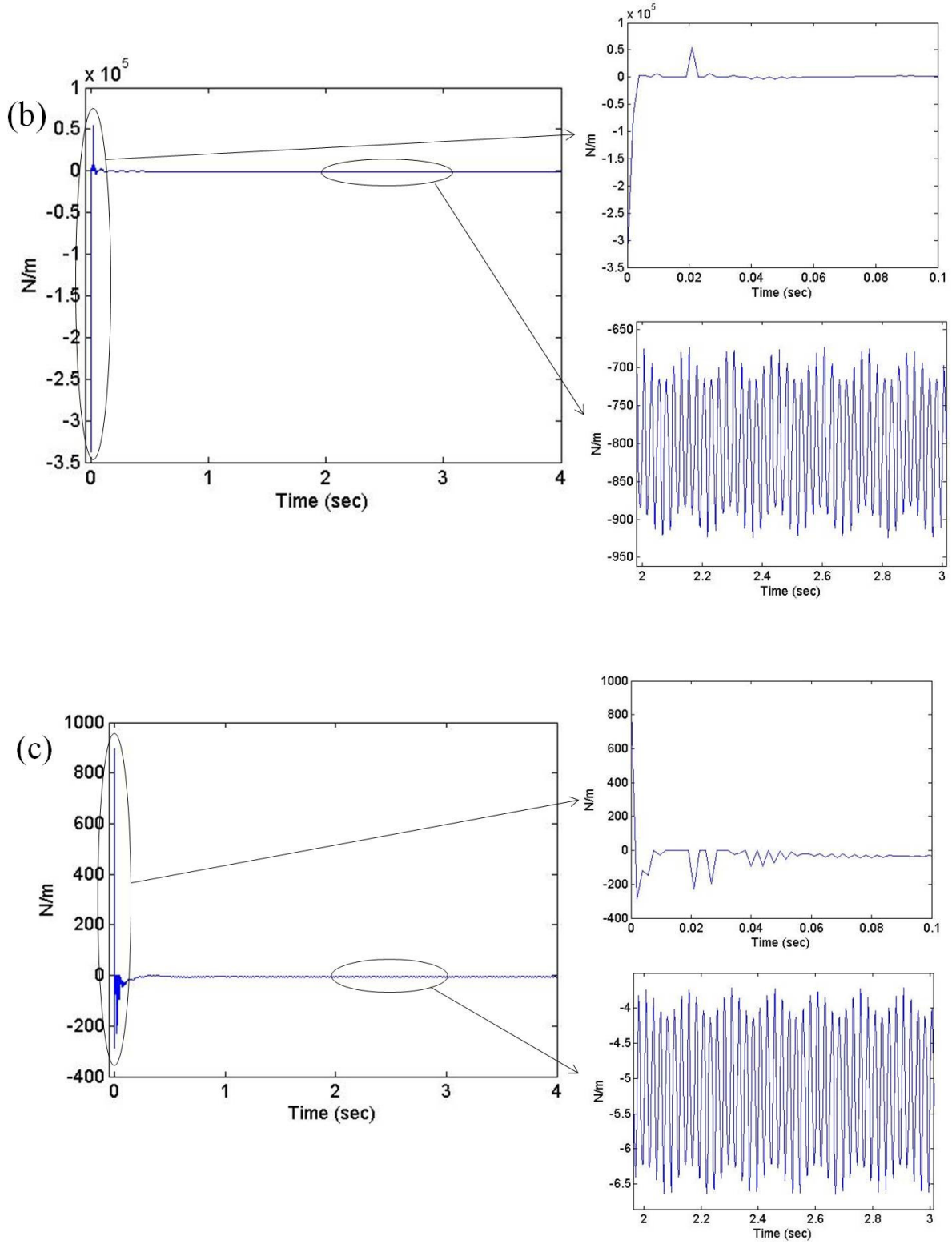

Figure 4.8 Creep forces: (a) longitudinal creep force, (b) lateral creep force, and (c) spin creep force

Using these results, CoFs are calculated and shown in Figure 4.9 and 4.10. The total CoF (μ_{total}) combines the slip CoF (μ_{slip}) and the stick CoF (μ_{stick}), i.e., $\mu_{total} = \mu_{slip} + \mu_{stick}$. In this study, the total CoF result has been scaled to fit in a common range of values by modifying c coefficients. Thus, they may not be 100% accurate but the relative behavior and overall trend is accurate.

The c coefficients from the original Soom's CoF model, as seen in Equation (2.17), were developed for the lubricated condition. For dry condition applications, c coefficients need to be modified using experimental data obtained under dry conditions. Currently, this experimental data has not been measured. Thus, all μ in this study are uncalibrated.

According to the Coulomb friction law, the maximum CoF occurs as soon as an object starts to move. CoF models which have previously been applied to study the wheel-rail dynamics could not capture this maximum CoF. The CoF model newly developed in this study for dry rail conditions captures this maximum CoF (an initial peak) when the wheel starts to move as shown in Figure 4.9 (a) and (c). After this initial peak, μ_{stick} shows dynamic fluctuation during a very short amount of time due to initial conditions. Then it increases until around 0.3 *sec* when almost all μ_{slip} values show zero. Thus, most of the contact patch experiences a 100% stick condition (pure rolling condition) and the size of the 100% stick contact patch increases during this time. After 0.3 *sec*, μ_{stick} decreases with increasing μ_{slip} since the slip region at the contact patch increases and the stick region at the contact patch decreases. Values of μ_{stick} are at steady state after 1*sec*. This means that the stick region at the contact patch is at steady state. The trend of μ_{stick} does not match any dynamic parameter trend since it is a function of the ratio of the semi-elliptical contact lengths and the relative wheel-rail vibration, as described in the stick component of Equation (3.4).

The μ_{slip} results shown in Figure 4.9 (b) has mostly null values during the first 0.3 *sec* due to pure rolling, i.e., both longitudinal and lateral creepages are zero as displayed in Figure 4.7 (a) and (b), as explained above. It displays a dramatic increase after 0.3 *sec* with decreasing μ_{stick}, and then it demonstrates steady state values at about 2 *sec*. Thus, a wheel starts to slide around 0.3 *sec* (i.e., the slip region at the contact patch starts to show) and the sliding keeps increasing

(i.e., the slip region at the contact patch increases) until reaching a steady state around 2 *sec* (i.e., the stick and slip region at the contact patch are at the steady state). The plotted shape of μ_{slip} does not match the shape of any other dynamic parameter above since it is a function of various dynamic parameters, as described in the slip component of Equation (3.4).

The term μ_{total} shows the combined result of μ_{stick} and μ_{slip}. Sometimes μ_{total} has a value of zero since the wheel is not in contact with the rail due to the initial condition. In addition, μ_{total} is in a steady state at around 2 *sec* when both μ_{slip} and μ_{stick} are in a steady state. This trend matches well with all the other dynamic parameters shown above. The trend of μ_{total} demonstrates that μ_{stick} is dominant during the first 0.3 *sec* since almost all values of μ_{slip} are zero during this time, as presented in Figure 4.10 (a) and (b). As explained above, it indicates that the whole contact patch is in the stick state and the sliding velocity is zero (pure rolling) during this time period, as in Equation (3.4). After 0.3 sec, μ_{slip} is dominant. Thus, the slip CoF may play a more important role than the stick CoF to control the total CoF when μ_{slip} starts to appear. The CoF results do not show temporal similarity with the evolution of any of the other dynamic parameters studied. In addition, the FFT analysis results of the total CoF shows that the frequency (40.25 *Hz* and 80.5 *Hz*) of the total CoF between 1.7 *sec* and 4 *sec* is different from the excitation frequency (80π *Hz*) of rail roughness. Thus, the CoF has a highly nonlinear dependence on those dynamic parameters.

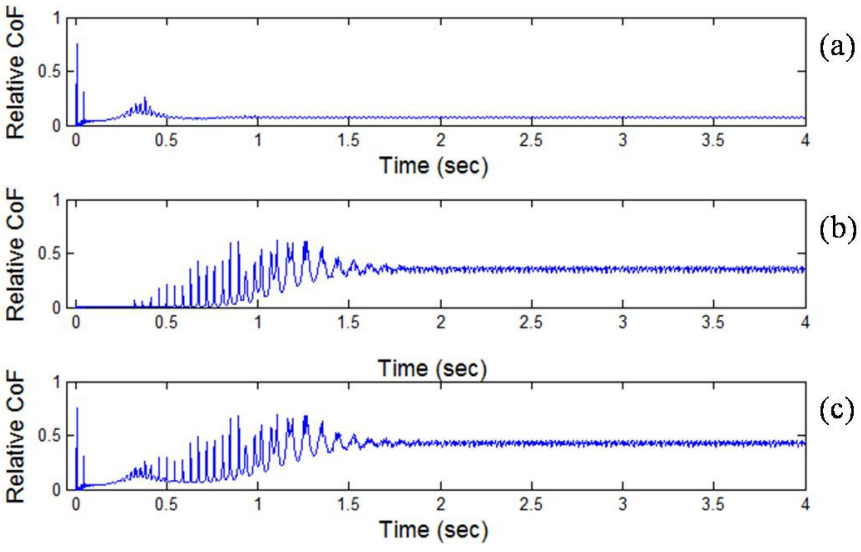

Figure 4.9 CoF results: (a) μ_{total}, (b) μ_{slip}, and (c) μ_{stick}

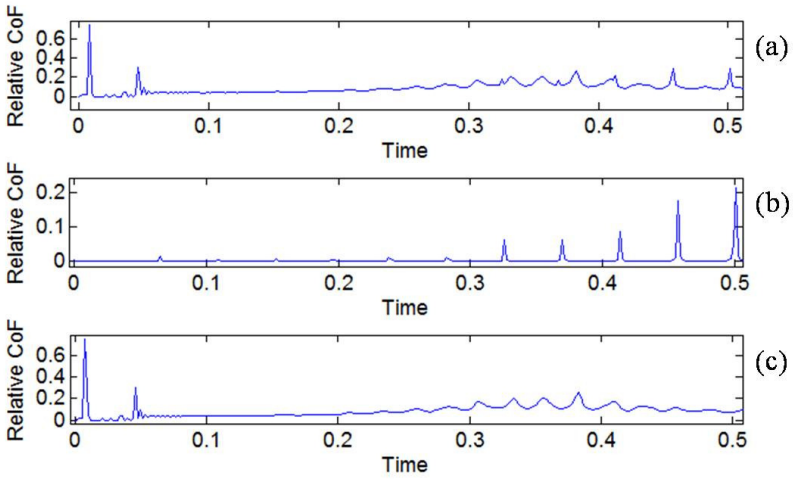

Figure 4.10 CoF results during 0.5 *sec*: (a) μ_{total}, (b) μ_{slip}, and (c) μ_{stick}

4.2 Stochastic Wheel-Rail Model

Uncertain variables include the MARR, semi-elliptical contact lengths, track stiffness, track damping coefficient, lateral displacement, and the sleeper distance. Each of the uncertain variables is tested individually, and combinations of two and three uncertain variables are also tested. Combinations of two uncertain variables include the MARR and the lateral displacement, *a* and *b*, the MARR and the sleeper distance, and the track stiffness and the track damping coefficient. Combinations of three uncertain variables include *a*, *b*, and the lateral displacement and the MARR, the track stiffness, and the sleeper distance. The uncertainty is set as 50% for testing under extremely uncertain conditions. Five poly-chaos expansion terms and 15 collocation points are used for studying the effects of one uncertain random variable. Fifteen poly-chaos expansion terms and 30 collocation points are used for studying the simultaneous effects of two independent uncertain random variables. Thirty five poly-chaos expansion terms and 70 collocation points are used for studying the simultaneous effect of three independent uncertain parameters on the CoF. The Jacobi polynomials, as in Equation (2.20), are employed as basis functions for the Karhunen-Loeve expansion of the parameters considered to have a beta distribution. The impact of uncertain variables on the CoF of the wheel-rail contact and on other dynamic parameters is quantified and analyzed at a train speed of 20 *m/s*. The probability density function (PDF) represents the impact of uncertain variables in this study. The PDF of

CoFs and dynamic parameter responses are found to provide information that is useful for making decisions regarding the wheel-rail maintenance, design, safety, and development.

The PDF is obtained by drawing histograms of their values and normalizing the area under the curves that are obtained. Thus, the area under the curves is always 1. The PDF is always displayed with 10 columns, and each column has a width of 1 along the x-axis, as shown in Figure 4.11. The sum of the y-values is 1. The calculated PDF at each time t is projected onto the μ-t plane and the color code is used to display the relative probability. The color red represents higher values of the PDF, and the color blue denotes the lower value of the PDF (Figure 4.12). If the poly-chaos PDF results show a very narrow range or no range, the system's responses are very close to or the same as the response of the deterministic model, respectively. The highest value of the PDF at a specific time t_1 is not always the same as the highest value of the PDF at a different time t_2, as displayed in Figure 4.11. Thus, different shades of red color or no red color can also be displayed at different time t. If red is not displayed, the PDF is more uniformly distributed, as shown in Figure 4.12.

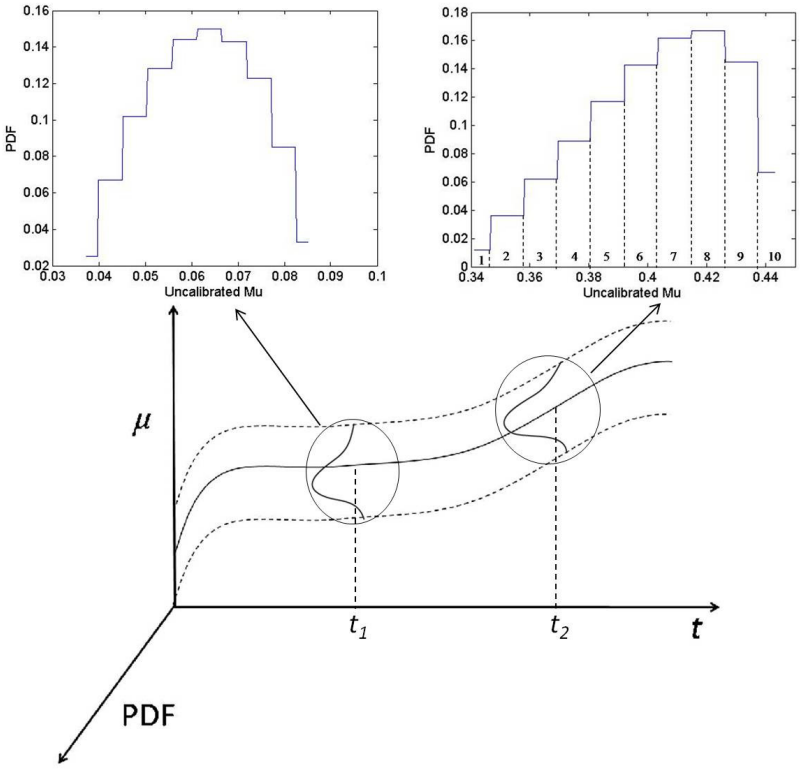

Figure 4.11 Example of representatives at different time t

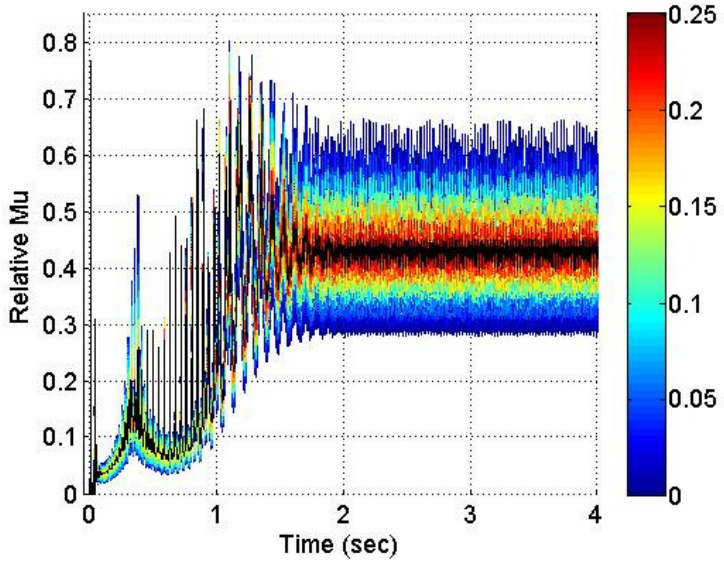

Figure 4.12 Collection (along the time axis) of the projections of the instantaneous PDF of μ_{total} for a combination of uncertain MARR and uncertain lateral displacement

4.2.1 One Uncertain Variable

Ratio of Semi-elliptical Contact Lengths (*a/b*)

This section focuses on the effect of the uncertain ratio of semi-elliptical contact lengths (*a/b*) on the CoF model, as in Equation (3.4). It is assumed that *a/b* has an uncertainty of 50% and a symmetric beta distribution. The values of μ_{stick}, μ_{slip}, and μ_{total} are calculated and analyzed since the *a/b* term occurs only in the CoF model.

Figures 4.13 through 4.15 represent the PDF of the CoFs, i.e., μ_{stick}, μ_{slip}, and μ_{total}, throughout the entire simulation. The PDF of μ_{stick}, as shown in Figure 4.13, shows that the highest PDF is close to the deterministic values, i.e., slightly below the deterministic value. In addition, the PDF is not symmetric but skewed upward with respect to the deterministic value. Please note that the uncertain input *a/b* had a symmetric beta distribution, so in this case the type of the input distribution and the type of the output distribution are not the same.

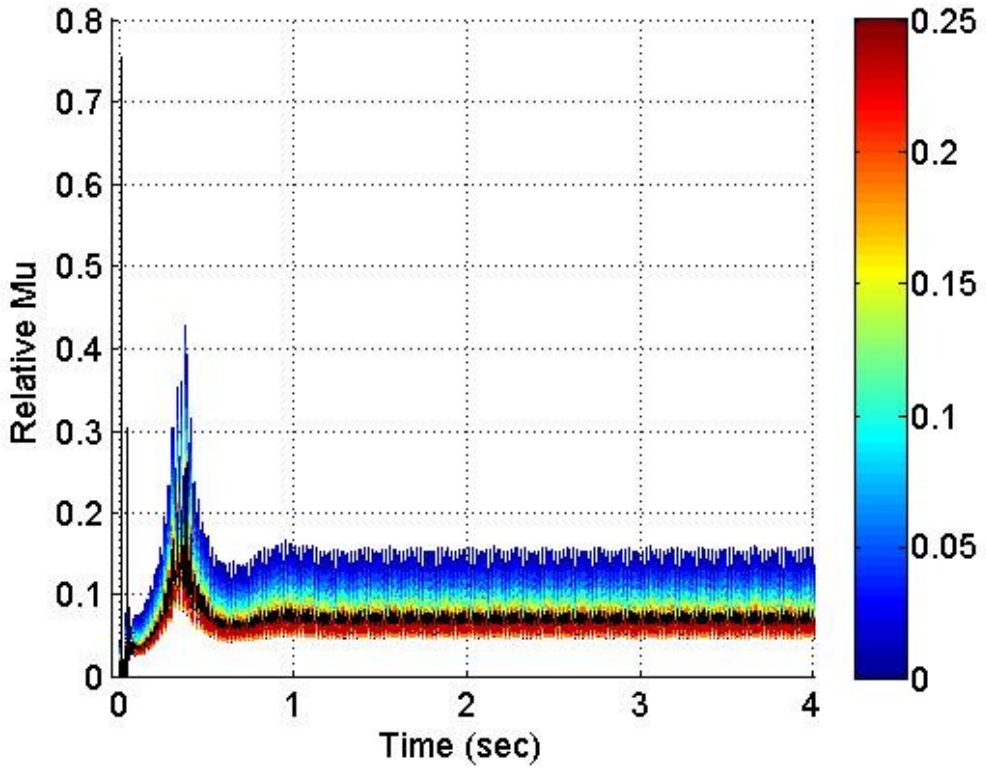

Figure 4.13 Collection (along the time axis) of the projections of the instantaneous PDF of μ_{stick} on the μ-t plane

The PDF of μ_{slip} is illustrated in Figure 4.14. The PDF of μ_{slip} does not appear during first 1 *sec*. Thus, the value of μ_{slip} is the same as the deterministic value, and the shape of μ_{slip} is similar to an impulse function during this time. This phenomenon has been reported by Sandu et al. [42]. They found that the poly-chaos PDF cannot be captured well when the real distribution approaches an impulse function. For this reason, the PDF becomes evident after about 1 *sec*, and it is skewed downward with respect to the deterministic value. The highest PDF of μ_{stick} is close to the deterministic value, i.e., a little bit higher than the deterministic value.

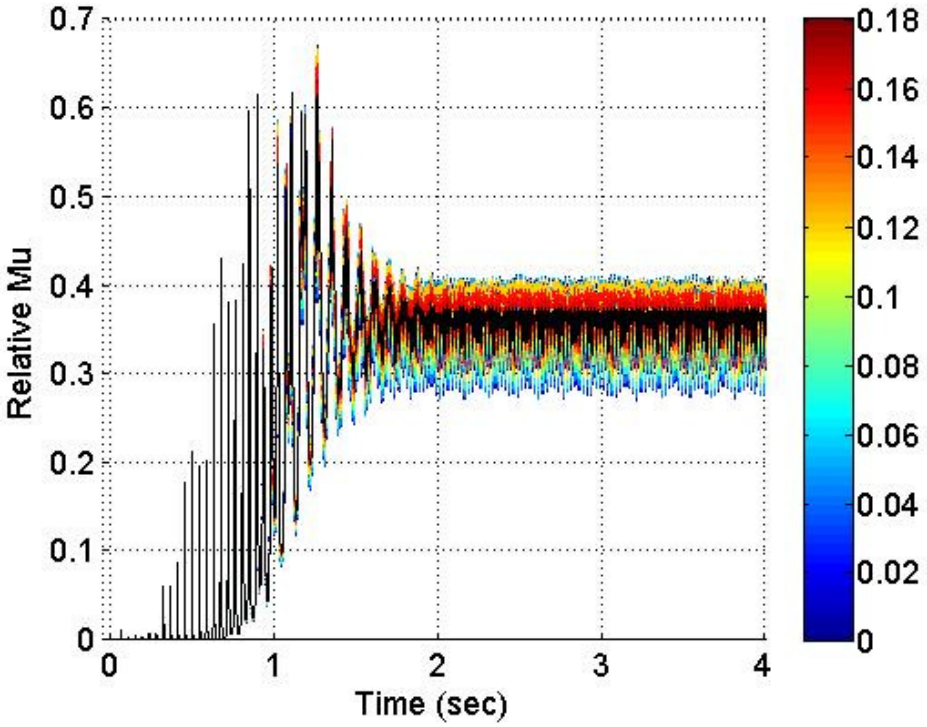

Figure 4.14 Collection (along the time axis) of the projections of the instantaneous PDF of μ_{slip} on the μ-t plane

Figure 4.15 shows the PDF of μ_{total} which combines the PDF of μ_{stick} and the PDF of μ_{slip}. This PDF of μ_{total} is mostly influenced by the PDF result of μ_{stick} before the first 1 *sec* since μ_{slip} shows little PDF during this time. Thus, the PDF of μ_{total} also displays a skewed shape as observed with the stochastic μ_{stick}. The PDF of μ_{total} after 1 *sec* seems to be influenced by both the PDF of μ_{stick} and μ_{slip} since the PDF trend is same as the PDF trend of μ_{stick}, i.e. skewed upward with respect to the deterministic value, but the highest PDF coincides with the same deterministic value as the μ_{slip}.

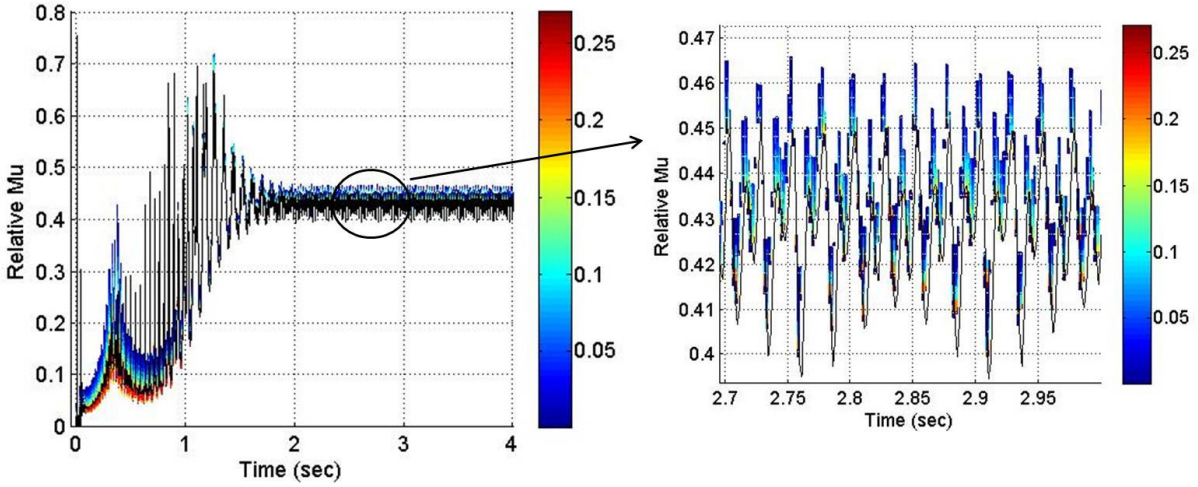

Figure 4.15 Collection (along the time axis) of the projections of the instantaneous PDF of μ_{total} on the μ-t plane, and a zoomed plot between 2.7 *sec* and 3 *sec*

Lateral Displacement

This section focuses on the effect of the uncertain lateral displacement. It is assumed that the lateral displacement has an uncertainty of 50% and a symmetric beta distribution. The PDF results of the dynamic parameters which are influenced by the lateral displacement (radii of curvature and semi-elliptical contact lengths) and the CoFs are calculated and analyzed.

Figure 4.16 represents the PDF results for the radii of curvature of the wheel (R_w) and the rail (R_r). The PDF of R_w is symmetric with respect to the deterministic value. The PDF of R_r is symmetric until 0.1 *sec* (first peak) and becomes skewed after 0.1 *sec*. R_w and R_r show wide distributions for the first 0.2 *sec* (first two peaks), which becomes narrower as time progresses. Finally, the width of the distribution stabilizes around 1 *sec*. The wide range of responses may result from the instability of the wheel-rail dynamics due to the initial conditions.

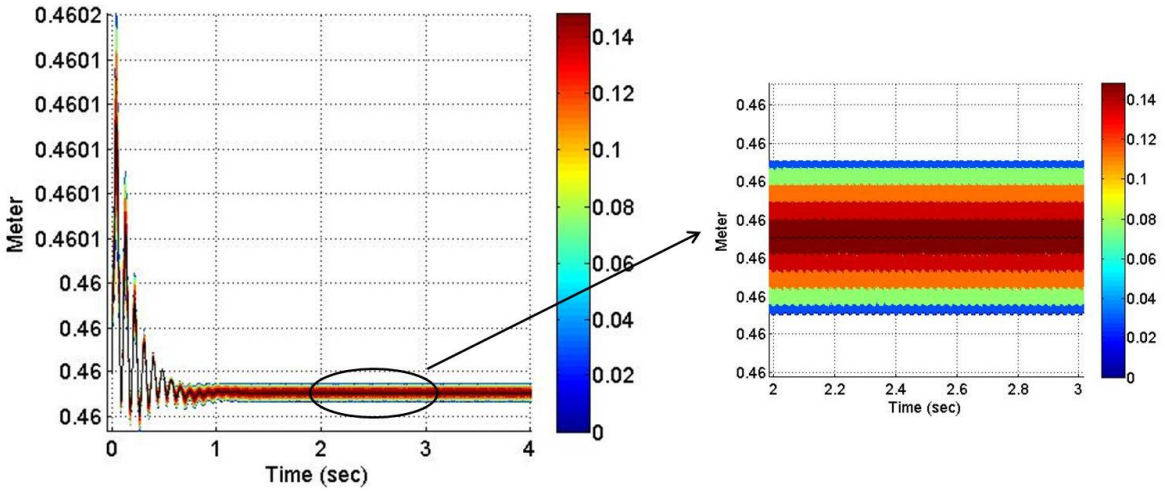

a. Collection (along the time axis) of the projections of the instantaneous PDF of R_w on the displacement-time plane, and a zoomed plot between 2 *sec* and 3 *sec*

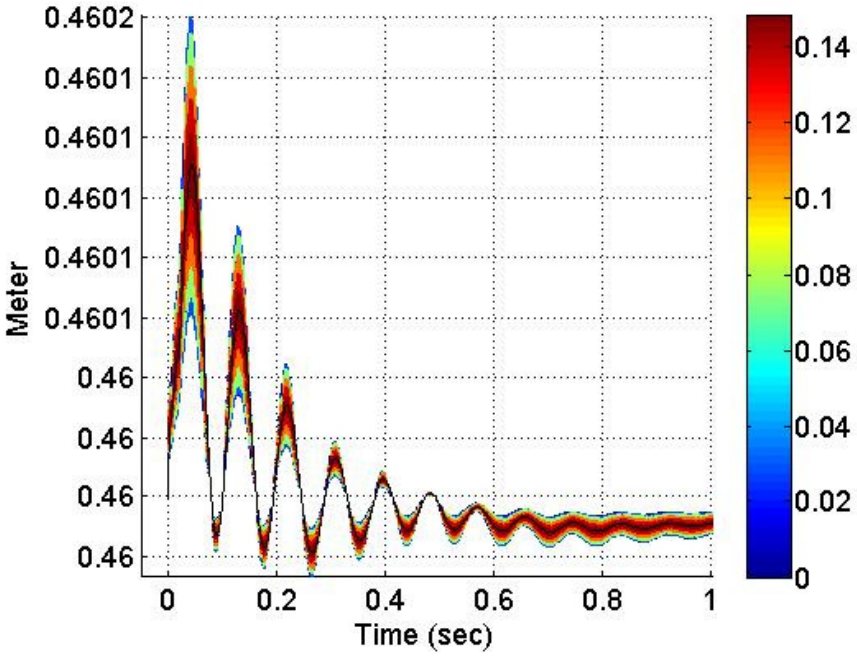

b. Collection (along the time axis) of the projections of the instantaneous PDF of R_w on the displacement-time plane for 1 *sec*

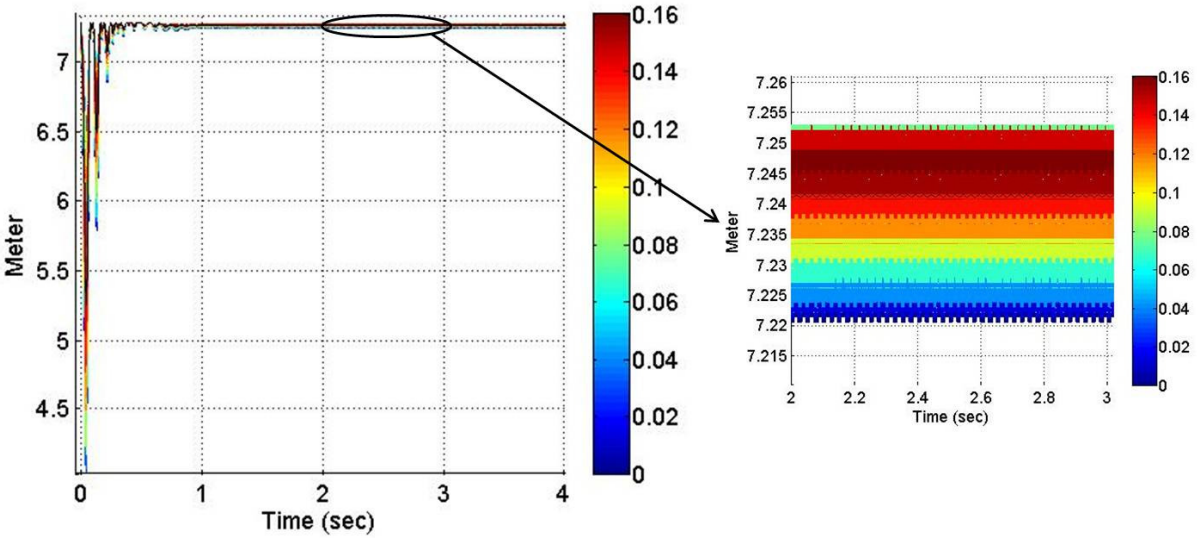

c. Collection (along the time axis) of the projections of the instantaneous PDF of the R_r on the displacement-time plane, and a zoomed plot between 2 *sec* and 3 *sec*

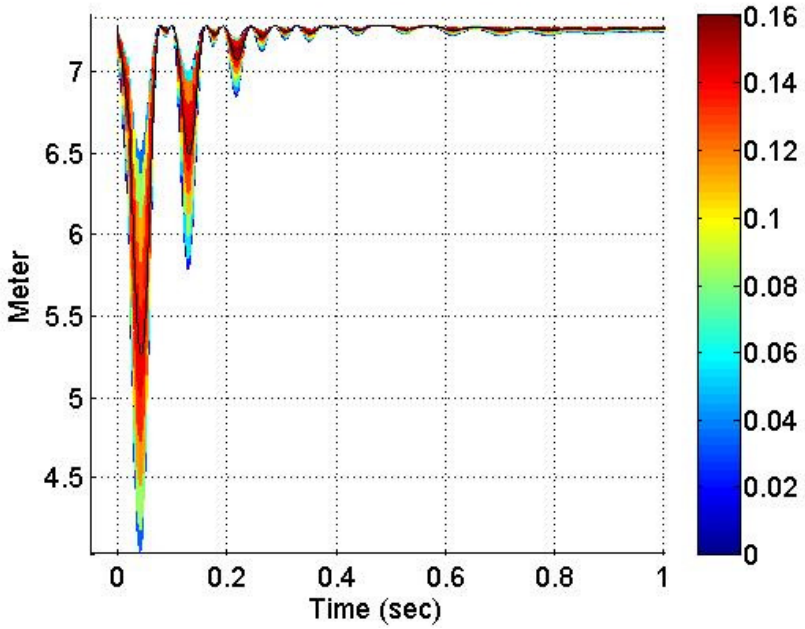

d. Collection (along the time axis) of the projections of the instantaneous PDF of the R_r on the displacement-time plane for 1 *sec*

Figure 4.16 Collection of the projections of the instantaneous PDF of the radii of curvature for the wheel and the rail

Figure 4.17 displays the PDF of semi-elliptical contact lengths. Both plots show that the PDF results for *a* and *b* are almost the same as the deterministic value, and sometimes the PDF is shown. Thus, the stochastic radii of curvature for the wheel and rail do not have much influence on the semi-elliptical contact lengths; although Equations (3.20) and (3.23) show that the semi-elliptical contact lengths are a function of the radii of curvature for the wheel and rail.

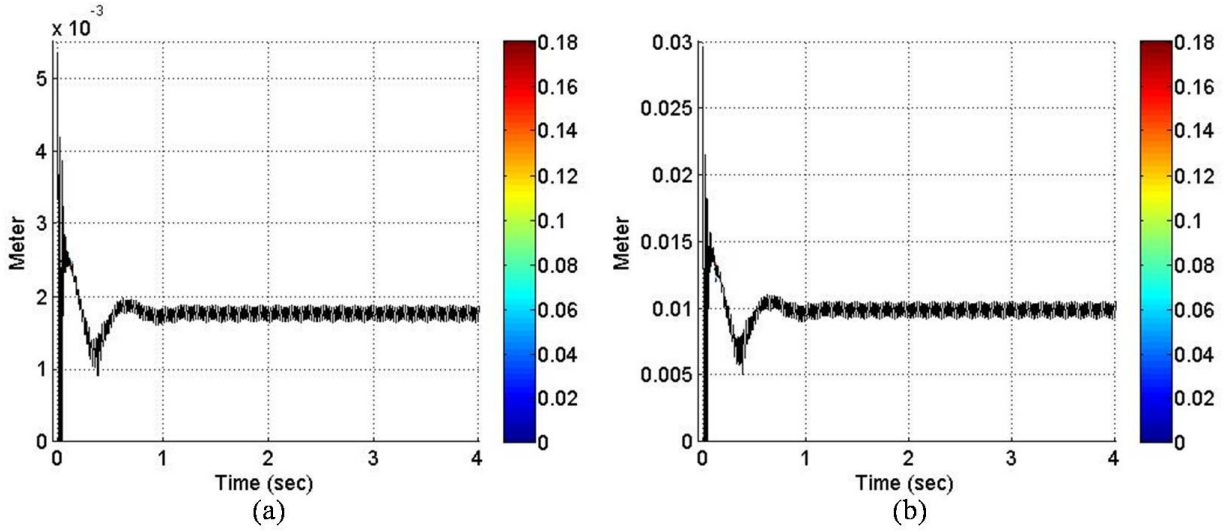

Figure 4.17 Collection (along the time axis) of the projections of the instantaneous PDF of semi-elliptical contact lengths on the contact length-time plane: (a) PDF of *a* and (b) PDF of *b*

Figure 4.18 represents the PDF of μ_{stick}. Figure 4.18 illustrates the fact that the uncertain lateral displacement does not influence the stick component since the semi-elliptical contact lengths, which are the only parameters influenced by the lateral displacement in the stick component, are not affected much by the uncertain lateral displacement, as shown in Figure 4.17. In other words, semi-elliptical contact lengths are mostly influenced by the vertical vibration.

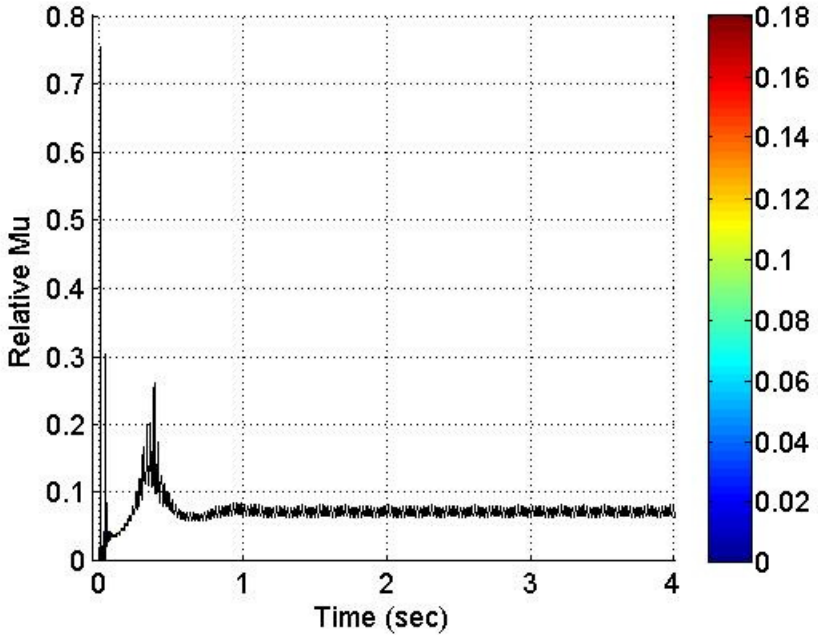

Figure 4.18 Collection (along the time axis) of the projections of the instantaneous PDF of μ_{stick} on the μ-t plane

The PDF of μ_{slip} is illustrated in Figure 4.19. The PDF of μ_{slip} shows no variation before 1 *sec* and shows the skewed PDF result higher than the deterministic value after 1 *sec*. The change of the lateral displacement leads to the change of the sliding velocity in the lateral direction. Thus, the sliding velocity in the tangential direction also changes, as shown in Equation (3.33). This change in sliding velocity influences the sliding component, i.e. V^*. Therefore, the uncertain lateral displacement causes the PDF of μ_{slip}.

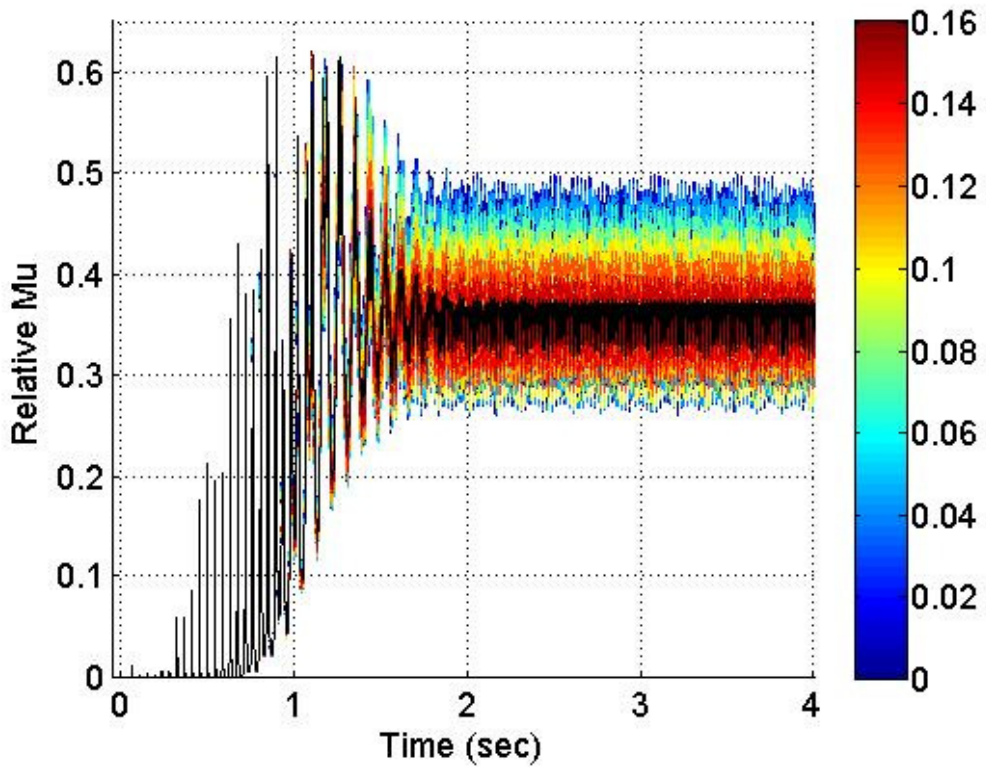

Figure 4.19 Collection (along the time axis) of the projections of the instantaneous PDF of μ_{slip} on the μ-t plane

Figure 4.20 represents the PDF result of μ_{total}. As explained before, the PDF of μ_{total} is dominantly influenced by the stick component before 1 *sec* and mainly influenced by the slip component after 1 *sec*. Thus, the PDF of μ_{total} does not show a variation before 1 *sec* and displays results similar to μ_{slip} after 1 *sec*, i.e., skewed upward with respect to the deterministic values. This trend, which is the dominant influence of μ_{stick} on the stochastic μ_{total} before 1 *sec* and the main effect of μ_{slip} on the stochastic μ_{total} after 1 *sec*, is the same for the PDF of μ_{total} through all case studies in this dissertation except the case of the uncertain *a/b*. The stochastic analysis with the uncertain lateral displacement demonstrates that the uncertain lateral displacement is an important parameter for understanding the slip CoF variation correctly.

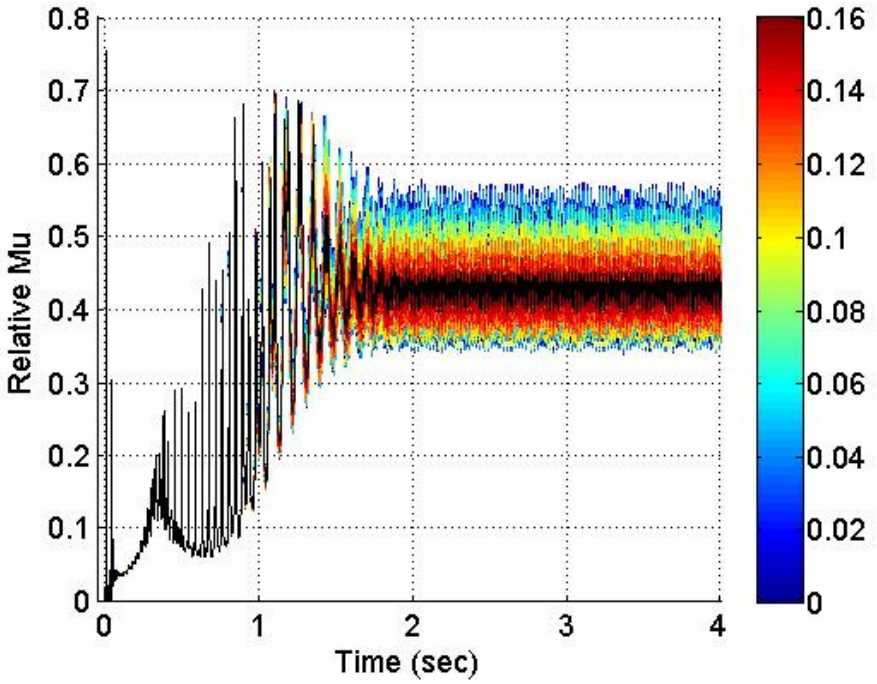

Figure 4.20 Collection (along the time axis) of the projections of the instantaneous PDF of μ_{total} on μ-t plane

Maximum Amplitude of Rail Roughness (MARR)

This section illustrates the effect of the uncertain MARR on the CoF and on several dynamic parameters (the relative wheel-rail vibrations, the normal contact force, and the semi-elliptical contact lengths). The PDF results for the CoF and for dynamic parameters are calculated and analyzed. The MARR is assumed to have 50% uncertainty and symmetric beta distribution.

The PDF of the relative wheel-rail vibration is presented in Figure 4.21. The results show some variation around the boundaries. The normal contact force is a function of the relative wheel-rail vibration since the shape of the normal contact force is the same as the shape of positive parts of the relative wheel-rail vibration, as demonstrated in Figure 4.21 and 4.22. Semi-elliptical contact lengths have almost the same shape as the normal contact force. Thus, these three results, i.e., the normal contact force, semi-elliptical contact lengths, and the relative wheel-rail vibration results, show similar PDF results, as presented in Figure 4.21 through Figure 4.23.

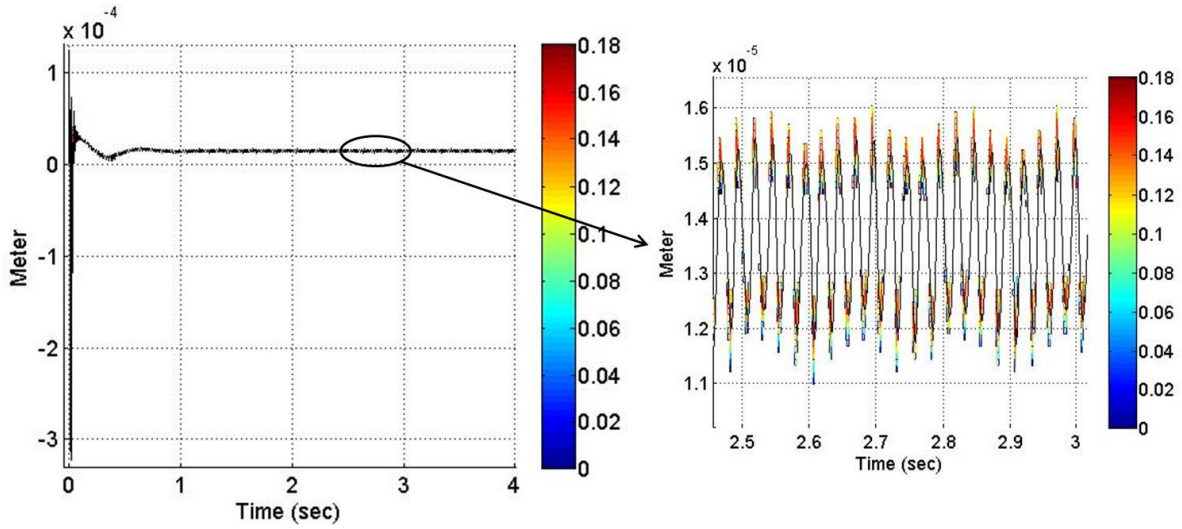

Figure 4.21 Collection (along the time axis) of the projections of the instantaneous PDF of h_o on the displacement-time plane, and a zoomed plot between 2.5 *sec* and 3 *sec*

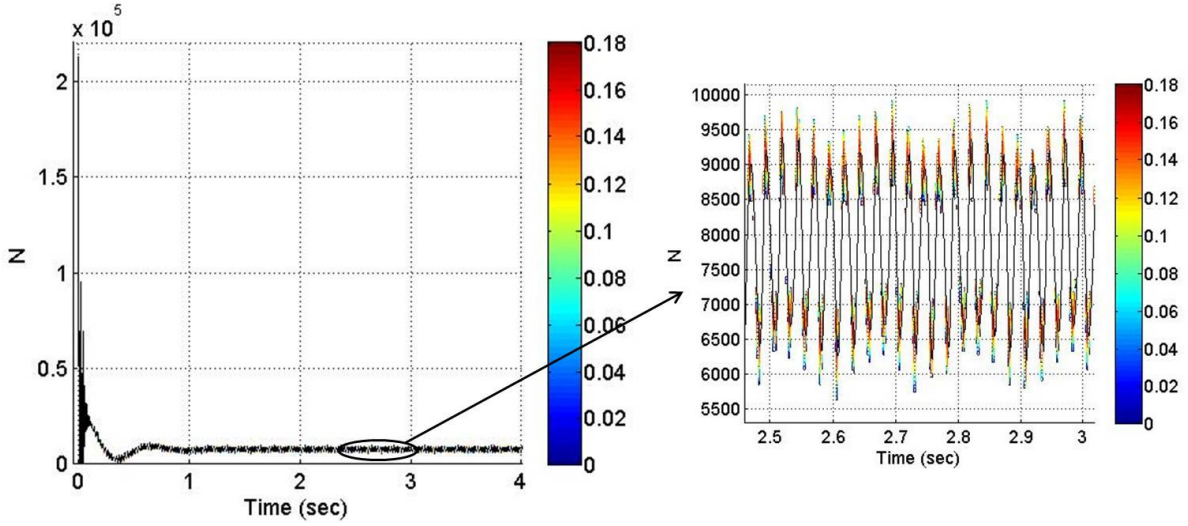

Figure 4.22 Collection (along the time axis) of the projections of the instantaneous PDF of F_n on the force-time plane, and a zoomed plot between 2.5 *sec* and 3 *sec*

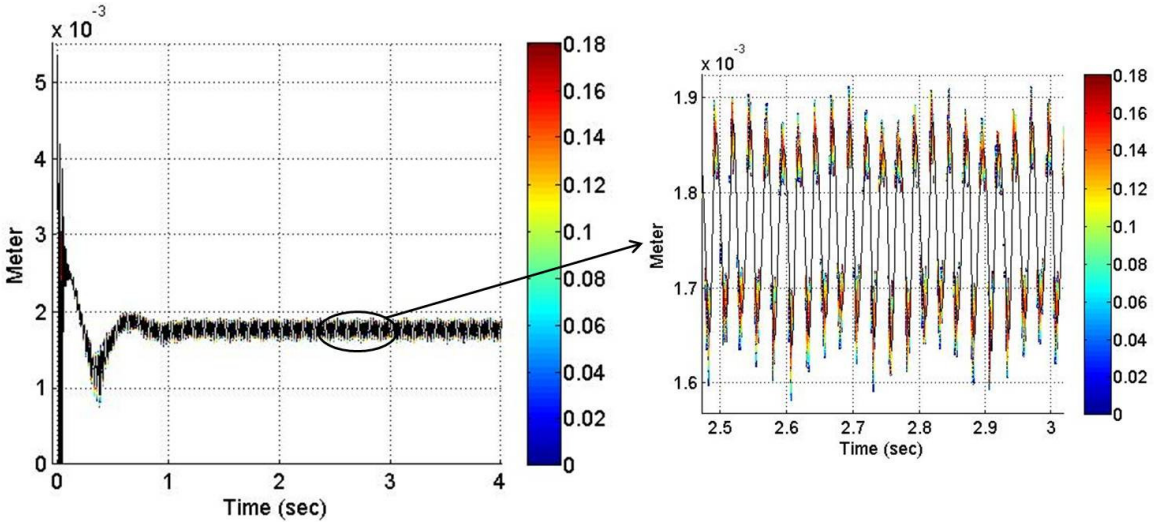

a. Collection (along the time axis) of the projections of the instantaneous PDF of *a* on the contact length-time plane, and a zoomed plot between 2.5 *sec* and 3 *sec*

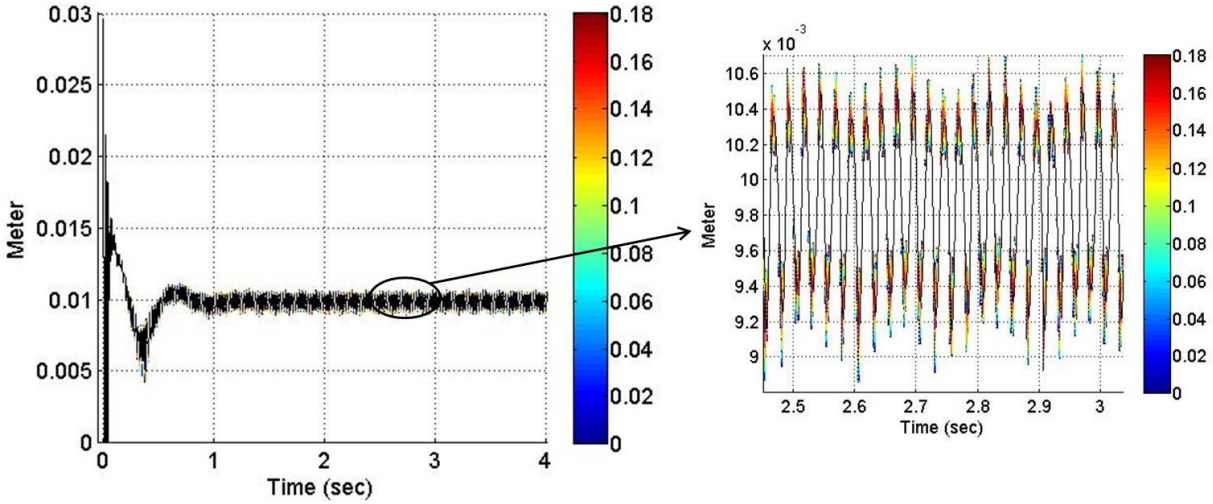

b. Collection (along the time axis) of the projections of the instantaneous PDF of *b* on the contact length-time plane, and a zoomed plot between 2.5 *sec* and 3 *sec*

Figure 4.23 Collection of the projections of the instantaneous PDF of the semi-elliptical contact lengths: (a) *a* and (b) *b*

The PDF results of the stochastic CoFs are shown in Figure 4.24 through 4.26. The PDF of μ_{stick} is shown in Figure 4.24. The PDF is symmetric with respect to the deterministic values unlike the PDF of μ_{stick} for the uncertain *a/b*. The highest PDF seems to coincide with the deterministic values. The PDF of μ_{slip} starts to show from 1 *sec* and it is skewed downward with

respect to the deterministic values, as shown in Figure 4.25. The PDF of μ_{slip} illustrates that the most probable stochastic realization is very close to the deterministic values. The PDF range of the stochastic μ_{slip} is wider than the PDF range of μ_{stick}. Therefore, the PDF of μ_{total} reflects the PDF of μ_{slip} after 1 *sec*. The PDF of the stochastic μ_{slip} before 1 *sec* is similar to or the same as the deterministic μ_{slip} values since the PDF from the poly-chaos theory cannot be captured well when the real distribution approaches an impulse function as explained above. Thus, the PDF of μ_{total} reflects the μ_{stick} PDF before 1 *sec*. For these reasons, the μ_{total} PDF shows the symmetric PDF trend before 1 *sec* and the skewed PDF trend after 1 *sec*. In addition, the highest PDF of μ_{total} coincides with the deterministic value before 1 *sec*, and it is slightly higher after 1 *sec*. The PDF of μ_{total} before 1 *sec* does not display the red color. Thus, the PDF of the stochastic μ_{total} has a more uniform distribution before 1 *sec* than the PDF after 1 *sec*. The change of the normal contact force leads to the variation of the contact patch size. Both stick and slip components in Equation (3.4) include the relative wheel-rail vibration term, h_o, in the R^* and semi-elliptical contact lengths, a and b. Thus, the uncertain MARR is a very important parameter for designing the wheel-rail system.

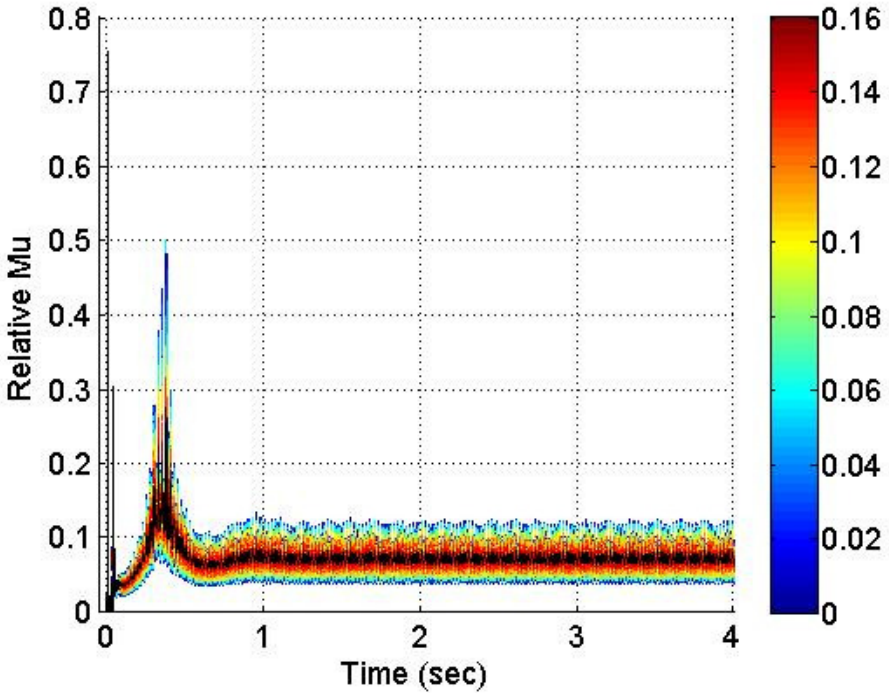

Figure 4.24 Collection (along the time axis) of the projections of the instantaneous PDF of μ_{stick} on the μ-t plane

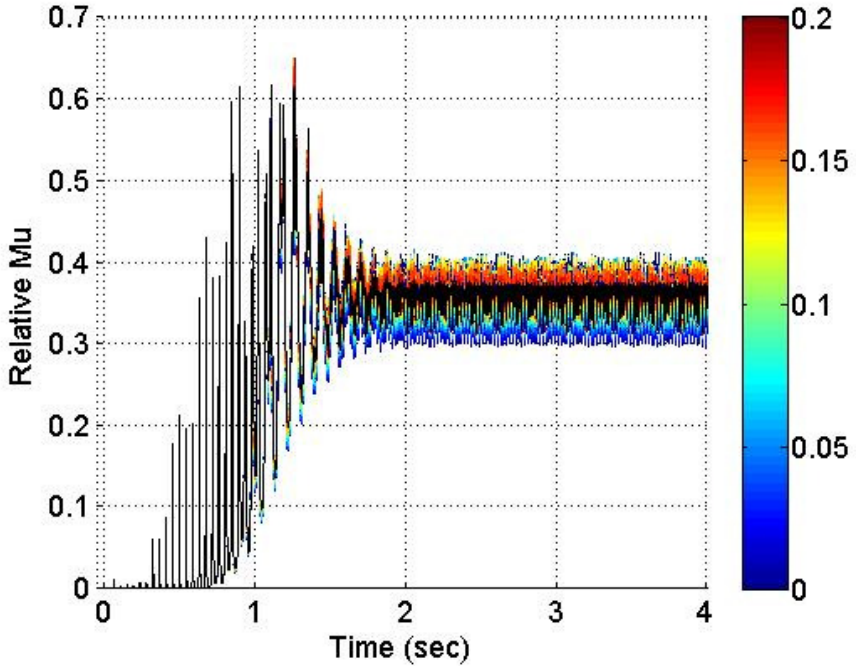

Figure 4.25 Collection (along the time axis) of the projections of the instantaneous PDF of μ_{slip} on the μ-t plane

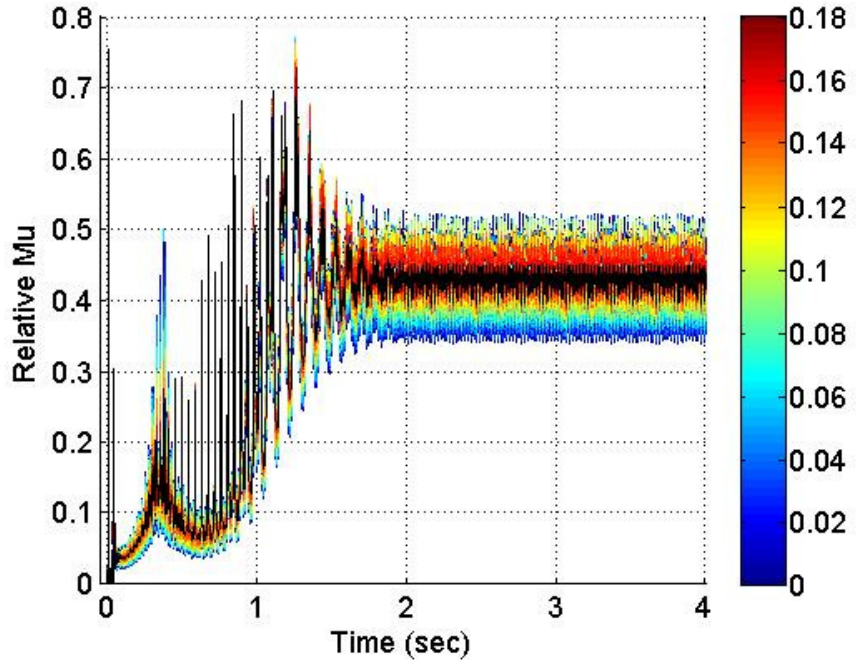

Figure 4.26 Collection (along the time axis) of the projections of the instantaneous PDF of μ_{total} on the μ-t plane

Sleeper Distance

The effect of the uncertain sleeper distance is calculated and analyzed. The PDF of CoFs and dynamic parameters are shown in Figure 4.27 through Figure 4.32. The PDF of the relative wheel-rail vibration is displayed in Figure 4.27. It shows a different PDF shape compared to the other PDF results shown above. In other words, some PDFs direct upward while the other PDFs direct downward. In addition, it has a very wide lower PDF value and a very narrow middle PDF value compared to the other PDF results. The PDF has a very wide range for the first 0.04 *sec*, and then it becomes very narrow. The some wide PDF range appears at around 0.4 *sec*. The most probable stochastic realization coincides with the deterministic value. The PDFs of the normal contact force, the semi-elliptical contact lengths, and the relative wheel-rail vibration demonstrate similar PDF trends due to their relationship explained above.

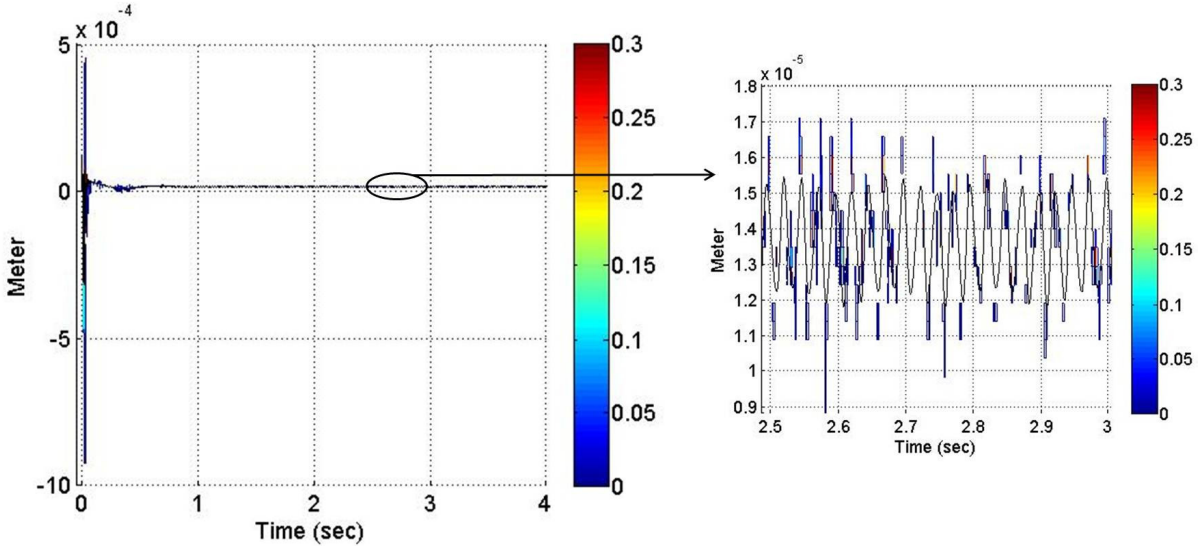

a. Collection (along the time axis) of the projections of the instantaneous PDF of h_o on the displacement-time plane, and a zoomed plot between 2.5 *sec* and 3 *sec*

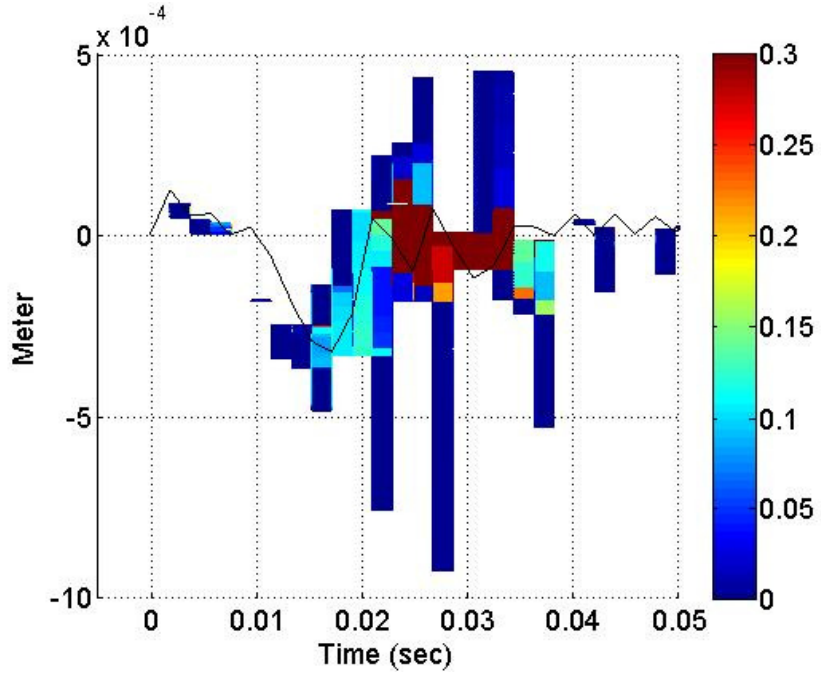

b. Collection (along the time axis) of the projections of the instantaneous PDF of h_o on the displacement-time plane for 0.5 *sec*

Figure 4.27 Collection of the projections of the instantaneous PDF of h_o

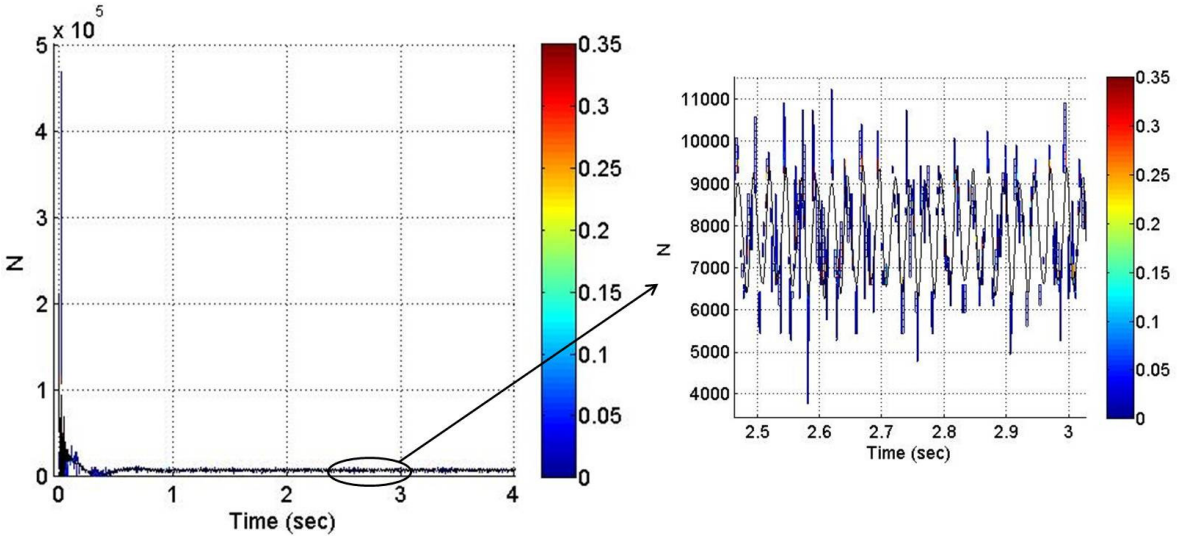

a. Collection (along the time axis) of the projections of the instantaneous PDF of F_n on the force-time plane, and a zoomed plot between 2.5 *sec* and 3 *sec*

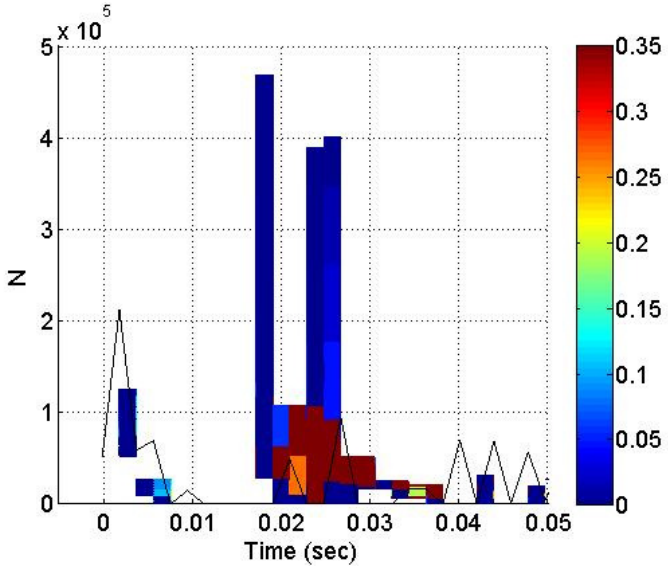

b. Collection (along the time axis) of the projections of the instantaneous PDF of F_n on the force-time plane for 0.05 *sec*

Figure 4.28 Collection of the projections of the instantaneous PDF of F_n

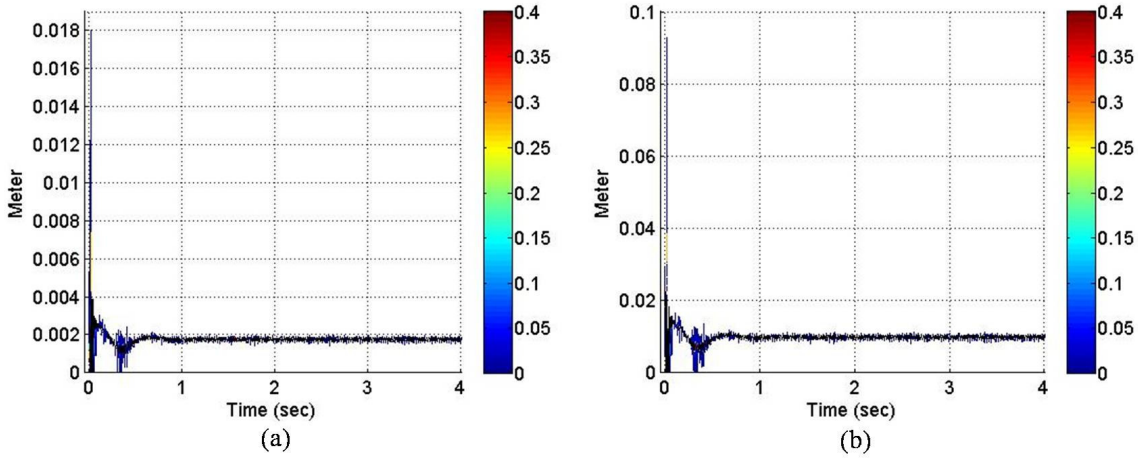

Figure 4.29 Collection (along the time axis) of the projections of the instantaneous PDF of semi-elliptical contact lengths on the contact length-time plane: (a) PDF of *a* and (b) PDF of *b*

Figure 4.30 presents the PDF of the stochastic μ_{stick}. The PDF shape is very similar to the PDF of dynamic parameters shown above. The PDF shape is skewed with respect to the deterministic value; however the skewed direction is not consistent. The PDF is not continuous unlike other stochastic CoF results shown above. The PDF has a much wider range at around 0.4 *sec* than the μ_{stick} CoF PDF of other uncertain parameters. This is due to the PDF of the wheel-

rail vibration, the semi-elliptical contact lengths, and the normal contact force at around 0.4 *sec*. However, most of the PDF range is narrower than the μ_{stick} PDF results of other uncertain parameters. It has very wide lower PDF value and a very narrow middle PDF value compared to the other stick CoF PDF results.

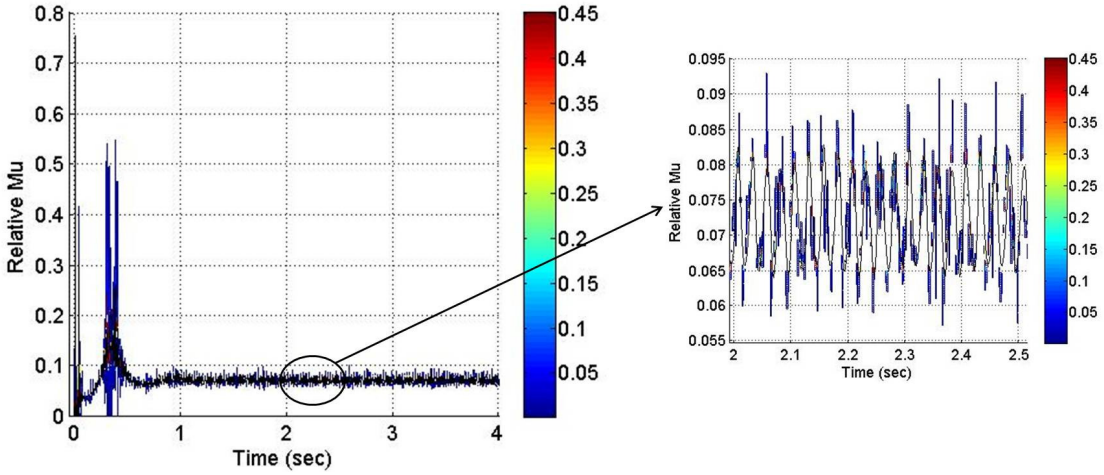

Figure 4.30 Collection (along the time axis) of the projections of the instantaneous PDF of μ_{stick} on the μ-t plane, and a zoomed plot between 2 *sec* and 2.5 *sec*

The stochastic result of μ_{slip} is shown in Figure 4.31. The distribution is skewed with respect to the deterministic value. Some PDFs direct upward while the other PDFs direct downward. The PDF range after 1 *sec* is wider for μ_{slip} than for μ_{stick}.

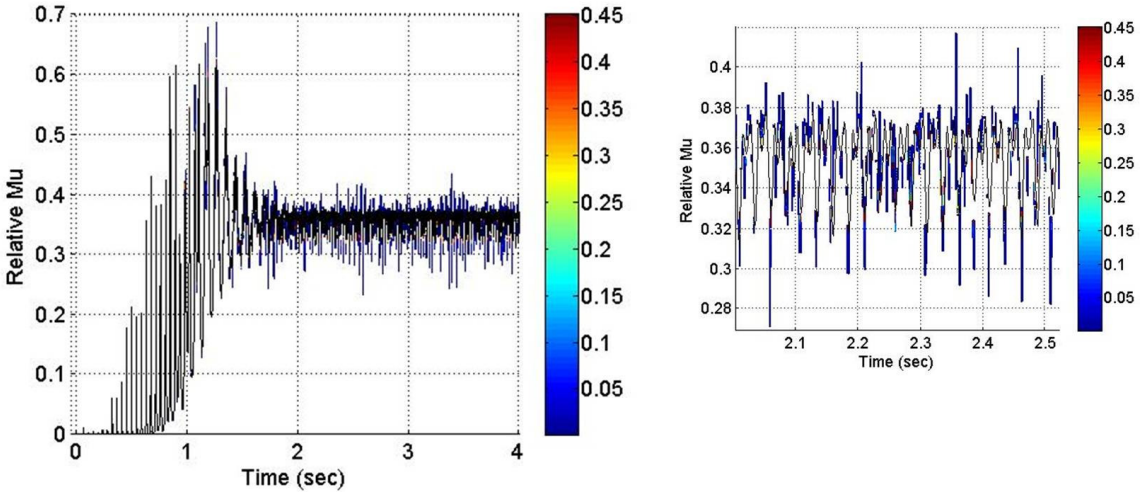

Figure 4.31 Collection (along the time axis) of the projections of the instantaneous PDF of μ_{slip} on the μ-t plane, and a zoomed plot between 2 *sec* and 2.5 *sec*

The stochastic total CoF result shows the combined PDF results of μ_{stick} and μ_{slip}. Thus, the PDF of μ_{total} reflects the PDF of μ_{stick} before 1 *sec* and the stochastic μ_{total} reflects the PDF of μ_{slip} after 1 *sec*. From the case study with the uncertain sleeper distance, it is obvious that the sleeper distance can influence the wheel-rail system by affecting the variation of the CoF values. Thus, the sleeper distance is one parameter which must be considered when designing track systems.

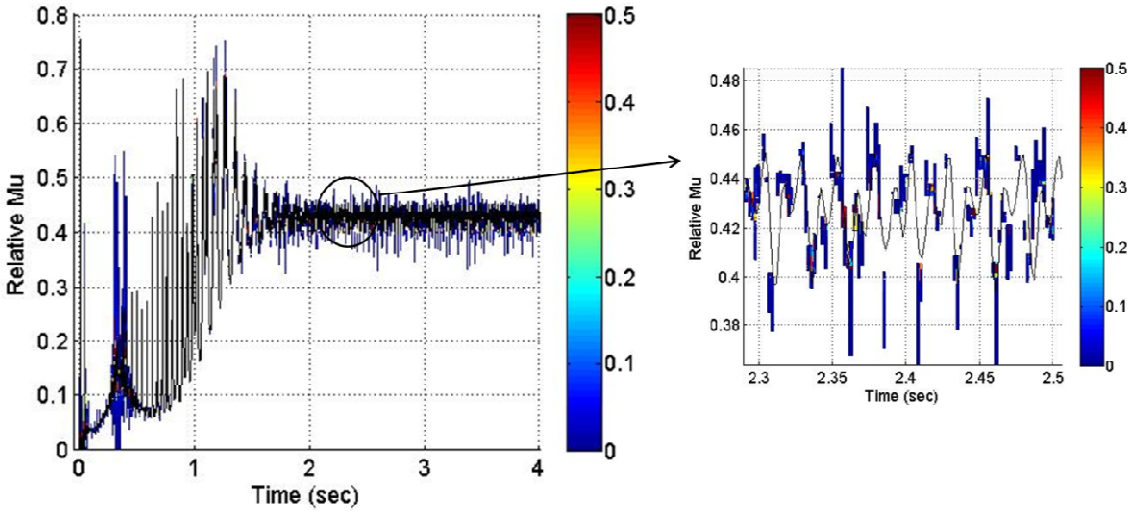

Figure 4.32 Collection (along the time axis) of the projections of the instantaneous PDF of μ_{total} on the μ-*t* plane, and a zoomed plot between 2.3 *sec* and 2.5 *sec*

Track Stiffness

The effect of the uncertain track stiffness is calculated and analyzed. It is assumed that the track stiffness has 50% uncertainty and a symmetric beta distribution. The stochastic results of the CoFs and dynamic parameters are presented in Figure 4.33-4.38. Figure 4.33 illustrates the PDF of h_o. It shows a wide range of PDFs for the first 0.03 *sec*, it narrows after 0.03 *sec*, as presented in Figure 4.33 (b), and then it is the same as the deterministic value at steady state, as shown in Figure 4.33 (a). The most probable stochastic realization is very close to the deterministic values. The PDF has a skewed shape, but it is not consistent. In other words, some PDFs are skewed upward and other PDFs are skewed downward. The normal contact force, the relative wheel-rail vibration, and semi-elliptical contact lengths PDFs display similar shapes, as illustrated in Figure 4.33-4.35. Unlike the PDF results of h_o, the normal contact force, *a*, and *b* have some PDFs around the boundaries at steady state.

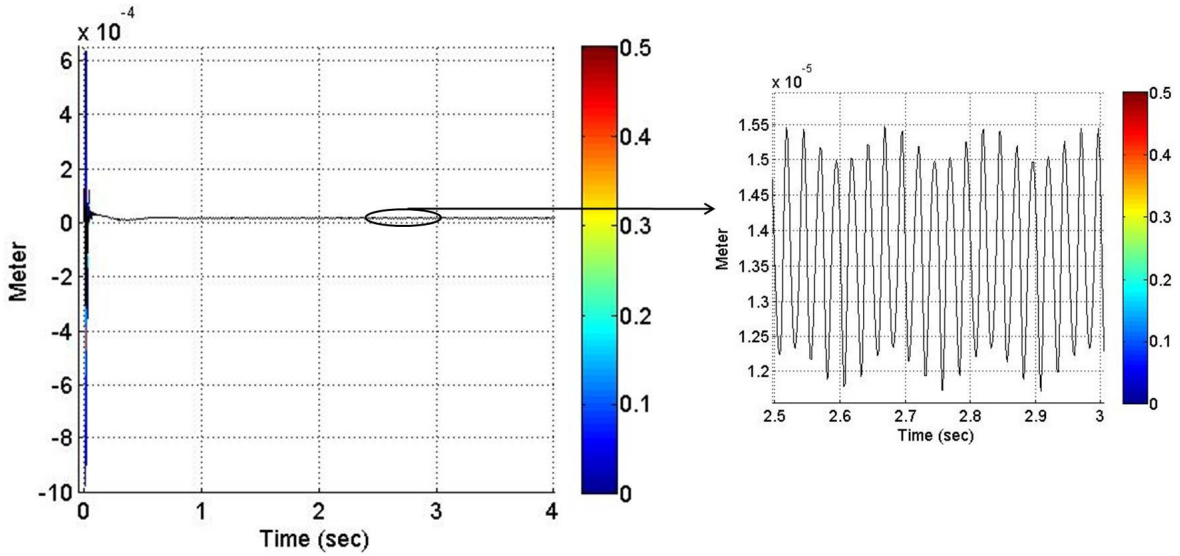

a. Collection (along the time axis) of the projections of the instantaneous PDF of h_o on the displacement-time plane, and a zoomed plot between 2.5 *sec* and 3 *sec*

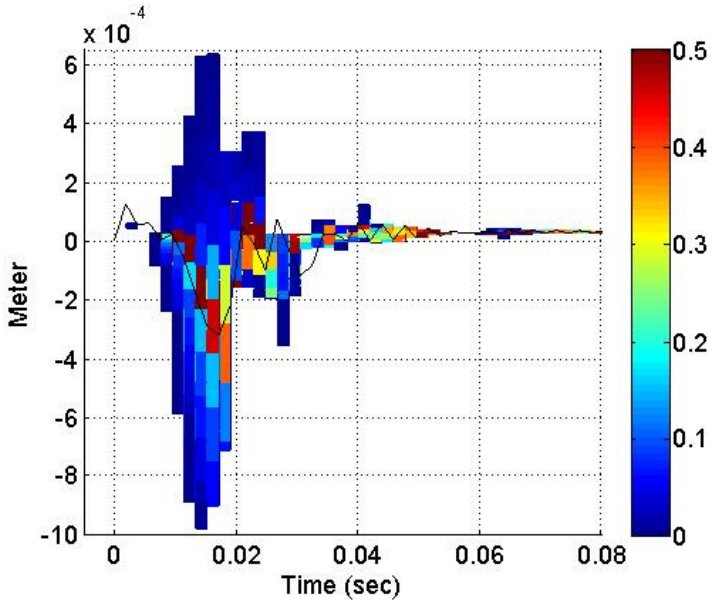

b. Collection (along the time axis) of the projections of the instantaneous PDF of h_o on the displacement-time plane for 0.08 *sec*

Figure. 4.33 Collection (along the time axis) of the projections of the instantaneous PDF of h_o

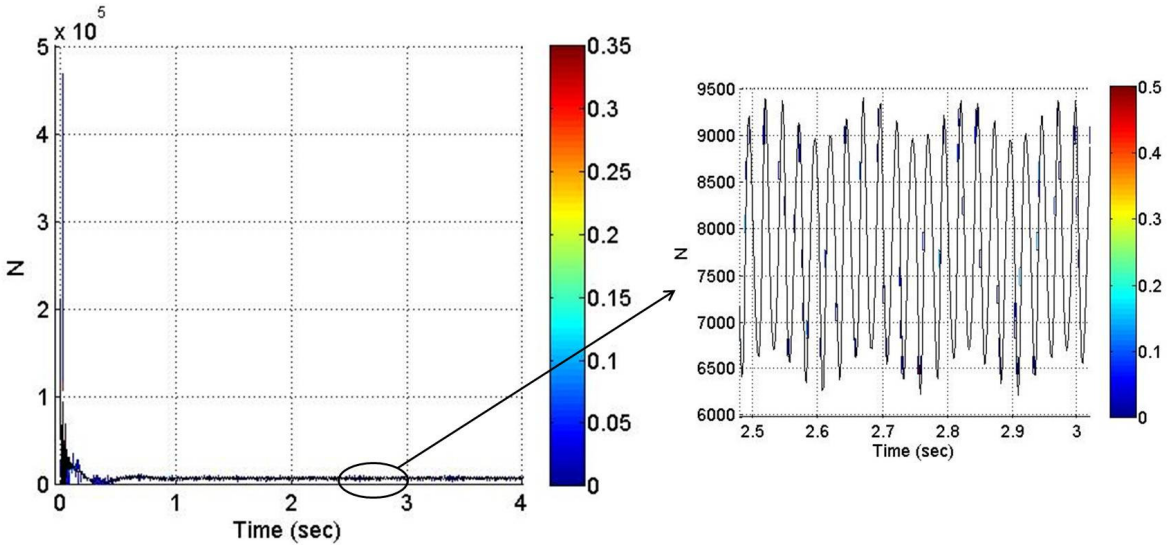

a. Collection (along the time axis) of the projections of the instantaneous PDF of F_n on the force-time plane, and a zoomed plot between 2.5 *sec* and 3 *sec*

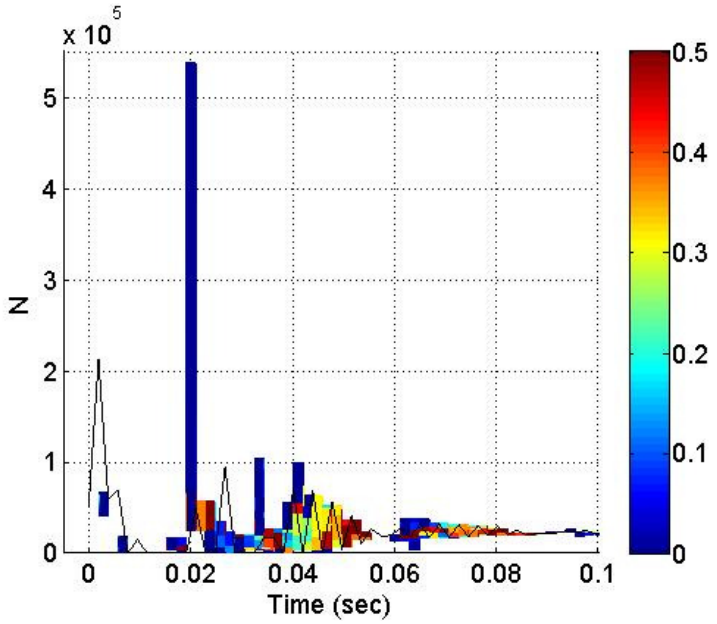

b. Collection (along the time axis) of the projections of the instantaneous PDF of F_n on the force-time plane for 0.1 *sec*

Figure 4.34 Collection (along the time axis) of the projections of the instantaneous PDF of F_n

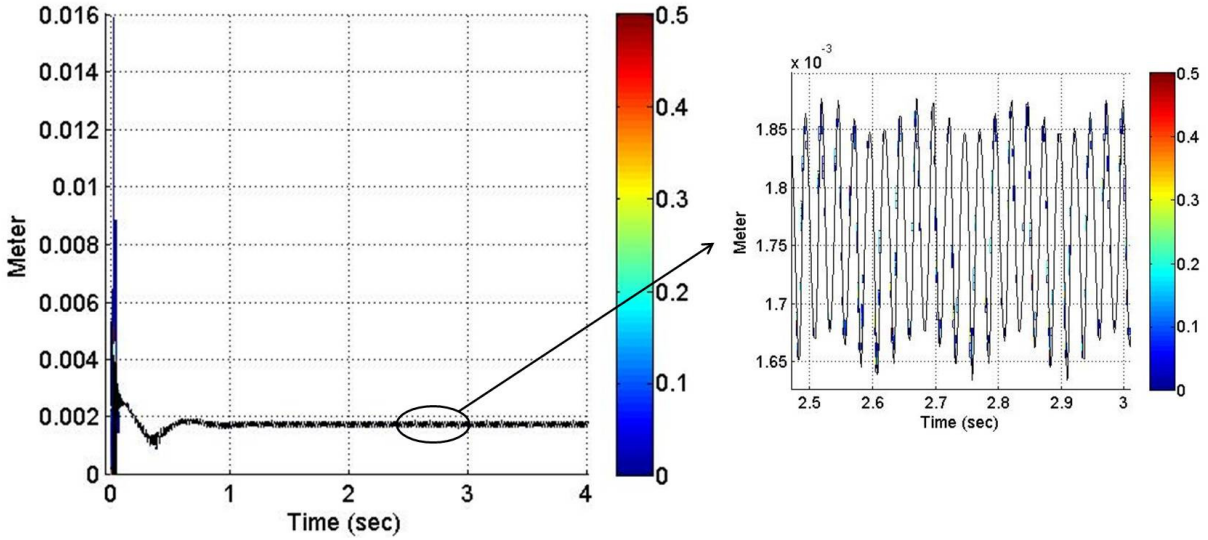

a. Collection (along the time axis) of the projections of the instantaneous PDF of *a* on the contact length-time plane, and a zoomed plot between 2.5 *sec* and 3 *sec*

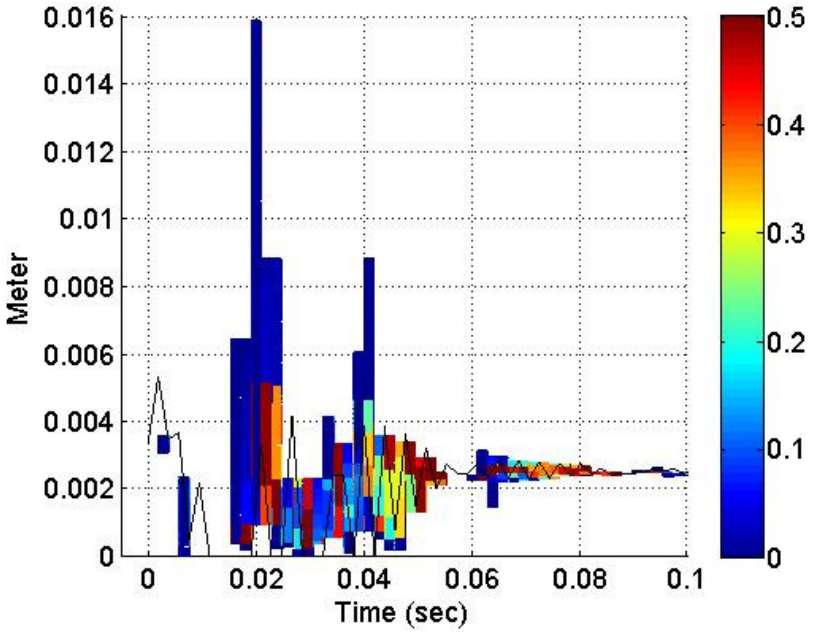

b. Collection (along the time axis) of the projections of the instantaneous PDF of *a* on the contact length-time plane for 0.1 *sec*

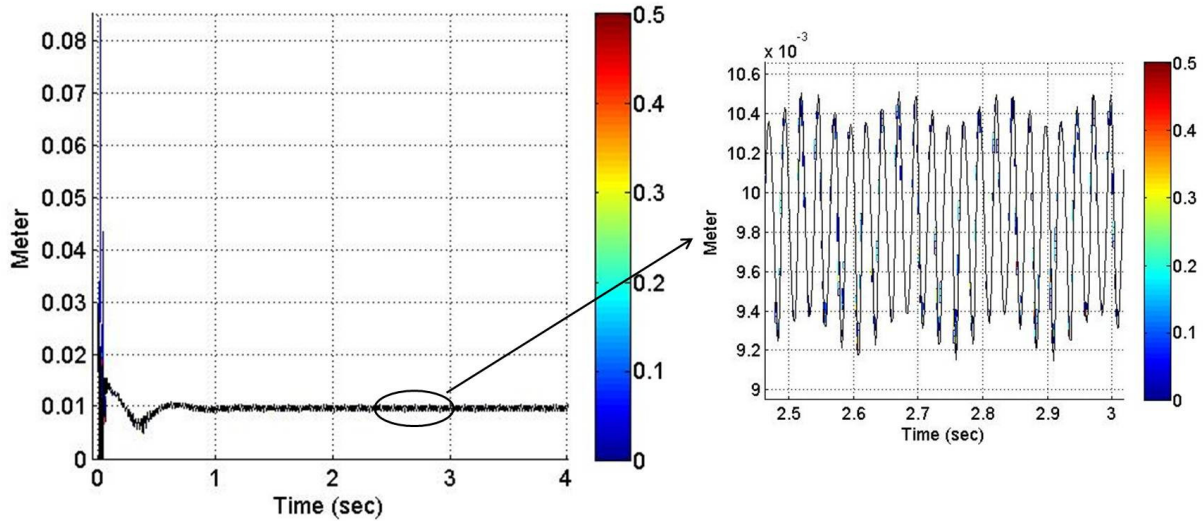

c. Collection (along the time axis) of the projections of the instantaneous PDF of *b* on the contact length-time plane, and a zoomed plot between 2.5 *sec* and 3 *sec*

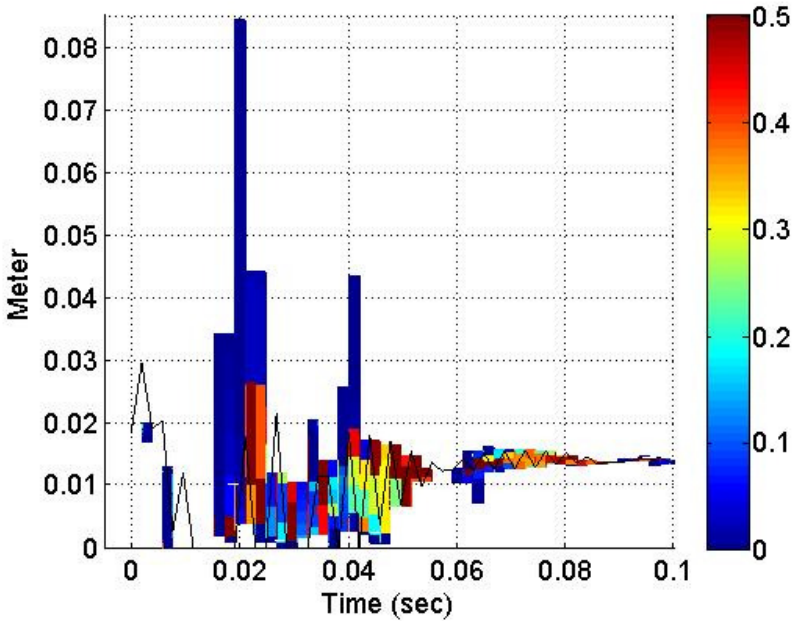

d. Collection (along the time axis) of the projections of the instantaneous PDF of *b* on the contact length-time plane for 0.1 *sec*

Figure 4.35 Collection (along the time axis) of the projections of the instantaneous PDF of semi-elliptical contact lengths

The stochastic μ_{stick} shows a PDF trend similar to that of the dynamic parameters above. In other words, it starts with a wide range of PDF, becomes narrower with time, and then shows

some PDFs around the boundaries, as demonstrated in Figure 4.36. The PDF of μ_{slip} and μ_{total} have similar PDF trends. Based on the results of this case study, the uncertain track stiffness has less effect on the CoF variation compared to other uncertain parameters, but it should still be considered for accurate design of the track system.

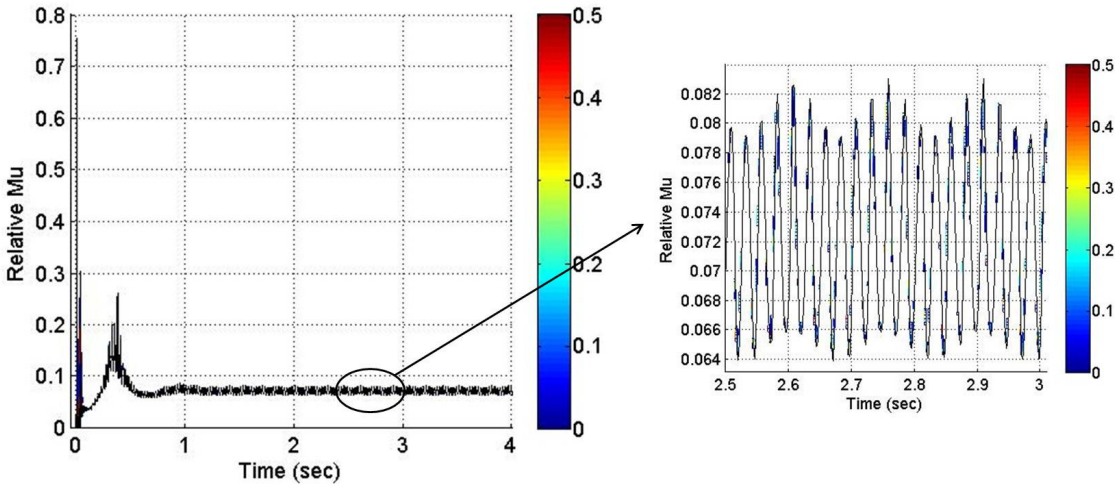

a. Collection (along the time axis) of the projections of the instantaneous PDF of μ_{stick} on the μ-t plane, and a zoomed plot between 2.5 *sec* and 3 *sec*

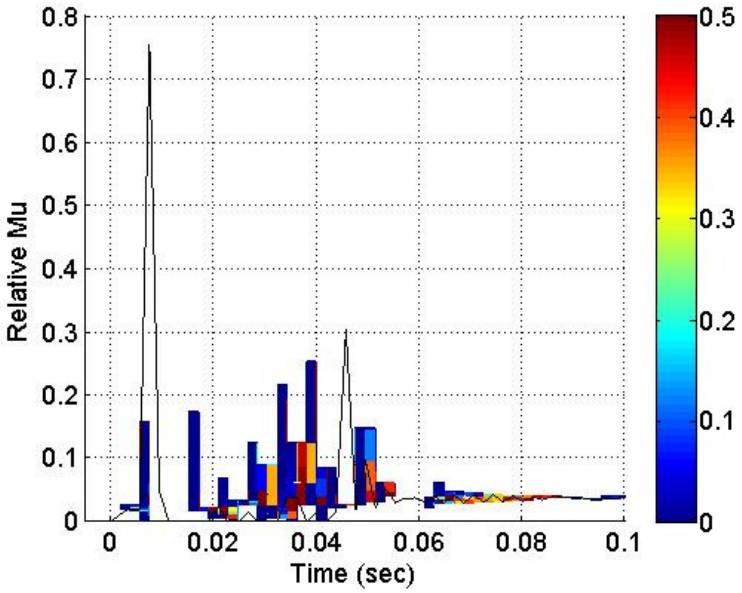

b. Collection (along the time axis) of the projections of the instantaneous PDF of μ_{stick} on the μ-t plane for 0.1 *sec*

Figure 4.36 Collection (along the time axis) of the projections of the instantaneous PDF of μ_{stick}

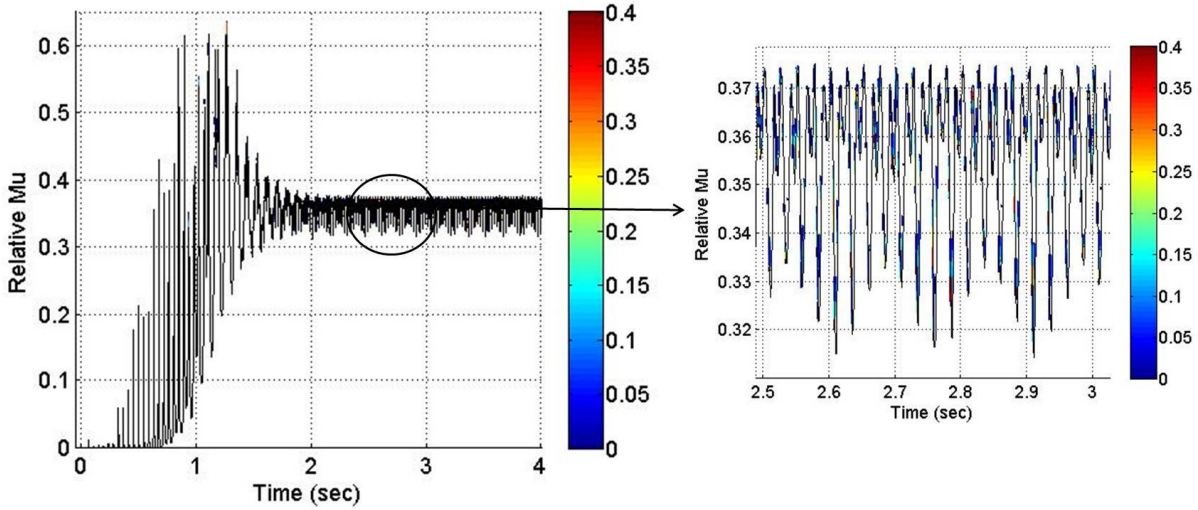

Figure 4.37 Collection (along the time axis) of the projections of the instantaneous PDF of μ_{slip} on the μ-t plane, and a zoomed plot between 2.5 *sec* and 3 *sec*

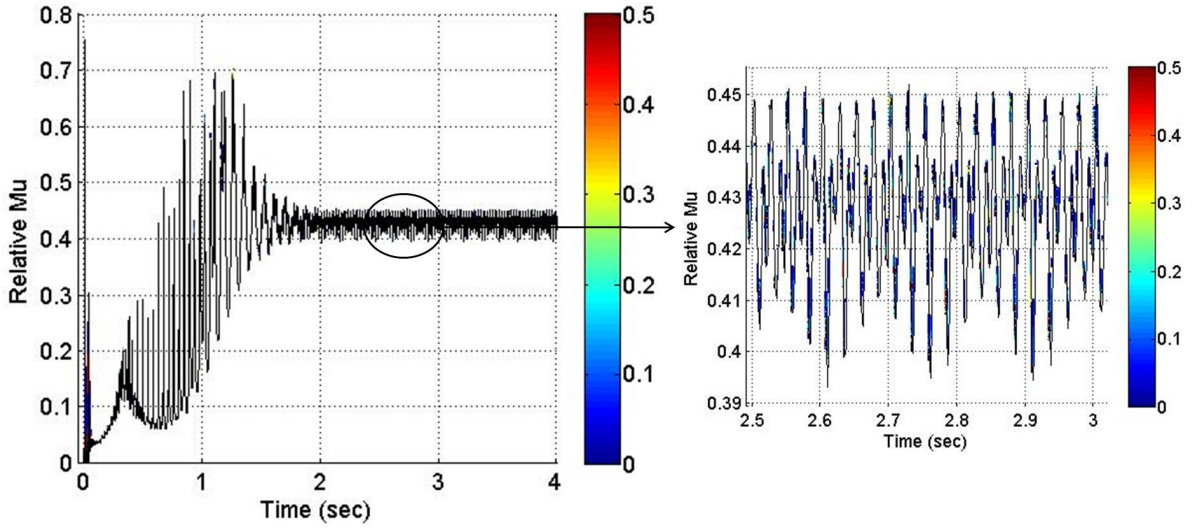

Figure 4.38 Collection (along the time axis) of the projections of the instantaneous PDF of μ_{total} on the μ-t plane, and a zoomed plot between 2.5 *sec* and 3 *sec*

Track Damping Coefficient

The effect of the uncertain track damping coefficient is calculated and analyzed. The PDF of CoFs and dynamic parameters are shown in Figure 4.39 through Figure 4.44. The effect of the uncertain track damping coefficient on the CoF is less than the effect of the track stiffness. The PDF results of the CoFs and of dynamic parameters are almost the same as the deterministic

value at steady state. A wide range of responses are shown for first 0.04 *sec*, and then it becomes narrower with time. These trends may result from instability of the wheel-rail dynamics due to the initial conditions. This case study shows that the effect of the uncertain track damping can potentially be neglected in the track design since the uncertain tack damping coefficient has very little effect on the dynamic parameters and on the CoFs compared to the PDF results of the uncertain track stiffness.

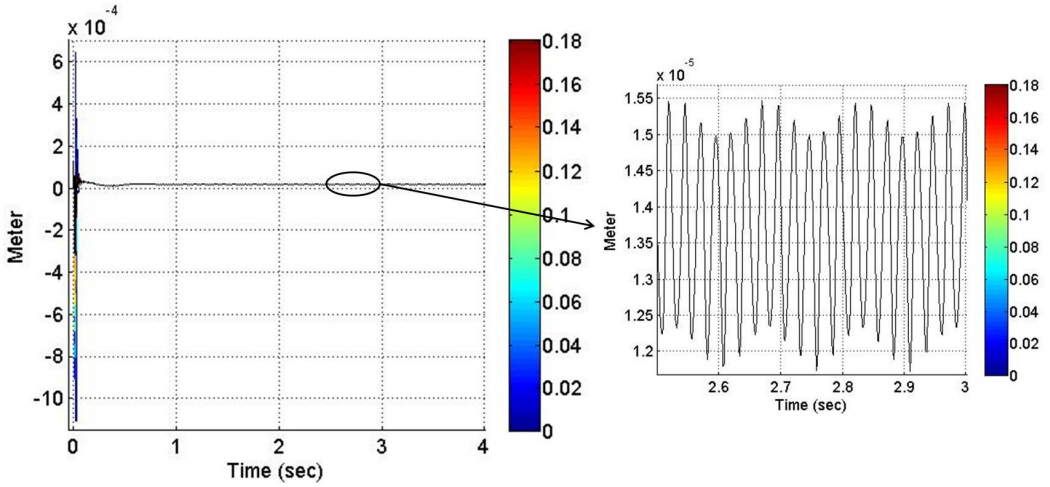

a. Collection (along the time axis) of the projections of the instantaneous PDF of R_w on the displacement-time plane, and a zoomed plot between 2.5 *sec* and 3 *sec*

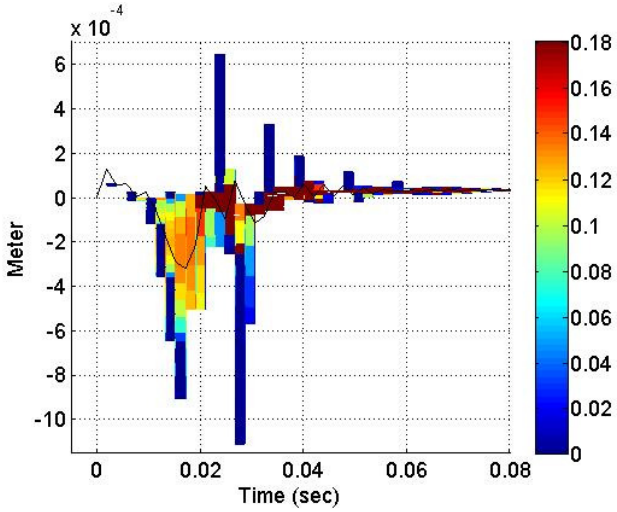

b. Collection (along the time axis) of the projections of the instantaneous PDF of R_w on the displacement-time plane for 0.08 *sec*

Figure 4.39 Collection (along the time axis) of the projections of the instantaneous PDF of R_w

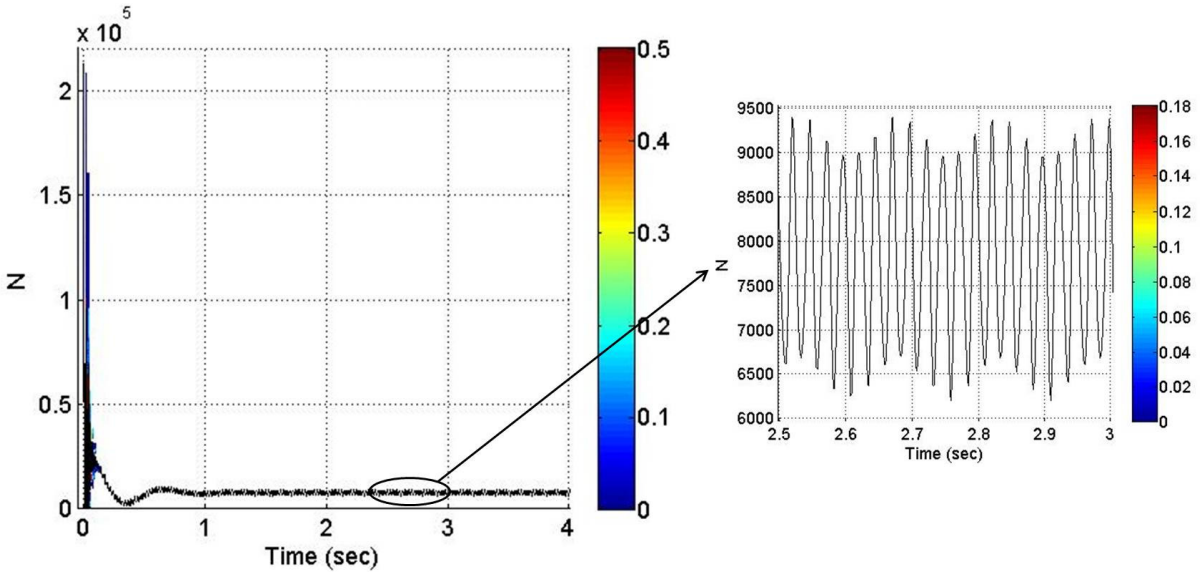

a. Collection (along the time axis) of the projections of the instantaneous PDF of F_n on the force-time plane, and a zoomed plot between 2.5 *sec* and 3 *sec*

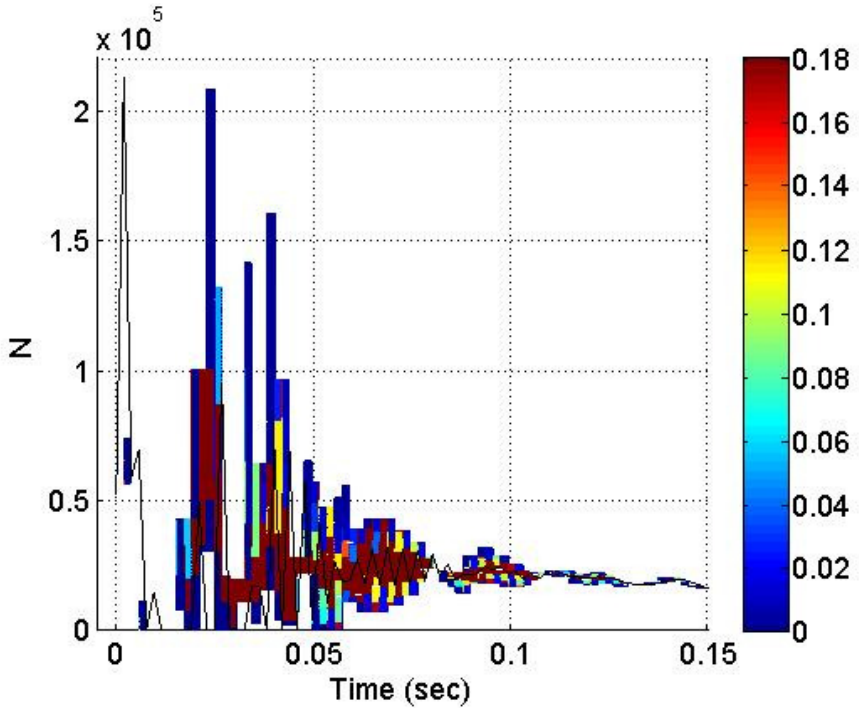

b. Collection (along the time axis) of the projections of the instantaneous PDF of F_n on the force-time plane for 0.15 *sec*

Figure 4.40 Collection (along the time axis) of the projections of the instantaneous PDF of F_n

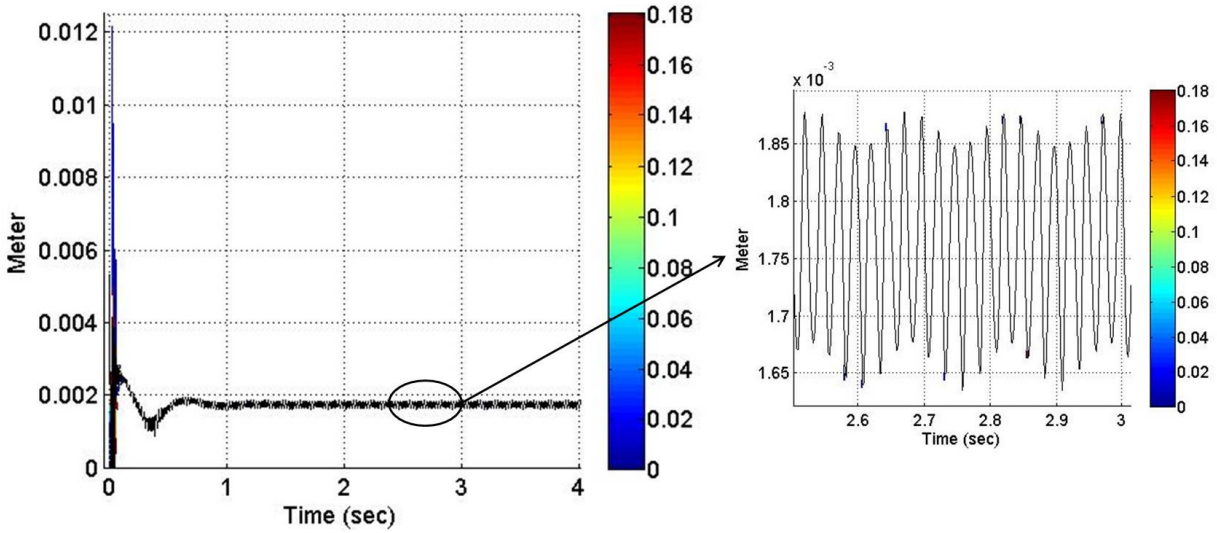

a. Collection (along the time axis) of the projections of the instantaneous PDF of *a* on the contact length-time plane, and a zoomed plot between 2.5 *sec* and 3 *sec*

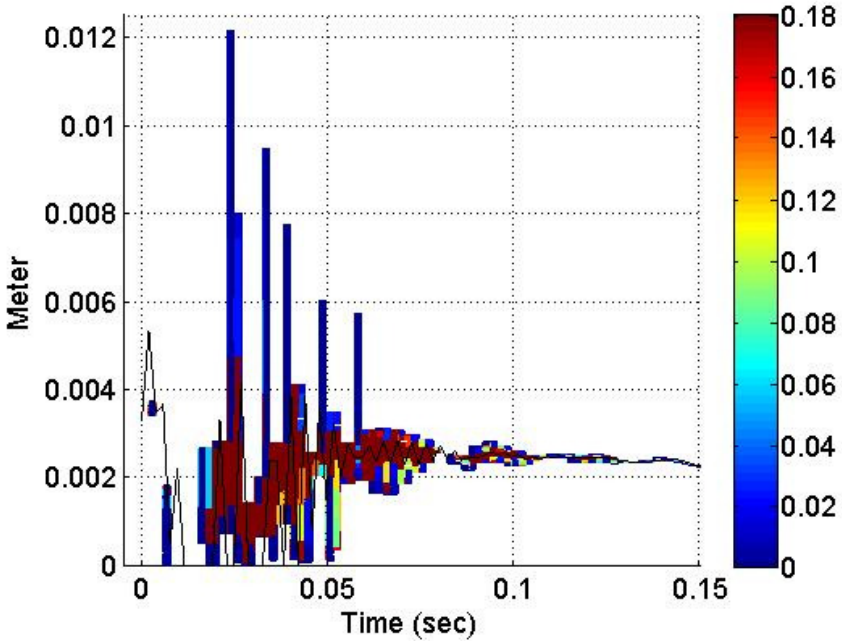

b. Collection (along the time axis) of the projections of the instantaneous PDF of *a* on the contact length-time plane for 0.15 *sec*

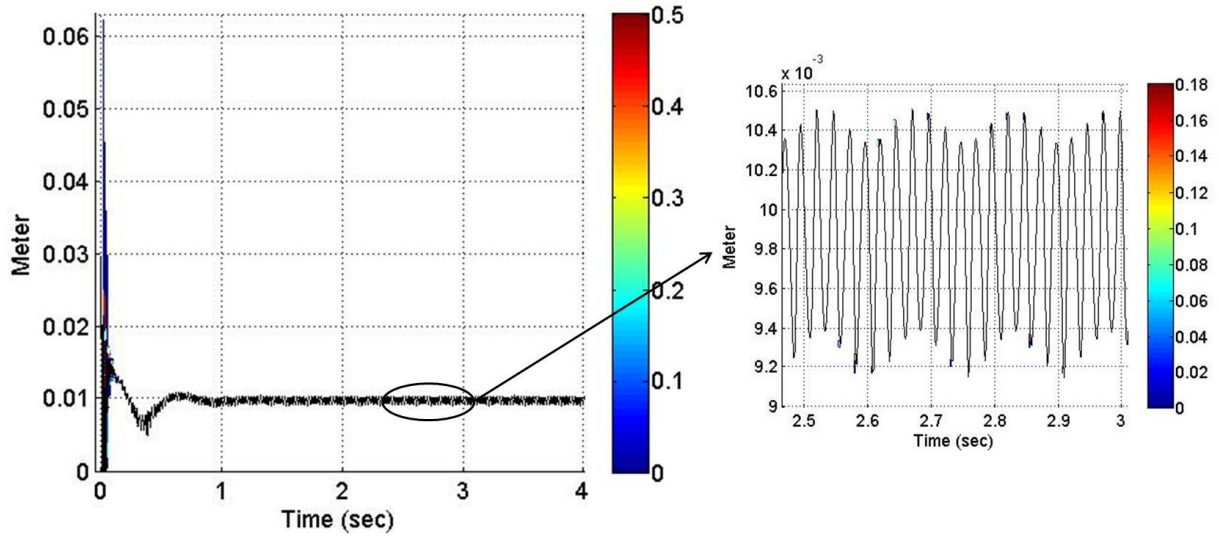

c. Collection (along the time axis) of the projections of the instantaneous PDF of *b* on the contact length-time plane, and a zoomed plot between 2.5 *sec* and 3 *sec*

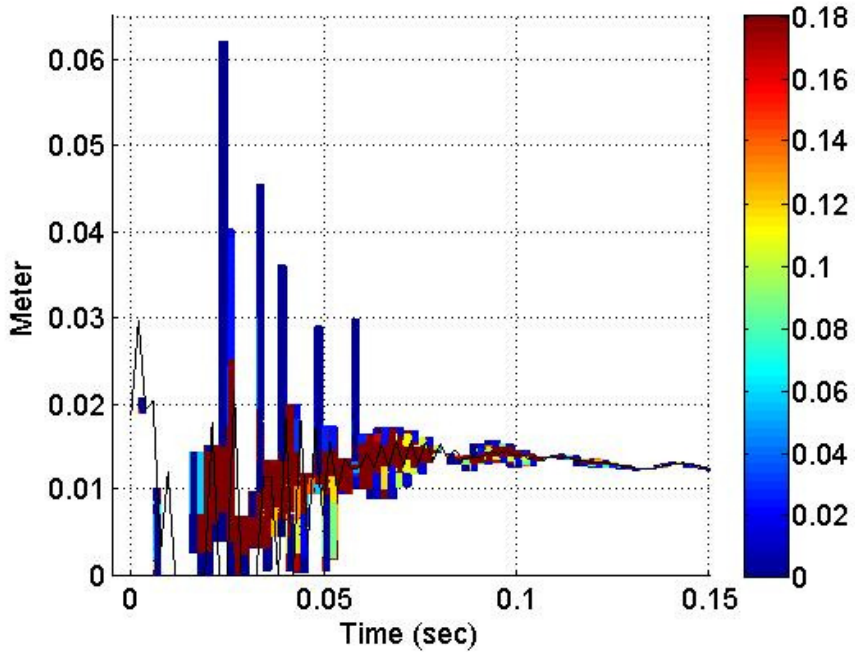

d. Collection (along the time axis) of the projections of the instantaneous PDF of *b* on the contact length-time plane for 0.15 *sec*

Figure 4.41 Collection (along the time axis) of the projections of the instantaneous PDF of semi-elliptical contact lengths

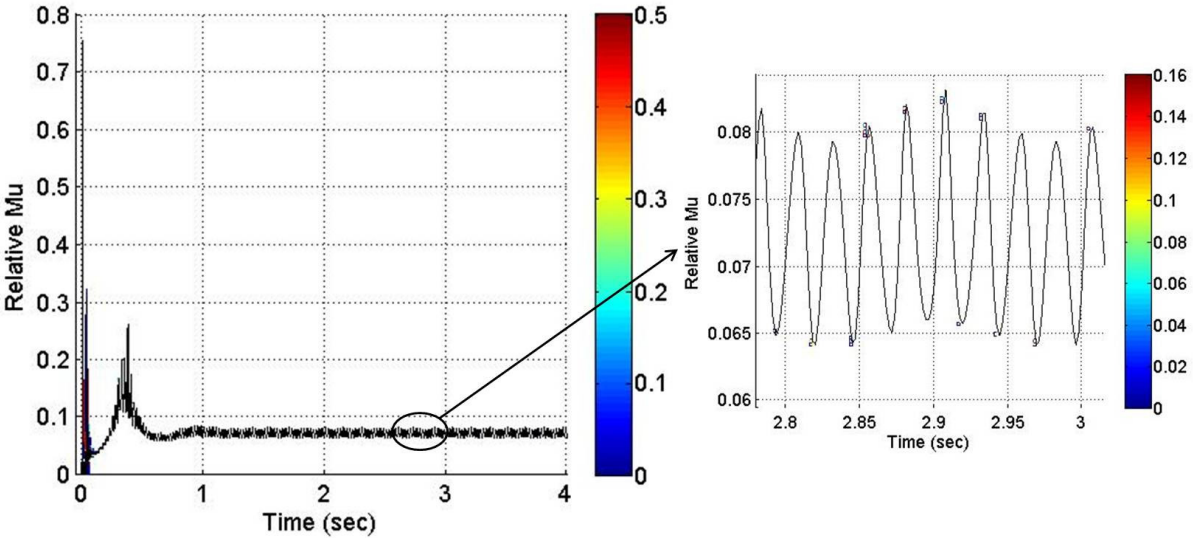

a. Collection (along the time axis) of the projections of the instantaneous PDF of μ_{stick} on the μ-t plane, and a zoomed plot between 2.8 *sec* and 3 *sec*

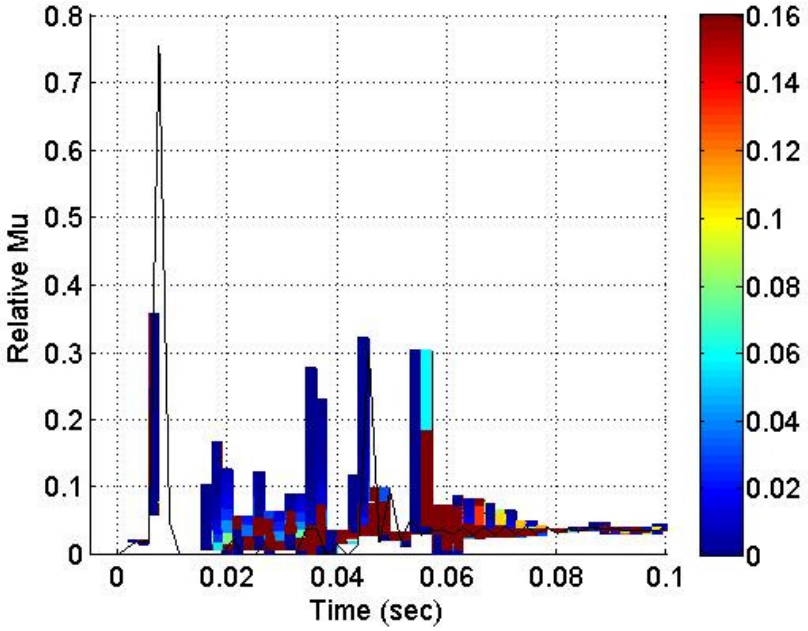

b. Collection (along the time axis) of the projections of the instantaneous PDF of μ_{stick} on the μ-t plane for 0.1 *sec*

Figure 4.42 Collection of the projections of the instantaneous PDF of μ_{stick}

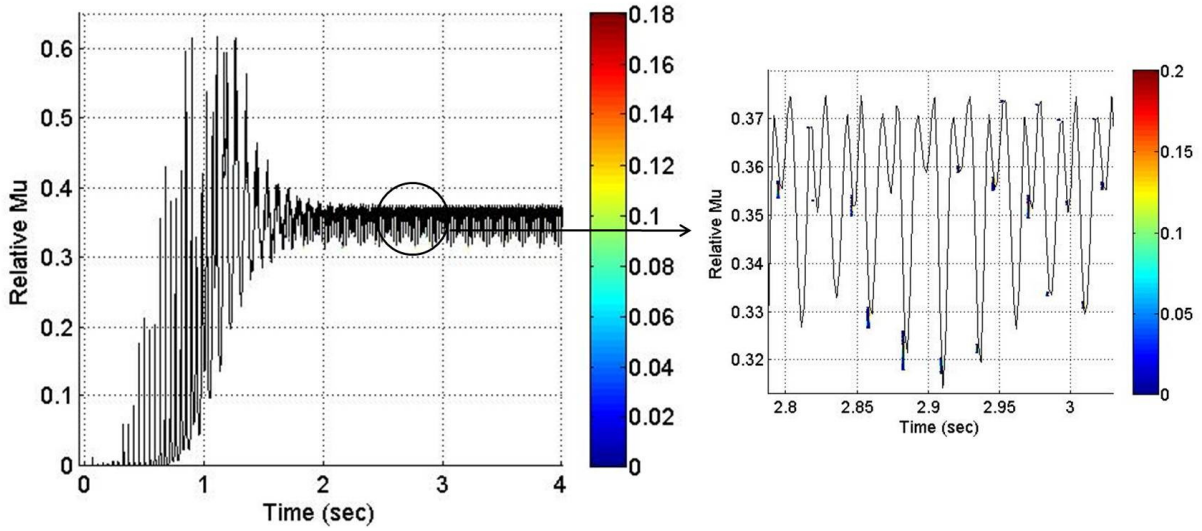

Figure 4.43 Collection (along the time axis) of the projections of the instantaneous PDF of μ_{slip} on the μ-t plane, and a zoomed plot between 2.8 *sec* and 3.1 *sec*

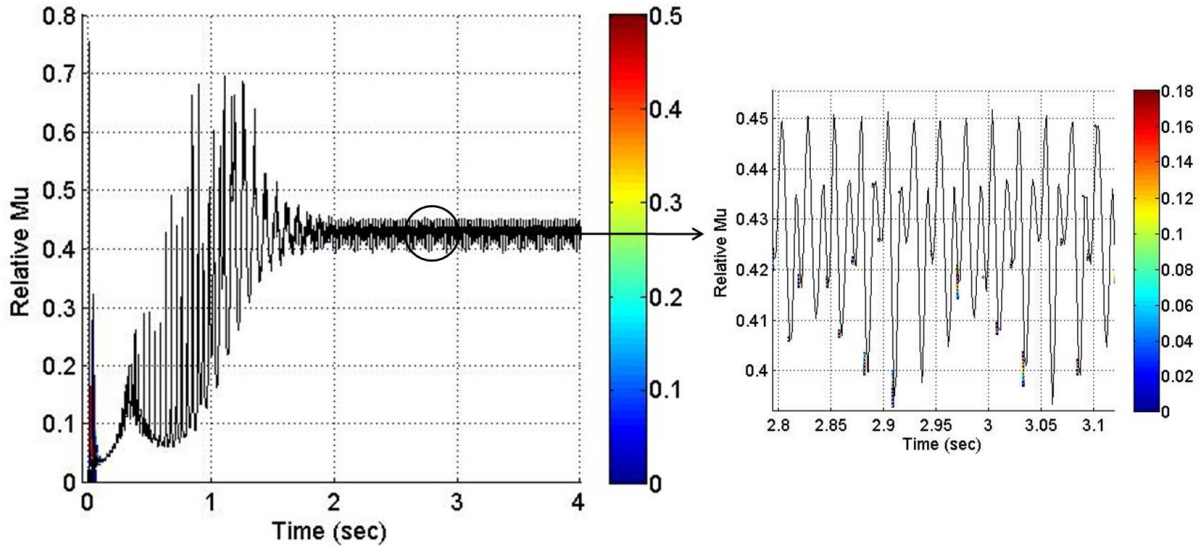

Figure 4.44 Collection (along the time axis) of the projections of the instantaneous PDF of μ_{total} on the μ-t plane, and a zoomed plot between 2.8 *sec* and 3.1 *sec*

4.2.2 Two Uncertain Variables

MARR and Lateral Displacement

This section focuses on the effect of two different uncertain variables, MARR and lateral displacement, on the CoFs and dynamic parameters to obtain more realistic stochastic results. It is assumed that these uncertain parameters have 50% uncertainty and symmetric beta distributions. The PDFs of the relative wheel-rail vibration and of the normal contact force are in Figure 4.45 and Figure 4.46, respectively. These results are almost the same as the PDFs considering only the uncertain MARR since both the relative wheel-rail vibration and the normal contact force has little influence on the uncertain lateral displacement due to the very small conicity. In other words, the vertical contact force is almost the same as the normal contact force. However, please note that there is still the effect of the uncertain lateral displacement, although it is very minor. The normal contact force is almost the same as a function of the relative wheel-rail vibration caused by the rail roughness excitation, as in Equation (3.26). The relative wheel-rail vibration is almost the same as a function of rail roughness and vibrations of the wheel and the rail, as described in Equation (3.27).

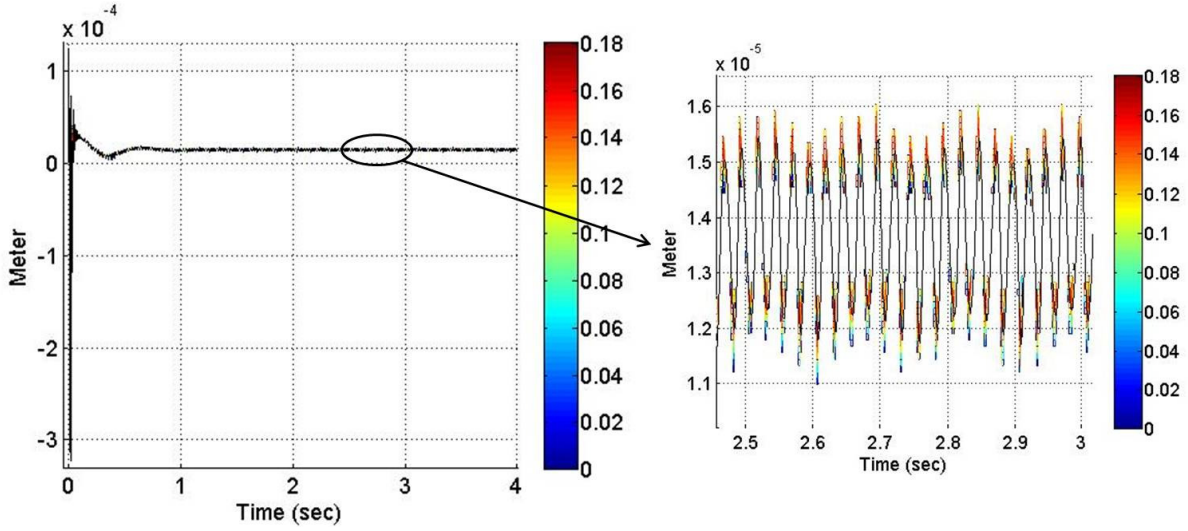

Figure 4.45 Collection (along the time axis) of the projections of the instantaneous PDF of h_o on the displacement-time plane, and a zoomed plot between 2.5 *sec* and 3 *sec*

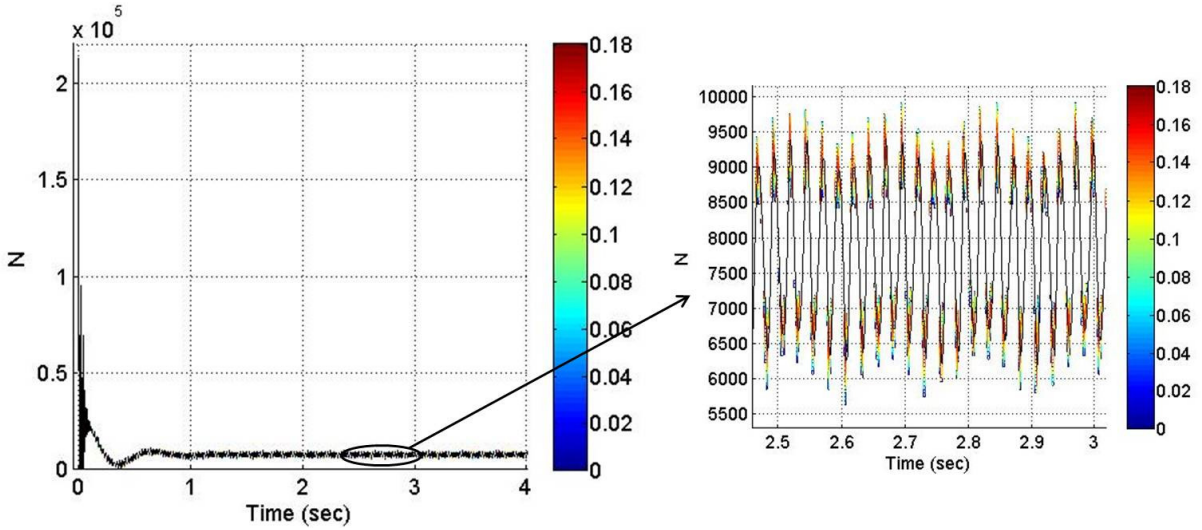

Figure 4.46 Collection (along the time axis) of the projections of the instantaneous PDF of F_n on the force-time plane, and a zoomed plot between 2.5 *sec* and 3 *sec*

The stochastic results of the radii of curvature for the wheel and the rail are presented in Figure 4.47. These results similar to the PDF obtained when only the uncertain lateral displacement was considered, since both of them are only a function of lateral displacement, as described in Equations (3.19) and (3.36).

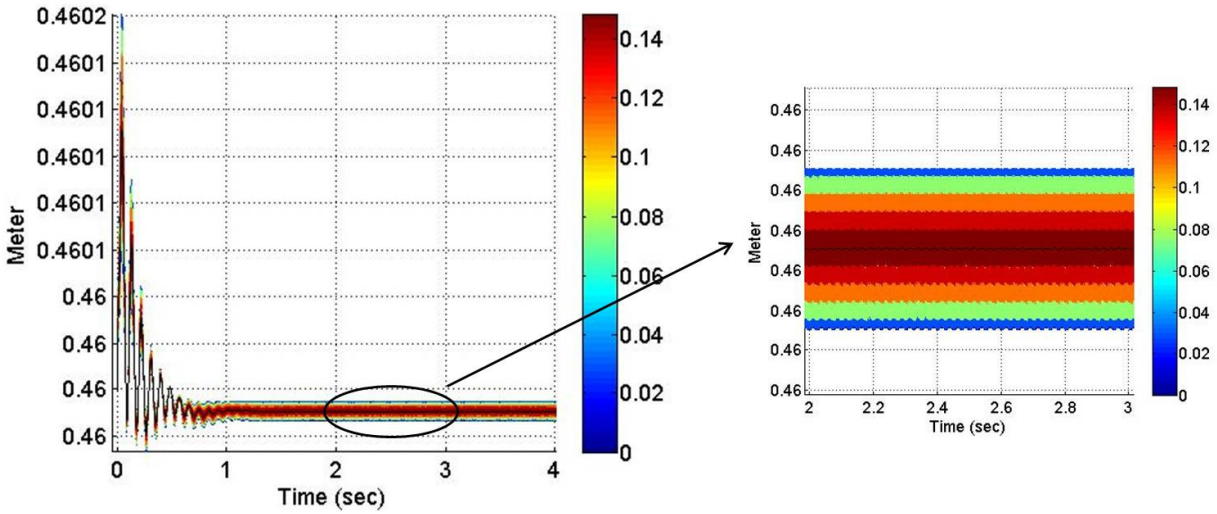

a. Collection (along the time axis) of the projections of the instantaneous PDF of R_w on the displacement-time plane, and a zoomed plot between 2 *sec* and 3 *sec*

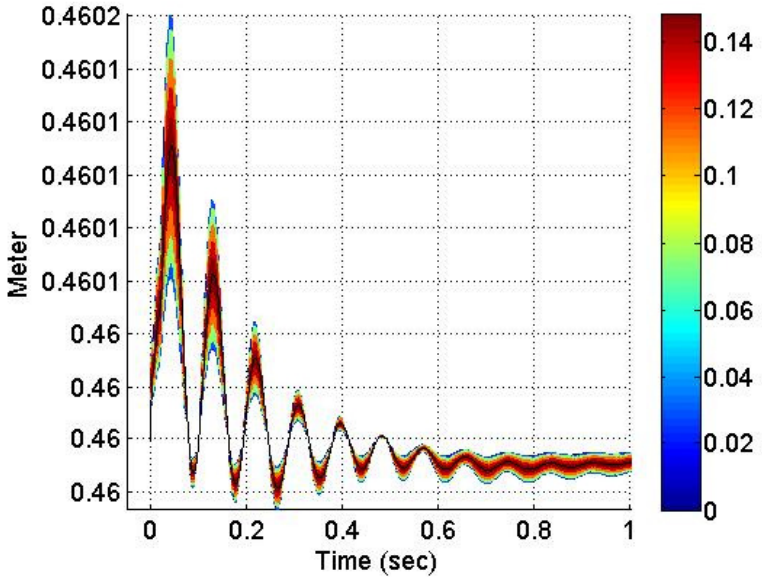

b. Collection (along the time axis) of the projections of the instantaneous PDF of R_w on the displacement-time plane for 1 *sec*

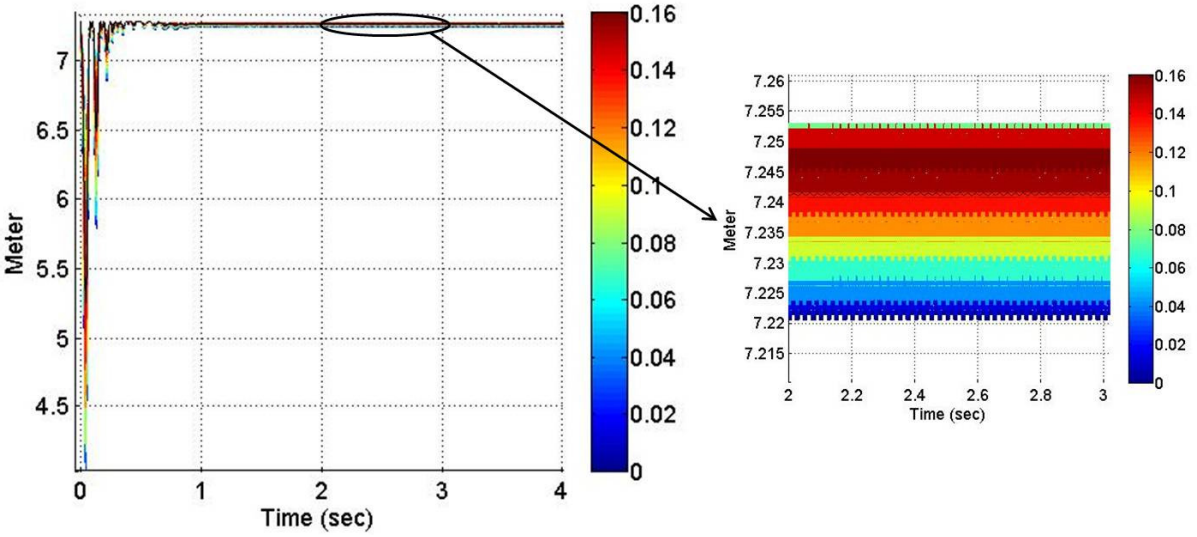

c. Collection (along the time axis) of the projections of the instantaneous PDF of R_r on the displacement-time plane, and a zoomed plot between 2 *sec* and 3 *sec*

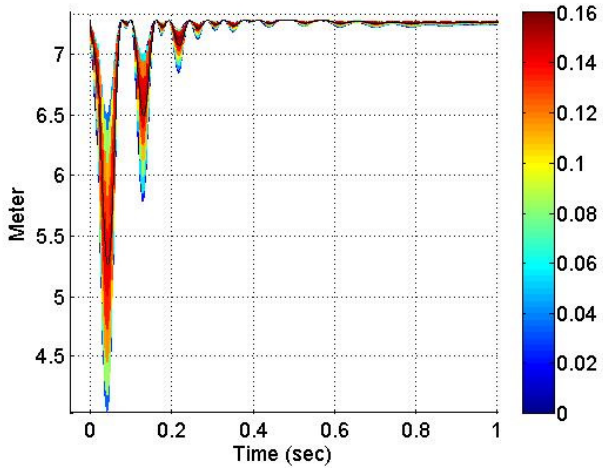

d. Collection (along the time axis) of the projections of the instantaneous PDF of R_w on the displacement-time plane for 1 *sec*

Figure 4.47 Collection (along the time axis) of the projections of the instantaneous PDF of radii of curvature for the wheel and the rail

Figure 4.48 illustrates the PDF of the semi-elliptical contact lengths, *a* and *b*. These results are very similar to the PDF results from the uncertain MARR due to the dominant influence of the uncertain MARR and the slight effect of the uncertain lateral displacement, as shown in Figure 4.17 and Figure 4.23. However, PDFs from a combination of the uncertain MARR and the lateral displacement display a wider PDF range than that of the uncertain MARR due to the effect, although minor, of the uncertain lateral displacement.

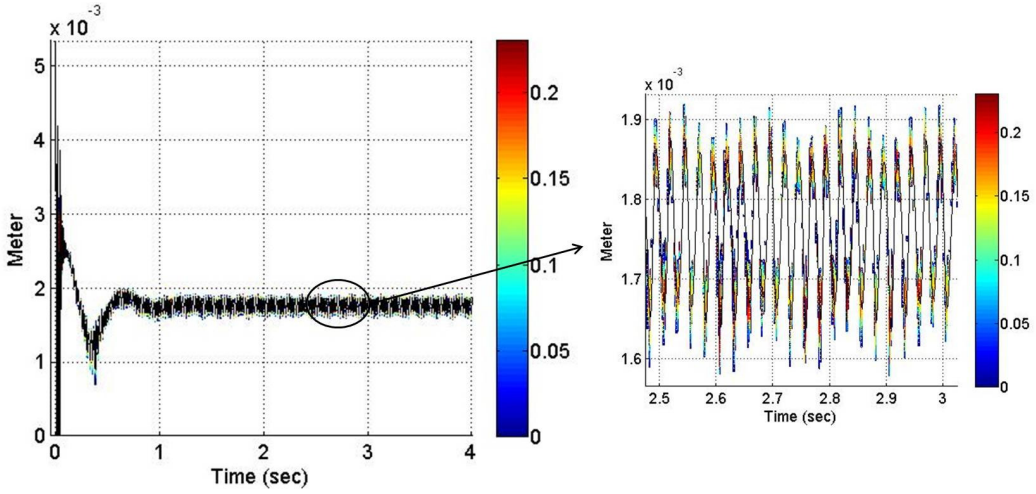

a. Collection (along the time axis) of the projections of the instantaneous PDF of *a* on the contact length-time plane, and a zoomed plot between 2.5 *sec* and 3 *sec*

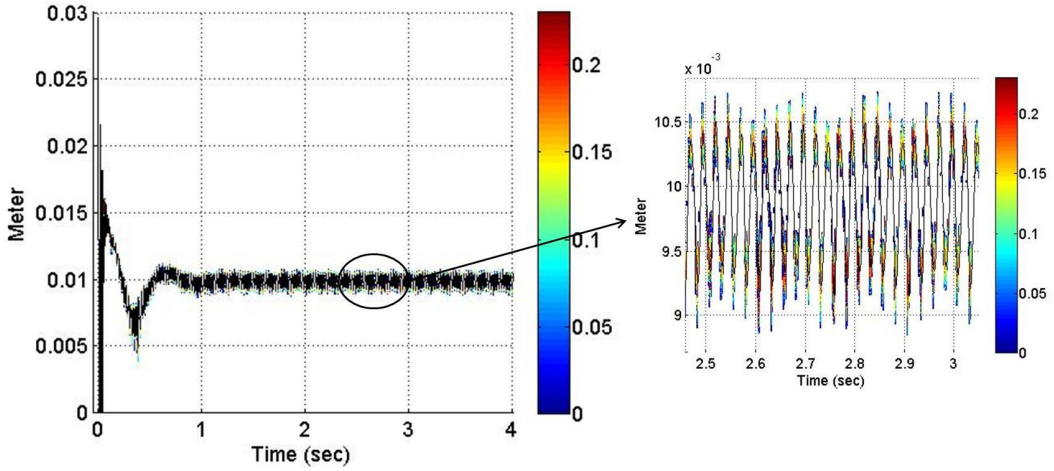

b. Collection (along the time axis) of the projections of the instantaneous PDF of *b* on the contact length-time plane, and a zoomed plot between 2.5 *sec* and 3 *sec*

Figure 4.48 Collection (along the time axis) of the projections of the instantaneous PDF of semi-elliptical contact lengths

The PDF of μ_{stick} is presented in Figure 4.49 and is the same as the PDF of μ_{stick} from the uncertain MARR, as illustrated in Figure 4.24, since the μ_{stick} component does not include any parameter that is dominantly affected by the lateral displacement. The distribution is symmetric with respect to the deterministic value.

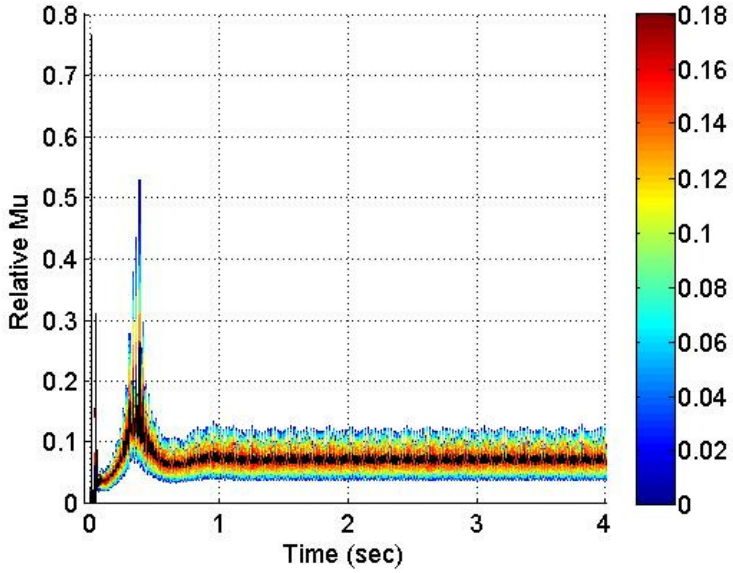

Figure 4.49 Collection (along the time axis) of the projections of the instantaneous PDF of μ_{stick} on the μ-*t* plane

Figure 4.50 displays the PDF of μ_{slip}. The PDF of μ_{slip} is skewed upward with respect to the deterministic value. The highest PDF is close to the deterministic value. The PDF of μ_{slip} from a combination of the uncertain MARR and the uncertain lateral displacement shows a wider PDF range than that from the uncertain lateral displacement only, as shown in Figure 4.19, or the uncertain MARR only, as presented in Figure 4.25. This is because the two uncertain variables influence the μ_{slip} component simultaneously.

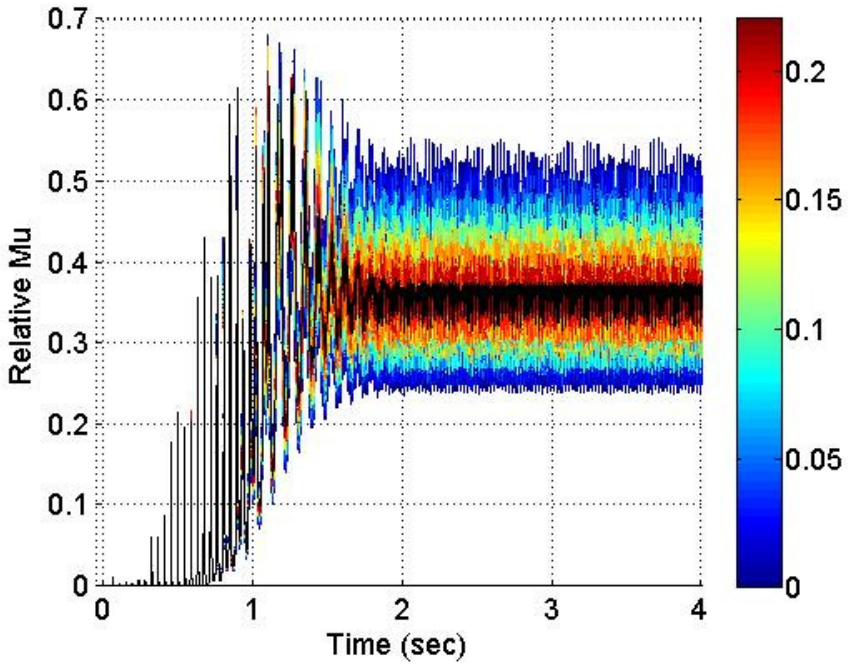

Figure 4.50 Collection (along the time axis) of the projections of the instantaneous PDF of μ_{slip} on the μ-t plane

According to the difference between the PDFs of μ_{stick} and μ_{slip} considering one uncertainty (the lateral displacement or the MARR) and two uncertainties (a combination of the MARR and the lateral displacement), the PDFs of μ_{total} also show the PDF range difference. The μ_{total} PDF before 1 *sec* is symmetric. During this time the highest PDF is not shown in red but in orange since the PDF is more uniformly distributed than the PDF after 1 *sec*, as explained above. The μ_{total} PDF after 1 *sec* is slightly skewed upward with respect to the deterministic values since it is mostly influenced by μ_{slip}. The μ_{total} PDF of a combination of the uncertain MARR and the uncertain lateral displacement has a lot wider range than the μ_{total} PDF of the uncertain MARR only and of the uncertain lateral displacement only after 1 *sec*.

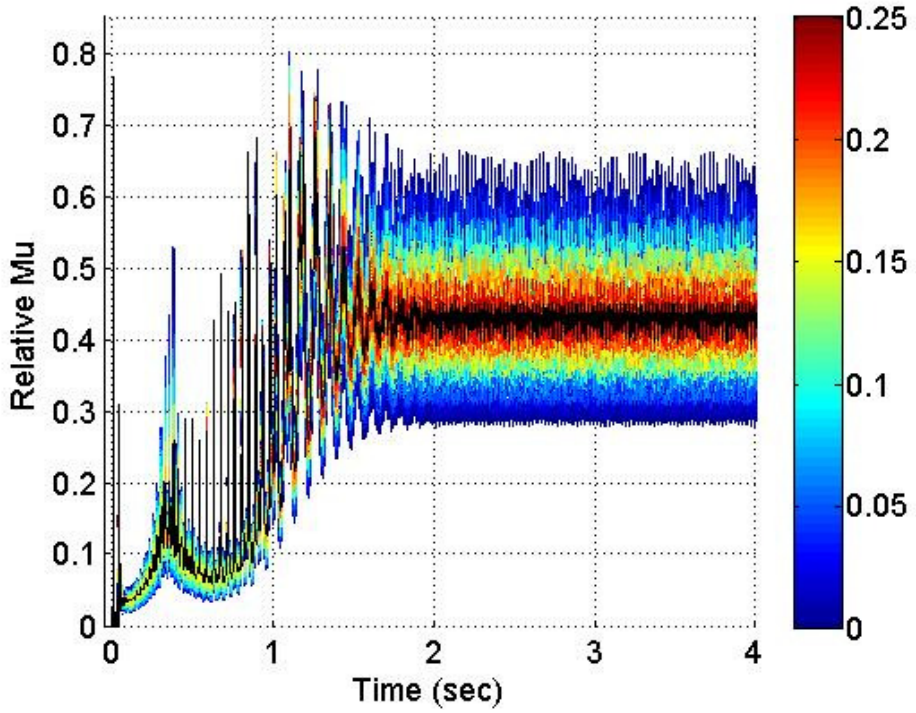

Figure 4.51 Collection (along the time axis) of the projections of the instantaneous PDF of μ_{total} on the μ-t plane

Semi-elliptical Contact Lengths, *a* and *b*

This section focuses on the effect of a combination of the uncertain semi-elliptical contact lengths (*a* and *b*) on the CoF model. Both uncertain parameters are assumed to have 50% uncertainty and symmetric beta distributions. The values of μ_{stick}, μ_{slip}, and μ_{total} are calculated and analyzed since *a* and *b* occurs only in the CoF model.

Figure 4.52 demonstrates the PDF of μ_{stick}. The PDF is skewed upward with respect to the deterministic value like the PDF of the uncertain *a/b* case. However, the PDF range is a lot wider than that of the uncertain *a/b*. The highest PDF is close to the deterministic value.

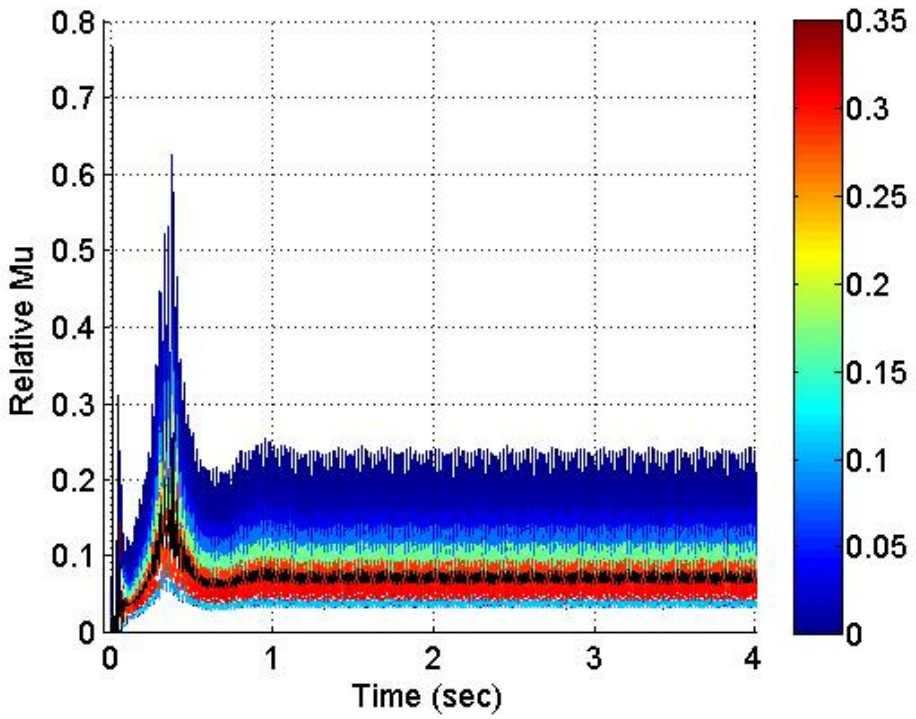

Figure 4.52 Collection (along the time axis) of the projections of the instantaneous PDF of μ_{stick} on the μ-t plane

The PDF of the stochastic μ_{slip} is displayed in the Figure 4.53. PDF's occurring before 1 sec are shown in Figure 4.53 (a). Of all the case studies in this dissertation, the combination of uncertain a and b is the only one to show PDFs. Thus, this result indicates that the semi-elliptical contact lengths are the most important parameters to characterize a correct CoF distribution. The highest PDF is very close to the deterministic value until around 1.5 *sec*, and then is shifted upward with respect to the deterministic values, as illustrated in Figure 4.53 (b). The PDF is skewed upward with respect to the deterministic value.

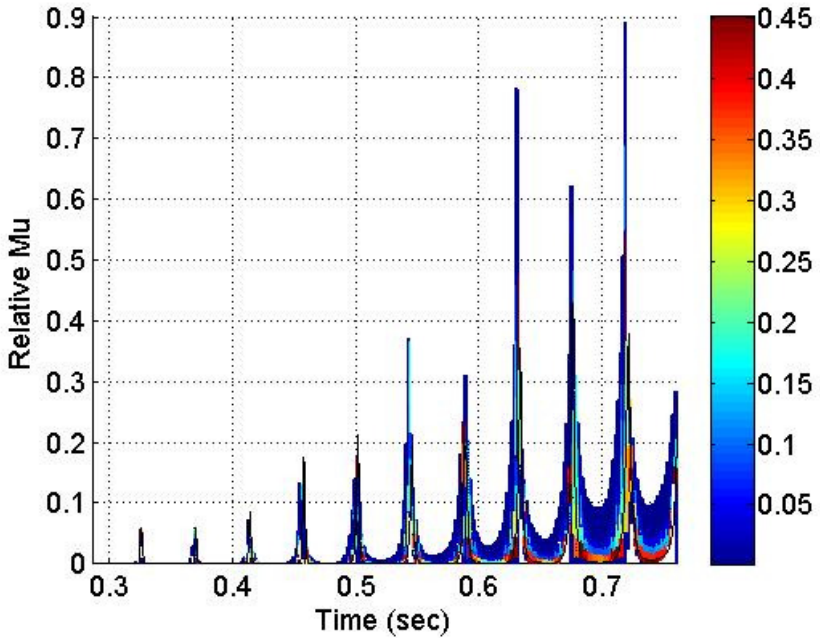

a. Collection (along the time axis) of the projections of the instantaneous PDF of μ_{slip} on the μ-t plane for 0.75 *sec*

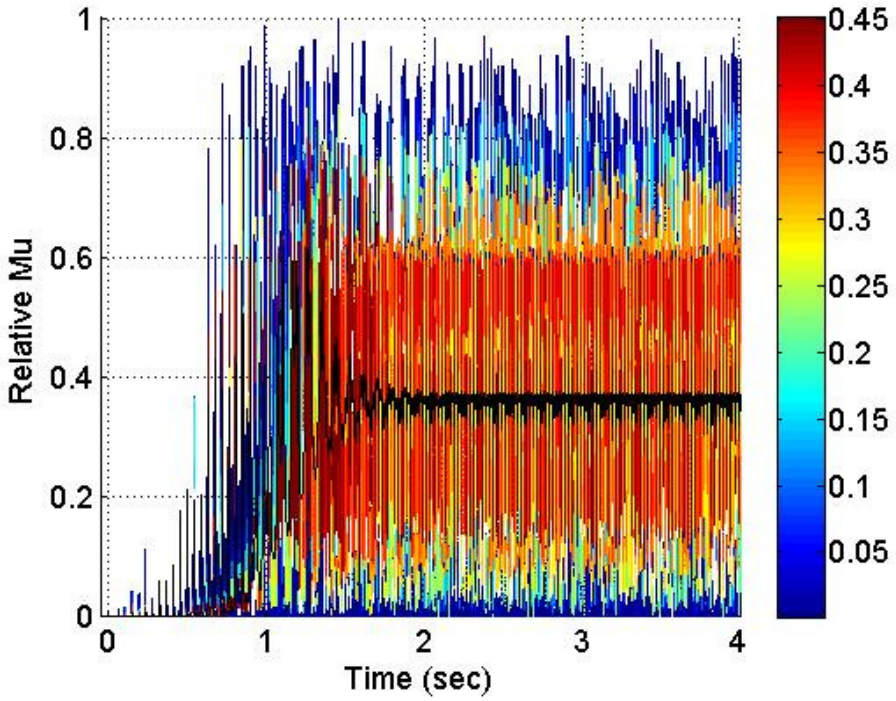

b. Collection (along the time axis) of the projections of the instantaneous PDF of μ_{slip} on the μ-t plane for 4 *sec*

Figure 4.53 Collection of the projections of the instantaneous PDF of μ_{slip}

The μ_{total} PDF is illustrated in Figure 4.54. As mentioned above, the contact patch size is directly related to the CoF variation. The PDF of μ_{total} is still mainly influenced by the stick CoF PDF before 1 *sec* since the PDF range of μ_{slip} is relatively small compared to the PDF of μ_{stick}. The PDF of μ_{slip} dominantly influences the stochastic μ_{total} after 1 *sec*. The highest PDF value, dark red color, is not close to the deterministic values, but it is shifted upward with respect to the deterministic values after 1 *sec*. The distribution of the μ_{total} PDF is more uniform before 1 *sec*. The range of PDF for a combination of the uncertain a and b is from 0 to almost 1. Thus, the μ_{total} PDF has a much wider range than the PDF result of any one uncertain parameter and the PDF combination of the uncertain MARR and the uncertain lateral wheel displacement. This result represents that the wrong calculation of semi-elliptical contact lengths leads to a big miss-calculation of the CoF.

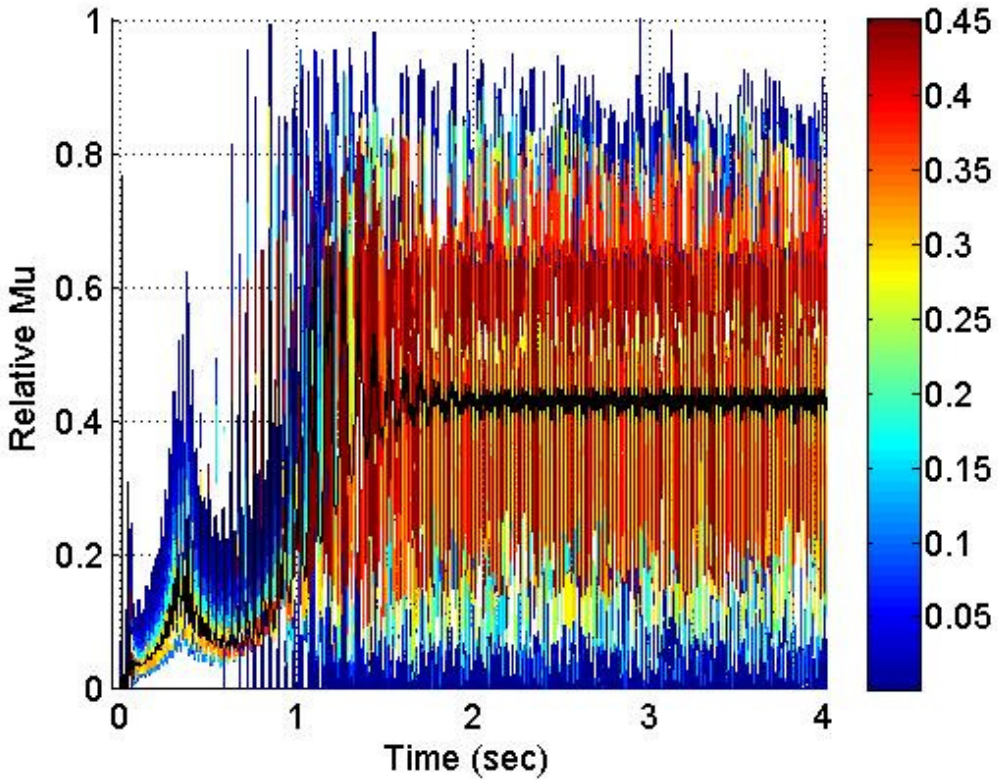

Figure 4.54 Collection (along the time axis) of the projections of the instantaneous PDF of μ_{total} on the μ-t plane

MARR and Sleeper Distance

This section illustrates the effect of a combination of uncertain MARR and uncertain sleeper distance on the CoF and on several dynamic parameters (the relative wheel-rail vibrations, the normal contact force, and the semi-elliptical contact lengths). The PDF results for the CoFs and for dynamic parameters are calculated and analyzed.

The PDFs of dynamic parameters are shown in Figure 4.55 through Figure 4.57. These PDF results illustrate similar trends. The PDF result shows a much wider range than the PDF result of the uncertain MARR and the PDF of the uncertain sleeper distance. In addition, the stochastic results are more frequently at steady state compared to the PDF result of the uncertain sleeper distance due to the effect of the uncertain MARR. However, the general PDF trend is very similar to the stochastic result of the uncertain sleeper distance. In other words, some PDFs are skewed upward while others are skewed downward with respect to the deterministic value. The highest PDF values coincide with the deterministic values, and the PDF range becomes narrower with time. The PDF range at around 0.4 *sec* is wider than the range after 0.4 *sec*.

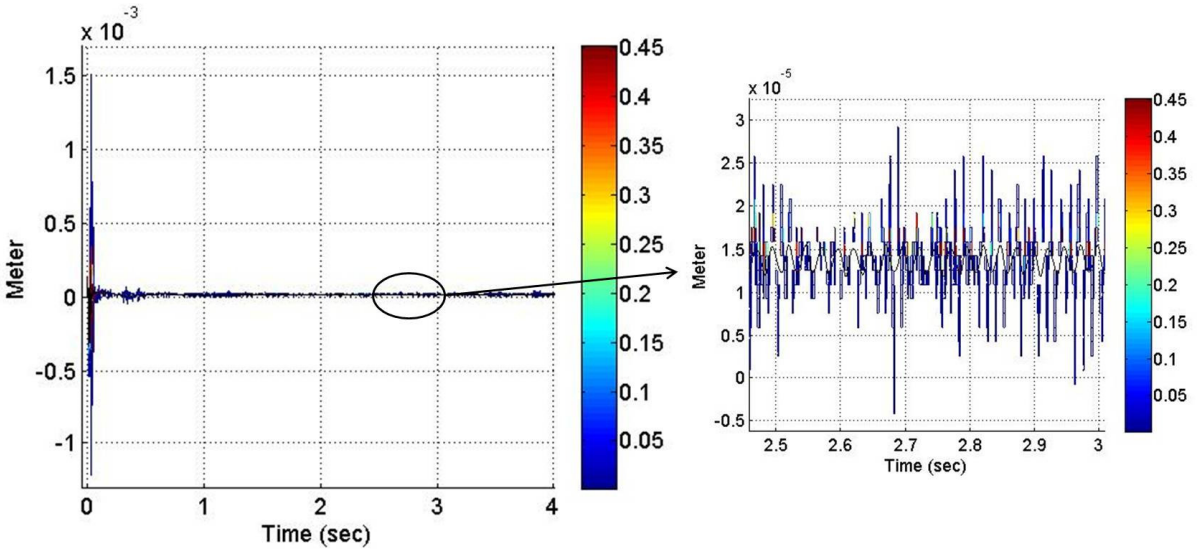

a. Collection (along the time axis) of the projections of the instantaneous PDF of h_o on the displacement-time plane, and a zoomed plot between 2.5 *sec* and 3 *sec*

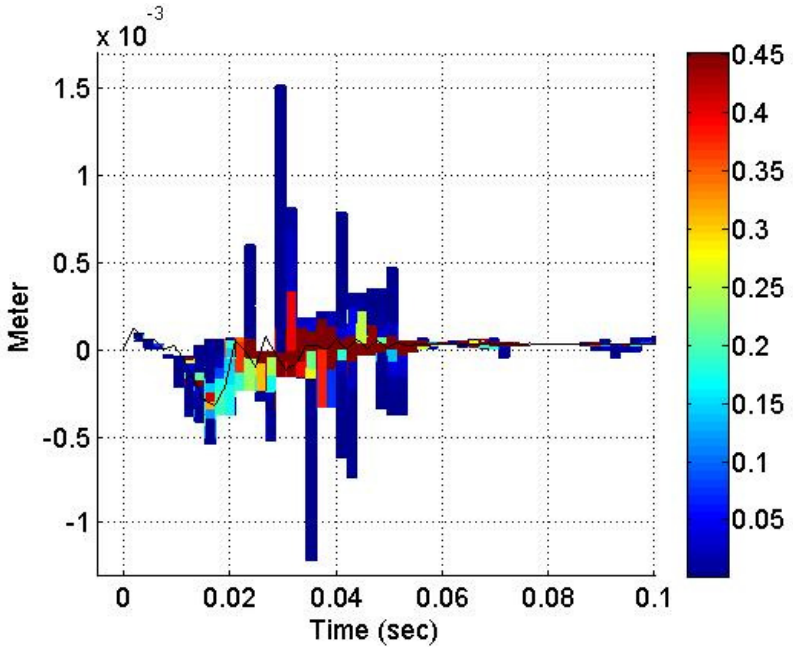

b. Collection (along the time axis) of the projections of the instantaneous PDF of h_o on the displacement-time plane for 0.1 *sec*

Figure 4.55 Collection of the projections of the instantaneous PDF of h_o

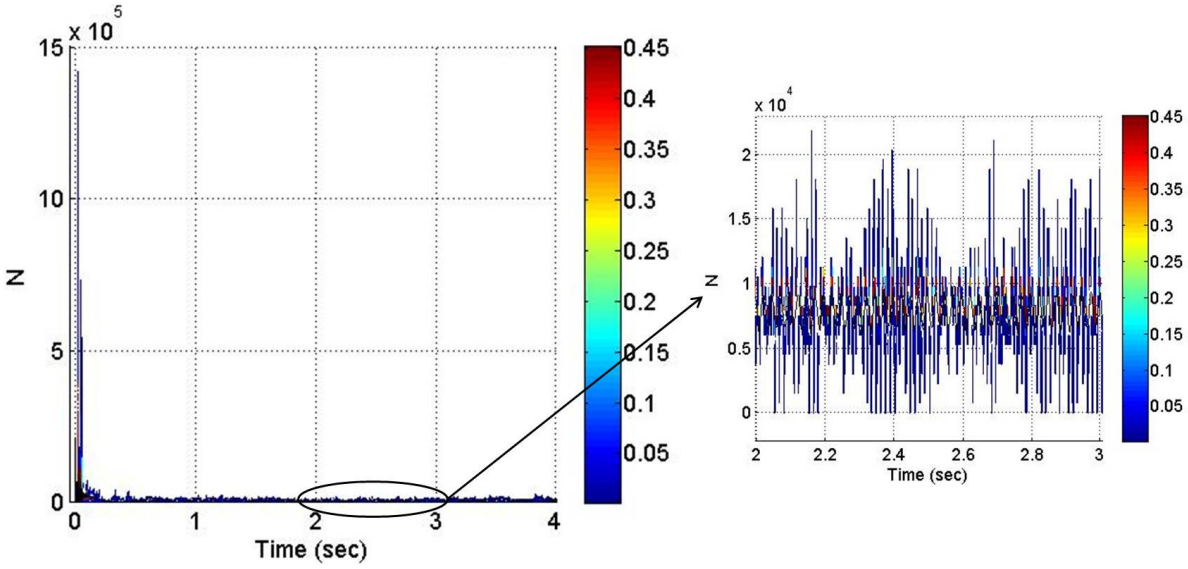

a. Collection (along the time axis) of the projections of the instantaneous PDF of F_n on the force-time plane, and a zoomed plot from 2 *sec* to 3 *sec*

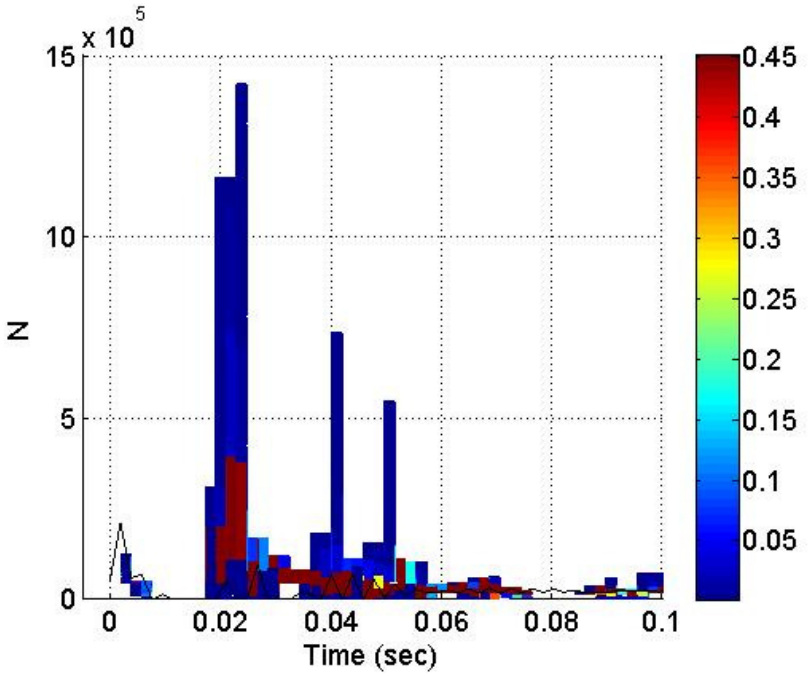

b. Collection (along the time axis) of the projections of the instantaneous PDF of F_n on the force-time plane for 0.1 *sec*

Figure 4.56 Collection of the projections of the instantaneous PDF of F_n

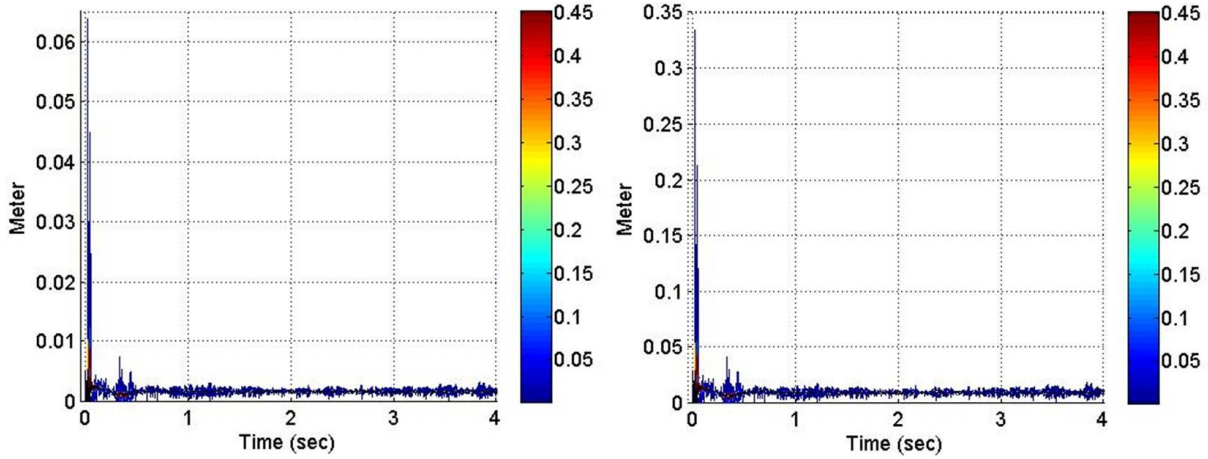

Figure 4.57 Collection (along the time axis) of the projections of the instantaneous PDF of *a* and *b* on the contact length-time plane

The PDFs of the CoFs are demonstrated in Figure 4.58 through 4.60. The stochastic μ_{stick} has a much wider PDF range than the PDF of any one uncertain parameter. Unlike the stick PDF of the uncertain sleeper distance, the stochastic μ_{stick} has a continuous PDF due to the effect of the uncertain MARR. The PDF is skewed upward, and the highest PDF value coincides with the deterministic values, as shown in Figure 4.68. The stochastic μ_{slip} also displays a continuous PDF and a much wider PDF range. The highest PDF value is close to the deterministic value. The PDF is skewed upward a little bit. The PDF of μ_{total} shows the dominant influence of μ_{stick} before 1 *sec* and the dominant effect of μ_{slip} after 1 *sec*. Thus, it illustrates a much wider PDF range and a skewed upward trend. Please note that the PDF of the total CoF at around 0.4 *sec* has a much wider range than the total CoF PDF range of any one uncertainty or two uncertainties discussed above. This is because the stochastic results of all dynamic parameters of a combination of the uncertain MARR and the uncertain sleeper distance demonstrate a much wider PDF range at around 0.4 *sec* unlike the PDF results for dynamic parameters of any one uncertain parameter and any two uncertain parameters.

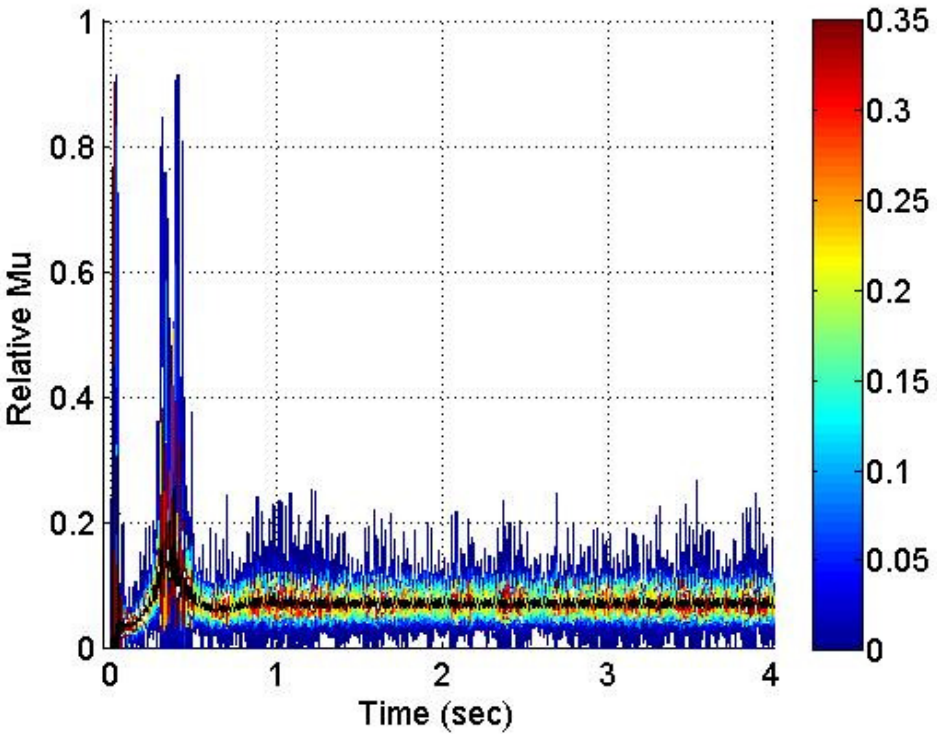

Figure 4.58 Collection (along the time axis) of the projections of the instantaneous PDF of μ_{stick} on the μ-t plane

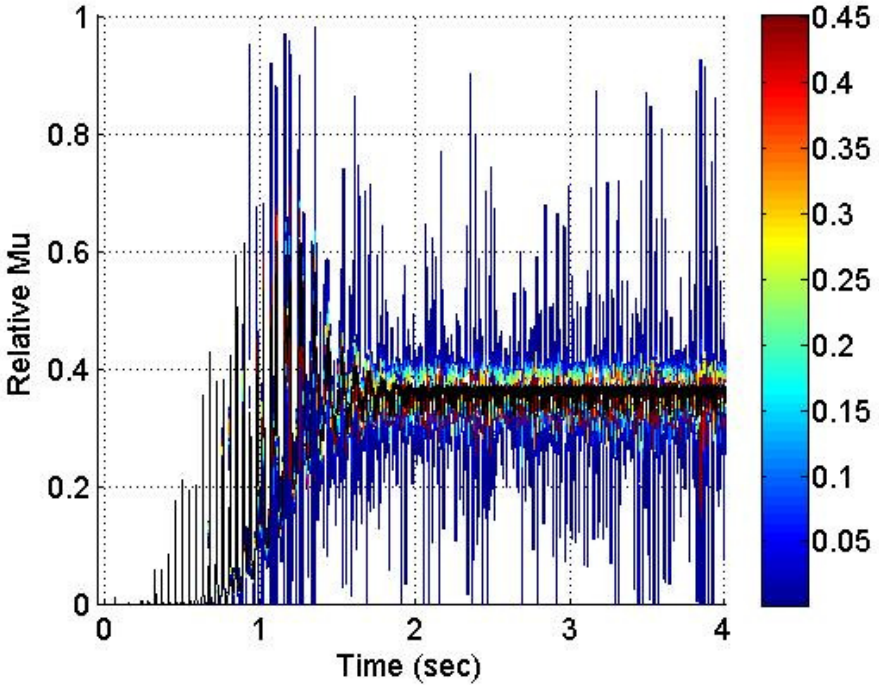

Figure 4.59 Collection (along the time axis) of the projections of the instantaneous PDF of μ_{slip} on the μ-t plane

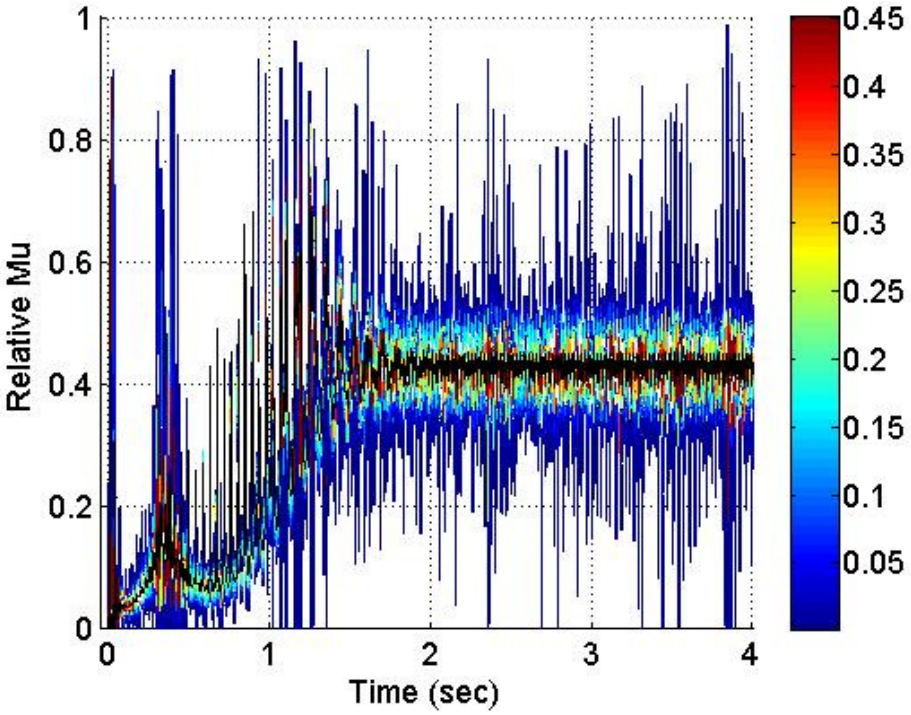

Figure 4.60 Collection (along the time axis) of the projections of the instantaneous PDF of μ_{total} on the μ-t plane

Track Stiffness and Track Damping Coefficient

In this section, the effect of a combination of the uncertain track stiffness and the uncertain track damping coefficient is calculated and analyzed. The PDFs of dynamic parameters, i.e., the relative wheel-rail vibrations, the normal contact force, and the semi-elliptical contact lengths, are illustrated in Figure 4.61 through 4.63, and the PDFs of the CoFs are demonstrated in Figure 4.64 through Figure 4.66.

The PDF of the stochastic relative wheel-rail vibration, as shown in Figure 4.61, is very similar to the PDF result of the uncertain track stiffness or the uncertain track damping coefficient. In other words, the PDF result is almost the same as the deterministic values at steady state, as illustrated in Figure 4.61 (a). The highest PDF value coincides with the deterministic value and the PDF range gets narrower with time. However, the PDF for the first 0.1 *sec*, as demonstrated in Figure 4.61 (b), shows a wider PDF range than the PDF result of one uncertain track parameter (stiffness or damping coefficient). In addition, the PDFs appear a little bit more frequently than the PDFs of the uncertain track stiffness and of the uncertain track damping coefficient. The PDF results of other dynamic parameters, i.e., the normal contact force, a, and b, and the PDF results of CoFs have the same trend as the PDF result of the stochastic h_o. This case study indicates that the effects of these uncertain track parameters on the CoFs have less influence than the other uncertain parameters on the CoFs.

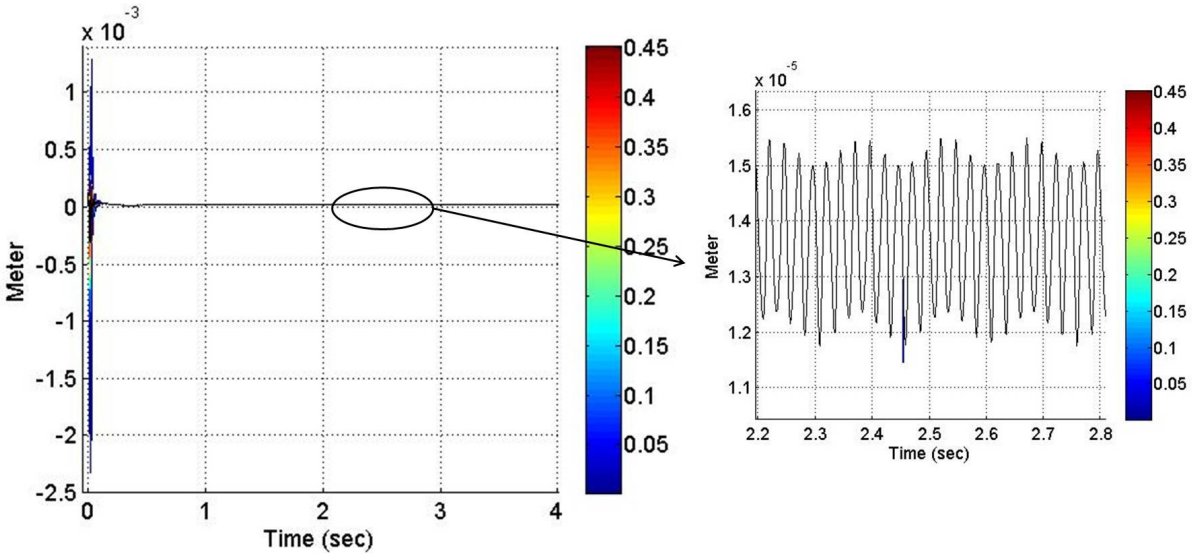

a. Collection (along the time axis) of the projections of the instantaneous PDF of h_o on the displacement-time plane, and a zoomed plot between 2.2 *sec* and 2.8 *sec*

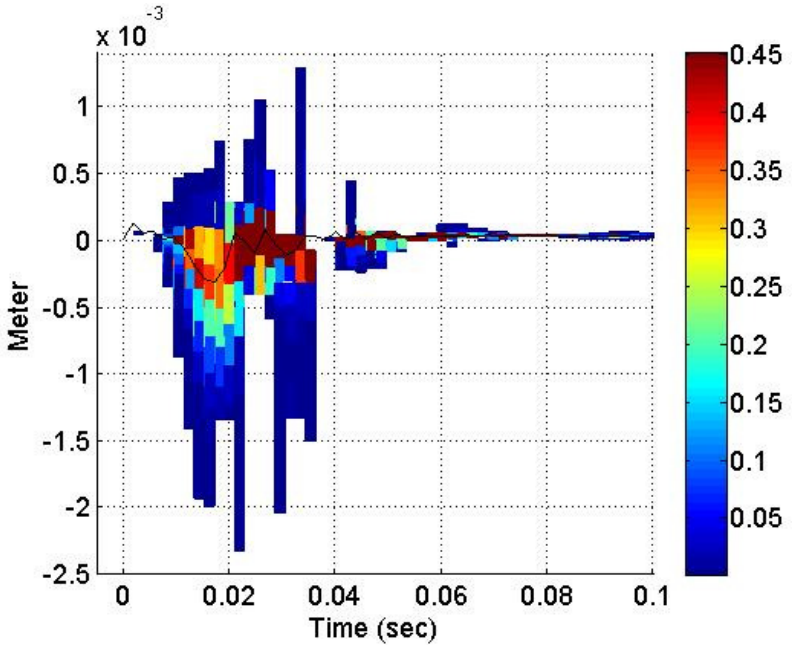

b. Collection (along the time axis) of the projections of the instantaneous PDF of h_o on the displacement-time plane for 0.1 *sec*

Figure 4.61 Collection of the projections of the instantaneous PDF of h_o

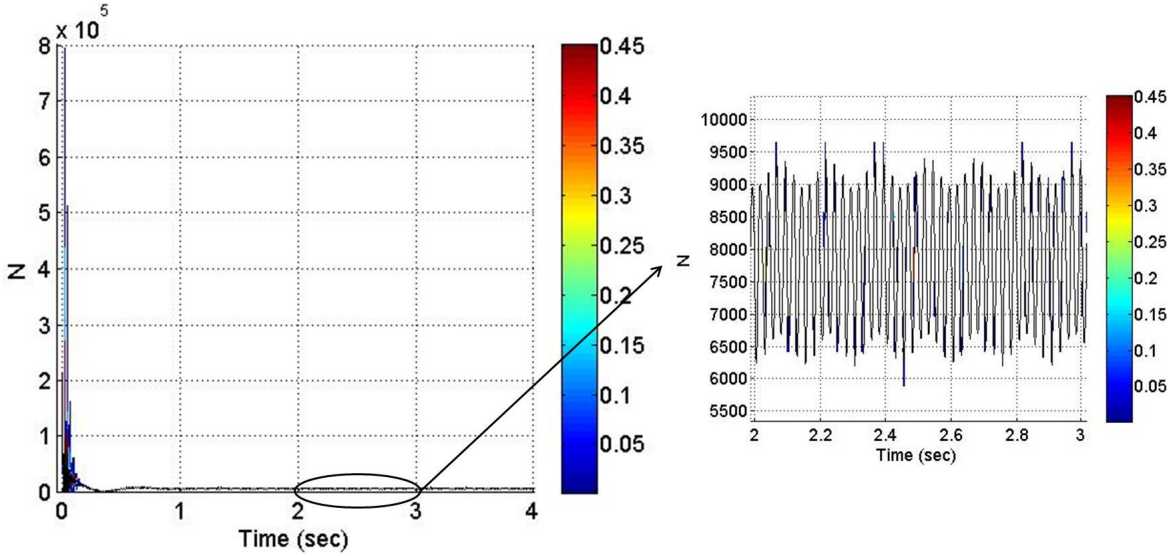

a. Collection (along the time axis) of the projections of the instantaneous PDF of F_n on the force-time plane, and a zoomed plot between 2 *sec* and 3 *sec*

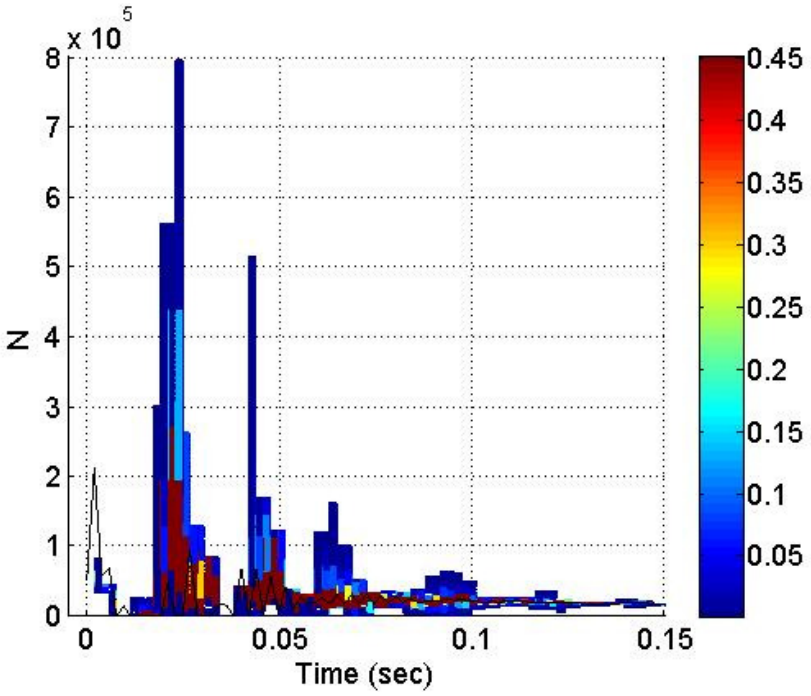

b. Collection (along the time axis) of the projections of the instantaneous PDF of F_n on the force-time plane for 0.15 *sec*

Figure 4.62 Collection of the projections of the instantaneous PDF of F_n

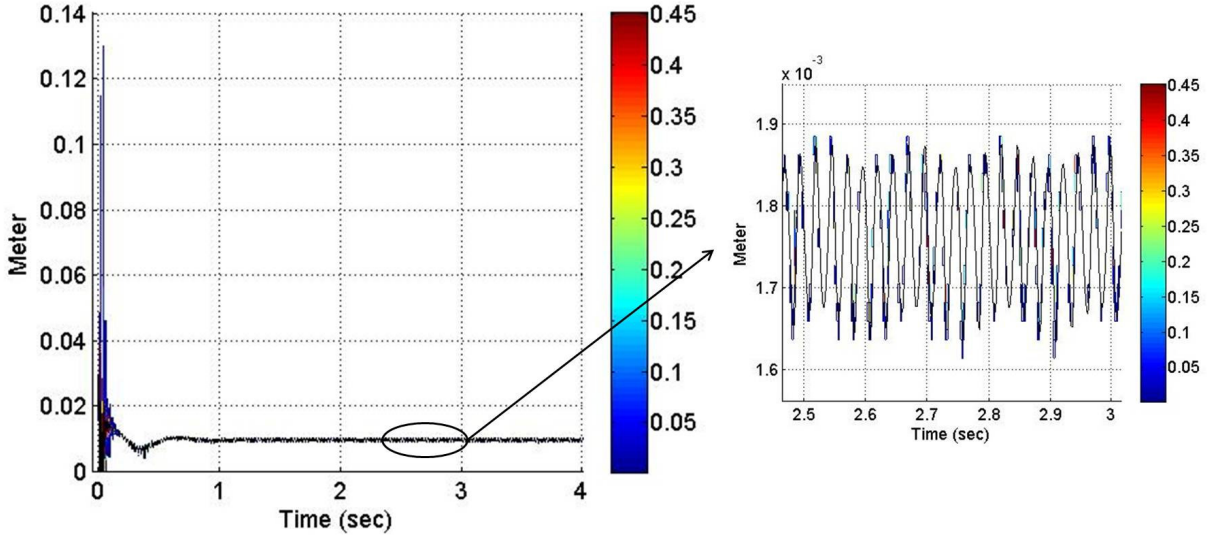

a. Collection (along the time axis) of the projections of the instantaneous PDF of *a* on the contact length-time plane, and a zoomed plot between 2.5 *sec* and 3 *sec*

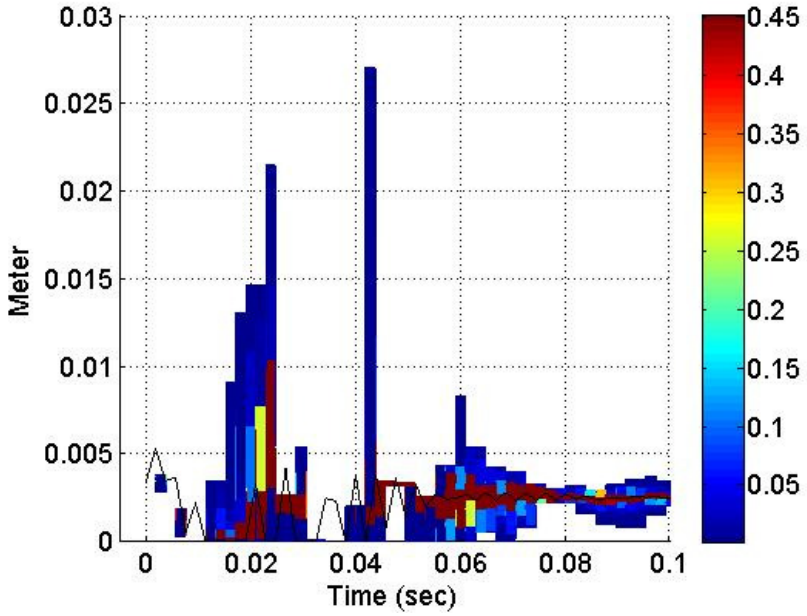

b. Collection (along the time axis) of the projections of the instantaneous PDF of *a* on the contact length-time plane for 0.1 *sec*

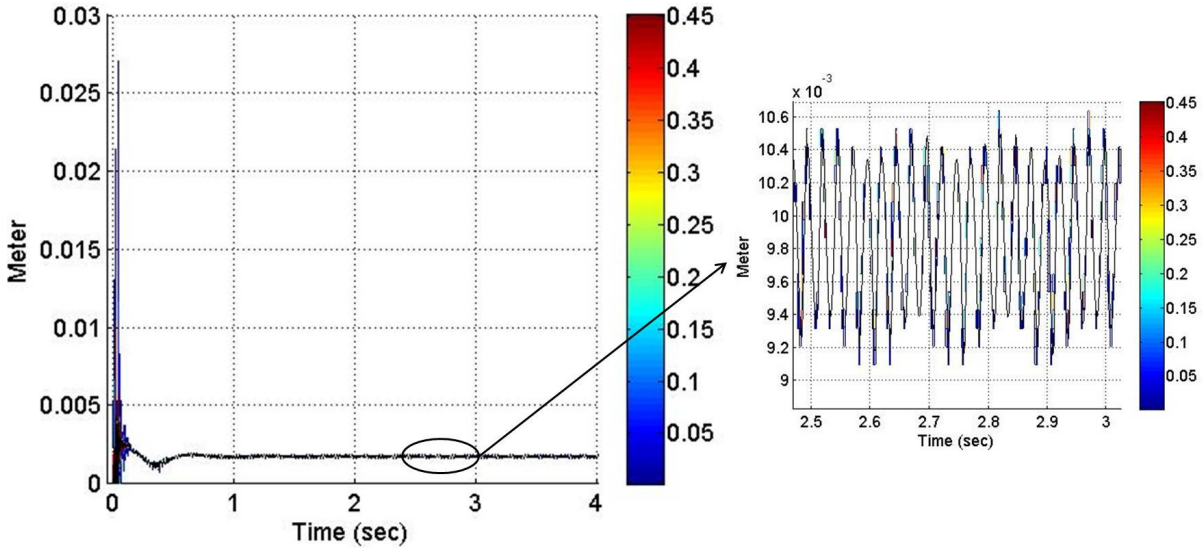

c. Collection (along the time axis) of the projections of the instantaneous PDF of *b* on the contact length-time plane, and a zoomed plot between 2.5 *sec* and 3 *sec*

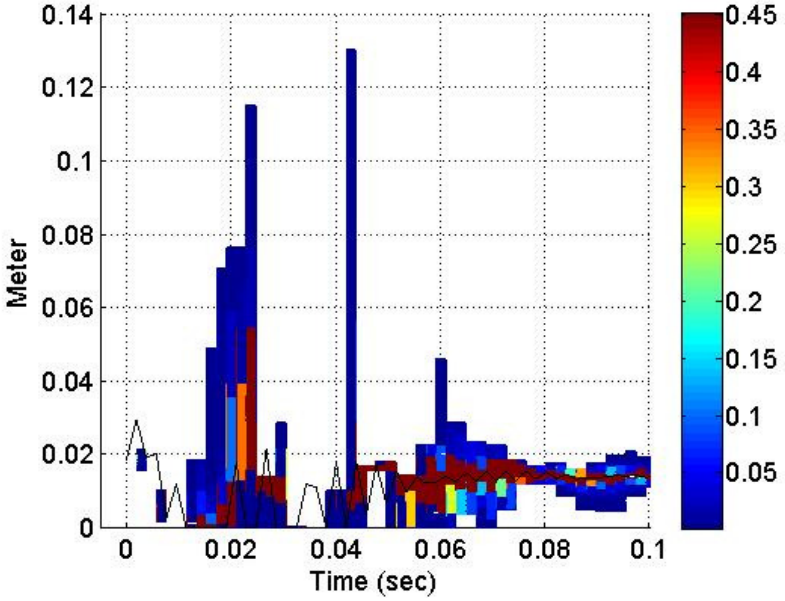

d. Collection (along the time axis) of the projections of the instantaneous PDF of *b* on the contact length-time plane for 0.1 *sec*

Figure 4.63 Collection of the projections of the instantaneous PDF of *a* and *b*

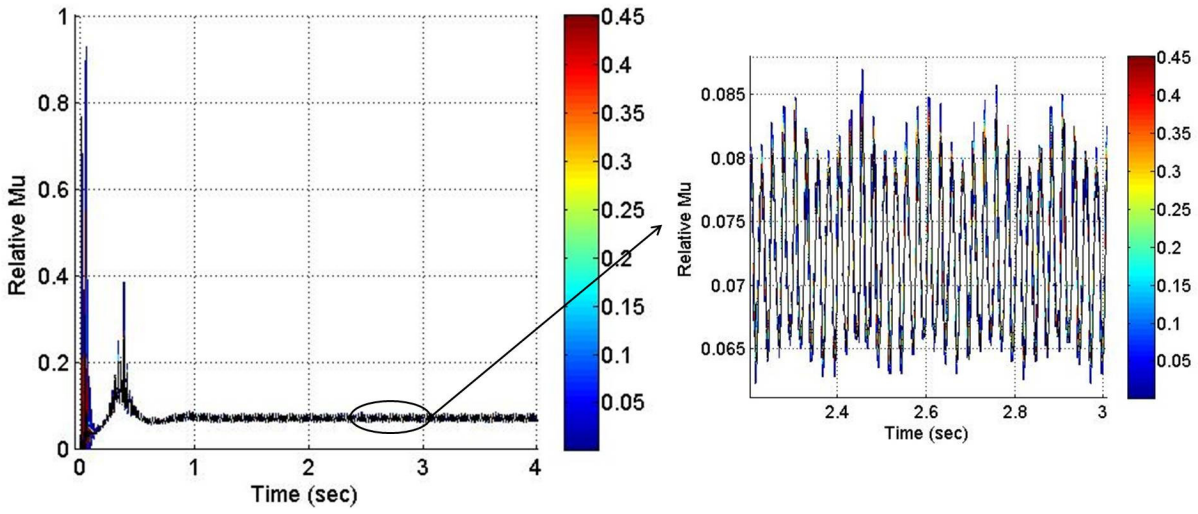

Figure 4.64 Collection (along the time axis) of the projections of the instantaneous PDF of μ_{stick} on the μ-*t* plane, and a zoomed plot between 2.5 *sec* and 3 *sec*

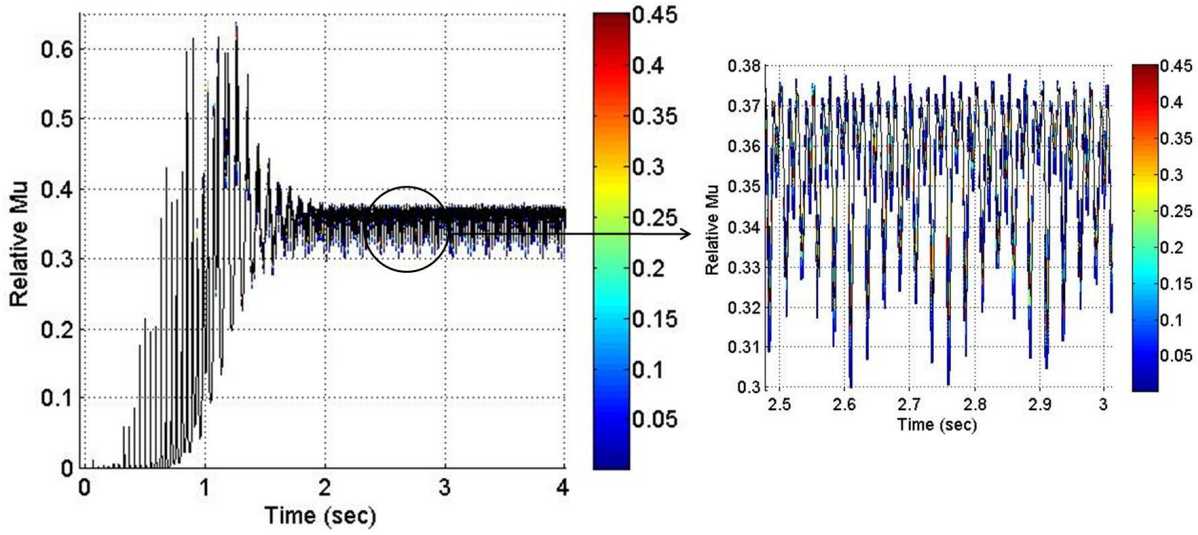

Figure 4.65 Collection (along the time axis) of the projections of the instantaneous PDF of μ_{slip} on the μ-t plane, and a zoomed plot between 2.5 *sec* and 3 *sec*

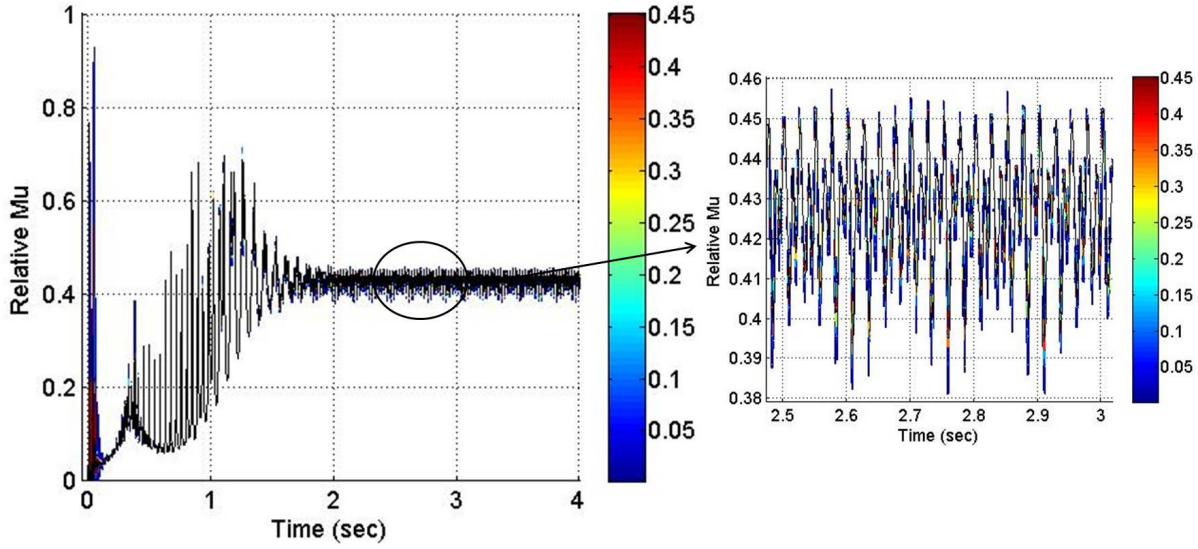

Figure 4.66 Collection (along the time axis) of the projections of the instantaneous PDF of μ_{total} on the μ-t plane, and a zoomed plot between 2.5 *sec* and 3 *sec*

4.2.3. Three Uncertain Parameters

Lateral Displacement and Semi-elliptical Contact Lengths (*a* and *b*)

This section focuses on the effect of a combination of the uncertain semi-elliptical contact lengths (*a* and *b*) and the uncertain lateral displacement on the CoF model. As explained above, the radii of curvature for the wheel and the rail are only a function of the lateral displacement. Thus, the stochastic results of radii of curvature for the wheel and the rail are exactly the same as the PDF results of the uncertain lateral displacement. Therefore, the PDF results of the CoFs are only analyzed and discussed.

The PDF results of CoFs are shown in Figure 4.67 through 4.69. The μ_{stick} PDF is skewed upward with respect to the deterministic values. It is almost the same as the μ_{stick} PDF of a combination of the uncertain *a* and *b* since the uncertain lateral displacement has very little effect on the stick CoF PDF, as explained in the case study of the uncertain lateral displacement (Figure 4.18).

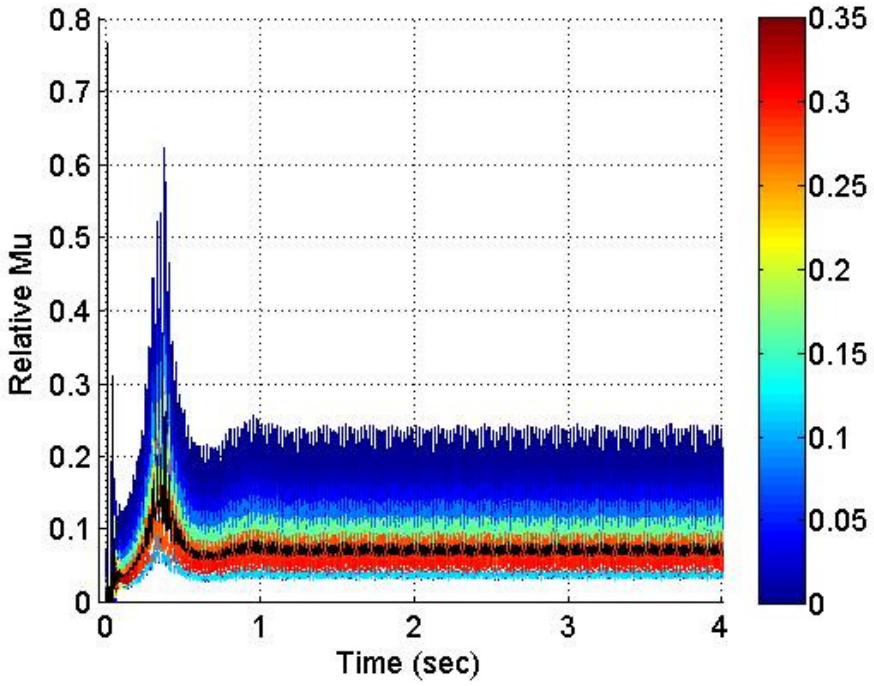

Figure 4.67 Collection (along the time axis) of the projections of the instantaneous PDF of μ_{stick} on the μ-*t* plane

The PDF of the stochastic μ_{slip} is very similar to the PDF of a combination of uncertain *a* and *b*. The stochastic μ_{slip} shows that the PDFs before 1 *sec* are like the PDF result of a combination of uncertain *a* and *b*. The stochastic μ_{slip} of three uncertain parameters demonstrates wider PDF ranges than the PDF of μ_{slip} of two uncertain parameters (*a* and *b*), as displayed in Figure 4.68, due to the effect of the uncertain lateral displacement. The highest PDF is very close to or coincides with the deterministic value until around 1.5 *sec*, and it is shifted upward with respect to the deterministic values after 1.5 *sec*. The displayed range of red coloring is narrower than that of two uncertainties (*a* and *b*) after 1 *sec*. The effects of the high frequency content increase in the PDF result of three uncertain parameters compared to the PDF result of the uncertain *a* and *b*.

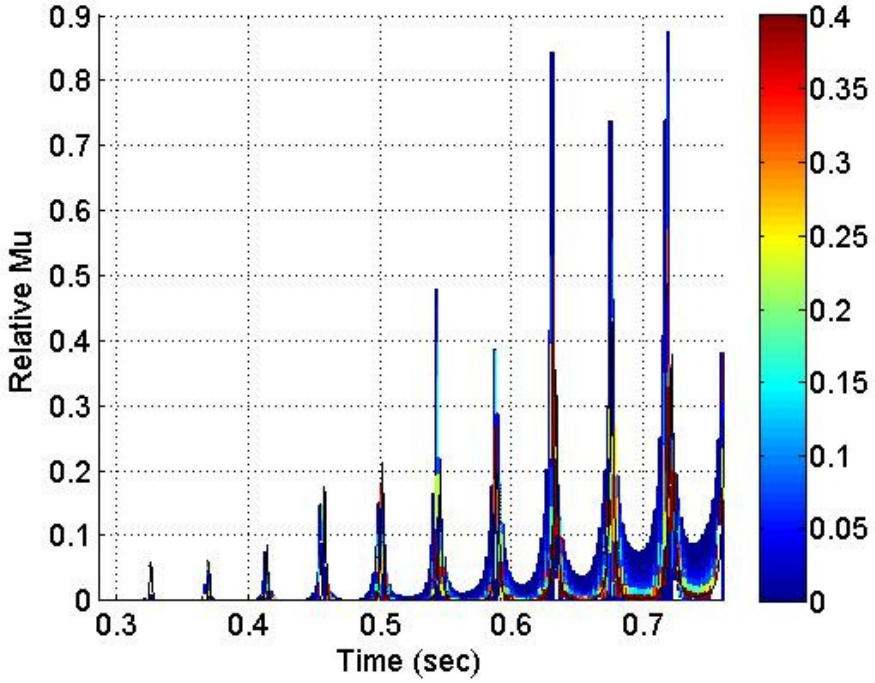

a. Collection (along the time axis) of the projections of the instantaneous PDF of μ_{slip} on the μ-*t* plane for 0.75 *sec*

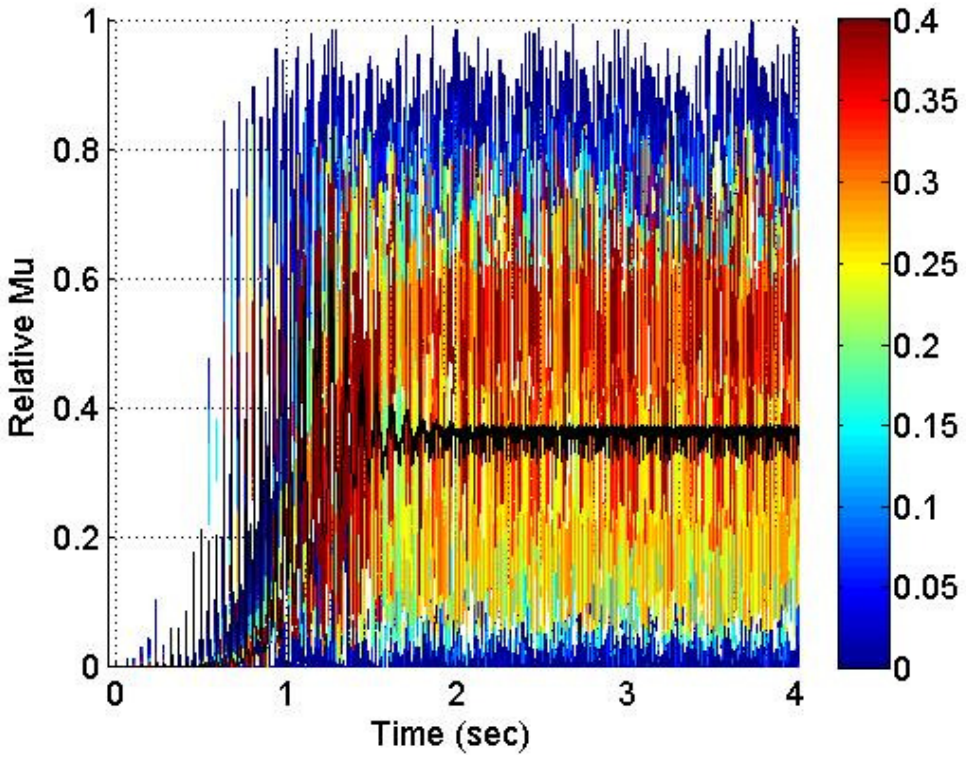

b. Collection (along the time axis) of the projections of the instantaneous PDF of μ_{slip} on the μ-t plane through entire simulation

Figure 4.68 Collection of the projections of the instantaneous PDF of μ_{slip}

The μ_{total} PDF, as illustrated in Figure 4.69, has a skewed PDF trend since both stick and slip CoF PDFs are skewed. The highest PDF is shifted upward after 1 *sec* since the PDF of μ_{slip} has the dominant effect on the total CoF PDF after 1 *sec*, as explained above. The difference between the total CoF PDF for a combination of the uncertain *a* and *b* and for a combination of the uncertain a, *b*, and the lateral wheel displacement, is that including the third uncertain parameter produces a PDF for the relative CoF with a slightly wider highest probability range. In addition, it increases the effect of the high frequency content compared to a combination of the uncertain *a* and *b*. The difference between the μ_{total} PDF of the uncertain *a* and *b* and the μ_{total} PDF of the uncertain a, *b*, and lateral wheel displacement is very small.

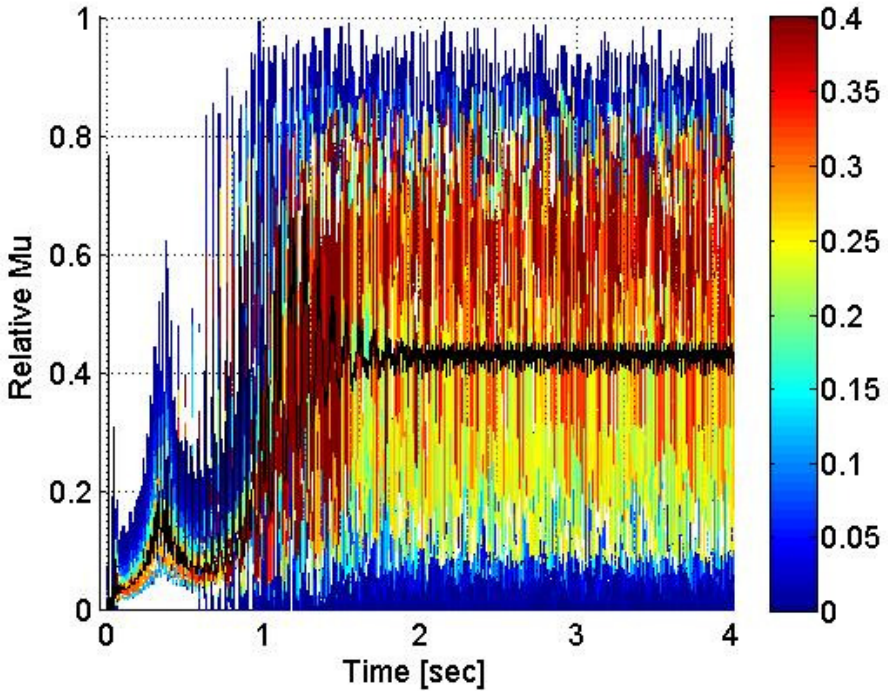

Figure 4.69 Collection (along the time axis) of the projections of the instantaneous PDF of μ_{total} on the μ-t plane

MARR, Track Stiffness, and Sleeper Distance

This section illustrates the effect of a combination of uncertain MARR, uncertain track stiffness, and uncertain sleeper distance on the CoF and on several dynamic parameters (relative wheel-rail vibrations, normal contact force, and semi-elliptical contact lengths). The PDF results for the CoFs and for the dynamic parameters are calculated and analyzed.

The PDFs of the dynamic parameters are shown in Figure 4.70 through Figure 4.72. The general PDF trend of h_o for a combination of three uncertain parameters (MARR, track stiffness, and sleeper distance) is very similar to the stochastic result of a combination of two uncertainties (MARR and sleeper distance). In other words, some PDFs are skewed upward while others are skewed downward with respect to the deterministic value. The highest PDF values coincide with the deterministic values, and the PDF range becomes narrower with time. However, the PDF result of h_o for a combination of three uncertain parameters shows a wider range of PDF than the combination of the uncertain MARR and the uncertain sleeper distance. The PDFs appear more frequently at the steady state than the PDFs of two uncertain parameters (MARR and sleeper

distance). In addition, the effects of the high frequency content increase in the PDF result of three uncertain parameters as compared to the PDF result of the uncertain MARR and sleeper distance. The PDF results of other dynamic parameters (the normal contact force, *a*, and *b*) have the same trend as the PDF result of the stochastic h_o.

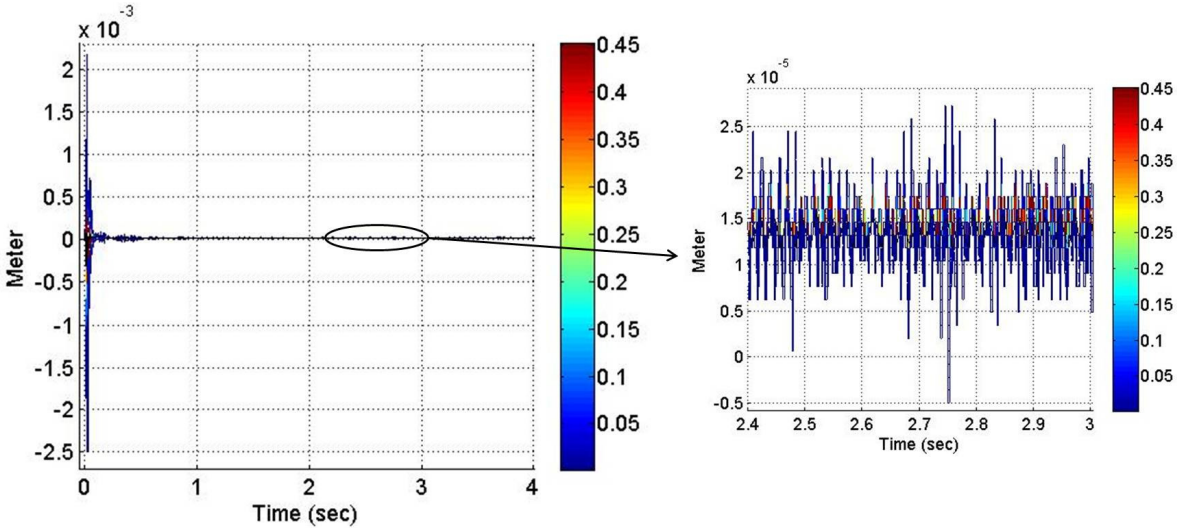

a. Collection (along the time axis) of the projections of the instantaneous PDF of h_o on the displacement-time plane, and a zoomed plot between 2.4 *sec* and 3 *sec*

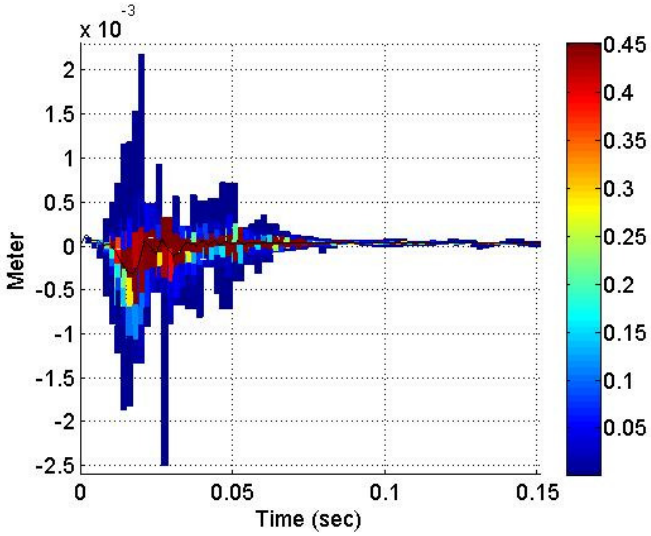

b. Collection (along the time axis) of the projections of the instantaneous PDF of h_o on the displacement-time plane for 0.15 *sec*

Figure 4.70 Collection of the projections of the instantaneous PDF of h_o

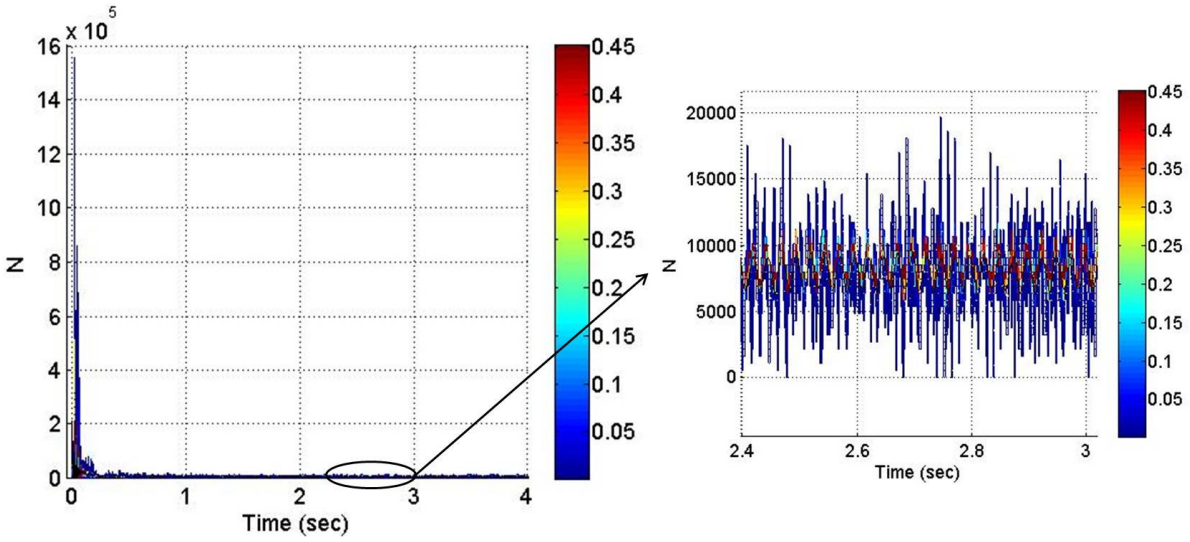

a. Collection (along the time axis) of the projections of the instantaneous PDF of F_n on the force-time plane, and a zoomed plot between 2.4 *sec* and 3 *sec*

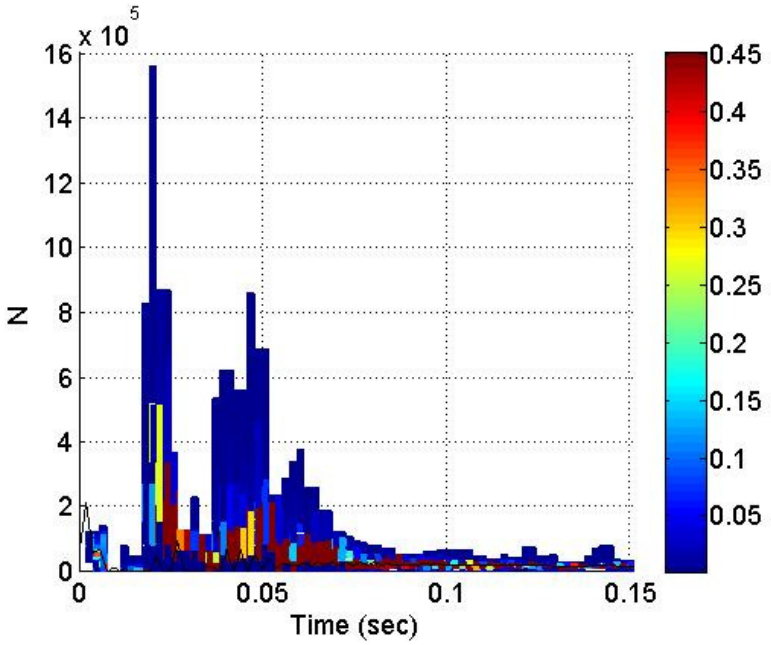

b. Collection (along the time axis) of the projections of the instantaneous PDF of F_n on the force-time plane for 0.15 *sec*

Figure 4.71 Collection of the projections of the instantaneous PDF of F_n

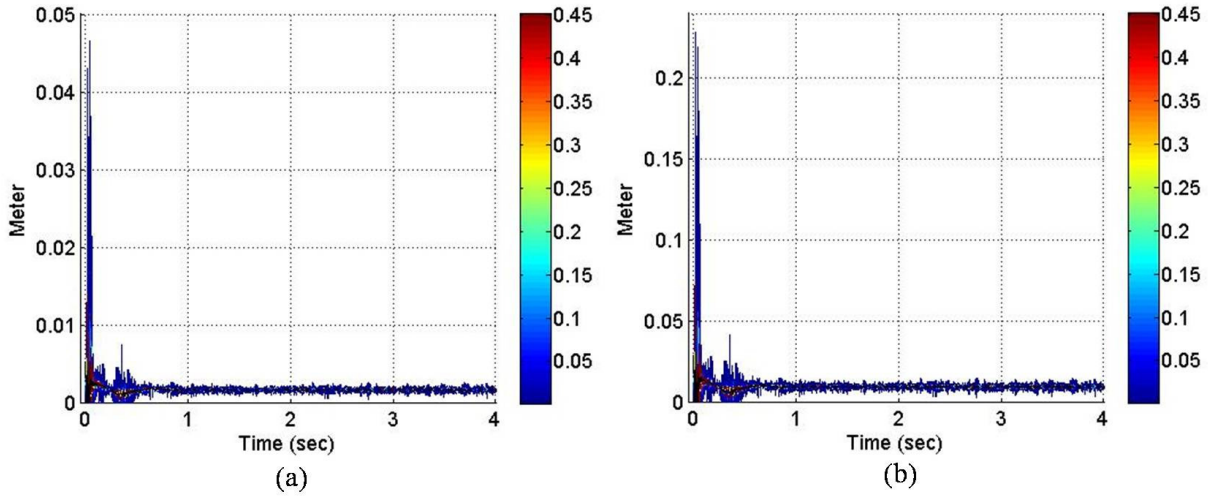

Figure 4.72 Collection (along the time axis) of the projections of the instantaneous PDF of *a* and *b* on the contact length-time plane: (a) *a* and (b) *b*

The PDFs of the CoFs are illustrated in Figure 4.73 through 4.75. The PDFs of the CoFs (μ_{stick}, μ_{slip}, and μ_{total}) for a combination of uncertain MARR, track stiffness, and lateral displacement do not demonstrate wide PDF ranges compared to the CoFs PDF results of a combination of uncertain MARR and uncertain sleeper distance. Contrary to other CoFs PDF results, the PDFs of three uncertainties have similar or slightly narrower ranges than the PDFs of two uncertainties (uncertain MARR and uncertain sleeper distance). However, the effect of the high frequency content increases in the PDF result of three uncertain parameters as compared to that of two uncertainties (uncertain MARR and uncertain sleeper distance). The PDF is slightly skewed upward since the PDFs directed downward with respect to the deterministic values have a limit, i.e., zero CoF value. The highest PDF values are very close to the deterministic values. As with other stochastic total CoF results, the PDF of μ_{total} is dominantly influenced by the stick PDF results before 1 *sec* and the slip PDF results mainly affect on the total stochastic results after 1 *sec*. The PDF at around 0.4 *sec* shows a wide PDF range due to the effect of the uncertain sleeper distance. This range is wider than the PDF range for a combination of uncertain MARR and uncertain sleeper distance due to the additional effect of the uncertain track stiffness. This case study demonstrates that the effect of the uncertain track stiffness needs to be considered to accurately design the wheel-rail-track system although its influence on the CoFs is not dominant.

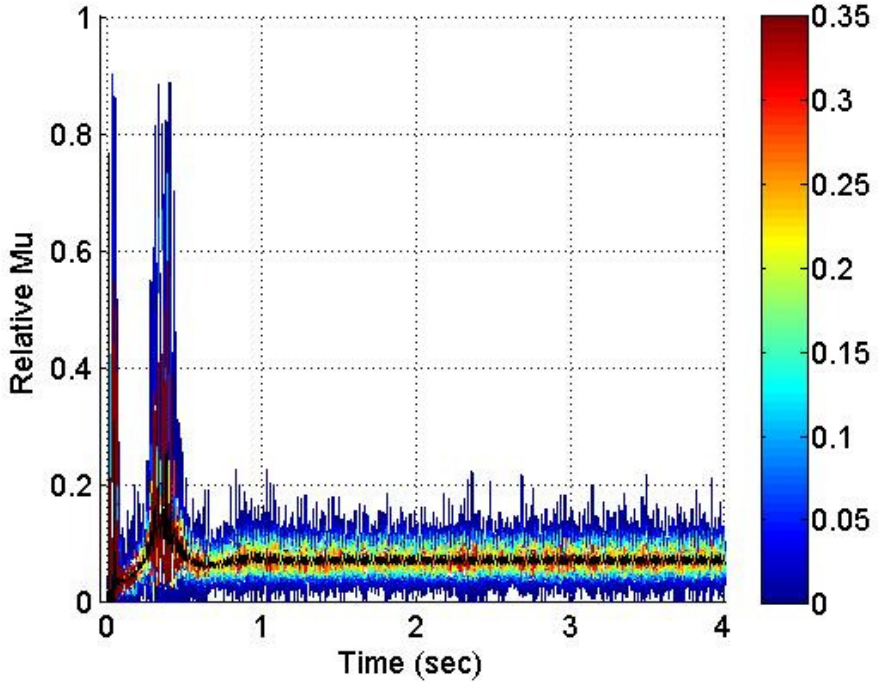

Figure 4.73 Collection (along the time axis) of the projections of the instantaneous PDF of μ_{stick} on the μ-t plane

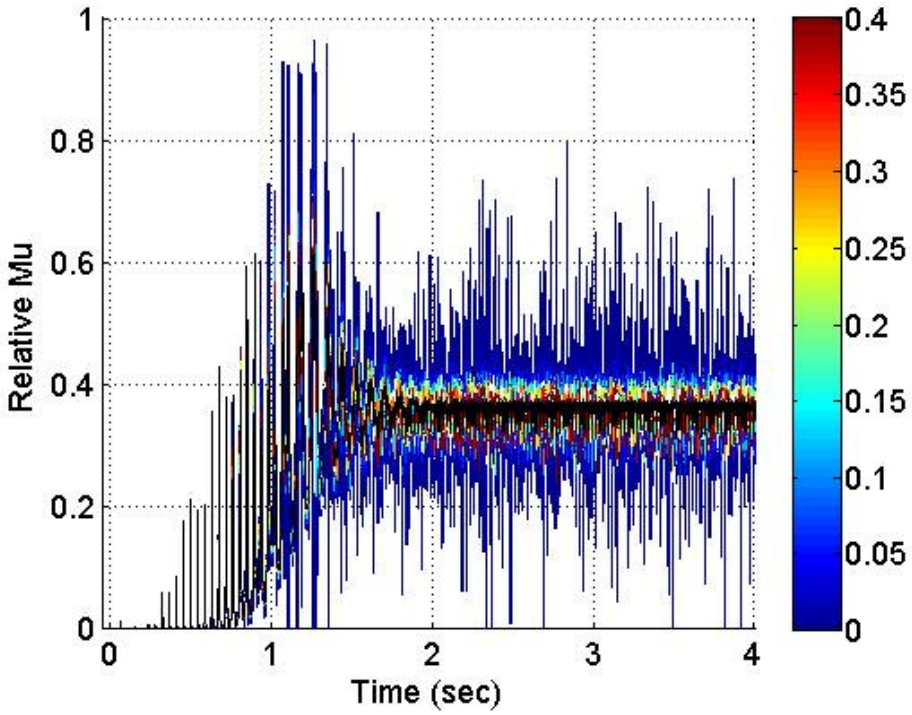

Figure 4.74 Collection (along the time axis) of the projections of the instantaneous PDF of μ_{slip} on the μ-t plane

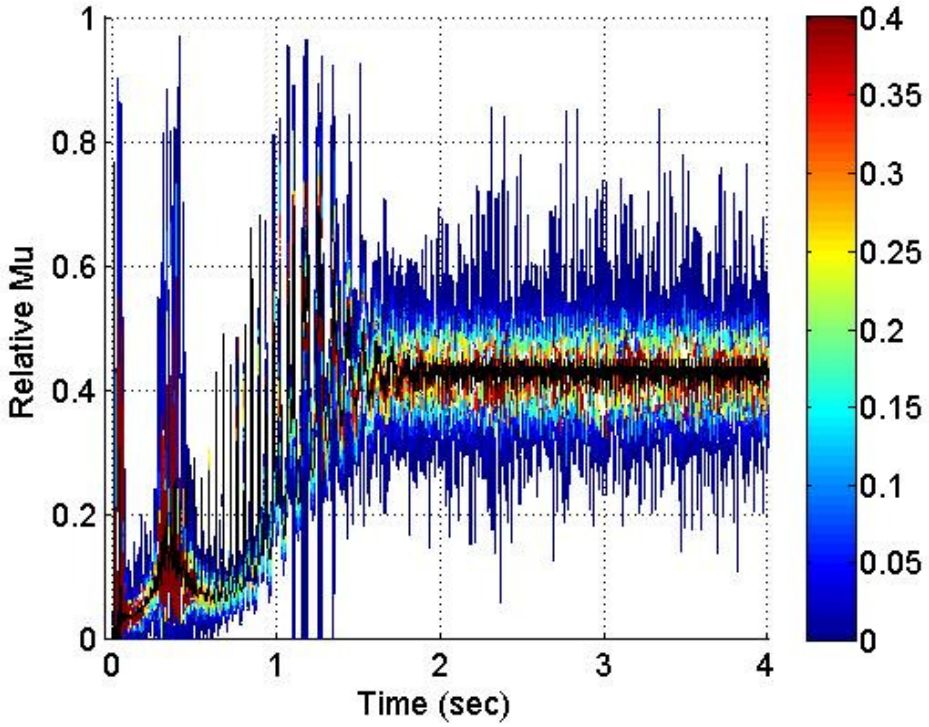

Figure 4.75 Collection (along the time axis) of the projections of the instantaneous PDF of μ_{total} on the μ-t plane

4.3 Qualitative Validation

Simulation results from the deterministic model and from the stochastic model with one, two, and three uncertainties were shown in Section 4.1 and 4.2 with no experimental validation. Experimental validation data was not included since obtaining quantitative data is beyond the scope of the current work. Further, the experimental data available to date, while qualitatively validating the modeling results in a generic sense, does not allow a direct comparison with model outputs. However, Fast Fourier Transform (FFT), frequency domain analysis may be able to provide some qualitative validation of the model's ability to accurately reflect a real-world physical system. FFT analysis of the stochastic model temporal results will inherently show different trends from the FFT analysis of the deterministic results, but again, both analyses should support key observations of the physical system if the modeling is valid and relevant to a real world observation. In this section, FFT analysis of the deterministic results is compared with the FFT analysis of the stochastic results.

An FFT analysis of the deterministic modeling results is illustrated in Figure 4.76. In this figure, the total CoF, the vertical wheel displacement, and the rail displacement results as a function of time are analyzed in the frequency domain using FFT methods. The rotational frequency of the wheel (angular velocity, ω) and encounter frequency of the sleeper (sleeper distance, *dist*) are considered in this study, as they appear in the modeling results. The rotational frequency of the wheel and the sleeper encounter frequency can be calculated from Equations 4.1 and 4.2, respectively. For a simplified calculation, the mean wheel radius of curvature, r_o, replaces the wheel radius of curvature, r. The rotational frequency of the wheel (f_w) according to Equation 4.1 is 6.9 *Hz* for the track speed used in the model simulations. The FFT analyses of both the wheel and rail temporal displacements yield a value of 7 *Hz* for f_w. The FFT result is reasonable since the wheel radius of curvature varies with time, as shown in Figure 4.4 and its average value over the duration of the FFT analysis window will therefore be slightly modified relative to a deterministic equation. In other words, the variation of r leads to the 0.1 *Hz* shift to higher frequencies. In this study, the sleeper distance is 0.6 *m*. According to Equation 4.2, given the simulation rail speed of 20 *m/s*, the sleeper encounter frequency ($f_{sleeper}$) is calculated to be 33.3 *Hz*. However, FFT analysis of the wheel and rail displacements yields a value of 40.25 *Hz* for $f_{sleeper}$ with an attendant wide bandwidth. This wide bandwidth occurs when the parameter under analysis is influenced by various other factors to yield variance in time. If a parameter signal is not contaminated and is not influenced by nonlinear effects (i.e., mixing, modulation, etc.) or other dynamic parameters the FFT analysis would show a very sharp peak with a very narrow bandwidth like a pure sinusoidal signal. Thus, the wide bandwidths shown in this study indicate that the system is highly nonlinear and that the rail displacement is influenced by the coupling between various other dynamic parameters, as well as being affected directly by the rail roughness. FFT analysis of the total CoF result (previously shown in Figure 4.1, blue line) also demonstrates: wide bandwidth; a shifted rotational frequency; and component frequency peaks after 40 *Hz* (as compared with the FFT analysis results of the wheel and rail displacements). This analysis of the deterministic results supports a conclusion that the CoF has highly nonlinear relationship with the dynamic parameters given in section 4.1. In contrast, the FFT analysis of the rail displacement temporal results shows f_w and $f_{sleeper}$ as the results of purely linear processes. Thus, the FFT analysis supports qualitative validation of the deterministic model.

.

Natural frequency of the wheel angular velocity $\left(f_{\omega}\right)$

$$f_{\omega}=\frac{V_{train}}{2\pi r}\left(\omega=\frac{V_{train}}{r}\ and\ \omega=2\pi f_{\omega}\right) \tag{4.1}$$

Natural frequency of the sleeper distance $\left(f_{sleeper}\right)$

$$f_{sleeper}=\frac{V_{train}}{dist} \tag{4.2}$$

$$y(t)=A(t)\cos(\omega(t)t+\phi(t))$$

Amplitude modulation (AM): modulate A(t)

Frequency modulation (FM): modulate $\omega(t)$ (4.3)

Phase modulation (PM): modulate $\phi(t)$

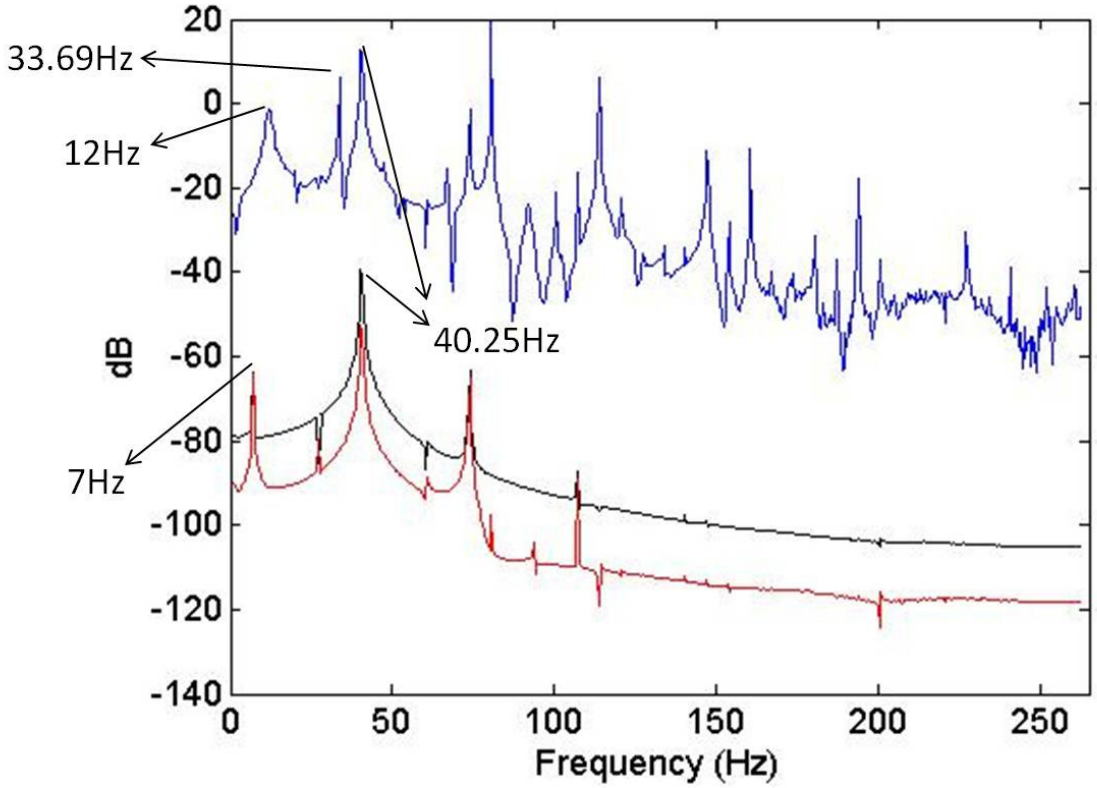

Figure 4.76 FFT analysis results of the deterministic modeling results for total CoF (blue line), the vertical wheel displacement (black line), and the rail displacement (red line)

A comparative FFT analysis of the deterministic rail displacement and of the stochastic rail displacement (conducted using directly the data obtained from the collocation method) with

the uncertain sleeper distance is illustrated in Figure 4.77. The effect of the uncertain sleeper distance is well illustrated by the red line used for the stochastic condition. The rotational frequency of the wheel is shifted from 7 *Hz* to 11.81 *Hz* and the signal's bandwidth is broadened. The average sleeper encounter frequency does not change relative to the deterministic case; however side bands are added to the right side of the frequency a result of temporal modulation by the stochastic rail displacement. Thus, adding uncertain sleeper distance results in the bandwidth broadening of both signals, a shifted rotational frequency, and the side band occurrence. These results are due to the various mixing and modulation effects (i.e., amplitude modulation (AM), frequency modulation (FM), and phase modulation (PM), as shown in Equation 4.3) imposed on the equation parameters by the addition of a 50% uncertainty factor in the sleeper distance [97].

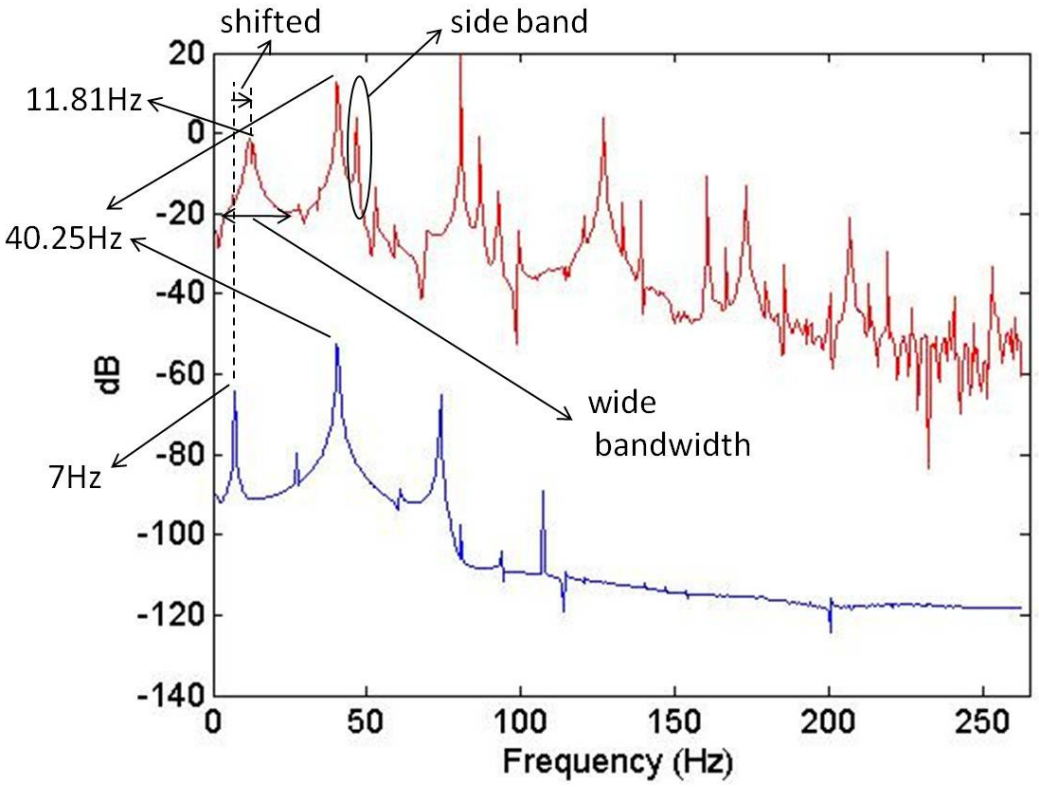

Figure 4.77 FFT analysis of the rail displacement: deterministic result (blue line) compared to a stochastic result with uncertain sleeper distance (red line, one uncertainty)

Figure 4.78 displays the FFT analysis of the deterministic rail displacement results compared with: the stochastic rail displacement results with one uncertainty (uncertain sleeper distance); two uncertainties (uncertain MARR and sleeper distance); and three uncertainties (uncertain MARR, track stiffness, and sleeper distance). The rotational frequency of the wheel does not show differences between the deterministic case and the cases with one, two, and three uncertainties. In other words, the bandwidth is almost the same and the rotational frequency is the same for all simulation conditions. However, the frequency component associated with the sleeper encounter rate shows significant variances between cases. The peak sleeper encounter frequency is still 40.25 *Hz*, but the side bands shift to low frequencies side with increasing uncertainty. As an example, the side band with one uncertainty (uncertain sleeper distance) appears to the right side (46.81 *Hz*) of the natural frequency of sleeper encounter at 40.25 Hz. The side band with two uncertainties (uncertain MARR and sleeper distance) shifts to the left side of the peak at 32.38 *Hz*. The side band with three uncertainties (uncertain MARR, track stiffness, and sleeper distance) shifts to 28 *Hz*. This trend of side band shifts leads to a conclusion that high frequency content is lost with increasing uncertainty in the system. The stochastic analysis previously showed that the total CoF range is also getting wider with the addition of more uncertain parameters (section 4.2). Thus, more energy from the wheel-rail system is changed into heat due to the wider range of the total CoF reducing the effective wheel traction. This means that more energy is dissipated and tractive efficiency is lost when more uncertainties are properly accounted for than it has been conventionally understood. This physical phenomenon matches well with the trend of the side band shifting with increasing uncertainty and the limited field data available from LIDAR wheel slip measurements.

The FFT analysis of the deterministic rail displacement and of the stochastic rail displacement with uncertainties demonstrates that consistent trends commensurate with loss of tractive efficiency, such as the bandwidth broadening, peak frequency shifts, and side band occurrence. Thus, the FFT analysis validates qualitatively that fact that the stochastic modeling with various uncertainties is well executed and is reflecting observable, real-world results. The effort of using the FFT analysis in this study also illustrates that the FFT itself can be a good method for the qualitative validation of the numerical simulations when comprehensive experimental data is not available.

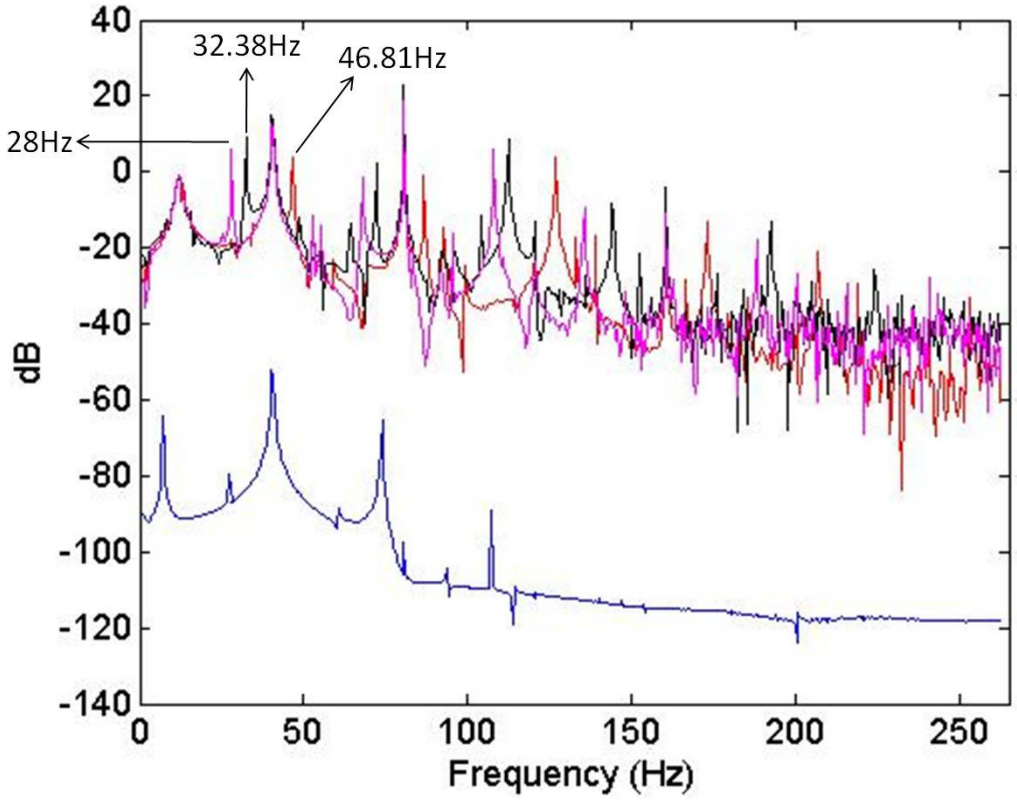

Figure 4.78 FFT analysis of the rail displacement: the deterministic result (blue line), the stochastic result with uncertain sleeper distance (red line), the stochastic result with uncertain MARR and sleeper distance (black line), and the stochastic result with uncertain roughness, track stiffness, and sleeper distance (magenta line)

4.4 Summary

In this chapter, wheel-rail dynamics model is simulated for the deterministic model to analyze the impact on the CoF newly developed for dry rail conditions. The polynomial chaos theory is applied for the stochastic analysis. The results from the deterministic model show acceptable vibration results for the body, the wheel, and the rail. Most parameters which are estimated for the deterministic model show significant variation during first 0.1 *sec* and then become steady at around 2 *sec*. The CoF model estimates the stick CoF component and the slip CoF component separately as well as the total CoF which combines the stick CoF and the slip CoF. The CoF model successfully captures the maximum CoF value and the CoF results show the nonlinear variation with time.

The simulation for the stochastic model using the polynomial chaos theory has also been performed in this study. Six uncertain parameters have been studied with an assumption of 50% uncertainty. A symmetric beta distribution is assumed for these six uncertain parameters. The PDF of the CoF has been obtained for each uncertain parameters study, for a combination of two different uncertain parameters, and also for a combination of three different uncertain parameters. The PDF results with the uncertain track stiffness and the uncertain track damping coefficient are similar to the deterministic results. The uncertain lateral displacement influences only the slip CoF. The other three uncertain parameters have a significant impact on the CoF variation. The uncertain sleeper distance induces the unique PDF trend, i.e., the direction of PDF distribution is not consistent. Most of the PDF results on the CoF illustrate skewed symmetric distribution, although a symmetric beta distribution is assumed for the uncertain input parameter. The combined two uncertain parameters lead to a wider distribution than those obtained for the individual effects of these parameters. The combination of a and b has the widest PDF ranges from 0 to almost 1 and it shows that the highest probability values are shifted upward with respect to deterministic results. The combination of three uncertain parameters results in a PDF range that is narrower and an increased high frequency impact as compared to the combination of two uncertain parameters.

The FFT analysis has been performed for the quantitative validation of the stochastic simulation results since the experimental data are not provided in this study. The FFT analysis

of the rail displacement shows that results of the FFT analysis with the stochastic results are significantly different from result of FFT analysis with the deterministic results. These differences are consistent with the uncertain parameters, and they match the physical phenomenon well.

Chapter 5. Conclusions and Future Work

This chapter provides a summary of this study followed by the conclusions. The conclusions of this study follow after a summary. Future work that should be conducted in this area of research is also discussed.

5. 1 Summary

A dynamic wheel-rail model has been developed to study the wheel-rail dynamic parameters and the CoF. The dynamic wheel-rail model is based on a mass-spring-damper system. This model can capture the most relevant dynamic parameters and CoFs related to the wheel-rail dynamics. The model accounts for wheel-rail contact, creepage effect, and creep force, among others. The new 3-D nonlinear CoF model for dry rail conditions is developed based on the Soom's 2-D model. This newly developed nonlinear model includes many of the possible dynamic parameters that could potentially influence the CoF. In this study, the simulation scenario considered a train traveling at 20 *m/s* for 4 *sec.*

Dynamic simulation has been performed for the deterministic model developed to analyze the impact of different parameters on the CoF. Moreover, an extensive analysis has been performed in the stochastic framework, by employing a polynomial chaos approach, as described in Chapter 4. The results from the deterministic model show acceptable vibration results for the body, the wheel, and the rail. The dynamics results of the deterministic model provide the starting point for the uncertainty analysis. Six uncertain parameters have been studied with an assumption of 50% uncertainty, intentionally imposed for testing extreme conditions. These parameters are: the maximum amplitude of rail roughness (MARR), the wheel lateral displacement, the track stiffness and damping coefficient, the sleeper distance, and semi-elliptical contact lengths. A symmetric beta distribution is assumed for these six uncertain parameters, although the methodology is general, and other types of distributions could be employed. The PDF of the CoF has been obtained for each uncertain parameter study, for a

combination of two different uncertain parameters, and also for a combination of three different uncertain parameters.

The stochastic results with one uncertainty show that the response of the system with the track stiffness and with the track damping coefficient is similar to the deterministic results. The other three uncertain parameters, MARR, *a/b*, and sleeper distance, influence the CoF in a significant manner, while the lateral displacement affects only the slip CoF, i.e., the stick component of the CoF remains close to its deterministic values. The uncertain sleeper distance induces the widest range of values for the CoF, but the direction of PDF distribution is not consistent. When investigating the combined effects of two independent uncertain parameters, it has been noticed that the combined two uncertain parameters leads to a wider distribution than those obtained for the individual effects of these parameters. Compared to other combination of two uncertainties, the uncertain track stiffness and damping coefficient has minor influence on the CoF. The remarkable results of the combination of *a* and *b* are that the highest probability values are shifted upward with respect to the deterministic results and the PDF ranges from 0 to almost 1. The combination of three uncertain parameters results in a PDF range that is narrower and an increased high frequency impact as compared to the combination of two uncertain parameters.

The FFT analysis has been performed for the qualitative validation of the stochastic simulation results due to the absence of the experimental data. The FFT analysis of the total CoF results reflects the various effects of the dynamic parameters. Thus, the FFT analysis of the rail displacement is used as an example study. Results of the FFT analysis with stochastic results illustrate a remarkable difference from the results of the FFT analysis with the deterministic results. These differences include the band width broadening, the side band, and the peak frequency shift. These trends are consistent with the uncertain parameters, and they match the physical phenomenon well.

5.2 Conclusions

From the results obtained, we conclude that:

1) A dynamic wheel-rail model and a new 3-D CoF model have been developed in this study. Due to the difficulties in capturing such complex phenomena in a deterministic model and the limited ability to collect detailed experimental data on such systems, an alternative technique was investigating to help deepen the understanding of wheel-rail contact. Thus, it has been shown in this study that the stochastic modeling approach is a viable venue for estimating the wheel-rail dynamics and the CoF.
2) The novelty of the newly developed nonlinear dry CoF model is that it simultaneously includes all major factors that impact the CoF variation in three dimensions. This model demonstrates the nonlinear variation of the total CoF, the stick component, and the slip component. In addition, it captures the maximum CoF value (initial peak) successfully.
3) The CoF results do not illustrate temporal similarity with evolution of any of the other dynamic parameters studied in this dissertation. Thus, the CoF has a highly nonlinear dependence on those parameters.
4) Hertzian stiffness reaches the steady state value very quickly. Thus, it can be replaced by a constant number for ease of implementation.
5) The uncertainties in the track stiffness and in the damping coefficient do not have substantial effect on the CoF, i.e., the response of the system is similar to the deterministic results. The other three uncertain parameters, MARR, *a/b*, and sleeper distance, influence the CoF in a significant manner. The lateral displacement affects only the slip CoF, and the stick component of the CoF remains close to its deterministic values.
6) The sleeper distance must be considered when the track is designed to control the CoF at the wheel-rail contact since it shows a unique PDF distribution trend such as the widest range of values for the CoF and the inconsistent PDF direction.
7) Although a symmetric distribution has been used for the uncertain parameters considered, the uncertainty in the response obtained displayed a skewed distribution for some of the situations investigated. This is due to the high degree of nonlinearity of the system analyzed. This phenomenon indicates that a stochastic analysis is necessary to provide correct CoF ranges with the highest probability zone for accurate design of the wheel-rail system and of the track system.

8) The stochastic CoF result for a combination of the uncertain *a* and *b* ranges from 0 to almost 1. Adding uncertain lateral displacement to this combination, i.e., three independent uncertainties, does not show remarkable difference from the stochastic CoF result of these two uncertainties (*a* and *b*). Thus, the uncertain semi-elliptical contact lengths are the most important parameters to characterize the CoF variation and to estimate the CoF ranges correctly. In addition, the semi-elliptical contact lengths cannot be directly measured from the real locomotive due to the limitation of the current technology, but they can be theoretically calculated. However, the deterministic calculation of the semi-elliptical contact lengths leads to an overestimate or an underestimate. Thus, the semi-elliptical contact lengths must be calculated through the stochastic approach.
9) The results of the FFT analysis show that it can be a good method for the qualitative validation of the numerical simulation when experimental data are not available.

In conclusions, the development of an effective model which helps understand the nonlinear nature of wheel-rail friction is critical to the progress of railroad component technology and rail safety. In the real world, accurate estimation of the CoF at the wheel-rail interface is very difficult since it is influenced by several uncertain parameters as illustrated in this study. Using the deterministic CoF value can cause underestimation or overestimation of CoF values leading to inaccurate decisions in the design of the wheel-rail system. Thus, the possible PDF ranges of the CoF according to key uncertain parameters must be considered in the design of the wheel-rail system.

5.3 Future Work

The future work should include:

1) The deterministic wheel-rail dynamics model is developed in this dissertation. In the wheel-rail dynamics simulation, the effective rail vibrating length was assumed to be the same as the sleeper distance in order to calculate the rail mass. In order to improve the simulation accuracy of the wheel-rail vibration, an accurate effective rail mass must be found from experimental data. In addition, relative CoF values are provided in this study

since the experimental data are not currently available. To validate the newly developed dry CoF model in a quantitative manner, experimental data are necessary to extract *c* coefficients. Thus, the experimental study is necessary to find the accurate effective rail mass and to validate the CoF model quantitatively.

2) The wheel-rail dynamics are only simulated for a tangential track in this study. The wheel-rail dynamics and the CoF variation of a curved track are different from those of the tangential track. Thus, further research can be focused on modeling the wheel-rail dynamics and the CoF variation for a curved track.

3) The 3-D dry CoF model is developed in this study. The CoF is directly related to the fuel consumption. If we can estimate the CoF changes accurately, then we can also predict the fuel consumption accurately. The traction force formulation proposed by Mazilu [96] includes the CoF term, as shown in Equation (5.1).

$$F_{traction} = -\frac{2F_n\mu_{total}}{\pi}\left(\frac{\varepsilon}{1+\varepsilon^2} + \arctan\varepsilon\right) \qquad \varepsilon = \frac{\pi}{4}\frac{abC_{11}G}{F_n\mu_{total}}\sqrt{\xi_{long}{}^2 + \xi_{lat}{}^2} \tag{5.1}$$

where $F_{traction}$ is the traction force and ε is the gradient of the tangential stress in the area of adhesion. Figure 5.1 is the stochastic result of the traction force achieved by using Equation 5.1 as an example. The model of the traction force is still under investigation, and it needs additional effort to better understanding and estimate accurate values.

4) This work only investigated the CoF for dry rail conditions. Top of rail (TOR) modifier is a very important factor in the railroad industry to control the CoF since it is directly related to railroad safety and fuel efficiency. It can be easily studied by expanding Soom's lubricated 2-D CoF model to a 3-D model and by developing the lubricated rail model. Thus, further research can be focused on this topic.

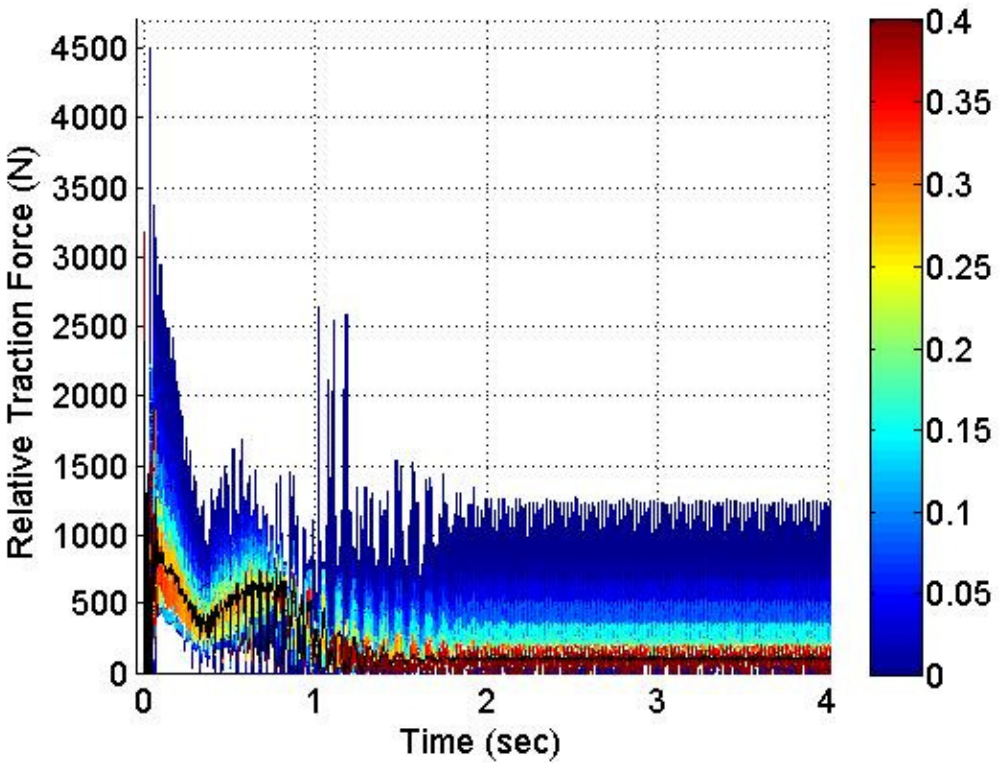

Figure 5.1 Collection (along the time axis) of the projections of the instantaneous PDF of traction force with the uncertain *a*, *b*, and lateral displacement on the force-time plane

References

1. V. L. Popov, S. G. Psakhie, E. V. Shilko, A. I. Dmitriev, 2002, "Friction Coefficient in Wheel-Rail Contacts as a Function of Material and Loading Parameters," *Physical Mesomechanics*, Vol 5, pp. 17-24.

2. F. Bucher, A. I. Dmitriev, M. Ertz, K. Knothe, V. L. Popov, S. G. Psakhie, E. V. Shilko, 2006, "Multiscale Simulation of Dry Friction in Wheel/Rail Contact," *Wear*, Vol. 261, pp. 874-884.

3. D. P. Hess, A. Soom, 1990, "Friction at a Lubricated Line Contact Operating at Oscillating Sliding Velocities," *ASME, Journal of Tribology*, Vol. 112, pp. 147-152.

4. T. Sakamoto, 1987, "Normal Displacement and Dynamic Friction Characteristics in a Stick-Slip Process," *Tribology International*, Vol. 20, pp. 25-31.

5. C. Puchalski, G. H. Brusewitz, Z. Slipek, 2003, "Coefficients of Friction for Apple on Various Surfaces As Affected by Velocity", *Agricultural Engineering International: the CIGR Journal of Scientific Research and Development*, Vol. V, Manuscript FP

6. P. R. Nayak, 1975, "Linearized Contact Vibration Analysis," *The Mechanics of Contact Between Solids*, ed. A. D. dePater and J. J. Kalker, Delft Univ. Press, pp. 393-414.

7. G. G. Gray, K. L. Johnson, 1972, "The Dynamic Response of Elastic Bodies in Rolling Contact to Random Roughness in Their Surfaces," *Journal of Sound and Vibration*, Vol. 22, pp. 323-342.

8. A. Soom, C. Kim, 1983, "Roughness-Induced Dynamic Loading at Dry and Boundary-Lubricated Sliding Contacts," *ASME, Journal of Lubrication Technology*, Vol. 105, pp. 514-517.

9. A. Soom, J. Chen, 1986, "Simulation of Random Surface Roughness-Induced Contact Vibrations at Hertzian Contacts during Steady Sliding," *Journal of Tribology*, Vol. 108, pp. 123-127.

10. W. X. Wu, B. V. Brickle, J. H. Smith, R. K. Luo, 1998, "An Investigation into Stick-Slip vibrations on Vehicle/Track Systems," *Vehicle System Dynamics*, Vol. 30, pp. 229-236.

11. D. P. Hess, A. Soom, 1991, "Normal vibrations and Friction under Harmonic Loads: Part I – Hertzian Contacts," *ASME, Journal of Tribology*, Vol. 113, pp. 80-86.

12. D. P. Hess, A. Soom, C. H. Kim, 1992, "Normal vibrations and Friction at a Hertzian Contact under Random excitation: Theory and Experiments," *Journal of Sound and Vibration*, Vol. 153, pp. 491-508

13. A. Soom, C. H. Kim, 1983, "Interactions between Dynamic Normal and Frictional Forces during Unlubricated Sliding," *ASME, Journal of Tribology*, Vol. 105, pp. 221-229.

14. C. H. Kim, 1981, "An Experimental Study of Dynamic Friction Processes at Concentrated Metallic Contacts during Sliding," *Ph.D Dissertation*, State University of New York at Buffalo.

15. D. M. Tolstoi, 1967, "Significance of the Normal Degree of Freedom and Natural Normal Vibrations in Contact Friction," *Wear*, Vol. 10, pp. 199-213.

16. D. M. Tolstoi, G. A. Borisova, S. R. Grigorova, 1973, "Friction Reduction by Perpendicular Oscillation," *Soviet Physics Doklady*, Vol. 17, pp. 907-909.

17. D. J. Thompson, 1993, "Wheel-Rail Noise generation, Part I: Introduction and Interaction Model," *Journal of Sound and Vibration*, Vol. 161, pp. 387-400.

18. D. J. Thompson, 1993, "Wheel- Rail Noise generation, Part IV: Contact Zone and Results," *Journal of Sound and Vibration*, Vol. 161, pp. 447-466.

19. T. X. Wu, D. J. Thompson, 2004, "Wheel/Rail Non-linear Interactions with Coupling between Vertical and Lateral Directions," *Vehicle System Dynamics*, Vol. 41. Pp. 27-49.

20. X. S. Jin, W. H. Zhang, J. Zeng, Z. R. Zhou, q. Y. Liu, Z. F. Wen, 2004, "Adhesion Experiment on a Wheel/Rail System and Its numerical Analysis," *Proceedings of the Institution for Mechanical Engineers, Part J: Journal of Engineering Tribolgy*, Vol. 218, pp. 293-303.

21. M. J. Rudd, 1976, "Wheel/Rail Noise – Part II: Wheel Squeal," *Journal of Sound and Vibration*, Vol. 46, pp. 381-394.

22. P. J. Remington, 1987, "Wheel/Rail Squeal and Impact Noise: What Do We Know? What Don't We Know? Where Do We Go From Here?," *Journal of Sound and Vibration*, Vol. 116, pp. 339-353.

23. U. Fingberg, 1990, "A Model for Wheel-Rail Squealing noise," *Journal of Sound and Vibration*, vol. 143, pp. 365-377.

24. F. G. de Beer, M. H. A. Janssens, P. P. Kooijman, 2003, "Squeal Noise of Rail-Bound Vehicles Influenced by Lateral Contact Position," *Journal of Sound and Vibration*, Vol. 267, pp. 497-507.

25. A. D. Monk-Steel, D. J. Thompson, F. G. de Beer, M. H. A. Janssens, 2006, "An Investigation into The Influence of Longitudinal Creepage on Railway Squeal Noise due to Lateral Creepage," *Journal of Sound and Vibration*, Vol. 293, pp. 766-776.

26. E. H. Gassenfeit, A. Soom, 1988, "Friction Coefficients Measured at Lubricated Planar Contacts during Start-Up," *ASME, Journal of Tribology*, Vol. 110, pp. 533-538.

27. D. P. Hess, A. Soom, 1991, "Normal Vibrations and Friction under Harmonic Loads: Part II – Rough planar Contacts," *ASME, Journal of Tribology*, Vol. 113, pp. 87-92.

28. D. P. Hess, A. Soom, 1992, "Normal and Angular Motions at Rough Planar Contacts during Sliding with Friction," *ASME, Journal of Tribology*, Vol. 114, pp. 567-578.

29. D. P. Hess, A. Soom, 1993, "Normal vibrations and Friction at a Hertzian Contact under Random Excitation: Perturbation Solution," *Journal of Sound and Vibration*, Vol. 164, pp. 317-326.

30. A. A. Polycarpou, A. Soom, 1995, "Boundary and Mixed Friction in the Presence of Dynamic Normal Loads: Part I – System Model," ASME, Journal of Tribology, Vol. 117, pp. 255-260.

31. A. A. Polycarpou, A. Soom, 1995, "Boundary and Mixed Friction in the Presence of Dynamic Normal Loads: Part I – Friction Transients," *ASME, Journal of Tribology*, Vol. 117, pp. 261-266.

32. A. A. Polycarpou, A. Soom, 1995, "Measured Transitions between Sticking and Slipping at Lubricated Line Contacts," *ASME, Journal of Vibration and Acoustics*, Vol. 117, pp. 294-299.

33. A. A. Polycarpou, A. Soom, 1995, "Two-Dimensional Models of Boundary and Mixed Friction at a Line Contact," *ASME, Journal of Tribology*, Vol. 117, pp. 178-184.

34. A. A. Polycarpou, A. Soom, 1996, "A Two-Component Mixed Friction Model for a Lubricated Line Contact," *ASME, Journal of Tribology*, Vol. 118, pp. 183-189.

35. V. K. Garg, R. V. Dukkipati, 1984, "Dynamics of Railway Vehicle Systems," *Academic Press*, New York.

36. D. Thompson, 2009, "Railway Noise and Vibration – Mechanisms, Modelling and Means of Control," *Elsevier*, 1st Ed., Oxford, UK.

37. A. H. Wickens, 2003, "Fundamentals of Rail Vehicle Dynamics – Guidance and Stability," *Swets & Zeitlinger Publishers*, Lisse, Netherlands.

38. S. Iwnicki, 2006, "Handbook of Railway Vehicle Dynamics," *CRC Press*, Florida.

39. L. Li, 2008, "Treatment of uncertainties in Vehicle and Terramechanics Systems Using a Polynomial Chaos Approach," *Ph.D Dissertation*, Virginia Tech.

40. E. Blanchard, 2008, "Polynomial Chaos Approaches to Parameter Estimation and Robust Control Design for Mechanical Systems with Uncertain Parameters," *Preliminary Exam Document*, Virginia Tech.

41. A. Sandu, C. Sandu, M. Ahmadian, 2006a, "Modeling Multibody Dynamic Systems with Uncertainties. Part I: Theoretical and Computational Aspects," *Multibody System Dynamics*, Vol. 15, pp. 1-23.

42. C. Sandu, A. Sandu, M. Ahmadian, 2006b, "Modeling Multibody Dynamic Systems with Uncertainties. Part II: Numerical Applications," *Multibody System Dynamics*, Vol. 15, pp. 241 - 262.

43. R. G. Ghanem, P. D. Spanos, 1990, "Polynomial Chaos in Stochastic Finite Element," *Journal of Applied Mechanics*, Vol. 57, pp. 197-202.

44. R. G. Ghanem, P. D. Spanos, 1991, "Spectral Stochastic Finite-Element Formulation for Reliability Analysis," *ASCE Journal of Engineering Mechanics*, Vol. 117, pp. 2351-2372.

45. R. G. Ghanem, P. D. Spanos, 1993, “A Stochastic Galerkin Expansion for Nonlinear Random Vibration Analysis”, *Probabilistic Engineering Mechanics*, Vol. 8, pp. 255-264.

46. R. G. Ghanem, P. D. Spanos, 2003, “Stochastic Finite Elements,” *Dover Publications Inc*, Mineola, New York.

47. R. G. Ghanem, W. Brzkala, 1996, “Stochastic Finite Element Analysis of Soil Layers with Random Interface,” *ASCE Journal of Engineering Mechanics*, Vol. 122, pp. 361-369.

48. R. G. Ghanem, S. Dham, 1998, “Stochastic Finite Element Analysis for Multiphase Flow in Heterogeneous Porous Media,” *Transport in Porous Media*, Vol. 32, pp. 239-262.

49. R. G. Ghanem, 1998, “Probabilistic Characterization of Transport in heterogeneous Media”, *Computer Methods in Applied Mechanics and Engineering*, Vol. 158, pp. 199-220.

50. R. G. Ghanem, 1999, “Stochastic Finite Elements for Heterogeneous Media with Multiple Random non-Gaussian Properties,” *ASME Journal of Engineering Mechanics*, Vol. 125, pp. 26-40.

51. O. P. L. Maitre, O. M. Knio, H. N. Najm, R. G. Ghanem, 2001, “A Stochastic Projection Method for Fluid Flow. I. Basic Formulation”, *Journal of Computational Physics*, Vol. 173, pp. 481-511.

52. O. P. L Maitre, M. T. Reagan, H. N. Najm, R. G. Ghanem, O. M. Knio, 2002, “A Stochastic projection Method for Fluid Flow. II. Random Process”, *Journal of Computation Physics*, Vol. 181, pp. 9-44.

53. M. T. Reagan, H. N. Najm, R. G. Ghanem, O. M. Knio, 2003, “Uncertainty Quantification in Reacting Flow Simulations through Non-intrusive Spectral Projection”, *Combustion and Flame*, Vol. 132, pp. 545-555.

54. S. E. Geneser, S. Choe, R. M. Kirby, R. S. MacLeod, 2005, "2-D Stochastic Finite Element Study of the Influence of Organ Conductivity in ECG," *International Journal Bioelectromagnetism*, Vol. 7, pp. 1-4.

55. S. S. Isukapalli, P. G. Georgopoulos, 1997, "Computationally Efficient Methods for Uncertainty Analysis of Environmental Models," *Proc. of the A&WMA specialty conference on Computing in Environmental Resource Management*, A&WMA VIP-68, pp. 656-665.

56. S. S. Isukapalli, P. G. Georgopoulos, 1998, "Development and Application of Methods for Assessing Uncertainty in Photochemical Air Quality Problems," *Interim Report, prepared for the U.S.EPA National Exposure Research Laboratory*, under Cooperative Agreement CR 823467.

57. S. S. Isukapalli, A. Roy, P. G. Georgopoulos, 1998, "Stochastic Response Surface Methods (SRSMs) for Uncertainty Propoagation: Application to Environmental and Biological Systems," *Risk Analysis*, Vol. 18, pp. 351-363.

58. O. M. Knio, O. P. L. Maitre, 2006, "Uncertainty Propagation in CFD using Polynomial Chaos Decomposition," *Fluid Dynamics Research*, Vol. 38, pp. 616-640.

59. D. Xiu, G. E. Karniadakis, 2002a, "The Wiener-Askey Polynomial Chaos for Stochastic Differential Equations," *Journal on Scientific Computing*, Vol. 24, pp. 619-644.

60. D. Xiu, G. E. Karniadakis, 2002b, "Modeling Uncertainty in Steady-state Diffusion Problems via Generalized Polynomial Chaos," *Computer Methods in Applied Mechanics and Engineering*, Vol. 191, pp. 4927-4928.

61. D. Xiu, G. E. Karniadakis, 2003, "Modeling Uncertainty in Flow Simulations via Generalized Polynomial Chaos," *Journal of Computational Physics*, Vol. 187, pp. 137-167.

62. D. Xiu, D. Lucor, C. H. Su, G. E. Karniadakis, 2002, "Stochastic Modeling of Flow-Structure Interactions using Generalized Polynomial Chaos," *Journal of Fluids Engineering*, Vol. 124, pp. 51-59.

63. C. Sandu, A. Sandu, B. J. Chan, M. Ahmadian, 2004, "Treating Uncertainties in Multibody Dynamic Systems using a Polynomial Chaos Spectral Decomposition," *Proceedings of the ASME IMECE*, 6th Annual Symposium on "Advanced Vehicle Technology," Paper number IMECE2004-60482, Anaheim, CA, November.

64. C. Sandu, A. Sandu, B. J. Chan, M. Ahmadian, 2005, "Treatment of Constrained Multibody Dynamic Systems with Uncertainties," *Proceedings of the SAE Congress 2005*, Paper number 2005-01-0936, Detroit, MI, April.

65. L. Li, C. Sandu, A. Sandu, 2005, "Modeling and Simulation of a Full Vehicle with Parametric and External Uncertainties," *Proceedings of the 2005 ASME Int. Mechanical Engineering Congress and Exposition*, 7th VDC Annual Symposium on "Advanced Vehicle Technologies", Session 4: Advances in Vehicle Systems Modeling and Simulation, Paper number IMECE2005-82101, Orlando, FL, November.

66. C. Sandu, A. Sandu, L. Li, 2006, "Stochastic Modeling of Terrain Profiles and Soil Parameters," *SAE 2005 Transactions Journal of Commercial Vehicles,* Vol. 114, pp. 211-220.

67. E. Blanchard, C. Sandu, A. Sandu, 2007a, "A Polynomial-Chaos-based Bayesian Approach for Estimating Uncertain Parameters of Mechanical Systems", *Proceedings of the ASME 2007 International Design Engineering Technical Conferences & Computers and Information in Engineering Conference IDETC/CIE 2007*, 9th International Conference on Advanced Vehicle and Tire Technologies (AVTT), Las Vegas, Nevada, September.

68. E. Blanchard, A. Sandu, C. Sandu, 2007b, "Parameter Estimation Method Using an Extended Kalman Filter," *Proceedings of the Joint North America, Asia-Pacific ISTVS Conference and Annual Meeting of Japanese Society for Terramechanics*, Fairbanks, Alaska, June.

69. H. Cheng, A. Sandu, 2007, "Numerical Study of Uncertainty Quantification Techniques for Implicit Stiff Systems", *Proceedings of the 45th Annual Southeast Regional Conference*, pp. 367 – 372. ACM Press New York, NY, USA.

70. J. M. Hammersley, 1960 "Monte Carlo Methods for Solving Multivariables Problems," *Annals of the New York Academy of Sciences*, Vol. 86, pp. 844–874.

71. J. H. Halton, G. B. Smith, 1964, "Radical-inverse Quasi-random Point Sequence", *Communications of the ACM*, Vol. 7, pp. 701–702.

72. S. Smolyak, 1963, "Quadrature and Interpolation Formulas for Tensor Products of Certain Classes of Functions", *Soviet Math. Dokl*., Vol. 4, pp. 240–243.

73. F. Nobile, R. Tempone, C. G. Webster, 2006 "A Sparse Grid Stochastic Collocation Method for Elliptic Partial Differential Equations with Random Input Data" Technical Report MOX 85, Politecnico di Milano, June.

74. C. G. Webster, 2007, "Sparse Grid Stochastic Collocation Techniques for the Numerical Solution of Partial Differential Equations with Random Input Data," PhD thesis, Florida State University.

75. K. L. Johnson, 1985, "Contact Mechanics," Cambridge University Press, Cambridge, UK.

76. P. J. Blau, 2009, "Friction Science and Technology – From Concepts to Applications," CRC Press, 2nd Ed., Florida.

77. K. C. Ludema, 1996, "Friction, Wear, Lubrication – A Textbook in Tribology," CRC Press, Florida.

78. A. Ruina, P. Rudra, 2009, “Introduction to Statics and Dynamics,” Oxford University Press, pp. 713.

79. R. C. Hibbeler, 2007, “Engineering Mechanics,” Pearson, Prentice Hall, 11th Ed., pp. 393.

80. J. L. Meriam, L. G. Kraige, 2002, “Engineering Mechanics,” John Willey & Sons, 5th Ed., pp. 328.

81. K. Baek, K. Kyogoku, T. Nakahara, 2008, “An Experimental Study of Transient Traction Characteristics between Rail and Wheel Low Slip and low Speed Conditions,” *Wear*, Vol. 265, pp. 1417-1424.

82. Iwnicki, S., 1999, “The Manchester Benchmarks for Rail Vehicle Simulation,” *Vehicle System Dynamics,* Vol. 31, Lisse, Netherlands.

83. J. J. Kalker, 1990, “Three-dimensional Elastic Bodies in Rolling Contact,” *Kluwer Academic Publishers*, AA Dordrecht, Netherlands.

84. J. C. O. Nielsen, 2008, “Book Chapter - Rail Roughness Level Assessment Based on High-Frequency Wheel-Rail Contact Force Measurements,” Noise and Vibration Mitigation for Rail Transportation Systems, Vol. 99, pp. 355-362.

85. T. Suzuki, M. Ishida, K. Abe, K. Koro, 2005, “Measurement on Dynamic Behavior of Track near Rail Joints and Prediction of Track Settlement,” Quarterly Report of Railway Technology Research Institute, Vol. 46, pp. 124-129.

86. A. A. Shabana, K. E. Zaazaa, H. Sugiyama, 2008, “Railroad Vehicle Dynamics – A Computational Approach,” CRC Press, Florida.

87. D. J. Thompson, 1990, “Wheel-Rail Noise: Theoretical Modelling of The Generation of Vibrations,” Ph.D. Thesis, University of Southampton.

88. T. X. Wu, D. J. Thompson, 2000, "Theoretical Investigation of Wheel/Rail Non-Linear Interaction due to Roughness Excitation," *Vehicle System Dynamics*, Vol. 34, pp. 261-282.

89. L. Frýba, 1988, "Dynamics of Rail and Track," ILR-Bericht, Vol. 58, pp. 9-38.

90. P. J. Remington, 1987, "Wheel/Rail Rolling Noise. I: Theoretical Analysis," Journal of the Acoustical Society of America, Vol. 81, pp. 1805-1823.

91. S. L. Grassie, R. W. Gregory, D. Harrison, K. L Johnson, 1982, "The Dynamic Response of Railway Track to High Frequency Vertical Excitation," Journal of Mechanical Engineering Science, Vol. 24, pp. 77-90.

92. S. Iwnicki, 2003, "Simulation of Wheel-Rail Contact Forces", Fatigue & Fracture of Engineering Material & Structures, Vol. 26, pp. 887-900.

93. A. A. Shabana, M. Berzeri, J. R. Sany, 2001, "Numerical Procedure for the Simulation of Wheel/Rail contact Dyanamics," *ASME Journal of Dynamic Systems, Measurement, and Control*, Vol. 123, pp. 168-178.

94. S. P. Timoshenko, J. N. Goodier, 1982, "Theory of Elasticity," McGraw-Hill, 3rd Ed.

95. T. A. Harris, 2001, "Roller Bearing Analysis," John Wiley & Sons, 4th Ed., New York.

96. T. Mazilu, 2007, "Some aspects about driving wheel-rail contact in steady state interaction," *10th International Conference on Tribology*, Bucharest, Romania.

97. L. W. Couch, 1997, "Digital and Analog Communications Systems", Prentice Hall, 5th Ed.

Nomenclature

c_1, c_2, c_3, c_4, c_5	coefficients of the CoF
η_o, η_i	dynamic viscosity of the lubricant [$Pa{\cdot}s$]
$V, V_{long}, V_{lat}, V_{\tan}$	sliding velocity [m/s]
V^*	dimensionless velocity parameter
R^*	dimensionless contact parameter
α	pressure viscosity coefficient [$1/Pa$]
a, b	semi-elliptical contact length [m]
F_n	normal contact force [N]
$c_{\tan}, c_{long\_contact}, c_{lat\_contact}$	damping coefficient at the contact patch [$N{\cdot}s/m$]
d	empirical constant fitted to the data
h_o	relative wheel-rail vibration [m]
$\sigma_{\tan}, \sigma_{long}, \sigma_{lat}$	surface roughness [m]
v, v^w, v^r	Poisson ratio
$V_{train}, V_{long}^w, V_{lat}^w, V_{long}^r, V_{lat}^r$	velocity [m/s]
E, E^w, E^r	Young's modulus [N/m^2]
M_b, M_w, M_r	mass [kg]
J_w	mass moment of inertia [$kg{\cdot}m^2$]
K_b, K_{lat}, K_θ	suspension stiffness [N/m]
C_b, C_{lat}, C_θ	suspension damping coefficient [$N{\cdot}s/m$]
$Area$	cross-sectional area of rail [m^2]
$dist$	sleeper distance [m]
$K_{pad}, K_{sleeper}, K_{ballast}, K_{track}$	track stiffness [N/m]
$C_{pad}, C_{sleeper}, C_{ballast}, C_{track}$	track damping coefficient [$N{\cdot}s/m$]
ρ	density [kg/m^3]

G, G_w, G_r	shear modulus of rigidity [N/m^2]
f_r	wheel excitation frequency (rail roughness) [Hz]
f_t	track excitation frequency [Hz]
γ	sinusoidal rail irregularity of wavelength [m]
K_H	nonlinear Hertzian stiffness [N/m]
R_w, R_r	radius of curvature [m]
r_o	mean wheel radius of curvature [m]
R_o	effective radius of curvature of the surfaces [m]
Ω^w, Ω^r	angular wheel velocity [$°/s$]
ψ	yaw angle [°]
$\dot{\psi}$	yaw angular velocity [$°/s$]
y	lateral displacement [m]
$\dot{y}$	lateral velocity [m/s]
l_o	half gage length [m]
λ	wheel conicisty [°]
ξ_{long}, ξ_{lat}, ξ_{spin}	creepage
F_{long}, F_{lat}, M_{spin}	creep force [N] and creep moment [$N \cdot m$]
C_{11}, C_{22}, C_{33}, C_{23}, C_{32}	Kalker's linear creep coefficient
F_v	vertical force applied to the wheel [N]
F_l	lateral force applied to the wheel [N]
M_z	moment applied to the wheel [$N \cdot m$]
z_b, z_w, z_r	vertical vibration [m]
r	rail roughness [m]
ε	gradient of the tangential stress in the area of adhesion

Appendix A

Table. The parameters that must be measured for the experimental validation

Mass

Locomotive body mass (M_b)
Wheelset mass (M_w)
Rail mass (M_r)
Wheelset mass moment of inertia (J_w)

Suspension

Vertical stiffness (K_b)
Vertical damping (C_b)
Lateral stiffness (K_{lat})
Lateral damping (C_{lat})
Yaw stiffness (K_θ)
Yaw damping (C_θ)

Track Property

Rail pad stiffness (K_{pad})
Rail pad damping (C_{pad})
Sleeper stiffness ($K_{sleeper}$)
Sleeper damping ($C_{sleeper}$)
Ballast stiffness ($K_{ballast}$)
Ballast damping ($C_{ballast}$)
Sleeper distance ($Dist$)
Cross-sectional area of rail ($Area$)

Material Property

Density (ρ)
Poisson ratio (υ)
Young's modulus (E)
Shear modulus of rigidity (G)

Velocity

Longitudinal wheel velocity (V_{long}^{w})

Longitudinal rail velocity (V_{long}^{r})

Lateral wheel velocity (V_{lat}^{w})

Lateral rail velocity (V_{lat}^{r})

Yaw angular velocity of the wheel ($\dot{\psi}$)

Angular wheel velocity (Ω^{w})

Displacement and Angle

Wheel vertical displacement (z^w)
Wheel lateral displacement (y)
Yaw angle of the wheel (ψ)

Others

Wheel conicity (λ)
Rail roughness (r)
Gage length ($2l_o$)
Mean wheel rolling radius of curvature (r_o)